On the Origin of Scales and Scaling Laws in Star Formation

Thesis by
Dávid Guszejnov

In Partial Fulfillment of the Requirements for the
Degree of
Doctor of Philosophy

Caltech

CALIFORNIA INSTITUTE OF TECHNOLOGY
Pasadena, California

2018
Defended 4/30/2018

ACKNOWLEDGEMENTS

This thesis would not have been possible without the tireless efforts of my adviser Philip Hopkins, who has been tremendously helpful from day one, AND who, when things were going poorly, always managed to find a way to rekindle my interest in research.

I would also like to thank Mark Krumholz for his patience, for all the stimulating discussions we had and for his continued help and support.

I am grateful to my former advisors Gergő Pokol, Tünde Fülöp and Attila Bencze for nurturing my interest in research and helping me start out in science.

I have been fortunate enough to be surrounded by an extraordinary group of friends at Caltech, people who not only lifted my spirit, but also inspired me to do my best.

To Chun Jun (Charles) Cao and Aidan Chatwin-Davies: Thank you for the great gaming sessions, we were a great team in all situations, be it flying a spaceship, or killing zombies.

To Mike Grudić: Thank you, not only for your great research ideas and the stimulating discussions we had about star formation, scaling laws and isothermal turbulence, but also for the great times we had together. I will never forget Chad, the barbarian dwarf who made every D&D session memorable.

To Florian Hofmann: You have been one of my first friends at Caltech. I thank you for all the fun we had together, and for teaching me that just like astrology is not astronomy, geography is not geology.

To Sinan Kefeli: Since we met at International Orientation I have always considered you my “comrade in study”, as we struggled together through courses (thank you again for helping me in GR) and the quals. Thank you for all your help.

To Muir and Rachel Morrison: You are among the most rational and open minded people I have met, I throughly enjoyed the great discussions we had. I will dearly miss our board game nights.

To Lena Murchikova: You went through hell, yet you kept your passion for science. Whether you know it or not, you are a great example of what talent and perseverance can together accomplish. Thank you for all your help in the past year and I wish you the best at IAS.

To Chris White: Talking with you always made my days brighter. You are one of the most enthusiastic and positive people I have ever met, I wish that you never change.

I thank The Dungeons & Dragons group at the Cahill Center for Astronomy. Playing with you kept me sane for the last two years of graduate school. I will always cherish the memories of being your Dungeon Master. I hope the group will endure and maybe become a TAPIR tradition.

I am thankful for the constant support that my mother and sister, Erika and Szabina Guszejnov, have provided to me through all these years. Although I could only go home every six months, those times were the highlights of my years.

Finally I would like to thank my wonderful wife Anna, who has stood by me all these years, who has believed in me even when I did not and who made this thesis a reality.

ABSTRACT

Stars are the fundamental objects of astrophysics and their formation is a key process that influences the evolution of galaxies and planets, and the development of life. Understanding how stars form is crucial even for seemingly unconnected fields of astronomy, as the interpretation of observed starlight from galaxies (even as a background) and other unresolved sources relies on our understanding of star formation. There is no comprehensive theory of star formation, despite intense effort on both the theoretical and observational sides, due to the complicated, non-linear physics involved (e.g., magnetohydrodynamics, gravity, radiation) and the enormous dynamic range of the problem. My goal has been to identify the role different physical processes (e.g., turbulence, feedback) play in star formation.

Using the semi-analytical framework that I developed, I found that a large number of star formation models are inherently sensitive to the initial conditions of the progenitor clouds (e.g., temperature). This led to another study where I predicted the expected variation of the initial mass function (IMF) of stars in a Milky-Way-like galaxy for different star formation models. I showed that IMF models where the peak is either set by turbulent properties or cooling physics (using an effective equation of state) are unable to reproduce the universal IMF of the Milky Way. I also utilized my semi-analytical tools to predict higher-order statistics of star formation: stellar correlation, multiplicity and the companion mass distribution for binaries. I showed that due to observational biases all explored models could roughly reproduce the observed multiplicity and companion mass distributions. This means that observations are currently unable to differentiate between most models.

While working on these projects I found that several scaling relations (e.g., the slopes of IMF, stellar correlation function and gas column density distribution) are insensitive to our choice of physical model; they are universal. Inspired by this I developed an analytic model that I used to show that scale-free structure formation inherently leads to these scaling relations. This provides a deep physical reason why the mass functions and correlation functions of very different systems (e.g., stars, protostellar cores, star clusters, Dark matter halos) follow roughly the same power-law relations.

My previous findings with my semi-analytical models indicated that isothermal collapse would lead to an infinite fragmentation cascade, i.e. there is no inherent low-mass cut-off. Part of the literature supports these findings and claims that additional physics is needed to imprint a mass scale into the problem, but there are theoretical models and simulations that claim that such a cut-off exists. Using GIZMO, a fully adaptive, meshless MHD code, I have carried out a convergence study and have shown that the isothermal fragmentation cascade continues to ever smaller scales without limit.

PUBLISHED CONTENT AND CONTRIBUTIONS

Guszejnov, D., Hopkins, P. F. (2015). "Mapping the core mass function to the initial mass function". In: *MNRAS* 450, pp. 4137–4149. DOI: `10.1093/mnras/stv872`.
DG participated in the conception of the project, developed the numerical code in Matlab, carried out the simulations and analyzed the results.

Guszejnov, D., Hopkins, P. F. (2016). "Star formation in a turbulent framework: from giant molecular clouds to protostars". In: *MNRAS* 459, pp. 9–20. DOI: `10.1093/mnras/stw619`.
DG participated in the conception of the project, developed the numerical code in C, carried out the simulations and analyzed the results.

Guszejnov, D., Krumholz, M. R., Hopkins, P. F. (2016). "The necessity of feedback physics in setting the peak of the initial mass function". In: *MNRAS* 458, pp. 673–680. DOI: `10.1093/mnras/stw315`.
DG participated in the conception of the project, carried out the simulations and analyzed the results.

Guszejnov, D., Hopkins, P. F., Krumholz, M. R. (2016). "Protostellar feedback in turbulent fragmentation: consequences for stellar clustering and multiplicity". In: *MNRAS* 468, pp. 4093–4106. DOI: `10.1093/mnras/stx725`.
DG participated in the conception of the project, carried out the simulations and analyzed the results.

Guszejnov, D., Hopkins, P. F., Ma, X. (2017). "Comparing models for IMF variation across cosmological time in Milky Way-like galaxies". In: *MNRAS* 472, pp. 2107–2116. DOI: `10.1093/mnras/stx2067`.
DG participated in the conception of the project and analyzed the results of previous FIRE simulations.

Guszejnov, D., Hopkins, P. F., Grudić, M. Y. (2017). "Universal Scaling Relations in Scale-Free Structure Formation". ArXiv preprint: `1707.05799`, accepted by *MNRAS*.
DG participated in the conception of the project, carried out the simulations and analyzed the results.

Guszejnov, D., Hopkins, P. F., Grudić, M. Y., Krumholz, M. and Federrath, C. (2018). "Isothermal Fragmentation: Is there a low mass cut-off?". ArXiv preprint: `1804.0857` To be submitted to *MNRAS*.
DG participated in the conception of the project, carried out the majority of the simulations (using the GIZMO code) and analyzed the results.

TABLE OF CONTENTS

LIST OF ILLUSTRATIONS

LIST OF TABLES

Number *Page*

NOMENCLATURE

Core. Protostellar core, smallest bound structure of molecular gas in a GMC. Cores are the progenitors of stars. Cores often have a protostar at their center; the ones without a protostar are refereed to as prestellar cores.

Excursion set formalism. Also known as the extended Press-Schecter formalism, a mathematical tool that allows the calculation of the statistics of objects defined by an arbitrary criterion in a stochastic density field. This is achieved by effectively mapping the problem onto random walks. The formalism was first applied in astrophysics to explain the distribution of dark matter (see Bond et al., 1991; Press & Schechter, 1974).

GMC. Giant Molecular Cloud, the largest bound structures of molecular gas in a galaxy. Most stars form inside such clouds.

IMF. Initial Mass Function, the mass distribution of newly formed stars, a key quantity in astrophysics.

IMF turnover mass. The IMF is observed to follow a power-law at higher masses in both the MW and neighboring galaxies. The mass scale below which it starts deviating from this power-law is often referred to as the IMF turnover mass. Note that since the turnover mass is within a factor of 2 of the IMF peak, the two terms are sometimes used interchangeably..

ISM. Interstellar Medium, the gas/plasma and radiation between star systems in a galaxy.

MHD. Magnetohydrodynamics, the study of the evolution of a fluid that is coupled to a magnetic field.

Protostar. A young star that is still accreting material from its gas reservoir, usually a protostellar disk.

Salpeter slope. The canonical power-law slope of the Milky Way's IMF ($\mathrm{d}N/\mathrm{d}M \propto M^{-2.35}$), first observed by Salpeter (1955).

Scale-free process. A process is considered scale-free if it contains no physical scales except the ones defined by the initial condition. Example: realizations of the Cantor-set or other fractals are scale-free .

Chapter 1

OVERVIEW

1.1 Motivation

Star formation is a key process of cosmic evolution that influences the formation of galaxies and planets, and the development of life. It influences virtually every field in astrophysics on all scales, from reionization of the Universe by the first stars (Gpc-Mpc scale), through the evolution of galaxies (kpc-pc) to the development of habitable planets (AU-km). Even though it is vital to our understanding of the Universe, there is no comprehensive theory of star formation, despite intense effort on both the theoretical and observational sides, due to the large amount of complicated, non-linear physics involved.

Star formation includes a wide range of physical phenomena: both super- and subsonic turbulence, magnetic fields, weakly ionized plasmas, continuum and line radiative processes compounded by complex chemical processes and (of course) gravity. These by themselves would be enough to make the search for a comprehensive theory of star formation extremely hard. The difficulty is further compounded by the wide dynamic range of the problem: the process of star formation is initiated in giant molecular clouds (GMCs), which are $\mathcal{O}\left(10-100\,\mathrm{pc}\right)$ in size, and eventually lead to the formation of $\mathcal{O}\left(R_{\odot}\right)\sim 10^{-8}\mathrm{pc}$ size protostars and stars. On these different size scales the system is governed by wildly different physics. On the largest, GMC scales the system can be modeled as supersonic, isothermal gas undergoing gravitational collapse (which is an extreme simplification of the problem, yet it is still poorly understood, see Chapter 8). On smaller scales the isothermal assumption breaks down (e.g. high opacity leads to inefficient cooling), while chemistry and magnetic fields are no longer negligible, making the modeling of such problems extremely complicated (see Klessen et al., 2011; Krumholz, 2014; McKee & Ostriker, 2007a, for detailed overviews of the theoretical and numerical challenges).

One of the most popular high level pictures of star formation is the "gravito-turbulent" model of star formation (see Fig. 1.1). In these models the initial evolution of gas clouds (part of which will eventually turn into stars) is governed by the interplay between gravity and turbulence, with gravity pushing the cloud towards local collapse, while random turbulent motion stabilizes it

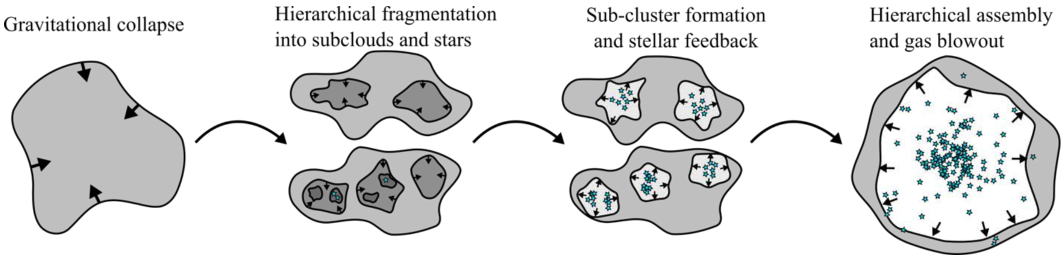

Figure 1.1: Cartoon illustration of the star formation process in the "gravito-turbulent" picture. An unstable molecular clouds undergoes gravitational collapse, while supersonic motions create self-gravitating subregions that collapse on their own. This leads to the hierarchical fragmentation of the cloud. Once some of these fragments become stars, their feedback unbinds the rest of the gas, terminating the star formation process. After the gas is blown out the remaining stars rearrange themselves into sub-clusters, which merge to form larger clusters, see Grudić et al. (2017).

against global collapse (see e.g., Padoan et al., 1997). Although turbulence is a stabilizing force on large scales, supersonic turbulence leads to the creation of high-density subregions (e.g. through shocks), which might be self-gravitating and thus start collapsing on their own. This leads to a hierarchical fragmentation (Ballesteros-Paredes et al., 2011b), which is terminated when the collapsing fragments reach the point that they turn into stellar-mass clumps. The feedback from the stars that form out of these unbinds the rest of the gas (stopping the formation of new stars), and the already formed stars rearrange themselves into clusters.

One of the most compelling questions in the field of star formation is the origin of the *IMF* (initial mass function), the mass distribution of newly formed stars. Observations in the Milky Way (MW) have found this quantity to be remarkably universal and independent of the age of the stellar population or the local galactic environment (see Bastian et al., 2010; Offner et al., 2014). The universality of the IMF in old stellar populations in the MW is widely taken as a suggestion that it may be near-universal in other galaxies, because older populations in the MW formed when the galaxy was much younger and very different, likely a typical high-redshift, gas-rich, metal-poor dwarf galaxy. There are indirect constraints on the IMF both from spectral features and integrated mass-to-light constraints in nearby galaxies: these mostly also favor a universal IMF (e.g. Andrews et al., 2013, 2014; Fumagalli et al., 2011; Koda et al., 2012; Weisz et al., 2015). More recently there have been more interesting hints of variation in the centers of massive elliptical galaxies (see Cappellari et al., 2012; Conroy & van Dokkum, 2012; Martín-Navarro et al., 2015c; Parikh et al., 2018; Posacki et al., 2015; Sonnenfeld et al., 2015; Treu et al., 2010; van Dokkum & Conroy, 2010). It should be noted that these variations of the IMF are well-correlated with changes in metallicity (Parikh et al., 2018), which might indicate that the inferred variations are due to poorly constrained stellar evolution models at high metallicity, and not a non-universal IMF.

Qualitatively the IMF is well approximated by a power-law at high masses ($\mathrm{d}N/\mathrm{d}M \propto M^{-2.35}$, see Salpeter 1955) and a turnover around $0.2\,\mathrm{M}_{\odot}$, fit either by a broken power-law (Kroupa, 2002) or a lognormal (Chabrier, 2005) distribution. A significant part of my research has been devoted to identifying what physical processes could be responsible for setting this characteristic scale of the IMF, considering its near-universality in the Milky Way (see Chapters 2-6). The universal power-law tail of the IMF is also an intriguing question, but in this case the challenge does not come from finding a theory that predicts a universal slope, but from the fact that nearly all theories of star formation predict a slope close to the observed value ("gravito-turbulent" models like Hennebelle & Chabrier 2008; Hopkins 2012b; Padoan et al. 1997, "competitive-accretion" models like Bonnell et al. 2007; Larson 1982; Zinnecker 1982 or even "fractal ISM" models like Chappell & Scalo 2001; Elmegreen 1997; Elmegreen & Falgarone 1996, see Chapter 7), making it difficult to distinguish between IMF models even if they are based on very different physics.

In summary, my work has addressed a number of pertinent questions of star formation, such as:

- What could set the IMF peak? (Chapters 2-5)
- Which IMF models are consistent with the universal MW IMF? (Chapter 5)
- Is there a one-to-one mapping between protostellar cores and stars? (Chapter 2)
- Why are stars clustered? (Chapters 6-7)
- Why is it so easy for models to reproduce the IMF power-law tail? (Chapter 7)
- What sets the column density distribution of star forming gas? (Chapter 7)

- Does the observed stellar multiplicity and companion distributions constrain star formation models? (Chapter 6)
- What happens when an isothermal cloud undergoes collapse? (Chapter 8)
- Is there a characteristic scale of isothermal turbulence and does it influence star formation? (Chapter 8)

The rest of this chapter is devoted to short summaries of my projects. The subsequent chapters contain my published works on these questions.

1.2 Semi-Analytical Modeling of Star Formation

Analytical models of star formation are useful for understanding the principal mechanism behind different observed phenomena. One of the most popular ideas is to assume that the formation of gas clouds (that will eventually turn into stars) is governed by the interplay between gravity and turbulence. For such models it is possible to "borrow" the *excursion set formalism*, a mathematical tool set originally used to explain the large scale structure of dark matter (Bond et al., 1991; Press & Schechter, 1974). This usually involves modeling the density field on different scales around a random point. As we go to smaller and smaller scales the average density fluctuates stochastically, allowing us to redefine the problem as a random walk. The properties of this random walk are prescribed by the stochastic properties of the density field, which in this case is often approximated with a lognormal distribution that is spatially uncorrelated (motivated by simulations of turbulent media, e.g. Kritsuk et al., 2011; Vazquez-Semadeni, 1994). Such models are able to predict several key properties of bound structures in dense gas, e.g. their mass function (Hennebelle & Chabrier, 2008; Hopkins, 2012a; Padoan & Nordlund, 2002). Since these models do not include the effects of gravity (other than using it to define structures), their results can be thought of as the instantaneous mass functions of bound objects (without accounting for further evolution) that make them the theoretical equivalents of the observed protostellar cores. Since these models calculate the properties of a randomly chosen point mass just as gravity is "turned on", it is hard to predict the time evolution and spatial structure of star formation (see e.g., Hennebelle & Chabrier, 2013a).

1.2.1 Expanding the Excursion set Formalism of Hopkins (2012b)

In my first project I expanded on the work done by Hopkins (2012b) by implementing time evolution, based on Hopkins (2013c). While the original excursion set model provided the equivalent of the observed core mass function (CMF), my expansion allowed it to follow the evolution down to the protostellar scales, effectively mapping cores to stars, the CMF to the IMF (see Chapter 2 or Guszejnov & Hopkins 2015b for details).

I found that the commonly quoted claim that "*1/3 of the core mass ends up in the star*" mapping between the CMF and the IMF is not correct: massive cores may develop strong turbulence that leads to fragmentation into smaller objects on a wide spectrum of masses.

1.2.2 Development of the MISFIT semi-analytic framework

As noted above, the excursion set approach has the major shortcoming that it only predicts the properties around a random Lagrangian point, making it hard to extract any kind of information about the spatial and temporal evolution of star formation (see Hopkins, 2013a, for an example). In order to overcome this issue I developed the MISFIT (*MInimalist Star Formation Including Turbulence*) semi-analytical framework (see Chapter 3 or Guszejnov & Hopkins 2016 for details).

MISFIT uses the same assumptions as Hopkins (2013c) and Guszejnov & Hopkins (2015b) while still preserving spatial and temporal information. This is accomplished by simulating the stochastic density field on a grid that represents a collapsing molecular cloud and recursively restarting the simulation for self-gravitating substructures. Due to its semi-analytical nature MISFIT can simulate a much wider dynamic range than conventional hydro codes: it can follow the evolution clouds from the scale of giant molecular clouds ($\sim 10\,\mathrm{pc}$) down to the scales of protostars ($\sim 0.1\,\mathrm{AU}$) at modest computational cost (a couple of CPU hours). MISFIT provides a way to explore different star formation models and parameters on a wide dynamic range and to generate statistically significant samples for them, which would be a hopelessly expensive exercise for detailed hydrodynamical simulations.

1.2.3 Testing IMF models with MISFIT

As the first application of MISFIT I set out to test different classes of IMF models, in collaboration with Mark Krumholz (UCSC, ANU), to see whether they can reproduce the IMF observed in the Milky Way (see Chapter 4 or

Guszejnov et al. 2016 for details).

I found that models based solely on isothermal turbulence and gravity (e.g. the excursion set model of Hopkins 2012b) lead to a purely power-law IMF without turnover. Meanwhile, models based on a transition from an isothermal to an adiabatic equation of state require fine tuning to reproduce observations and are inherently sensitive to the initial conditions of the progenitor clouds, making them incompatible with the apparent universality of the MW IMF (see Chapter 5 or Guszejnov et al. 2017c for details). I also tested an IMF model based on protostellar feedback, where the accretion luminosity from the protostar heats up the surrounding gas, preventing further fragmentation (see Krumholz, 2011). I found that this model not only reproduces the observed IMF peak but is also insensitive to the initial conditions of the progenitor cloud (Chapter 4).

1.2.4 Stellar Correlation and Multiplicity with MISFIT

As a follow-up to the previous projects I took advantage of MISFIT's ability to provide information about the spatial structure of star formation to compare the predictions of the isothermal and the protostellar feedback-regulated models with observations. I calculated the stellar correlation function, multiplicity, companion mass and period distributions and compared them with observations (see Chapter 6 or Guszejnov et al. 2017b for details). It is important to note that apart from MISFIT there is no analytical framework for star formation where such spatial information is readily available.

When investigating the initial clustering of stars, I found that regardless of the underlying small scale physics (e.g. isothermal or adiabatic EOS, protostellar heating) the two-point correlation function of stars is a power law with a fixed slope (see Chapter 7 or Guszejnov et al. 2017a for an explanation of this behavior).

Using MISFIT I predicted the multiplicity and companion mass distributions for stellar binaries (Chapter 6). I found that observational biases can severely distort the results so that all models roughly reproduce the observed multiplicity and companion mass distributions. To break the degeneracy, observations need to extend their completeness limit to companions with very low relative mass. Interestingly, the protostellar feedback model can reproduce the observed companion mass distributions for both Solar type and very low mass (VLM) stars with or without the observational biases.

All models included in the study under-predict the number of short-range binaries. Since MISFIT only treats fragmentation out of a common protostellar core, the cause of the discrepancy is likely due to the fragmentation of protostellar disks (disk physics are not included in MISFIT). This implies that short-range binaries likely form out of a single protostellar disk.

1.3 IMF variations in a MW-like Galaxy

With my semi-analytical models I discovered that the position of the IMF peak is sensitive to the initial conditions of the parent cloud in several classes of star formation models. Meanwhile the IMF in the Milky-Way is observed to be almost universal (see e.g. Offner et al., 2014) which provides a way to test the predictions of these models. By convolving the initial conditions of progenitor clouds (e.g. GMCs) with the analytical scaling laws I predicted for different IMF models, I showed that all but the protostellar heating model (detailed in Krumholz, 2011) are incompatible with the apparent universality of the MW IMF (see Chapter 5 or Guszejnov et al. 2017c for details).

While the idea of convolving the initial conditions with the analytic models seems simple at first, it is complicated by the fact that the characteristic stellar mass (IMF peak) depends on the *at-formation* properties of star-forming clouds, which can be wildly different from the properties of clouds that are forming stars today. To model these progenitor clouds I utilized simulated MW-like galaxies from the Feedback in Realistic Environments (FIRE) project (see Hopkins et al., 2017a, for details about the simulations). These simulations have a mass resolution of $\sim 10^4\,\mathbf{M}_\odot$ and include much of the relevant physics on these scales. This is insufficient to resolve the IMF but enough to resolve the bulk properties of GMCs and thus provide the initial conditions for star forming clouds, which then can be convolved with my semi-analytical predictions for each IMF model. With these, I showed that models attributing the IMF peak to the Jeans mass, sonic mass or an isothermal-adiabatic transition are incompatible with a universal IMF in the MW.

1.4 Universal Scaling Laws

While investigating the effects of different star formation models on the IMF and the stellar correlation function, I noticed that several predictions are insensitive to the underlying model. This prompted me to develop analytical models to show that these scaling relations are universal to all models featuring scale-free structure formation (see Chapter 7 or Guszejnov et al. 2017a for details).

I found that structure formation models that are scale-free in a wide dynamic and have uncorrelated scales[1] predict a number of universal power-law relations:

- $\mathrm{d}N/\mathrm{d}M \propto M^{-2}$ for the mass functions of stars, protostellar cores, star clusters and dark matter halos.
- $\xi_{\mathrm{2D}} \propto R^{-1}$ for the two-point correlation function of these objects.
- $\mathrm{d}A/\mathrm{d}\Sigma \propto \Sigma^{-1}$ for the gas column density distribution.

These predictions all agree with observations and simulations to first order, with the caveats that the observed correlation function steepens at smaller scales (likely due to binaries) and that the observed column density only matches this trend at the high density end (it is obscured by non-star-forming gas at lower densities).

This provides a deep physical reason for why seemingly unrelated systems (e.g. stars, GMCs, star clusters and dark matter halos) have similar scaling relations. The effects of additional physics are captured by the deviations from these relations, which are often comparable to the uncertainties of observations.

1.5 Isothermal Collapse

The last project of my PhD focused on the fundamental question "*Is there a characteristic scale in isothermal collapse?*". There is some confusion about this in the literature as some claim to produce a converged IMF in pure-isothermal collapse (Gong & Ostriker, 2015; Haugbølle et al., 2017) while others argue that there is no inherent low mass cut-off and the system should undergo an infinite fragmentation cascade (Krumholz, 2014). Furthermore, a large number of analytical theories of star formation assume such a cut-off scale exists and that it sets the peak of the IMF (e.g. Hennebelle & Chabrier, 2008; Hopkins, 2012b; Padoan & Nordlund, 2002), while others argue that the turnover can *only* come from additional physics (e.g. Bonnell et al., 2006; Guszejnov et al., 2016; Jappsen et al., 2005a; Krumholz, 2014; Larson, 2005). My previous semi-analytical results indicated the latter, but to rigorously answer this question I ran detailed hydrodynamical simulations with high enough

---

[1] In other words: scale free systems where the process does not "know" how far it is from the starting scale, the initial microstate is "forgotten".

dynamic range to resolve multiple generations of fragmentation (see Chapter 8 or Guszejnov et al. (2018) for details).

Carrying out this convergence study required a simulation with extremely high mass resolution, so I utilized GIZMO, a fully adaptive, meshless MHD code (Hopkins, 2015). None of the previous works have probed the problem of isothermal fragmentation with such a high dynamic range (highest resolution I ran had $\Delta m/M_{\mathrm{cloud}} = 7\times10^{-9}$), which enabled me to establish the following:

1. Isothermal clouds have two modes of collapse: either all the mass ends up in a few massive objects (homologous collapse) or the cloud breaks into a spectrum of smaller objects (fragmentation).
2. Contrary to claims in the field that "*Subsonic clouds collapse without fragmentation*", I found that a low turbulent Mach number does not necessarily indicate homologous collapse, and that it is possible to construct subsonic clouds that undergo fragmentation. The actual indicator is the number of infall Mach number (the Mach number derived from the large-scale characteristic gravitational freefall speed of the system, $v_{\mathrm{freefall}}\ \sqrt{(GM/R_{\mathrm{cloud}})}$ or the number of initial thermal Jeans masses in the cloud, which are simple functions of each other.
3. Isothermal fragmentation continues to ever smaller scales *without limit*. Any mass scale imprinted by initial conditions (e.g. Jeans mass, sonic mass) is "forgotten" due to the non-linear behavior of the system. I demonstrated this non-convergence over an 8 dex mass range.

Note that I also carried out several tests and found these answers to be unchanged if I used use a different hydrodynamic scheme (e.g. smoothed particle hydrodynamics based on Hopkins 2013b), changed the method of sink particle formation, added random noise to the initial conditions or if turbulent driving is involved.

These findings further reinforce the conclusions of Guszejnov et al. (2016) that isothermal turbulence and gravity by themselves cannot explain the IMF, it requires additional physics.

1.5.1 Future Plans

The IMF in dwarf galaxies is observed to be similar to the MW IMF (e.g. Weisz et al., 2015), while it is also observed to be "bottom-heavy" (more low mass stars compared to MW) within massive elliptical galaxies (e.g. van Dokkum, 2008). I am currently conducting a study similar to Guszejnov et al. (2017c), where I utilize FIRE simulations of dwarf and massive elliptical galaxies to model the initial conditions of progenitor clouds and then convolve these properties with different star formation models. The aim of this study is to show how these observations constrain IMF models and to see which models would be compatible with both these extragalactic constrains and the universal MW IMF.

In the future several new high resolution telescopes will come online (e.g., JWST, TMT, GMT) that will be able to resolve individual stars or star forming regions/clusters in nearby galaxies in both IR and optical bands. These will provide an unprecedented amount of new data on star formation in different environments, ranging from galaxy and cluster scale IMFs and their variations in extragalactic sources to the properties of protostars and stellar binaries. By combining these data with my results I will attempt to further constrain which IMF models could satisfy all observational constraints. This will culminate in cosmological simulations of galaxies where the stellar populations and the local environment are evolved self-consistently[2]. After having identified the star formation models that satisfy the observational constraints on the stellar initial mass function (IMF) in these new simulations, I will start exploring higher order statistics (e.g. correlation, multiplicity) and their variations in different galactic environments.

---

[2] A significant caveat of the post-processing of galaxy simulations is that the simulations themselves include no IMF variations, so the inferred results neglect the feedback from having a non-MW IMF. Having the IMF variations built-in as a subgrid prescription would make the simulation self-consistent.

Chapter 2

MAPPING THE CORE MASS FUNCTION TO THE INITIAL MASS FUNCTION

Guszejnov D., Hopkins P. F., 2015, MNRAS, 450, 4137

Abstract

It has been shown that fragmentation within self-gravitating, turbulent molecular clouds ("turbulent fragmentation") can naturally explain the observed properties of protostellar cores, including the core mass function (CMF). Here, we extend recently-developed analytic models for turbulent fragmentation to follow the time-dependent hierarchical fragmentation of self-gravitating cores, until they reach effectively infinite density (and form stars). We show that turbulent fragmentation robustly predicts two key features of the IMF. First, a high-mass power-law scaling very close to the Salpeter slope, which is a generic consequence of the scale-free nature of turbulence and self-gravity. We predict the IMF slope (-2.3) is slightly steeper than the CMF slope (-2.1), owing to the slower collapse and easier fragmentation of large cores. Second, a turnover mass, which is set by a combination of the CMF turnover mass (a couple solar masses, determined by the 'sonic scale' of galactic turbulence, and so weakly dependent on galaxy properties), and the equation of state (EOS). A "soft" EOS with polytropic index $\gamma < 1.0$ predicts that the IMF slope becomes "shallow" below the sonic scale, but fails to produce the full turnover observed. An EOS which becomes "stiff" at sufficiently low surface densities $\Sigma_{gas} \sim 5000\,M_{\odot}\,\mathrm{pc}^{-2}$, and/or models where each collapsing core is able to heat and effectively stiffen the EOS of a modest mass ($\sim 0.02\,M_{\odot}$) of surrounding gas, are able to reproduce the observed turnover. Such features are likely a consequence of more detailed chemistry and radiative feedback.

2.1 Introduction

The mass distribution of newly formed stars, often referred to as the *Initial Mass Function* or *IMF*, is fundamental in many aspects of astrophysics. Understanding the processes leading to the observed IMF provides valuable insight into not only star formation but into the evolution of galactic structures and the formation of planets. So far observations of different galaxies and regions within the Milky Way suggest that some qualitative features of the IMF are universal (Offner et al. 2014, Bastian et al. 2010). These include:

- a power law-like slope ($dn/dM \propto M^{-2.3}$) for large masses;
- turnover around 0.1-1.0 solar mass;
- lognormal-like or power law-like behavior for small masses.

The universality of these properties implies that some fundamental physical process influences the initial stellar mass distribution. It is important to note that, of these three properties, the power law-like slope is also ubiquitous to wildly different systems including dark matter halos (Press & Schechter 1974), giant molecular clouds (Rosolowsky & Blitz 2005), young star clusters (Portegies Zwart et al. 2010) and HI holes in the interstellar medium (Weisz et al. 2009). The exponent of $dn/dM \propto M^{-2.3}$ is close to that which implies that an equal amount of mass is distributed in every logarithmic interval in mass, which points to a self-similar process being the main driving force behind these distributions.

A candidate for such process is turbulent fragmentation. It is widely accepted that stars are formed by the gravitational collapse of dense molecular clouds (McKee & Ostriker 2007b). Gas in these clouds is highly turbulent, which leads to large fluctuations in density that in turn then lead to the emergence of subregions that are independently collapsing (see Fig. 2.1). Denser regions collapse faster, turning into stars whose feedback (e.g. radiation, solar winds) heats up or blows the surrounding gas away, effectively preventing further star formation in that area.

This process is inherently hierarchical, which suggests that it should be possible to derive a single model which simultaneously links the largest scales of collapse all the way down to the smallest (the scales of individual stars). This is not possible in simulations because of resolution limitations, but can be approximately treated in analytic models.

This paradigm was explored by Padoan et al. (1997) and Padoan & Nordlund (2002), then made more rigorous by Hennebelle & Chabrier (2008) who attempted to approximate the IMF in a manner analogous to Press & Schechter (1974). Hopkins (2012a) expanded upon these works by using an excursion set formalism to calculate the distribution of first crossing mass scales in galactic disks[1]. This yielded mass functions very similar to the mass distribution of

---

[1] In the usual terminology the largest collapsing scale is referred to as the scale of *first crossing* while the smallest collapsing subregion is at the scale of *last crossing*.

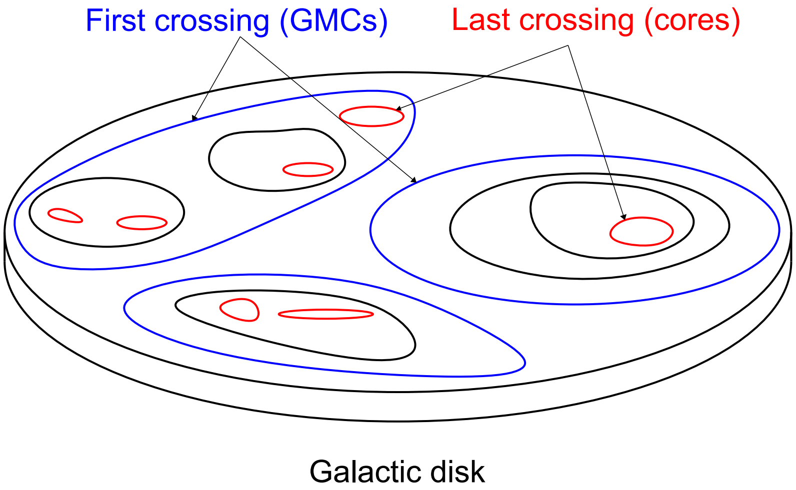

Figure 2.1: Cartoon illustration of hierarchical turbulent fragmentation in a galactic disk. The scale of the largest self gravitating clouds is called the "first crossing" (largest scale where the density $\rho > \rho_{\rm crit}$, see Eq. 2.6), which corresponds to giant molecular clouds (GMCs) while the scale of the smallest clouds (usually embedded in larger ones) is the last "crossing scale" which correspond to protostellar cores.

giant molecular clouds (GMCs) which are the largest known bound collections of gas in a galaxy. Meanwhile Hopkins (2012b) found that the mass function of structures at the last crossing scale show a striking similarity to the distribution of protostellar cores (also referred to as *cores*). This core mass function (CMF) is remarkably similar to the IMF, the only difference being the position of the turnaround which is at a mass scale 3 time larger than the case of the IMF (Alves et al. 2007; Rathborne et al. 2009; Sadavoy et al. 2010). Building on these results Hopkins (2013c) generalized the formalism to be applicable to a wide range of phenomena by incorporating gases with arbitrary equation of state, magnetic fields, intermittency etc. They also showed that this naturally predicts observed cloud and protostellar core properties such as the "Larson's laws" scalings of cloud size, mass, and linewidth (Brunt et al. 2009; Enoch et al. 2008; Larson 1981), stellar clustering and correlation functions from scales $\sim 0.1-1000\,\mathrm{pc}$ (Lada & Lada 2003; Portegies Zwart et al. 2010) as a consequence of turbulent fragmentation.

Nevertheless a major shortcoming of these models is that they only extend to the CMF[2]. It is by no means clear that the "mapping" from CMF to IMF is

---

[2] Other attempts were made to connect the IMF and CMF, notable examples are Padoan & Nordlund (2011), which used the IMF predicted by Padoan & Nordlund (2002) to 'guess'

simple or universal. And in fact some of the simple assumptions in these previous works – for example, that of isothermal gas – must break down on small scales. Therefore, in this paper we expand upon these works and argue that it is possible to bridge the gap between the CMF and the IMF by analytically following the collapse of protostellar cores. Gravitational collapse takes place during a finite amount of time during which collapse pumps energy into turbulence, causing the cloud to fragment. We are able to build a simple model meant to capture this, and from it derive the principal qualitative features of the IMF. We will show that the high mass IMF slope can be explained purely by turbulent fragmentation and that the turnover position is dependent on the underlying thermodynamics and galactic properties, while the low mass end is highly influenced by the aforementioned processes and feedback physics.

The paper is organized as follows. A general overview of the excursion set formalism is given in Sec. 2.2, including several further assumptions regarding the collapsing medium (Sec. 2.2.3) and the time evolution of collapsing protostellar cores (Sec. 2.2.4). In Sec. 2.3 the model we developed for mapping between CMF and IMF is described in detail. The final results and their implications are discussed in Sec. 2.4.

2.2 Methodology

To map the CMF to the IMF one needs to describe the transition from protostellar cores into protostars. To do that we employ the excursion set formalism outlined in Hopkins (2012a) and Hopkins (2012b) with the addition of time dependence from Hopkins (2013c). Only a broad summary of the method will be given here; see the references for more details.

2.2.1 Density Field Evolution

The aim of the model is to describe the properties of self gravitating turbulent medium (see Sec. 2 of Hopkins (2013c) for detailed description). In the case of an isothermal medium, ignoring (for now) self-gravity, the density fluctuations in both sub and supersonic cases have lognormal statistics[3], which means that the density contrast $\delta(\mathbf{x}) = \ln\left[\rho(\mathbf{x})/\rho_0\right] + S/2$, where $\rho(\mathbf{x})$ is the local density,

---

the CMF, and Clark et al. (2007), which discussed some general properties of the mapping. Both drew attention to the problem of time dependence as the time scales of forming stars of different sizes differs greatly (this has been shown to be important by the simulations of Padoan et al. 2014). Our model attempts to partially address this issue.

[3] As shown in Hopkins (2013d) the statistics are not perfectly lognormal even in the isothermal case, however those particular corrections have very little effect on our results.

ρ_0 is the mean density and S is the variance of $\ln\rho$, would follow a normal distribution, thus

$$P(\delta|S) = \frac{1}{2\pi S}\exp\left(-\frac{\delta^2}{2S}\right). \tag{2.1}$$

It is a property of Gaussian and lognormal random variables that an integral over such fields is also Gaussian/lognormal. Thus let us define the average density on scale λ as

$$\rho(\lambda, \mathbf{x}) = \int \rho(\mathbf{x}')W_\lambda(\mathbf{x}' - \mathbf{x})d^3x', \tag{2.2}$$

where $W_\lambda(\mathbf{x}' - \mathbf{x})$ is the window function for averaging. Then, according to the theorem $\delta(\lambda, \mathbf{x})$ will be also Gaussian. For the sake of brevity from this point on let us drop the $\mathbf{x}$ coordinate from these quantities. Also, to simplify the formulas the Fourier transform of the window function ($W(\mathbf{k})$) is assumed to be a Heaviside function (cut-off at k) [4].

Instead of dealing with δ directly it is more convenient to introduce a new quantity $\Delta\delta\left(\lambda_2|\delta\left[\lambda_1\right]\right) = \delta(\lambda_2) - \delta(\lambda_1)$ which is the contribution to the logarithmic density by scales between λ_1 and λ_2. This way we can express δ as

$$\delta(\lambda_i) = \sum_j^{\lambda_j>\lambda_i} \Delta\delta_j, \tag{2.3}$$

where we use the fact that the density on the largest scale is by the definition the mean density with no variance thus $\delta(\lambda_{\max}) = 0$.

In a turbulent system the variance of the logarithmic density field ($\sigma^2(\lambda)$) will tend to an equilibrium value $S(\lambda)$ prescribed by the turbulence. It is well known in the isothermal case that the variance of density is related to the variance of velocity as $S \approx \ln\left(1 + \mathcal{M}^2_{\text{compressive}}\right)$ where $\mathcal{M}^2_{\text{compressive}}$ is the compressive Mach number related to the turbulent velocity dispersion (Federrath et al. 2008). Following the derivation of Hopkins (2013c):

$$S(\lambda) = \int_0^\lambda \Delta S(\hat{\lambda})d\ln\hat{\lambda} \approx \int_0^\lambda \ln\left[1 + \frac{b^2 v_t^2\left(\hat{\lambda}\right)}{c_s^2 + \kappa^2\hat{\lambda}^2}\right] d\ln\hat{\lambda}, \tag{2.4}$$

where $v_t(\lambda)$ is the turbulent velocity dispersion on scale λ, c_s is the thermal

---

[4] The calculation could be repeated with $W(k)$ corresponding to real space spheres or filaments but that would have < 10% effect on the final results.

sound speed, b is the fraction of the turbulent velocity in compressive motions, which we take to be about $1/2$ (appropriate for randomly driven, super-sonic turbulence, though we have experimented with $b \sim 1/4 - 1$ and find it makes no qualitative difference to our conclusions), and κ is the epicyclic frequency which represents angular momentum suppressing large-scale density fluctuations. Note that this particular scaling for $S(\lambda)$, as well as the functional form for the density statistics on different scales $\rho(\lambda)$ which we adopt, have been directly measured in numerical simulations (Federrath et al. 2010a; Kowal et al. 2007).

Let us suppose that instead of an isothermal medium we have gas which follows a polytropic equation of state as

$$c_s^2 = c_{s0}^2 \left(\frac{\rho}{\rho_0}\right)^{\gamma-1}, \tag{2.5}$$

where c_{s0} is the sound speed at the mean density (ρ_0) and γ is the polytropic index. In this case (for $0.3 < \gamma < 1.7$), the statistics can still be approximated as *locally* lognormal (i.e. lognormal for differentially small perturbations; Passot & Vázquez-Semadeni 1998) if we apply the replacement $c_s^2 \rightarrow c_{s0}^2 \left(\rho/\rho_0\right)^{-(\gamma-1)}$ to Eq. 2.4, which means that we get $S(\lambda) \longrightarrow S(\lambda, \rho)$ so S becomes a functional of ρ. This scheme is also an acceptable approximation for gases with more complex equation of states (e.g. $\gamma(\rho)$). Note that this means the total PDF can differ significantly from a lognormal; for $\gamma > 1$ large positive-density fluctuations become rarer while $\gamma < 1$ makes them more common (producing a power-law high-density tail).[5] It should be noted that previous treatments (e.g. Hennebelle & Chabrier 2008) ignored the effect of γ on the distribution of ρ despite the fact that it can produce radically different PDFs. For more details see Sec. 3 of Hopkins (2013c).

2.2.2 The Collapse Threshold

Various authors (e.g. Chandrasekhar 1951, Elmegreen 1987) have shown that including the effects of turbulence and finite vertical disk thickness into a Toomre-type analysis yields a simple scaling for the critical density (ρ_{crit}) above which a spherical subregion of size λ embedded in a larger disk or cloud

---

[5] These effects and the validity of our analytic expressions have been directly verified in simulations (Scalo et al. 1998a, Lynn & Quataert, private communication).

becomes gravitationally unstable and collapses. This can be written

$$\frac{\rho_{\mathrm{crit}}(\lambda)}{\rho_0} = \frac{Q}{2\tilde{\kappa}}\left(1+\frac{h}{\lambda}\right)\left[\frac{\sigma_g^2(\lambda)}{\sigma_g^2(h)}\frac{h}{\lambda}+\tilde{\kappa}^2\frac{\lambda}{h}\right], \tag{2.6}$$

where h is the vertical scale of the disk, $\sigma_g^2(\lambda) \approx c_s^2 + v_t^2(\lambda)$ is the total velocity dispersion on scale λ where $v_t^2(\lambda)$ is the turbulent velocity dispersion at that scale, $\tilde{\kappa} = \kappa/\Omega$ where $\Omega = v_{\mathrm{circ}}/r_{\mathrm{d}isk}$ is the orbital frequency at the location $r_{\mathrm{d}isk}$, κ is the epicyclic frequency, and $Q = \sigma_g(h)\kappa/(\pi G\Sigma)$ is the Toomre parameter, where Σ is the surface density of the disk. For the scales of interest here, λ is in the inertial-range of turbulence where turbulent kinetic energy scales as $E(\lambda) \propto \lambda^p$ with p being the turbulent spectra index; generally $p \in [5/3; 2]$, but in this paper we assume $p = 2$ for our calculations based on the observed linewidth-size relations (Larson 1981; Bolatto et al. 2008; Enoch et al. 2008), theoretical expectations (Burgers, 1974, 1995; Murray, 1973), and numerical simulations (Schmidt et al., 2009)). This leads to the following scaling of the turbulent velocity dispersion and Mach number $\mathcal{M}$

$$\mathcal{M}^2(\lambda) \equiv \frac{v_t^2(\lambda)}{\langle c_s^2\,(\rho_0)\rangle} = \mathcal{M}^2(h)\left(\frac{\lambda}{h}\right)^{p-1}. \tag{2.7}$$

Since we are only interested in protostellar cores, which are much smaller than their parent galactic disk, it is justified to take the limit of $\lambda \ll h$ leading to

$$\frac{\rho_{\mathrm{crit}}(\lambda)}{\rho_0} = \frac{Q'}{1+\mathcal{M}_{\mathrm{edge}}^2}\tilde{\lambda}^{-2}\left[\left(\frac{T(\lambda)}{T_0}\right)+\mathcal{M}_{\mathrm{edge}}^2\tilde{\lambda}^{p-1}\right], \tag{2.8}$$

where $T(\lambda)$ is the temperature averaged over the scale λ, while T_0 is the mean temperature of the whole collapsing cloud.

If we further assume that the gas has a polytropic equation of state then Eq. 2.8 becomes

$$\frac{\rho_{\mathrm{crit}}(\lambda)}{\rho_0} = \frac{Q'}{1+\mathcal{M}_{\mathrm{edge}}^2}\tilde{\lambda}^{-2}\left[\left(\frac{\rho_{\mathrm{crit}}(\lambda)}{\rho_0}\right)^{\gamma-1}+\mathcal{M}_{\mathrm{edge}}^2\tilde{\lambda}^{p-1}\right], \tag{2.9}$$

where $\tilde{\lambda} = \lambda/h$ is the normalized size scale, $Q' = Q/(2\tilde{\kappa})$ and $\mathcal{M}_{\mathrm{edge}} = \mathcal{M}(h)$ is the Mach number for the turbulent velocity dispersion at the largest scale[6].

---

[6] Once again we note that direct simulations (Federrath & Klessen 2012; Hennebelle & Chabrier 2013b; Zentner 2007) have confirmed that this is a good approximation for the

This is an implicit equation in case $\gamma \neq 1$ which always has a unique solution for $\gamma < 2$. Note that this equation applies identically for sub-structures *inside* a core, where in that case ρ_0, Q', and $\mathcal{M}_{edge}$ are defined at the scale of the core. For collapsing cores the core scale itself has to be unstable, which prescribes $Q' = 1$, which we will adopt for the rest of the paper.

For $\mathcal{M}_{\rm edge}^2 \tilde{\lambda}^{p-1} \gg 1$ turbulence dominates over thermal support and the critical density becomes roughly

$$\rho_{\rm crit}(\lambda) \approx \rho_0 \tilde{\lambda}^{p-3}, \tag{2.10}$$

while in the opposing, subsonic limit

$$\rho_{\rm crit}(\lambda) \approx \rho_0 \left[\left(1 + \mathcal{M}_{\rm edge}^2\right)\tilde{\lambda}^2\right]^{-1/(2-\gamma)}. \tag{2.11}$$

Since we are in the $\lambda \ll h$ limit, the mass of a structure with size scale λ and density $\rho(\lambda)$ is just $M(\lambda) = (4\pi/3)\,\lambda^3\,\rho(\lambda)$. And since protostellar cores begin themselves as "last-crossings" (smallest collapsing subregions of the galactic disk) in this formalism, they are at the critical density (if they were above it, some smaller scale would necessarily also be self-gravitating), so we can use this equation with $\rho(\lambda) = \rho_{\rm crit}(\lambda)$ and Eq. 2.10-2.11 to obtain their size-mass relation (see Sec. 2.3).

2.2.3 The Equation of State

For the purpose of modeling a collapsing protostellar core, a simple polytropic equation of state is not sufficient due to the highly complex heating and cooling processes involved. As a first approximation one can describe the whole cloud as having an *effective polytropic index* which is dependent on global properties (e.g. size, mass). Since the primary physical quantity for radiation absorption is surface density Σ, we choose to have a polytropic index dependent on this global quantity. Sufficiently dense clouds become optically thick to their own cooling radiation, meaning that blackbody radiation is the primary cooling mechanism. For realistic temperatures molecular hydrogen has a polytropic index of $\gamma = 7/5$. In case of less dense clouds, line cooling is the dominant cooling mechanism whose rate is $\propto n^2$, where n is the cloud's number density, while the dominant heating mechanism is cosmic radiation which depends only linearly on the density. This means that an increase in density leads to an effective decrease in temperature, and thus $\gamma < 1$. Based on these assumptions and

---

collapse criterion. Even for highly non-spherical, filamentary clouds, the corrections are of $O\,(10\%)$ to the final predicted mass function.

on the works of Masunaga & Inutsuka (2000) and Glover & Mac Low (2007), who calculated effective equation of state using full chemical networks in radiation hydrodynamics simulations, we define a simple interpolating equation of state which reproduces the aforementioned two limits:

$$\gamma(\Sigma) = \begin{cases} 0.7 & \Sigma < 3\,\mathrm{M_\odot/pc^2} \\ 0.094\log_{10}\left(\frac{\Sigma}{3\,\mathrm{M_\odot/pc^2}}\right) + 0.7 & 3 < \frac{\Sigma}{\mathrm{M_\odot/pc^2}} < 5000\,, \\ 1.4 & \Sigma > 5000\,\mathrm{M_\odot/pc^2} \end{cases} \tag{2.12}$$

where $\Sigma = M/(4\pi R^2)$ is defined for each "fragment" (cloud or sub-cloud, if it has collapsed independently). This $\gamma(\Sigma)$ equation of state does capture the physics of the limit where the cloud is optically thick to its own cooling radiation, however in the optically thin limit the local density ρ determines the effective polytropic index, not Σ. Nevertheless this EOS is still useful as the optically thin limit is populated by massive clouds whose fragmentation is barely dependent on the value of γ (see Fig. 2.11) so changing to a ρ dependent EOS for less dense clouds would not make a significant difference. In any case the effects of variations in the equation of state are investigated in Sec. 2.3.1.1.

It should be noted that the global parameter of our EOS (Σ surface density) changes on the dynamical time scale so for sufficiently small Δt time step the temperature field evolution can be approximated with the polytrope

$$T(\lambda, t+\Delta t) = T(\lambda, t)\left(\frac{\rho(\lambda, t+\Delta t)}{\rho(\lambda, t)}\right)^{\gamma(\Sigma)-1}. \tag{2.13}$$

2.2.4 Time-Dependent Collapse of Cores

One of the key physical processes in mapping the CMF to the IMF is the non-linear density field evolution during the collapse phase, which can cause the fragmentation of the cloud (see Fig. 2.2). To get a handle on this problem, let us first look at the time evolution of the density field in a stationary (statistically time-steady e.g. not globally collapsing/expanding) background. Using the notation of Sec. 2.2.1 and Eq. 2.3, we consider not the density contrast itself, but its modes in Fourier space, as their time evolution simply follows the generalized Fokker-Planck equation (see Sec. 9 of Hopkins 2013c)

$$\Delta\delta(\tilde{\lambda}, t+\Delta t) = \Delta\delta(\tilde{\lambda}, t)\,(1-\Delta t/\tau_\lambda) + \mathcal{R}\sqrt{2\Delta S(\tilde{\lambda})\Delta t/\tau_\lambda}, \tag{2.14}$$

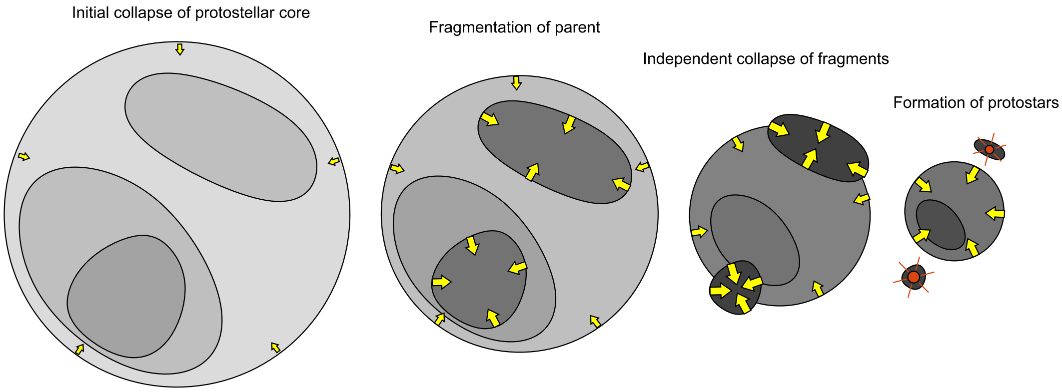

Figure 2.2: Evolution of collapsing protostellar cores, with time increasing from left to right (darker subregions are higher-density, arrows denote regions which are independently self-gravitating and become thicker with increasing collapse rate). As the initial core collapses, density fluctuations increase (because gravitational energy pumps turbulence), creating self-gravitating subregions. These then collapse independently from the parent cloud, forming protostars at the end.

where $\mathcal{R}$ is a Gaussian random number with zero mean and unit variance while $\tau_\lambda \sim \lambda/v_t(\lambda)$ is the turbulent crossing time on scale λ, and the turbulence dispersion obeys $v_t^2(\lambda) \propto \lambda$ thus $\tau_\lambda \propto \sqrt{\tilde{\lambda}}$ which we normalize as $\tau_\lambda(\lambda_{\rm max}) = 1$ thus setting the time units for our problem (see collapse time in Eq. 2.15). This formalism holds for polytropic gases too if we apply the substitution $\Delta S(\tilde{\lambda}) \rightarrow \Delta S(\tilde{\lambda}, \rho)$ and set it according to Eqs 2.4-2.5 and Eq. 2.7. For verification of evolution timescale in simulations, see Pan & Scannapieco (2010).

Note that, as the sub-regions collapse the total ensemble density distribution – even for isothermal gas – will deviate significantly from a lognormal. In fact what we predict is that self-gravitating regions develop a power-law tail in their "total" (ensemble) density PDFs, as sub-regions collapse on power-law (free-fall) time-scales. This is, of course, exactly what is observed in real dense molecular clouds (see Kainulainen et al. 2009), and it has been previously shown in simulations that it results naturally from such a fragmentation cascade (see e.g. Ballesteros-Paredes et al. 2011b; Federrath et al. 2010b; Kritsuk et al. 2011; Schmalzl et al. 2010; Veltchev et al. 2011).

2.2.4.1 Turbulent Density Fields in a Collapsing Background

In the case of collapsing protostellar cores the density evolution is influenced by the gravitational collapse which pumps energy into turbulence, potentially leading to large density fluctuations and further fragmentation of the cloud. Hopkins (2013c) developed a simple model for collapsing spherical clouds which assumes a constant virial parameter (based on Robertson & Goldreich 2012a and Murray & Chang 2015)[7]. Of course a perfectly spherical collapse would not drive turbulence, but any inhomogeneity in a 'roughly' homogenous media would be greatly amplified by the collapse which will drive the turbulence. Instead of dealing with the microscopic details our model assumes that virial equilibrium is realized between turbulence and gravity on the largest scale, thus the contraction is set by the rate of turbulent energy dissipation whose characteristic time scale is the crossing time τ_λ. This leads to an equation for the contraction of the cloud:

$$\frac{d\tilde{r}}{d\tilde{\tau}} = -\tilde{r}^{-1/2}\left(1 - \frac{1}{1+\mathcal{M}_{\mathrm{edge}}^2}\right)^{3/2}, \tag{2.15}$$

where $\tilde{r}(t) = r(t)/r_0$ is the relative size of the cloud at time t while $\tilde{\tau} \equiv t/t_0$ is time, normalized to the initial cloud dynamical time $t_0 \sim 2Q'^{-3/2}\left(GM_0/R_0^3\right)^{-1/2}$ (see Fig. 2.3 for solutions and Hopkins (2013c) for derivation). In this case the initial dynamical time (t_0) and crossing time only differ by a freely-defined order unity constant, so in our simulations we consider them to be equal without loss of generality. Virial equilibrium implies that that during the collapse of the cloud:

$$\frac{d\left(\mathcal{M}_{\mathrm{edge}}^2\right)}{d\tau} = \left(1+\mathcal{M}_{\mathrm{edge}}^2(t=0)\right)\left(-1+3\left(\gamma-1\right)\right)\tilde{r}^{-2+3(\gamma-1)}\frac{d\tilde{r}}{d\tau}, \tag{2.16}$$

which for constant γ simplifies to

$$1+\mathcal{M}_{\mathrm{edge}}^2(t) = \left(1+\mathcal{M}_{\mathrm{edge}}^2(t=0)\right)\tilde{r}^{-1+3(\gamma-1)}. \tag{2.17}$$

In the case $\gamma > 4/3$, after some time the sound speed c_s will begin growing faster than v_t, stabilizing against collapse. Thus the contraction will seize at a finite $\tilde{r}$ value (see Figs. 2.3-2.4). In this case we consider the collapse "done" when this size limit is reached. However, if $\gamma < 4/3$ then $\tilde{r} = 0$ is reached in a finite amount of time. This also means that the cloud cannot fragment on arbitrarily small scales as there is not enough time for these fluctuations to

---

[7] It should be noted that based on current data it is not at all clear that these collapses really happen at constant virial parameter, however we believe it is a reasonable approximation.

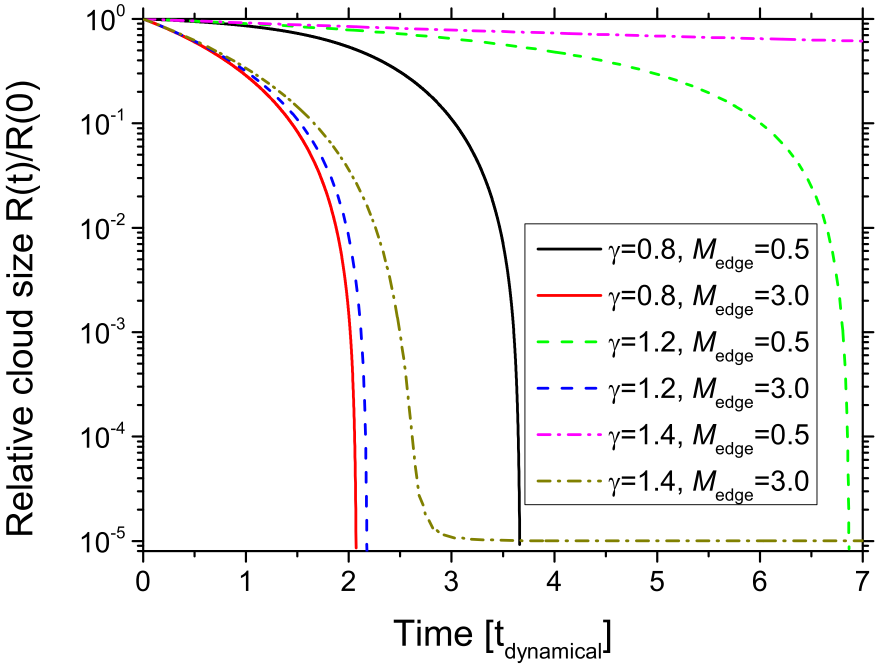

Figure 2.3: Contraction of a self gravitating, collapsing, turbulent parent cloud in time according to Eq. 2.16 for different polytropic indices γ and edge Mach numbers $\mathcal{M}_{\text{edge}}$ (Mach number of the turbulence on the cloud scale). For high Mach numbers the equation of state (e.g. different γ values) has little effect on the collapse rate, because the cloud is supported by turbulence. However, for $\gamma > 4/3$ the contraction ceases at a finite scale.

grow. For sufficiently small $\tilde{r}$ the collapse becomes scale-free ($d\tilde{r}/d\tau \approx -\tilde{r}^{-1/2}$). In this limit the collapse also becomes independent of γ.

2.3 Mapping From CMF to IMF

In this section we discuss an algorithm for mapping an initial CMF to a simulated IMF. For that we carry out several Monte Carlo simulations, which calculate the time evolution of last crossing surfaces around a randomly chosen point in a collapsing medium. This means solving the stochastic differential equation of Eq. 2.14 for the case of a collapsing protostellar core.

In our simulation the cores start out internally homogeneous (this is a good approximation for the density and temperature below the last crossing scale of a full galaxy calculation) and start to collapse following Eq. 2.15. As Fig. 2.5 shows, this leads to increased turbulence, which in turn leads to large density

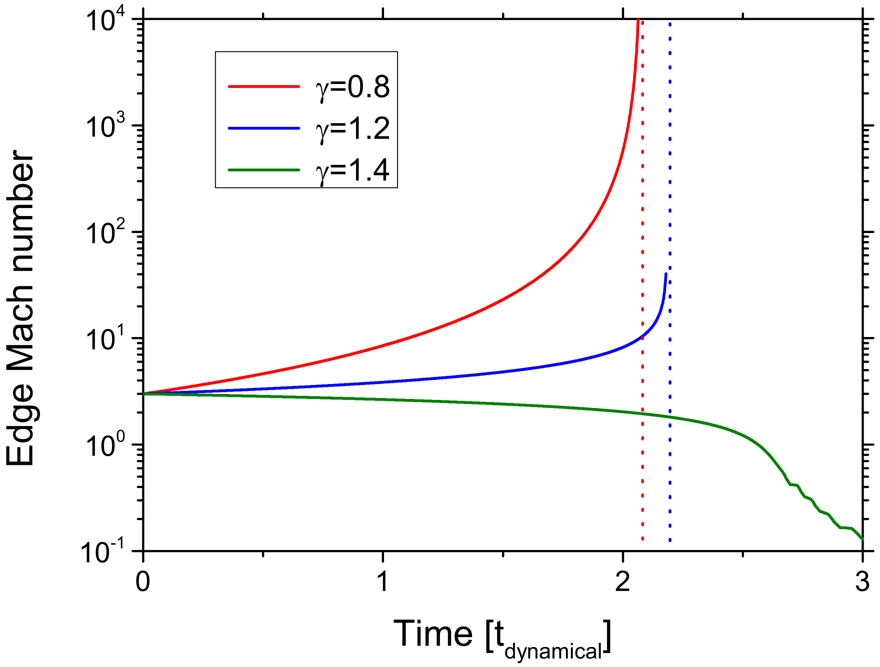

Figure 2.4: Evolution of the edge Mach number (Mach number of turbulence on the cloud scale) in collapsing clouds for different polytropic indices. For $\gamma < 4/3$ the contraction of the cloud pumps energy into turbulence, thus the $\mathcal{M}_{edge}$ diverges as we approach the time of collapse (marked with dotted lines). In the opposite case the sound speed increases faster than the turbulent velocities, pushing the cloud into the subsonic limit (where fragmentation becomes inefficient).

fluctuations (Eq. 2.4). Through pumping turbulence, the collapse also modifies the critical density (Eq. 2.8), combined with the aforementioned density fluctuations, this can lead to the formation of self gravitating subregions and thus the fragmentation of the parent cloud (see Fig. 2.2). Fig. 2.6 shows the time evolution of the averaged and critical density on a specific scale for a subsonic and a supersonic cloud. The first time the density reaches the critical density on some scale, a self gravitating subregion appears, which is subsequently assumed to evolve independently from the parent cloud. This assumption is supported by the fact that the collapse timescale $t_0 \sim (GM/\lambda^3)^{-1/2} \propto 1/\sqrt{\rho}$ and $\rho_{\mathrm{crit}} > \rho_0$ so smaller regions collapse faster, meaning that a small fragment can form a protostar much sooner than its parent could.

Based on these assumption our model follows the scheme:

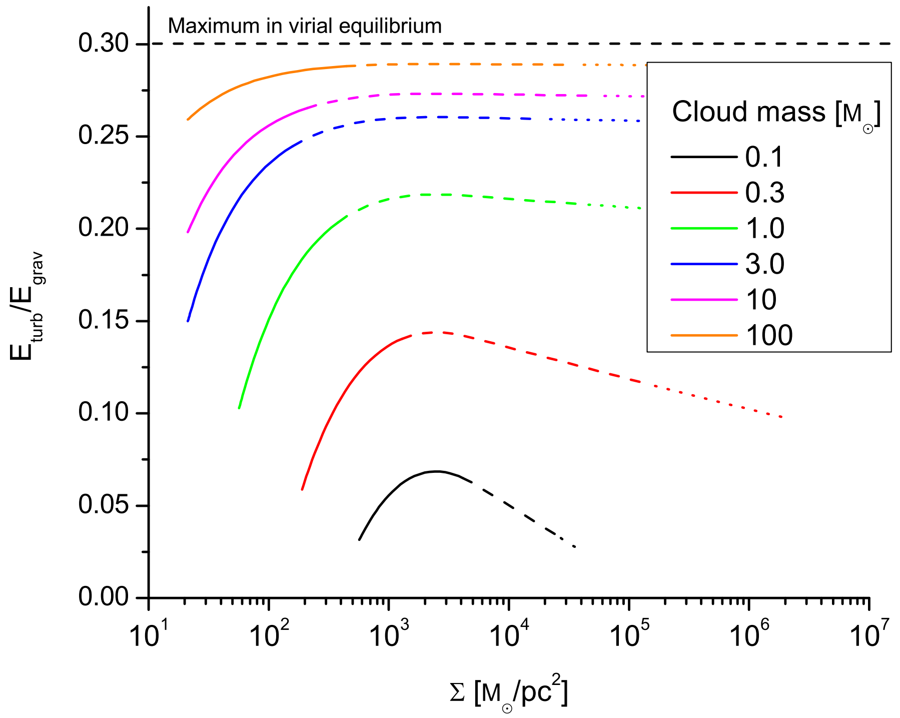

Figure 2.5: Evolution of the ratio of turbulent to gravitational energy as a function of surface density in clouds during collapse ($\gamma(\Sigma)$ from Eq. 2.12 used as EOS). The solid, dashed and dotted lines show the evolution during the first 50%, 90% and the entirety of the collapse time (collapse is achieved when the cloud size reached 10^{-4} pc which is roughly the size of a protostar). It is apparent that smaller clouds are mainly supported by thermal pressure and the relative importance of turbulence increases as the cloud collapses until $\gamma = 4/3$ is reached (at $\Sigma \approx 2500\,\mathrm{M}_\odot/\mathrm{pc}^2$ for this EOS) after which thermal energy grows faster than turbulent energy and starts dominating (see Eq. 2.16). For this plot $E_{turb} \sim M\frac{v_t^2}{2}$ and $E_{grav} \sim M\frac{5GM}{3R}$. Virial equilibrium implies $c_s^2(1+\mathcal{M}^2) = GM/R$, leading to $\frac{E_{turb}}{E_{grav}} \sim \frac{3\mathcal{M}^2}{10(1+\mathcal{M}^2)}$, which sets 0.3 as the theoretical maximum.

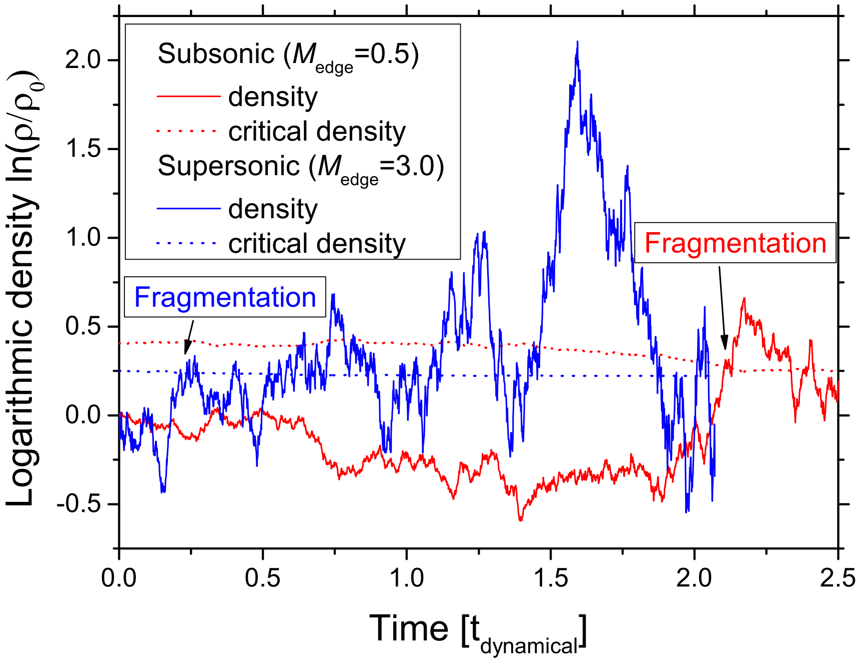

Figure 2.6: Time evolution of the averaged density (smoothed on some subscale λ around a specific random point within a cloud) and the critical density on the same scale (the density above which a region of this size becomes independently self gravitating). The curves follow a region whose size evolves with the parent cloud (it is a constant fraction of the parent cloud size). We consider both a supersonic (blue) and subsonic (red) cloud. The density field follows an essentially random walk. The first time it reaches the critical threshold, the subregion becomes self gravitating and starts to collapse on its own, thus fragmenting the cloud.

1. Initialize a cloud (e.g. density and temperature distribution).
2. Evolve the density and temperature (assuming locally polytropic behavior) on all scales within the cloud until the first collapsing subregion appears (see Fig. 2.6).
3. If there is a self gravitating subregion, evolve it forward starting again from step 1 using the parameters of the fragment at the moment of fragmentation as initial conditions.

This scheme yields the so called *collapse history*, which contains the time evolution of the last crossing scale around a point. It is important to note that this model makes no assumptions about the relative position of the fragment within the parent cloud, thus what we calculate is the collapse history of a random point. By carrying out a large number of these simulations we can determine the statistical collapse history of a random Lagrangian point for a specific initial cloud. In other words we calculate the probability that a Lagrangian point/volume element inside the cloud "ends up" in a final fragment of some mass.

The initial clouds represent the smallest self gravitating structures formed by fully developed turbulence in a galactic disk, which we consider to be equivalent to the observed protostellar cores. Their distribution has been calculated by Hopkins (2012b) using the same excursion set formalism, which naturally predicts their global parameters (see Fig. 2.7). By definition these clouds "start out" at the critical density so according to Eqs. 2.10-2.11 in the supersonic limit $M_{core} \propto \lambda_{core}^{p}$ (we took $p = 2$ for the turbulent power index in our simulations) meaning a constant surface density Σ, and thus constant $\gamma(\Sigma)$ (see Sec. 2.2.3). Meanwhile in the subsonic limit $M_{core} \propto \lambda_{core}^{3-2/(2-\gamma)}$ which we can further approximate by taking the isothermal $\gamma = 1$ case yielding $M_{core} \propto \lambda_{core}$. To get absolute scales let us assume virial equilibrium at cloud's scale which yields $c_s^2 + v_t^2(R) \sim GM/R$. Now we can introduce the sonic scale R_{sonic}, which correspond to the scale where $v_t^2(R_{\mathrm{sonic}}) = c_s^2$, and the sonic mass M_{sonic} which is the minimum self-gravitating mass contained in this subregion of size R_{sonic}. These assumptions lead to the following mass-size relation for the initial cores:

$$R(M) = \begin{cases} R_{\mathrm{sonic}} \frac{M}{M_{\mathrm{sonic}}} & M < M_{\mathrm{sonic}} \\ R_{\mathrm{sonic}} \sqrt{\frac{M}{M_{\mathrm{sonic}}}} & M > M_{\mathrm{sonic}} \end{cases} \tag{2.18}$$

By substituting in typical values for cores ($T = 30\,\mathrm{K}$, $R \sim 0.1\,\mathrm{pc}$, see Mac Low & Klessen 2004) we get $M_{\mathrm{sonic}} \sim 3\,\mathrm{M}_\odot$ for the sonic mass and

$$R(M) = \begin{cases} 0.1 \frac{M}{3\mathrm{M}_\odot}\,\mathrm{pc} & M < 3\mathrm{M}_\odot \\ 0.1 \sqrt{\frac{M}{3\mathrm{M}_\odot}}\,\mathrm{pc} & M > 3\mathrm{M}_\odot \end{cases} \tag{2.19}$$

Note that the predicted size-mass relation agrees with that observed (Bolatto et al., 2008; Larson, 1981; Pineda et al., 2009); we would obtain nearly identical results if we simply took the observed relation as our input.

Since the protostellar core in question has not yet started collapsing, the turbulent velocity at its edge must (initially) obey the turbulent power spectrum.

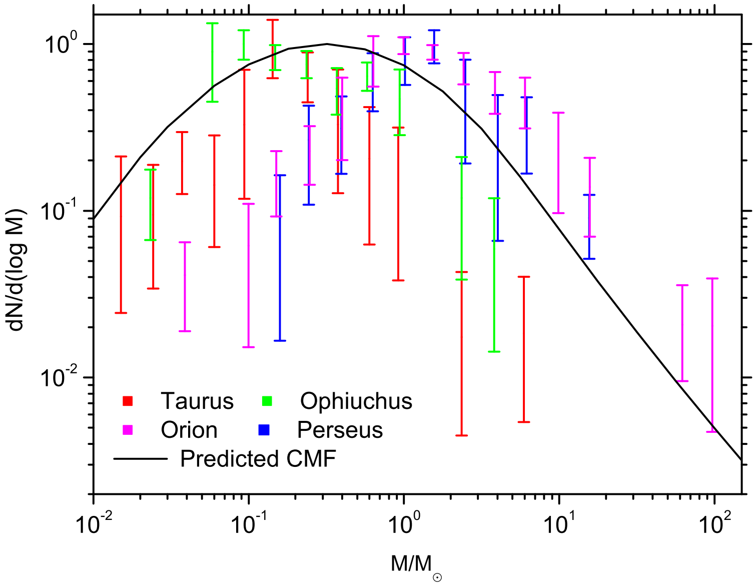

Figure 2.7: Comparison between the CMF used in our calculations (the result of the excursion set model from Hopkins 2012b) and a compilation of observed core mass functions from Sadavoy et al. (2010). Since the exact scaling of the CMF is determined by the sonic mass, which depends on the parameters of the galactic disk, it was set in a way that the CMF turnover mass is between the observational limits. Effects of deviations from this default CMF are investigated in Sec. 2.3.1.2.

Thus $v_t^2(R) \propto R$ for the supersonic and $v_t^2(R) \propto R^{2/3}$ (the Kolmogorov scaling) for the subsonic case. Using the mass-size relations of Eq. 2.18 leads to the following fitting function:

$$\frac{\left(1+\mathcal{M}_{\mathrm{edge}}^{2}\right)\mathcal{M}_{\mathrm{edge}}^{2}}{1+\mathcal{M}_{\mathrm{edge}}^{-1}} = \frac{M}{M_{\mathrm{sonic}}}, \tag{2.20}$$

which exhibits scalings of $M \propto \mathcal{M}^3$ for the subsonic and $M \propto \mathcal{M}^4$ for the supersonic case respectively, and (coupled to the size-mass relation above) very closely reproduces the observed linewidth-size relations (Bolatto et al. 2008; Lada & Lada 2003; Larson 1981).

This means that an initial parent cloud can be described with only one physical parameter, which we chose to be its mass (see Fig. 2.8). Using the aforementioned Monte Carlo algorithm it is possible to calculate $P_V(M_0, M)$, which is

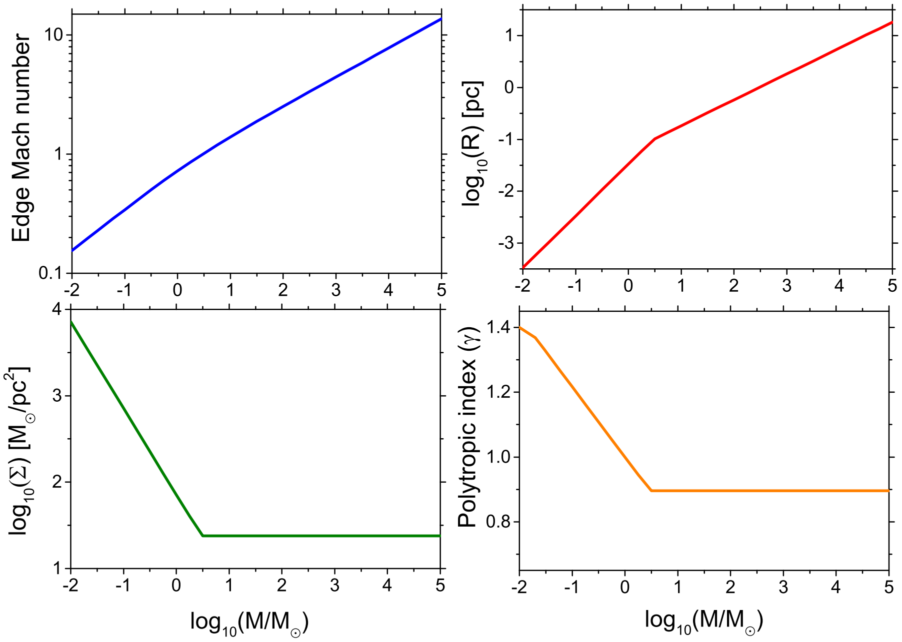

Figure 2.8: Mass dependence of the initial parent core properties of the clouds on the observed CMF, used as the initial conditions for our calculation. We show the initial cloud scale or "edge" Mach number (top left), cloud radius R (top right), cloud-averaged surface density Σ (bottom left), and effective polytropic index γ (bottom right) for protostellar cores before the collapse begins, each as a function of the initial core mass. These are calculated from the same excursion-set models from which the CMF in Fig. 2.7 is derived. But the mass-size relation we adopt agrees well with Larson's law for both small and large masses (Bolatto et al. 2008; Larson 1981; Pineda et al. 2009) as does the Mach number-mass relation (or equivalently, the linewidth-size relation).

the probability that a randomly chosen initial Lagrangian point, within a parent core with initial mass M_0, ends up in a fragment of mass M after collapse (see Fig. 2.9). Thus $P_V = 0.1$ means that 10% of the initial points (thus 10% of the total mass) will end up in fragments of size M. The number of initial subregions containing M mass is just M_0/M so assuming the subregions are independent, the expected number of fragments becomes $P_V(M_0, M)M_0/M$. Thus, if the CMF is given by $n_{core}(M)$ then the stellar IMF is

$$n_{stars}(M) = \int_M^\infty n_{core}(M')P_V(M', M)\frac{M'}{M}dM'. \tag{2.21}$$

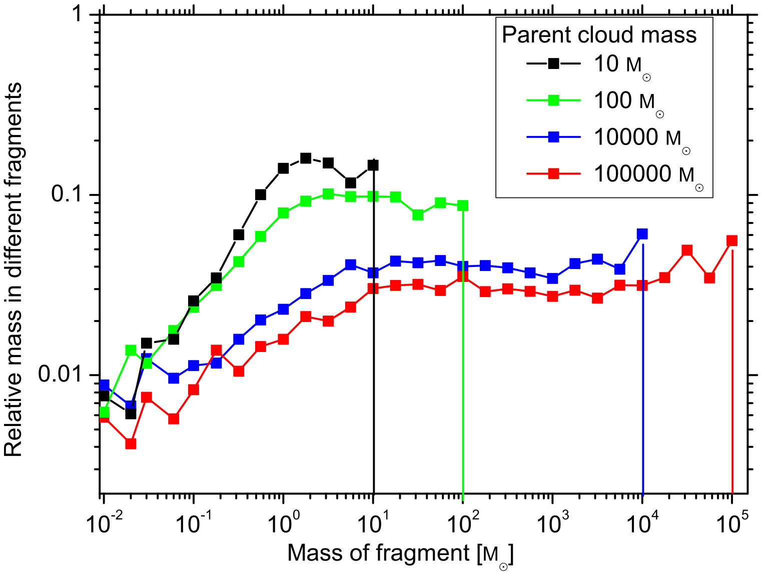

Figure 2.9: Distribution of final (successfully collapsed to formally "infinite" density) fragments of different masses (total mass of fragments per logarithmic interval in fragment mass $dM/d\log M_{\mathrm{fragment}} = M\,dN/d\log M_{\mathrm{fragment}} = M^2\,dN/dM_{\mathrm{fragment}}$ so it is trivial to get $dN/dM_{\mathrm{fragment}}$ which is a more natural observable). We consider this for initial parent cores with different masses (and the surface density-dependent equation of state from Eq. 2.12). Massive fragments can form (albeit rarely) without sub-fragmentation. In all cases where the parent is sufficiently large, there is a flat distribution ($dN/dM \propto M^{-2}$, approximately) at high fragment masses $\gtrsim M_{\odot}$, which is cut-off at the mass of the parent cloud. This self-similar mass function owes to the fact that this is the "scale free" regime where turbulence and gravity dominate. The stiffer equation of state at higher densities, and sub-sonic nature of turbulence on small scales, suppress the number at low masses. Although only a small fraction of mass ends up in these fragments, this corresponds to a large number of individual stars. Also, a significant amount of mass ends up in substellar sized fragments which may either be destroyed by feedback mechanisms or form gas giants.

It should be noted that the CMF have significant uncertainties (Pineda et al. 2009); to account for that the effect of variations in the CMF are investigated in Sec. 2.3.1.2.

It should be noted that Eq. 2.21 neglects two important effects: geometry and feedback. Geometry becomes important as more fragments collapse to stars, leaving behind "holes" in their parent cloud which hinder the formation of large scale substructures. This is related to the so-called "sphere packing problem" that only a fraction of a sphere's volume (e.g. parent cloud) can be filled by non-overlapping spheres[8]. Furthermore, Eq. 2.21 assumes stars form independently and have no feedback on their parent cloud. This is not the case, especially if numerous small fragments form. We can imagine that when a protostar forms, it heats a region around it, preventing that region from collapsing and forming protostars, with some mass $M_{\rm exc}$ which we call the *exclusion mass*. We can crudely account for this effect by by taking the number of independent regions to be $M_0/M \rightarrow M_0/(M + M_{\rm exc})$. Essentially this "excludes" $M_{\rm exc}$ mass from further collapse each time a protostar forms.

What is a reasonable choice for the exclusion mass? Krumholz (2011) argue that young, low-mass protostars accrete gas at a very high rate (leading to a luminosity $L \propto G\,M\,\dot{M}/R$ which grows rapidly in time) until they reach the mass required for deuterium burning, which leads to a characteristic luminosity and correspondingly, a characteristic mass of the surrounding median-density cloud which can be heated to the point where it is no longer gravitationally unstable. In their argument, depending on the background pressure, this produces an effective "exclusion mass" which varies between $10^{-2} - 10^{0}\,\mathrm{M}_{\odot}$. Based on this as a first approximation we will experiment with an exclusion mass of $\mathcal{O}\,(0.01\,\mathrm{M}_{\odot})$. It should be noted that our intention with this crude assumption is not at all to give a full account of stellar feedback but to provide a simple correction mechanism for the overabundance of small mass fragments. In future work, we will explore a more self-consistent accounting for feedback in these calculations.

Another uncertainty is introduced by the fact that protostellar discs can fragment, creating further brown dwarf sized objects. This combined with the sensitivity of the low mass end of the IMF to the equation of state of the gas and the crude approximation of feedback means that the model is highly uncertain in the very low mass region of the IMF.

We now consider the results of our calculation. Figure 2.10 shows the core mass function before any collapse ($n_{core}(M)$) and after collapse ($n_{stars}(M)$). Compare this to the three qualitative properties of the IMF mentioned in Sec. 2.1. We find that it exhibits

---

[8] Preliminary results from spatially resolved simulations suggest that these geometric effects cause only order of unity differences.

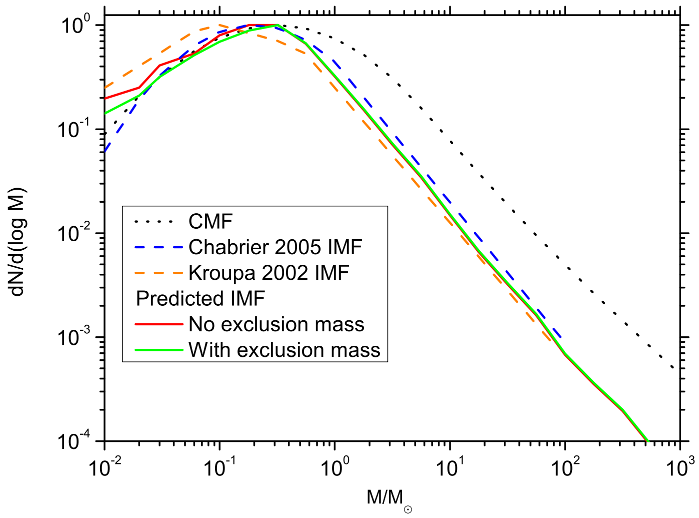

Figure 2.10: Core mass function before and after final collapse compared with IMFs by Kroupa (2002) and Chabrier (2005). Note that the absolute number (vertical normalization) is arbitrary, so we normalize each to the same peak value. After collapse/fragmentation, the high mass slope becomes slightly steeper, and the turnover point and cut-off mass move to lower masses. The model provides a near perfect fit to the observed IMF at the high mass end (the predicted slope of 2.32 is well within the error of the nominal 2.35). The calculations here use the surface density-dependent equation of state Eq. 2.12; this preserves the turnover at low masses; crudely the difference resembles a "shift" of the IMF peak by a factor of $\sim 2-3$. However even in this case, there is some pile-up at small masses $< 0.1\,\mathrm{M}_\odot$, which may disagree with observations (depending on the preferred "correct" IMF); this can be mitigated by applying an appropriate exclusion mass (here we show the results for $M_{\mathrm{exc}} = 0.02\,\mathrm{M}_\odot$), which accounts for the protostars heating up their surroundings and preventing fragmentation.

1. a power law scaling of of $\mathcal{O}\left(M^{-2}\right)$ for high masses;
2. turnover at $\mathcal{O}\left(0.5\,\mathrm{M}_\odot\right)$;
3. close to lognormal dependence at low mass scales.

In summary, it seems that this excursion set formalism can reproduce the main qualitative features of the IMF, and potentially provide an explanation for the universality of these properties. In the following subsections we consider these properties in more detail.

2.3.1 Dependence of the IMF on System Properties and Robustness of These Results

Considering the the ubiquity of these IMF features in nature, and the number of assumptions in the model, it is critical to investigate the robustness of our results. The two primary parameters of our model are the initial CMF, which is dependent on the parameters of the original galactic disk for which the pre-collapse “last crossing scale” calculation was carried out, and the equation of state, which is highly uncertain.

2.3.1.1 Dependence on the Equation of State

First, we have repeated our calculations using different functional forms for the equation of state γ. Fig. 2.11 shows the resulting IMFs for constant γ values (pure polytropes), for the original equation of state $\gamma_1(\Sigma)$ and for shifted equations of states ($\gamma_2(\Sigma)$ and $\gamma_3(\Sigma)$), where the upper surface density limit corresponding to $\gamma = 1.4$ is set to $\Sigma = 2 \cdot 10^4\,\mathrm{M}_\odot/\mathrm{pc}^2$ and $\Sigma = 2 \cdot 10^5\,\mathrm{M}_\odot/\mathrm{pc}^2$ respectively (see Eq. 2.12 for original).

By analyzing the collapse histories, we have found that turbulent fragmentation occurs in a top-down cascade as large clouds fragment into clouds of smaller, but still comparable sizes (i.e. the largest scales tend to fragment first), which then undergo fragmentation again. Based on Fig. 2.11, it is apparent that the high-mass power-law slope of the IMF is unaffected by the choice of γ, as all solutions tend to a power-law like slope which is slightly steeper than the original CMF slope, and is in good agreement with the observed Salpeter slope. That is because they are in the super-sonic regime (i.e. clouds have virial motions and/or initial turbulent motions which are firmly super-sonic); so the cloud dynamics and fragmentation are, to first order, dependent on turbulence and gravity, not on the thermal pressure of the gas, and the fragmentation cascade is inherently scale-free (as are both turbulence and gravity).

Note that our calculation predicts that “final” objects (which have successfully collapsed to infinitely high densities) can exist at high masses; successful collapse without fragmentation is rare, but not impossible. Because the cloud collapses in finite time, and the turbulent fluctuations are self-similar in the scale-free regime, the probability of avoiding a density fluctuation which would cause fragmentation is only power-law suppressed, not exponentially suppressed. Thus high-mass “final” cores can form. In fact our calculation

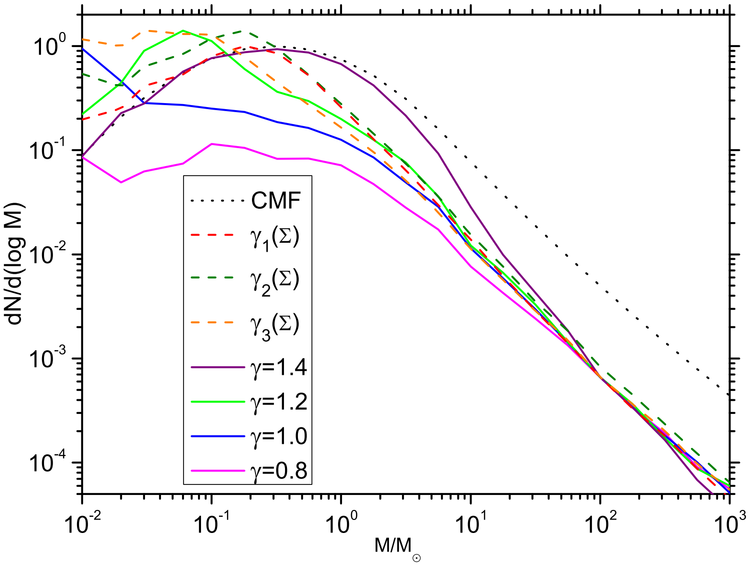

Figure 2.11: Predicted IMF for different equations of state (constant polytropes, the original $\gamma\,(\Sigma)$ from Eq. 2.12, and the shifted equations of state $\gamma_2\,(\Sigma)$ and $\gamma_3\,(\Sigma)$, where the upper surface density limit corresponding to $\gamma = 1.4$ is set to $\Sigma = 2 \cdot 10^4\,\mathrm{M_\odot/pc^2}$ and $\Sigma = 2 \cdot 10^5\,\mathrm{M_\odot/pc^2}$ respectively, with no exclusion mass correction. The high mass end is insensitive to the choice of γ, as massive clouds are highly turbulent (see Eq. 2.10), leading to scale free fragmentation. We normalize the IMFs at $100\,\mathrm{M_\odot}$ for ease of comparison. A “soft” EOS with $\gamma < 4/3$ at all density scales would predict an excess (relative to observations) of fragmentation into brown dwarfs and sub-stellar objects ($M \lesssim 0.1\,\mathrm{M_\odot}$). Some fragmentation can occur even with a “stiff” ($\gamma > 4/3$) EOS, but only at very high masses where the turbulence is highly super-sonic. Lower γ values lead to an increase in the number of small fragments, as there is less thermal pressure to resist fragmentation (see Eq. 2.9). Changing between the different functional forms of $\gamma\,(\Sigma)$ (which means increasing the upper density limit of the EOS) shifts the turnover point to lower masses and increases the number of small fragments as a higher surface density is required to reach high enough γ values to resist further collapse.

predicts that the Salpeter slope continues to $\sim 10^4 \mathrm{M}_\odot$. If there is an actual "maximum" stellar mass – i.e. if the actual stellar IMF cuts off at $O(100\,\mathrm{M}_\odot)$, other factors besides pure turbulent fragmentation (e.g. fragmentation within the protostellar disk, or stellar stability at high masses, feedback from smaller stars, that form faster), must play a role. However whether such a cut-off exists is still uncertain.

Meanwhile, Fig. 2.11 also shows that the low-mass end of the IMF is heavily dependent on the equation of state. A stiff EOS ($\gamma > 4/3$) basically freezes the CMF shape at solar and lower masses (no fragmentation occurs on small scales), while small values of γ lead to increased fragmentation (Fig. 2.11), which predict either no turnover in the IMF, or a turnover at much too-low masses. Note that in Fig. 2.11 it might at first appear that fragmentation is stronger in the $\gamma = 1.0$ case than in the $\gamma = 0.8$ case, however this is just an effect of the limited range and normalization of the plot, as there are actually a significant number of fragments which have smaller masses than $0.01\,\mathrm{M}_\odot$ when $\gamma = 0.8$. Fig. 2.12 shows more clearly the fraction of the total mass ending up in substellar ($M < 0.01\,\mathrm{M}_\odot$) fragments, as a function of the EOS assumed[9]. As expected, the formation of small fragments decreases monotonically with γ, and falls rapidly as we approach $\gamma = 4/3$.

2.3.1.2 Dependence on the Core Mass Function

The initial CMF used in our calculation is, itself, the prediction of turbulent fragmentation theory (it is the result of a similar excursion-set calculation of the "last-crossing" scales in a galactic disk; see Hopkins 2012a). But the CMF could vary, or be different than predicted by this calculation owing to additional physics. We therefore next consider the IMF which results from different initial CMFs.

To clearly isolate the most important dependencies and physics, it is actually much more instructive to adopt the following simple approximation of the

---

[9] Our preliminary calculations with an explicitly 3D spatially dependent version of the model indicate that the substellar fraction is overestimated in Fig. 2.12 because it is assumed that all mass ends up in bound structures while it is possible in reality for loose material to become unbound after fragmentation (see sphere packing considerations in Sec. 2.3). The same discrepancy occurs in the cosmological Press-Schecter treatment, where it amounts to a factor of 2 at low masses. In case of our default EOS the difference is about a factor of 5.

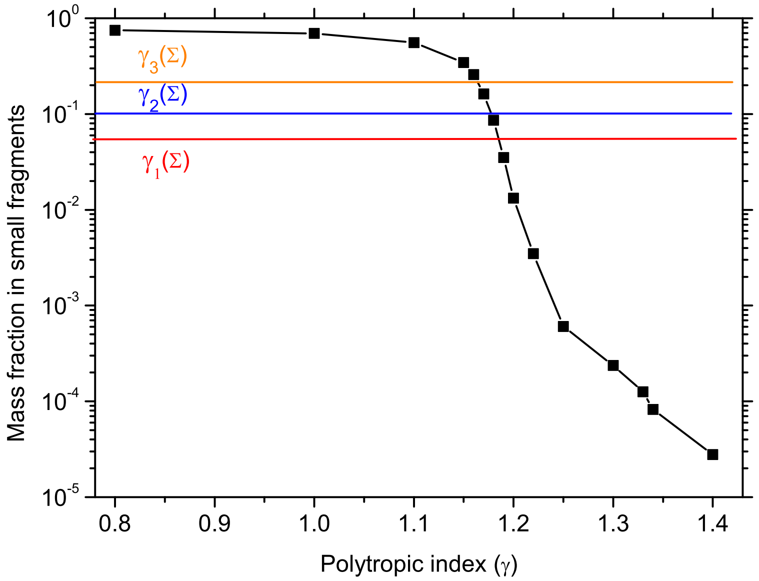

Figure 2.12: Fraction of the total "original CMF" mass which ends up in sub-stellar ($M < 0.01\,\mathrm{M}_\odot$) fragments, for different equations of state. The single value lines correspond to our default (surface density-dependent) equation of state $\gamma\,(\Sigma)$ and the shifted $\gamma'\,(\Sigma)$; otherwise we assume a constant polytropic EOS and show the fraction as a function of that γ. For very soft (sub-isothermal) EOS values $\gamma < 1$, the fragmentation cascades tend to proceed without limit, and most of the initial core mass ends up in arbitrarily small fragments! Higher γ values allow the clouds to resist fragmentation, and above $\gamma = 4/3$ small fragments basically vanish. No exclusion mass correction is applied here.

CMF, rather than some more complicated functional form:

$$\frac{\mathrm{d}N}{\mathrm{d}\log M} \propto \begin{cases} M^{\alpha} & M < M_T \\ M^{-\beta} & M > M_T \end{cases}, \tag{2.22}$$

where in our "default" CMF, $\alpha = 1/2$ and $\beta = 1.1$ are the approximate exponents of the low and high mass slopes, respectively, while $M_T = 0.5\,\mathrm{M}_\odot$ is the turnover mass. This allows us to systematically vary these three parameters and examine their impacts on the IMF. In each case, we will hold the equation of state $\gamma(\Sigma)$ fixed to our "default" value, and include no exclusion mass correction, so that the changes are purely a consequence of the CMF variation.

In the turbulent framework we don't expect the high mass slope of the CMF (β) to vary as it is set by purely supersonic turbulence (see Hopkins (2013e)), however it is instructive to see whether the initial distribution (CMF) or the turbulent fragmentation sets the slope of the IMF. As Fig. 2.13 shows fragmentation at the high mass end is close to scale free – i.e. the slope of the IMF is always a power-law, which is systematically steeper than the CMF by a small, approximately fixed amount, independent of the actual initial high-mass slope of the CMF (or turnover mass, or low-mass CMF slope). The high-mass steepening is systematically $\Delta\beta \sim 0.2 - 0.25$. Let us consider now how much of a steepening would we expect. The IMF reflects the average rate at which final fragments collapse. The collapse time of a cloud is approximately $T_{collapse} \sim t_{\rm dynamical} \sim 1/\sqrt{GM/R^3}$, which in the high-mass, supersonic limit ($R \propto \sqrt{M}$; see Eq. 2.10) gives $T_{collapse} \propto M^{1/4}$. So in the time for one high-mass core to collapse, multiple generations of low-mass cores can be spawned and collapse; to first approximation the ratio of the number of stars produced if we integrate over a fixed timescale (the collapse time of the large clouds) will be $n_{stars}/{\rm n}_{cores} \propto 1/T_{collapse} \propto M^{-1/4}$, meaning $\Delta\beta = 0.25$.

The low mass end of the CMF is heavily dependent on galactic properties (see Fig. 2 of Hopkins (2013e)) so the value of α is far from fixed. However, small cores tend to collapse without further fragmentation so their effect on the IMF is just providing an initial population of small stars which is increased by the smaller fragments of high mass cores. This means that the low-mass end of the predicted IMF is sensitive to all changes in the CMF (Figs. Fig. 2.13-2.14). If we adopt an unphysical but instructive toy model where there are initially no low-mass cores, we see a sizable population of low-mass objects still appears in our final IMF. This is clear also from Fig. 2.9; cores fragment into a very broad mass spectrum, and even high-mass cores can form very low-mass fragments. This is also evident if we adopt an initial CMF which has an (unphysically) shallow high-mass slope, such that there is an unlimited mass supply of very high-mass cores – in turn there would be far too many small cores. It is also worth nothing that we appear to robustly predict that the approximate total number density ($dN/d\log M$) of objects with sub-stellar masses ($\sim 0.01 - 0.1\,\mathrm{M}_{\odot}$) is never much less than $\sim 10\%$ that of objects with $\sim 0.1 - 1\,\mathrm{M}_{\odot}$.

Finally, the turnover mass of the CMF (M_T) is proportional to the the sonic mass $M_{\rm sonic} \sim c_s^2 R_{\rm sonic}/G$ which is set by both galactic and local properties. This means that there could be some variation in the CMF turnover point

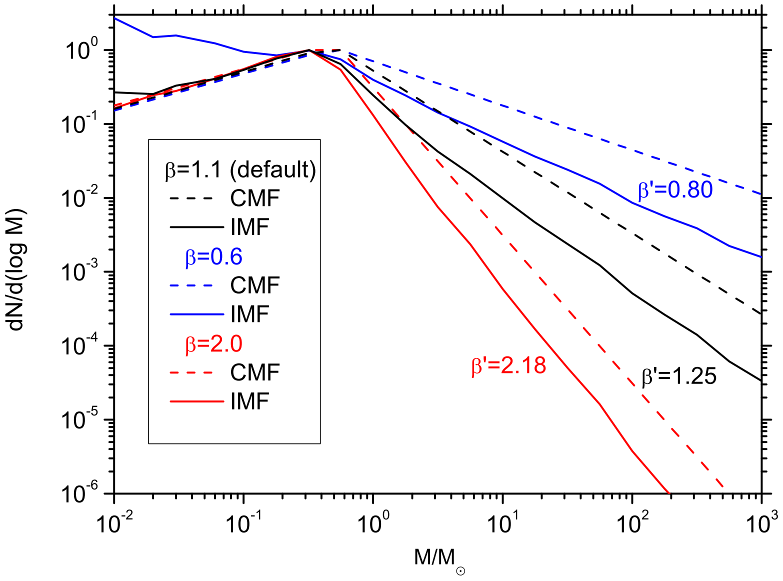

Figure 2.13: Effects on the predicted IMF from having different slopes ($dN/d\log M \propto M^{-\beta}$) for the initial CMF. For each we keep all other parameters (e.g. $\gamma(\Sigma)$) fixed at their default values from Fig. 2.10, and include no exclusion mass correction. We show the resulting IMF, with the final high-mass power-law (β') scaling. It is clear that fragmentation is close to scale-free as the IMFs produce high-mass power-law slopes close to the "progenitor" CMF slope, but steeper by a systematic $\Delta\beta \sim 0.2$. This systematic change can be understood as a consequence of time-dependent fragmentation at high masses; it also naturally explains the difference between the observed Salpeter slope of the IMF (~ 1.3) and the predicted slope of the CMF from turbulent fragmentation models (closer to $\beta \approx 1.0-1.1$; see Hennebelle & Chabrier 2013b; Hopkins 2012b). Note that if the high-mass slope is sufficiently shallow ($\beta < 1$), a pile-up at low masses results from fragmented large cores. However such shallow values are unphysical (they imply a divergent amount of mass in large cores).

(as noted by Hennebelle & Chabrier (2013b); Hopkins (2012b)) which is in agreement with the observations (see Fig. 2.7). Interestingly, the position of the turnover point in the initial CMF only determines the point where the IMF starts to "flatten"; however the details here are also dependent on the underlying physics (e.g. the equation of state). Nevertheless we can say that the turnover mass for reasonable parameters resides around $O(0.5\,\mathrm{M}_\odot)$.

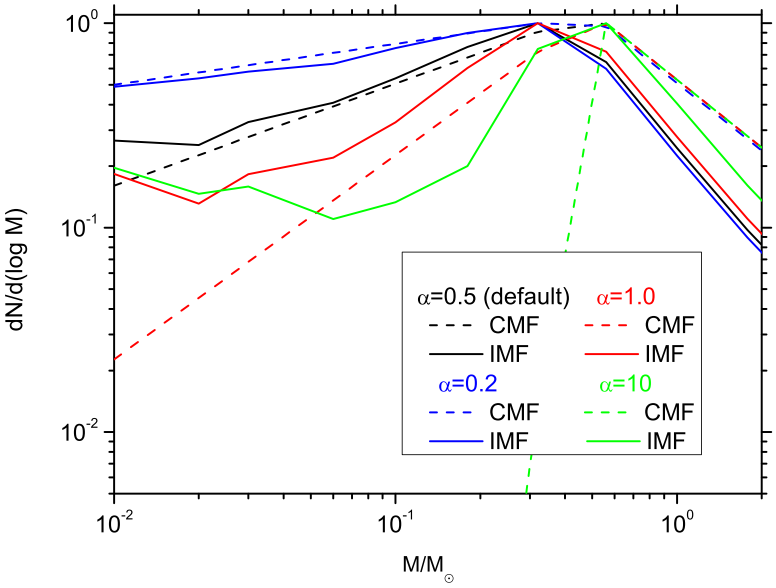

Figure 2.14: Effects from different having slopes ($dN/d\log M \propto M^{+\alpha}$) at the low mass end of the initial CMF. As Fig. 2.13, we keep all other parameters fixed. Since fragmentation is top-down, the low-mass CMF slope has no impact on the high-mass IMF. It is apparent that a significant fraction of the low-mass objects in the IMF are in fact fragments from much larger "parent" cores – most clear when there are essentially no small cores to begin (the unphysical but instructive $\alpha = 10$ case). However, for "shallower" initial CMF low-mass slopes, the IMF tends to trace the CMF, and the low mass stars are predominantly formed from low mass cores.

2.4 Conclusions

The aim of this paper was to provide a feasible candidate for the primary physical phenomena that determine the qualitative properties of the stellar initial mass function. This was achieved by expanding upon the excursion set formalism outlined in more detail by Hopkins (2013c), and applying it to follow the time-dependent collapse of protostellar cores into protostars. This improves on previous work done by Padoan et al. (1997), Hennebelle & Chabrier (2008) and Hopkins (2012b), by following fragmentation down to stellar scales while taking into account the nonlinear time dependence and complicated equations of state (and their effects in making the density PDFs deviate dramatically from log-normal distributions). We found that this simple model reproduces the main qualitative features of the IMF, and it allows us to answer several

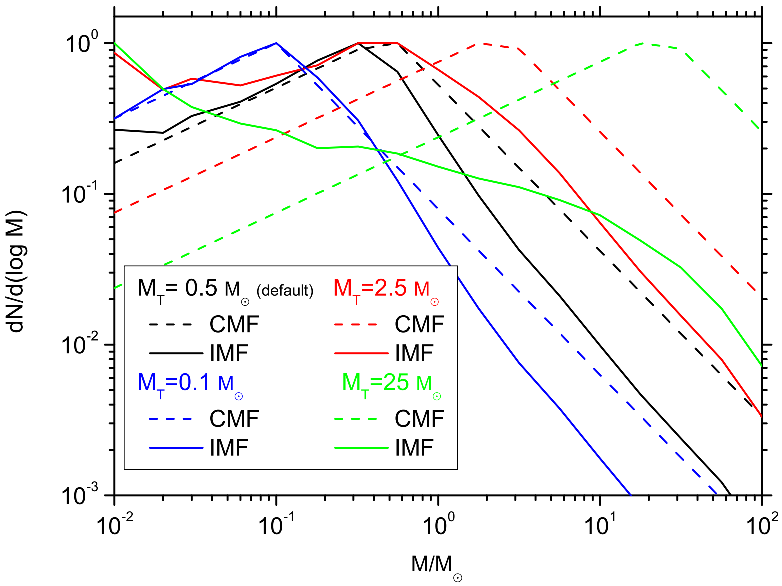

Figure 2.15: Effects from moving the turnover mass (M_T) of the initial CMF. As Fig. 2.13, we keep all other parameters fixed. The high-mass slope is unchanged by this choice, as in the turbulence-dominated regime the behavior becomes scale free (see Eq. 2.10). But the turnover point of the predicted IMF (or more accurately, where the resulting IMF becomes "shallow" and the total mass in stars converges, even if the IMF it does not completely turn over) clearly scales here with the turnover mass of the CMF.

critical unresolved questions in the theory of turbulent fragmentation.

The fact that both turbulence and gravity are scale free robustly predicts a CMF – an instantaneous mass function of "last-crossings" – with a high-mass slope $dN/dM \propto M^{-(2.0-2.1)}$ (see references above). This is the inevitable result of any scale-free, self-similar fragmentation process (basically, a slope of -2, which implies equal mass per log interval in mass, with a small logarithmic correction which depends on the properties of the medium but only very weakly). Time-dependent turbulent fragmentation slightly steepens this slope by a systematic $\Delta\beta = 0.25$, creating a near-perfect fit with the canonical Salpeter slope of the observed IMF. The results are very robust to changes in both the initial conditions of the galactic disk, the equation of state of the gas, the presence of stellar feedback, the strength of the turbulence and the form of the CMF. Thus we can say that the Salpeter slope is an inevitable consequence of turbulent fragmentation and is expected to be "universal."

Observed IMFs and CMFs have very similar shapes, and it appears as if the IMF is just a "shifted" version of the CMF. The simplest explanation would be that a constant fraction $\sim 1/3$ of each core ends up in a single star. This is not the case in turbulent fragmentation. Rather, the apparent shift is the result of the nearly scale-free fragmentation in the high mass regime, and the flattening/turnover imprinted by the CMF and equation of state. We showed that, in fact, a high-mass core (which has initially no self-gravitating substructure) is typically expected to fragment into a broad range of masses, with comparable mass in fragments of all masses down to sub-solar masses. However, because this fragmentation produces a similar power-law slope for the IMF and CMF (see above), the result looks like a "shift." We stress that the shift should not even be interpreted as an "average fragment size" – that is actually much smaller (factor < 0.1 of the original core size, for $\gg 10\,\mathrm{M}_{\odot}$ cores). It is more accurate to say that sufficiently massive cores fragment into a spectrum of masses which resembles the IMF mass spectrum itself; since the convolution of a lognormal (or power-law) with another lognormal (or power-law) yields the same function, this produces the observed IMF shape. There is no one-to-one relation between cores and stars (far from it).

It has been argued that purely isothermal turbulent fragmentation cannot produce the observed universal IMF, because collapsing clouds will inevitably become supersonically turbulent as gravitational energy pumps random motions, until fragmentation occurs. We confirm this is the case. Thus a CMF model based purely on isothermal turbulence – or any simple polytrope – is incomplete. However, that does not mean there could be no "flattening" of the IMF. Even for pure isothermal gas, the IMF still becomes more shallow than Salpeter around the "sonic scale." This is related to what has been shown for the CMF: there is a characteristic scale in isothermal turbulence, the sonic scale, around which fragmentation becomes more or less "easy." (It is only if one considers only thermal pressure, i.e. the Jeans length, that there is no characteristic scale). However, with isothermal gas, there is no true "turnover" in the IMF; moreover, most of the core mass ends up in very small (substellar) fragments.

We found that the turnover point in the initial CMF determines the point at which the IMF first "flattens" from the Salpeter slope. However, this does not necessarily amount to a full "turnover" in the IMF. Observationally, this "flattening" mass occurs at $\sim 0.5\,\mathrm{M}_{\odot}$; for reasonable assumptions, we obtain a similar result. The CMF turnover point in turbulent fragmentation is robustly set by the "sonic mass" $M_{\rm sonic} \sim c_s^2\,R_{\rm sonic}/G$, the minimum self-gravitating mass at the sonic scale. Below this scale, the turbulence is sub-sonic, so large density fluctuations (in the parts of the medium which are not already self-gravitating) are not generated. As a result, we predict a "flattening mass" that scales as $\sim 0.5\,{\rm M}_{\odot}\,(T_{{\rm m}in}/30\,K)\,(\langle R_{\rm sonic}\rangle/0.1\,{\rm p}c)$, where $T_{{\rm m}in}$ is the minimum temperature reached by molecular cooling, and $\langle R_{\rm sonic}\rangle$ is the sonic length of the *pre-collapse* clouds – i.e. the mean sonic length in the galactic disk (not a cloud-by-cloud quantity, since this changes as the cloud starts collapsing). As noted in Hopkins (2013e), this predicts a very close to universal flattening mass within the Milky Way and nearby galaxies, but a lower flattening mass in extreme (high-Mach number) environments, where the sonic length is smaller, at the center of starburst galaxies and ellipticals. We will investigate this further in future work.

The choice of equation of state, and effects of stellar feedback (crudely modeled here via an "exclusion mass" which is heated by each protostar) have some effect on the "flattening mass," but a surprisingly weak one (shifting it by factors ~ 2, for a fixed CMF). However, they critically determine the behavior below this mass. In particular, whether the IMF actually "turns over," or simply flattens, depends on these effects. If we assume any polytropic equation of state with $\gamma < 4/3$, the IMF will still flatten, but will not turn over as observed (the IMF peak, in $dN/d\log M$, which is observed to be between $\sim 0.1-0.3\,{\rm M}_{\odot}$, does not occur until $\ll 0.1\,{\rm M}_{\odot}$). However, a surface-density dependent EOS, motivated by direct numerical calculations, is able to produce a reasonable turnover. This is because the characteristic surface density required for such a fragment to be self-gravitating is $\gtrsim 1\,{\rm g}\,cm^{-2}$ (higher if the fragment is embedded in an already-collapsing core, as we find is usually the case), and so approaches the limit where it becomes optically thick to its own cooling radiation. If the this is indeed the relevant limit, we expect this mass to be weakly dependent on the minimum cooling temperature and the metallicity of the gas: requiring that a thermally pressure-supported cloud be self-gravitating, we predict this mass scales as $\sim\,0.1\,{\rm M}_{\odot}\,(T_{{\rm m}in}/10\,K)^2\,(\kappa/\kappa_{{\rm M}ilkyWay})\,\sim\,0.1\,{\rm M}_{\odot}\,(T_{{\rm m}in}/30\,K)^2\,(Z/Z_{\odot})$ – this is weakly-varying in most systems, since $T_{{\rm m}in}$ tends to decrease with metallicity (as low-temperature cooling is more efficient), while κ increases. The presence of an "exclusion mass" further influences the details of the low-mass turnover, and may lead to a "more universal" behavior. We argue below that the key effects of feedback may be in preventing other effects we have ignored in our calculations.

2.4.1 Speculations

We found that fragmentation usually occurs on a scale comparable to the parent cloud (because in turbulence, the power in density fluctuations is dominated by the large-scale fluctuations), which means that the fragmentation of collapsing cores can be accurately modeled as a top-down cascade. On average a large cloud loses equal amounts of mass to fragments per logarithmic interval in "fragment mass" (see Fig. 2.9), demonstrating the scale-free nature of the process. But even the largest, supersonic clouds have a nonzero chance of not fragmenting. This leads to an interesting prediction: turbulent fragmentation alone predicts that the Salpeter slope in a galactic disk continues to very high masses, $\sim 10^4\,\mathrm{M}_{\odot}$. Whether such stars actually exist is still a matter of debate; however, it is commonly assumed that the most massive stars have masses $\sim 100-200\,\mathrm{M}_{\odot}$. If this is the case, some other physics (e.g. fragmentation in proto-stellar disks, or stellar stability) must be the reason.

The fragmentation cascade predicted by the model can lead to the creation of substellar sized fragments, which could theoretically condense into gas giants. The amount of mass ending up in such fragments is heavily dependent on the initial CMF and the equation of state. Nevertheless, it is important to note that these fragments would not be visible in numerical simulations (due to their resolution limits), but could lead to a large population of gas giant sized objects – "free-floating planets" – in the ISM. This, however, might not be the case if some physical process (e.g. stellar feedback) stops the cascade at smaller scales.

It should be noted that this model incorporates no real feedback physics, and does not take accretion by the protostars into account. Considering how well the results fit to the observed IMF, we tentatively conclude that those processes have negligible effect on the high-mass slope of the IMF. However, we believe stellar feedback could potentially solve the problem of the model predicting extremely massive ($\sim 10^3\,\mathrm{M}_{\odot}$) stars. Since small objects collapse faster, there would be a significant number of realistic sized stars before a substructure of $10^3\,\mathrm{M}_{\odot}$ could collapse. The more massive of these stars have a lifetime of several Myr which is comparable to the collapse time of the substructure. This means the cloud could be unbound by neighboring supernovae before it could collapse.

Meanwhile at the low-mass end, there is clearly a very strong effect from feedback, which we crudely modeled by way of either the "effective equation of state" or "exclusion mass." However, even there, we do not necessarily expect feedback to strongly modify the "top-down" cascade we model. What may be more important, instead, is that feedback could prevent runaway accretion. Turbulent fragmentation naturally produces an IMF with the Salpeter slope and a turnover mass at the appropriate scale: subsequent "competitive accretion" would make the IMF more and more shallow, and turn sub-stellar fragments into brown dwarfs, leading to an excess population of such objects. The key role of feedback may therefore be to prevent such accretion – i.e. "shut down" further accretion after the "initial" collapse (the part we model here). And in fact, this has been suggested in numerical simulations, where the "initial" IMF formed by turbulent fragmentation looks reasonable, but (without feedback) increasingly deviates from the observations as the system evolves (Bate 2009a, 2012b; Krumholz 2011; Offner et al. 2009a).

2.4.2 Future Work and Caveats

Of course, although this model represents a qualitative improvement on the previous work in this area, further work is needed:

- Many of the above points have been suggested by simulations (Federrath et al. 2010b; Krumholz 2011; Offner et al. 2009a etc.), however our analytical model allows us to follow an arbitrarily large range of scales (well beyond the resolution of numerical simulations). With our analytic model, we can also obtain statistically robust results, and easily explore a huge parameter space. Nevertheless it is necessary to test these results in full radiation hydrodynamics experiments.

- Due to its simplicity the model ignores several physical processes which could have a significant effect on star formation. An obvious omission is accretion, however the results do reproduce the observed IMF remarkably well, so the question is: does it not matter? An extension of the model which includes accretion (like done by Veltchev et al. (2011)) could answer that question.

- Our model ignores magnetic fields, which may be an acceptable approximation in the high mass limit where the clouds are supersonic, but in the subsonic case ambipolar diffusion could be a serious factor in the collapse of clouds. It may, however, be possible to implement the most important effects of magnetic fields into the model by integrating it into the "effective" equation of state.

- The fragmentation cascade predicts a large number of substellar fragments which could potentially collapse into gas giants. In future work, we will investigate in more detail the formation and evolution of such fragments, and compare their statistics to observational constraints.

- Another key observable is the spatial correlation function of star clusters and young stars. In future work, we will extend the models here to explore these observational constraints.

Chapter 3

STAR FORMATION IN A TURBULENT FRAMEWORK: FROM GIANT MOLECULAR CLOUDS TO PROTOSTARS

Guszejnov D., Hopkins P. F., 2016, MNRAS, 459, 9

Abstract

Turbulence is thought to be a primary driving force behind the early stages of star formation. In this framework large, self gravitating, turbulent clouds fragment into smaller clouds which in turn fragment into even smaller ones. At the end of this cascade we find the clouds which collapse into protostars. Following this process is extremely challenging numerically due to the large dynamical range, so in this paper we propose a semi analytic framework which is able to model star formation from the largest, giant molecular cloud (GMC) scale, to the final protostellar size scale. Due to the simplicity of the framework it is ideal for theoretical experimentation to explore the principal processes behind different aspects of star formation, at the cost of introducing strong assumptions about the collapse process. The basic version of the model discussed in this paper only contains turbulence, gravity and crude assumptions about feedback, nevertheless it can reproduce the observed core mass function (CMF) and provide the protostellar system mass function (PSMF), which shows a striking resemblance to the observed IMF, if a non-negligible fraction of gravitational energy goes into turbulence. Furthermore we find that to produce a universal IMF protostellar feedback must be taken into account otherwise the PSMF peak shows a strong dependence on the background temperature.

3.1 Introduction

Finding a comprehensive description of star formation has been one of the principal challenges of astrophysics for decades. Such a model would prove invaluable to understanding the evolution of galactic structures, binary star systems and even the formation of planets.

It has been long established that stars form from collapsed dense molecular clouds (McKee & Ostriker 2007b). Currently the most promising candidate for a driving process is turbulence, as it can create subregions with sufficiently high density so that they become self gravitating on their own, while also exhibiting close to scale free behavior (in accordance with the observations of

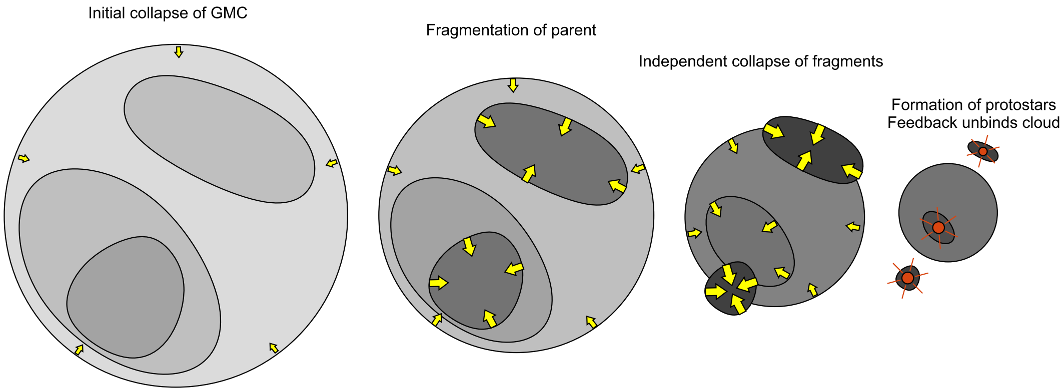

Figure 3.1: Evolution of collapsing clouds, with time increasing from left to right (darker subregions are higher-density, arrows denote regions which are independently self-gravitating and become thicker with increasing collapse rate). As the initial cloud collapses, density fluctuations increase (because gravitational energy pumps turbulence), creating self-gravitating subregions. These then collapse independently from the parent cloud, forming protostars at the end. These protostars can provide a sufficiently strong feedback that the rest of the cloud becomes unbound and ceases to collapse.

Bolatto et al. 2008; Larson 1981). These fragments are inherently denser than their parents so they collapse faster, quasi independent from their surroundings. However, once they turn into stars they start heating up the surrounding gas (by radiation, solar winds or supernova explosions), preventing it from collapsing and forming stars (see Fig. 3.1). This process is inherently hierarchical so it should be possible to derive a model that follows it from the scale of the largest self gravitating clouds, the GMCs ($\sim 100\,\mathrm{pc}$), to the scale of protostars ($\sim 10^{-5}\,\mathrm{pc}$). This is not possible in direct hydrodynamic simulations due to resolution limits, but can be treated approximately in analytic and semi-analytic models.

This paradigm has been explored by Padoan et al. (1997) and Padoan & Nordlund (2002), and then made more rigorous by Hennebelle & Chabrier (2008), who attempted to create an analytic model analogous to Press & Schechter (1974), which approximates the background density field as a Gaussian random field. A similar model was developed by Zamora-Avilés et al. (2012), however that did not rely on turbulence. Later Hopkins (2012a) expanded on these works by adopting the excursion set formalism to find the distribution of the largest self gravitating structures, which was found to be very similar to the observed distribution of GMCs. Similarly Hopkins (2012b) found that the distribution of the smallest self gravitating structures fit well the observed CMF. Building on these results Hopkins (2013c) generalized the formalism to be applicable to systems with different equations of state and turbulent properties.

Observed cores are sub-sonic and show no clear sign of fragmentation and the CMF looks very similar to the IMF apart from a factor of ~ 3 shift in the mass scale (Offner et al. 2014). However, if no other physics is assumed other than isothermal turbulence and gravity, during the collapse the cores develop strong turbulence and eventually sub-fragment into smaller objects (Goodwin et al. 2004; Walch et al. 2012a, for discussion see Krumholz 2014). This implies that some additional physics must play a role, but there is no clear consensus on what it could be; e.g., magnetic fields (McKee & Ostriker 2007a; Nakano & Nakamura 1978), radiation (Krumholz 2011), cooling physics (Jappsen et al. 2005a) etc. Using a cooling physics motivated "stiff" EOS Guszejnov & Hopkins (2015b) incorporated the time dependent collapse of the cores into the excursion set formalism and found that the distribution of protostars closely reproduced the observed IMF.

These excursion set models did successfully reproduce the CMF, IMF and the GMC mass function, however they had several shortcomings. First, they did not account for the differences in formation and collapse times of clouds of different sizes (e.g. small clouds form faster and collapse faster). Secondly, the excursion set formalism describes the density field around a random Lagrangian point. This means that the spatial structure of a cloud cannot be modeled directly (e.g. there is no way to find if a cloud forms binary stars). Finally, there is no self consistent excursion set model that follows from the GMC to the protostar scale (i.e. Hopkins 2012b covered scales between the galactic disk and cores, Guszejnov & Hopkins 2015b between cores and protostars). We believe these shortcomings can be overcome by moving away from the analytic excursion set formalism and instead adopting a simple semi-analytical approach with the same random field assumption. This framework would allow us to follow the evolution self gravitating clouds while resolving both the GMC and protostellar scales and preserving spatial information. In this paper we will outline a possible candidate for such a model.

The paper is organized as follows. Sec. 3.2 provides a general overview of the model, including the primary assumptions and approximations and briefly outlines its numerical realization. Sec. 3.3 shows the simulated time evolution of the CMF and the protostellar system mass function (PSMF), which shows a striking similarity to the IMF. Sec. 3.3.2 also discusses the effects of having a temperature independent equation of state on the peak of the PSMF and the universality of the IMF. Finally, Sec. 3.4 discusses the results and further applicability of the model.

3.2 Methodology

In short, instead of doing a detailed hydrodynamical simulation involving gravity and radiation, our model assumes a simple stationary model for the density field, collapse of structures at constant virial parameter and an equation of state that depends on cloud properties. Starting from a GMC sized cloud it evolves the density field as the cloud collapses and pumps turbulence (this is not a bad approxiation, see Murray & Chang 2015; Murray et al. 2015; Robertson & Goldreich 2012b). Note that our assumptions do not necessarily mean that all clouds have supersonic turbulence. Paper II has shown that if a medium has a "stiff" equation of state ($\gamma > 4/3$), then turbulence is dampened during collapse. Since it is observed that dense, low mass cores are subsonic while high mass, low density clouds are supersonic, some form of physics is needed to remove the turbulent energy. For that purpose we are using an equation of state that becomes stiff at high densities, which in combination with the constant virial parameter assumption makes dense clouds sub-sonic, arresting fragmentation.

In the model, at each time step we search for self gravitating structures which we treat as new fragments, for which the process is repeated in recursion until a substructure is found that collapses to protostellar scale without fragmenting. Our assumptions will be discussed in more detail in the following subsections while a step-by-step description of the algorithm is provided in Sec. 3.A.

Our model is a modified version of the excursion set model used by Guszejnov & Hopkins (2015b) (henceforth referred to as Paper I) using the theoretical foundation of Hopkins (2013c) (henceforth referred to as Paper II). Due to the significant overlap between models we show only the essential equations and emphasize the differences and their consequences. If the reader is familiar with Paper I we suggest skipping to Sec. 3.2.3.

3.2.1 The Density Field

It is known that the density field in the cases of both sub and supersonic, isothermal flows follows approximately lognormal statistics (for corrections see Hopkins (2013d)). This means that if we introduce the density contrast $\delta(\mathbf{x}) = \ln[\rho(\mathbf{x})/\rho_0] + S/2$, with $\rho(\mathbf{x})$ as the local density, ρ_0 as the mean density and S as the variance of $\ln\rho$, it would follow a close to Gaussian distribution[1]; thus

$$P(\delta|S) \approx \frac{1}{2\pi S}\exp\left(-\frac{\delta^2}{2S}\right). \tag{3.1}$$

It is a property of normal and lognormal random variables that a linear functional of these variables will also be normal/lognormal, and thus the averaged density in a region has lognormal equilibrium statistics whose properties are prescribed by turbulence. Following Paper II this yields

$$S(\lambda) = \int_0^\lambda \Delta S(\lambda) d\ln\lambda \approx \int_0^\lambda \ln\left[1 + b^2\mathcal{M}^2(\lambda)\right]\mathrm{d}\ln\lambda, \tag{3.2}$$

where λ is the averaging scale, $\mathcal{M}(\lambda)$ is the Mach number of the turbulent velocity dispersion on scale λ and b is the fraction of the turbulent kinetic energy in compressive motions, which we take to be about $1/2$ (this is appropriate for an equilibrium mix of driving modes, see Federrath et al. 2008 for details. Paper I experimented with $b \sim 1/4 - 1$ and found no qualitative differences).

It is important to note that although ρ is lognormal, which means δ is Gaussian, there is significant spatial correlation (i.e. ρ cannot change instantly over arbitrarily small spatial intervals) so it is not possible to model the density field as a spatially independent random field. To circumvent this issue we solve the problem in Fourier space since $\delta(k)$ is also lognormal, while there is little correlation between modes so it is acceptable to assume them to be independent (note: having correlated modes in Fourier space introduces only mild effects on the final mass functions, see Appendix A of Paper II for details). Combined with the fact that the number of modes in the $[k, k+\mathrm{d}k]$ range is $\mathrm{d}N(k) = \left(4\pi k^2\mathrm{d}k\right) n_k$, where n_k is the mode density, we get the variance for an

---

[1] It is a common misconception that analytical models such as the one presented in this paper take the total density distribution to be purely lognormal. While the density distribution in each cloud/fragment is indeed assumed to be locally lognormal on a single timestep, these have different means and deviations (see Eq. 3.2) depending on their initial conditions and time, which means that the total distribution will be different. If we measure the density distribution in our calculations (see Fig. 3.2), we find it is approximately lognormal at low densities (set by the lowest density structure: the parent cloud), while the high mass end becomes a power law as it is a mass weighted average of the distributions for different substructures whose mass distribution is a power law (see Fig. 3.4).

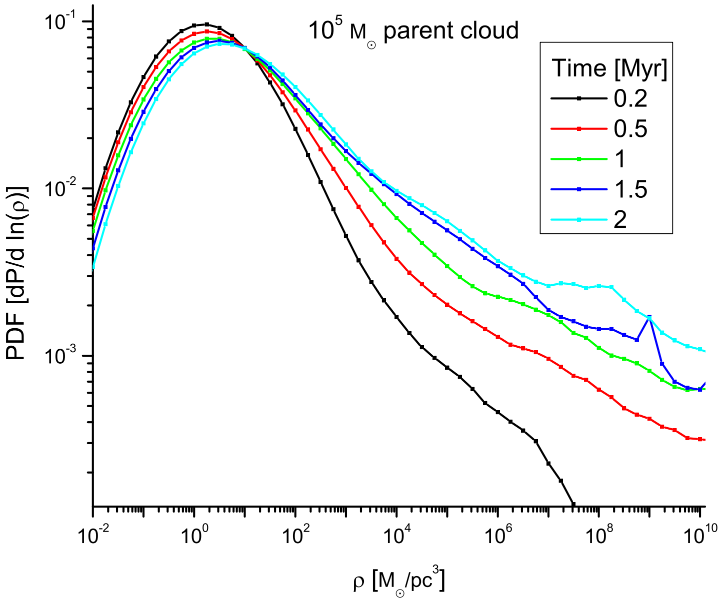

Figure 3.2: Time evolution of the distribution of density in a parent GMC of $10^5\,\mathbf{M}_\odot$. This is a mass weighted average of the density distribution of all substructures in the parent cloud (which are all assumed to be lognormal with different parameters), thus the low mass end is set by the lowest density structure which is the parent cloud while the high mass end is a power law due to the power law like distribution of fragments (see Fig. 3.4). There is also a clear trend as the high mass end tail rises in time. This is caused by the formation of new self gravitating substructures (Federrath & Klessen 2013).

individual density contrast mode:

$$S_{\mathrm{mode}}(\mathbf{k}) = \frac{\ln(1+b^2\mathcal{M}(k)^2)}{4\pi k^3 n_k}. \tag{3.3}$$

Paper II showed that to realize a steady state density contrast field with such variance and zero mean, the Fourier component $\delta(\mathbf{k},t)$ must evolve as

$$\delta(\mathbf{k},t+\Delta t) = \delta(\mathbf{k},t)\,(1-\Delta t/\tau_k) + \mathcal{R}\sqrt{2S_{\mathrm{mode}}(\mathbf{k})\Delta t/\tau_k}, \tag{3.4}$$

where $\mathcal{R}$ is a Gaussian random number with zero mean and unit variance while $\tau_k \sim v_t(k)/\lambda$ is the turbulent crossing time on scale $\lambda \sim 1/k$, and the turbulence dispersion obeys $v_t^2(\lambda) \propto \lambda^{p-1}$, thus $\tau_\lambda \propto \lambda^{\frac{p-3}{2}}$ (in our simulations we use $p = 2$, appropriate for supersonic turbulence, see (Federrath, 2013; Murray, 1973; Schmidt et al., 2009)).

3.2.1.1 The Equation of State

It is easy to convince oneself that a purely isothermal or polytropic equation of state (EOS) would be a very poor description of the complex physical processes contributing to the cooling and heating of clouds, however, modeling these processes in detail would require full numerical simulations. Instead we try to find a simple, heuristic EOS that captures the behaviors critical to our calculation. One of the most important effects during collapse is the transitioning from the state where the cooling radiation efficiently escapes from the cloud to the state where the cloud becomes optically thick to it and heats up as it contracts. As the virial parameter is assumed to be constant, this leads to a decrease in turbulence, which effectively arrests fragmentation. This is essential to reproduce the IMF shape as pure isothermal collapse would lead to an infinite fragmentation cascade. We adopt the same effective polytropic EOS model as Paper I where for small time steps (compared to the dynamical time):

$$T(\mathbf{x}, t+\Delta t) = T(\mathbf{x}, t)\left(\frac{\rho(\mathbf{x}, t+\Delta t)}{\rho(\mathbf{x}, t)}\right)^{\gamma(t)-1}, \tag{3.5}$$

where $\gamma(t)$ is the effective polytropic index of the cloud at time t.

One of the main goals and advantages of our framework is that it allows the exploration of different physical EOS models simply and efficiently. For example, let us consider first the volume-density (n) dependent EOS model based on works like Glover & Mac Low 2007; Masunaga & Inutsuka 2000 that follows the form

$$\gamma(n) = \begin{cases} 0.8 & n < 10^5\,\mathrm{cm}^{-3} \\ 1.0 & 10^5 < \frac{n}{\mathrm{cm}^{-3}} < 10^{10} \\ 1.4 & n > 10^{10}\,\mathrm{cm}^{-3} \end{cases}. \tag{3.6}$$

Simulations have shown that this leads to a “turnover” only at extremely low masses ($\sim 0.001\,\mathrm{M}_\odot$, Fig. 3.9 later), making the IMF nearly a pure power-law at the observable masses. We will explore this model and some of its physical consequences for observables in more detail in a future paper, but explicitly show below that our semi-analytic model also captures this behavior. This is a valuable vindication both of the accuracy of the semi-analytic model (compared to full numerical simulations), and of the need for additional physics to establish the turn-over of the IMF.

For the purposes of this study, let us assume that we do not know the detailed origin of such physics (it may be due to magnetic fields, or radiative heating, for example, both of which we will explore in detail in follow up papers). The simplest approach, and one commonly adopted in numerical simulations, is to parametrize their effects via an "effective equation of state". Motivated by the work on radiative feedback from [(Bate 2009c; Krumholz 2011), let us consider a toy model where the effective EOS is not volume-density but surface-density (Σ) dependent:

$$\gamma(\Sigma) = \begin{cases} 0.7 & \Sigma < 3\,\mathrm{M}_\odot/\mathrm{pc}^2 \\ 0.094\ln\left(\frac{\Sigma}{3\,\mathrm{M}_\odot/\mathrm{pc}^2}\right) + 0.7 & 3 < \frac{\Sigma}{\mathrm{M}_\odot/\mathrm{pc}^2} < 5000\ . \\ 1.4 & \Sigma > 5000\,\mathrm{M}_\odot/\mathrm{pc}^2 \end{cases} \tag{3.7}$$

This is the same EOS as we used in Paper I. Note that the "turnover" where this becomes "stiff" is at much lower surface densities than we would obtain if we modeled cooling physics alone (Glover & Mac Low 2007) which would essentially give the same answer as our $\gamma(n)$ case above (for a comparison of the two types of EOS models, see Guszejnov et al. (2016). Instead, we are assuming some form of physics makes the EOS stiffen at much higher surface densities – we choose the particular value here *empirically*, because it provides a reasonable fit to the observed IMF. We will then explore the consequences of such a parametrization, for the IMF and its time-evolution in different clouds

3.2.2 Collapse: criterion and evolution

It has been shown in Paper I and Paper II that the critical density for a (compared to the galactic disk) small, homogeneous, spherical region of radius R to become self gravitating is

$$\frac{\rho_{\mathrm{crit}}(R)}{\rho_0} = \frac{1}{1+\mathcal{M}_{\mathrm{edge}}^2}\left(\frac{R}{R_0}\right)^{-2}\left[\left(\frac{T(R)}{T_0}\right) + \mathcal{M}_{\mathrm{edge}}^2\left(\frac{R}{R_0}\right)^{p-1}\right], \tag{3.8}$$

where the two terms represent thermal and turbulent energy, respectively. $T(\lambda)$ is the temperature averaged over the scale λ, while T_0 is the mean temperature of the whole collapsing cloud and we used the following scaling of the turbulent velocity dispersion and Mach number $\mathcal{M}$

$$\mathcal{M}^2(R) \equiv \frac{v_t^2(R)}{\left\langle c_s^2\left(\rho_0\right)\right\rangle} = \mathcal{M}_{edge}^2\left(\frac{R}{R_0}\right)^{p-1}, \tag{3.9}$$

where R_0 is the size of the self gravitating parent cloud and p is the turbulent spectra index, so the turbulent kinetic energy scales as $E(R) \propto R^p$; generally $p \in [5/3; 2]$, but in this paper, just like in Paper I we assume $p = 2$ as is appropriate for supersonic turbulence.

It should be noted that the fragmentation process is complex even in the idealized case of homologous collapse (see Hanawa & Matsumoto 1999; Ntormousi & Hennebelle 2015). This means that our method of finding self gravitating subregions using Eq. 3.8 is a strong approximation; however, a proper treatment would require drastically more computation power, which would go against one of the primary goal of the framework: the rapid exploration of parameter space and testing of physical models.

Our goal is to create a model that resolves clouds from GMC to protostellar scales, so the initial structures of the model are the GMCs which themselves are self gravitating (first crossing scale in the excursion set formalism). This means they must satisfy Eq. 3.8, which for spherical clouds ($M(R) = (4\pi/3)\, R^3\, \rho(R)$) in isothermal parents yields the mass-size relation:

$$M = \frac{M_{\rm sonic}}{2}\frac{R}{R_{\rm sonic}}\left(1 + \frac{R}{R_{\rm sonic}}\right). \tag{3.10}$$

Note that for very high mass clouds a correction containing the angular frequency of the galactic disk would appear, however this term is small (see Paper II for details). Eq. 3.10 introduces $R_{\rm sonic}$, which is the sonic length, the scale on which the turbulent velocity dispersion is equal to the sound speed, so in an isothermal cloud using the scaling of Eq. 3.9, we expect

$$R_{\rm sonic} = R_0 \mathcal{M}_{\rm edge}^{-2/(p-1)}. \tag{3.11}$$

Meanwhile $M_{\rm sonic}$ is defined as the minimum mass required for a sphere with $R_{\rm sonic}$ radius to start collapsing, so

$$M_{\rm sonic} = \frac{2}{Q_{coll}}\frac{c_s^2 R_{\rm sonic}}{G}, \tag{3.12}$$

where G is the gravitational constant and Q_{coll} is the virial parameter for a sphere of the critical mass for collapse (see Eq. 3.15 later). For reasonable galactic parameters and temperatures $R_{\rm sonic} \approx 0.1\,{\rm pc}$ and $M_{\rm sonic} \approx 6.5\,{\rm M}_{\odot}$ (assuming we use the value for Q_{coll} we specify in Sec. 3.2.2.1).

Since the GMC in question has just started collapsing, the turbulent velocity at its edge must (initially) obey the turbulent power spectrum. Thus $v_t^2(R) \propto R$ for the supersonic and $v_t^2(R) \propto R^{2/3}$ (the Kolmogorov scaling) for the subsonic case. Using the mass-size relation of Eq. 3.10 leads to the following fitting function:

$$\frac{\left(1+\mathcal{M}_{edge}^2\right)\mathcal{M}_{edge}^2}{1+\mathcal{M}_{edge}^{-1}} = \frac{M}{M_{\rm sonic}}, \tag{3.13}$$

which exhibits scalings of $M \propto \mathcal{M}^3$ for the subsonic and $M \propto \mathcal{M}^4$ for the supersonic case, respectively, and (coupled to the size-mass relation above) very closely reproduces the observed linewidth-size relations (Bolatto et al. 2008; Lada & Lada 2003; Larson 1981). Note that dense regions will deviate from this scaling, as observed (see references above), because collapse "pumps" energy into turbulence (Murray & Chang 2015; Murray et al. 2015; Robertson & Goldreich 2012b).

3.2.2.1 Evolution of Collapsing Clouds

One of the key assumptions of the previous models in Paper I and Paper II is that the kinetic energy of collapse pumps turbulence (Murray & Chang 2015; Murray et al. 2015; Robertson & Goldreich 2012b) whose energy is dissipated on a crossing time. As turbulent motion provides support against collapse, the collapse can only continue after this extra energy has been dissipated by turbulence (see Sec. 9.2 in Paper II for details). This leads to the following equation for the contraction of the cloud:

$$\frac{{\rm d}\tilde{r}}{{\rm d}\tilde{\tau}} = -\tilde{r}^{-1/2}\left(1-\frac{1}{1+\mathcal{M}_{\rm edge}^2(\tilde{\tau})}\right)^{3/2}, \tag{3.14}$$

where $\tilde{r}(t) = R(t)/R_0$ is the relative size of the cloud at time t while $\tilde{\tau} \equiv t/t_0$ is time, normalized to the initial cloud dynamical time $t_0 \sim 2Q_{coll}^{-3/2}\left(GM_0/R_0^3\right)^{-1/2}$ (see Paper II for derivation). In this case the initial dynamical time (t_0) and the crossing time only differ by a freely-defined order unity constant, so in our simulations we consider them to be equal without loss of generality.

The other key assumption of the model is that collapse happens at constant virial parameter. We define Q_{coll} as

$$Q_{\mathrm{coll}}\frac{GM}{R} = c_s^2 + v_t^2 = c_s^2\left(1 + \mathcal{M}_{\mathrm{edge}}^2\right). \tag{3.15}$$

Note that Q_{coll} is not the Toomre Q parameter, merely the ratio of kinetic energy to potential energy needed to destabilize the cloud, thus the higher Q_{coll} the more unstable clouds are to fragmentation. One can find Q_{coll} using the Jeans criterion:

$$0 \geq \omega^2 = \left(c_s^2 + v_t^2\right)k^2 - 4\pi G\rho, \tag{3.16}$$

which for the critical case ($\omega = 0$) leads to

$$Q_{coll} = \frac{3}{k^2 R^2}. \tag{3.17}$$

One would be tempted to substitute in $k = 2\pi/R$, but that would be incorrect, as we have a spherical overdensity with R radius to which the corresponding sinusoidal wavelength is not R. We therefore chose $k = \frac{\pi}{2R}$, which yields $Q_{coll} = 12/\pi^2 \approx 1.2$. Note that all formulas contain $c_s^2/Q_{coll} \propto T/Q_{coll}$, so an uncertainty in the virial parameter is degenerate with an uncertainty in the initial temperature.

Combined, the above equations completely describe the collapse of a spherical cloud, as the EOS (Eq. 3.5-3.7) sets the temperature and thus the sound speed. Using that, Eq. 3.15 provides the edge Mach number, which allows us using Eq. 3.14 to calculate the contraction speed.

3.2.3 Differences from previous models

So far we are following the same assumptions as Paper I and Paper II, however, instead of simulating a stochastic density field averaged on different scales around a random Lagrangian point (the basis of analytic excursion set models) we use a grid in space and time. This means that we directly evolve the $\delta(k)$ modes to simulate the density field. This allows us to preserve spatial information as we now have information about the relative positions and velocities of substructures.

Having a proper density field not only allows us to take basic geometrical effects into account (as substructures are still assumed to be spherical) but it allows a proper application of the self gravitation condition of Eq. 3.8. The excursion set formalism finds the smallest self gravitating structure a point is embedded in. The problem is that this "last crossing" structure may have further self gravitating fragments which do not contain the aforementioned point. These substructures will form protostars of their own (see Fig. 3.1) leaving their parent cloud with less mass which in turn might not be self gravitating anymore. This is not addressed in excursion set models which instead simply assume 100% of the mass ending up in protostars of different sizes (which of course is not realistic), while the proposed grid model predicts only about 5% (see Sec.3.3.2), which in fact depends on the physical assumptions of the model (i.e. how to deal with unbound material).

It should be noted that like the model of Paper I, in this first study we include no explicit feedback mechanism. Instead the model utilizes a few crude approximations to account for the qualitative effects of feedback. First, it is assumed that the clouds that become unbound by fragmentation stop collapsing and "linger" for a few dynamical times (during which they may form new self gravitating fragments) before being heated up/blown up/disrupted by feedback from the newly created protostars in such a fashion that they can no longer participate in star formation[2]. Note that this assumption is made for convenience, and is not inherent in the code as it is possible to implement direct feedback prescriptions. Similarly magnetic fields are neglected in this base model, but can be easily implemented into the framework. Like in Paper I we neglected the effects of accretion and protostellar fragmentation when comparing to the IMF as the protostellar system mass function (from now on *PSMF*) is already a good enough qualitative fit so their effects are assumed to be modest (except for the very high and low mass ends where fragmentation could provide a high mass cut-off while accretion could affect the turnover point, see McKee & Offner 2010 for details on the protostellar mass function). We would also like to note that it is possible to apply a crude implementation of supernova feedback by simply stopping the evolution after a few Myrs (when enough supernovae have exploded to unbind the GMC). Since the simulation provides a time dependent output, it can be done during post-processing. Of course, the point of our framework is that one could easily add models for feedback and/or accretion if desired.

We would like to note that using hydrodynamical simulations would allow a much more realistic treatment of certain details of the problem; however the

---

[2] For example photoionization can destroy the molecular cloud (Dale et al. 2012; Geen et al. 2015; Walch et al. 2012b), while both supernovae (Iffrig & Hennebelle 2015) and outflows (Arce et al. 2007) can provide momentum for turbulence or eject material.

large dynamic range ($10^{-5} - 100\,\mathrm{pc}$) and the long range gravitational interactions make such attempts extremely computationally intensive, preventing one from getting substantial statistics. A further issue with direct hydrodynamical simulations is that they involve the full, detailed form of all physical interactions, making it harder to pinpoint the primary driving mechanisms behind certain phenomena.

In summary we propose a semi-analytical model which has negligible computational cost but still captures phenomena (e.g. spatial correlation, motion of objects, complicated time dependence) which are beyond the capabilities of the analytical excursion set formalism. Our intention in this paper is not to present a "complete" model of star formation, but rather to illustrate the power of this approach with a first study involving only turbulence and self-gravity.

3.3 Evolution of the IMF and CMF in GMCs

In this section we present an application of the model for simulating the collapse of an ensemble of GMCs (distributed following the first crossing mass function obtained by Hopkins 2012b, see Fig. 3.3). This includes simulating a number of GMCs of different masses where the initial conditions are set by Eq. 3.9 and Eq. 3.10. The clouds are assumed to start with fully formed turbulence (as GMCs form out of an already turbulent medium) which means that before simulating the collapse the density field is initialized to have the appropriate lognormal distribution. The output of the code contains the formation time and properties (e.g. mass, position, velocity) of individual protostars along with snapshots of the hierarchical structure of bound objects at different times. In Sec. 3.3.1 we investigate the latter and compare the distribution of nonfragmented structures with the observed CMF. Later, in Sec. 3.3.2 we discuss the time evolution of PSMF and how it relates to the IMF and whether it can be universal without invoking feedback physics.

3.3.1 Fragmentation and self-gravitating substructures: the observed CMF

It is well known that during their collapse clouds fragment into smaller self gravitating structures (see Fig. 3.1). It is instructive to see how much mass is bound in structures of different sizes. Fig. 3.4 shows the time evolution of the number of structures of different sizes counting all "clouds-in-clouds", which follows a distribution similar to the observed IMF and CMF (for quick overview

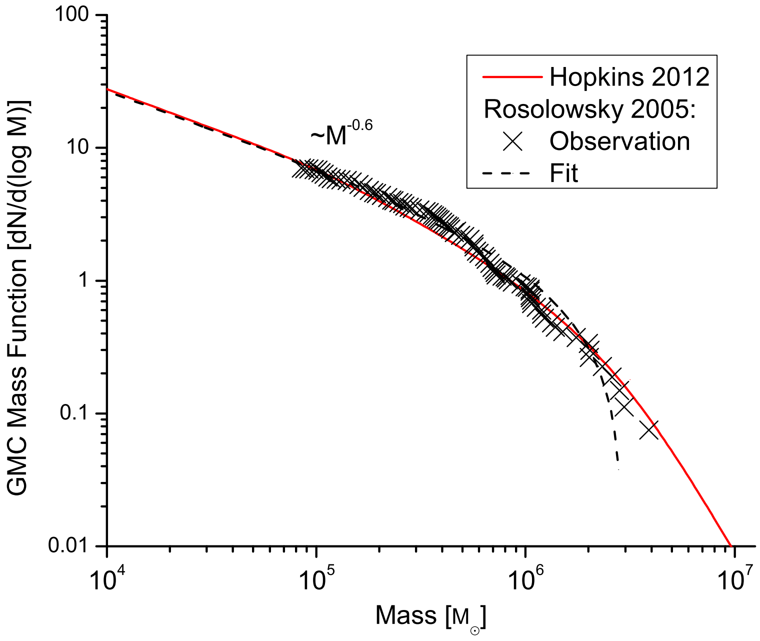

Figure 3.3: Initial mass function of GMCs according to the excursion set model of Hopkins (2012b) compared to the observations (X symbols) and empirical fitting function (dashed black line) of Rosolowsky (2005). The normalization of the plot is arbitrary.

see Offner et al. 2014), however it has a significantly shallower slope[3] of roughly $M^{-0.3}$. The distribution is established fairly quickly and is maintained until the collapse of the parent cloud ends. This mass function of bound structures is consistent with the cloud in cloud picture shown in Fig. 3.1 in that there is a vast hierarchy of bound structures embedded in each other.

Observationally finding the substructure of a GMC is very challenging (although see Rosolowsky et al. 2008), most observers instead concentrate on the so called *cores* which are collapsing clouds that have no self gravitating fragments. Figure 3.5 shows the total CMF (time and mass averaged over an ensemble of GMCs following the distribution shown in Fig. 3.3) for different inital parameters. The simulated CMF reproduces the shape of observed results, having both a turnover point and a slightly shallower high mass slope

---

[3] In this paper the approximate high mass end behavior is estimated by fitting a power law between $0.5\,M_\odot$-$100\,M_\odot$. The error presented in the figures only accounts for the uncertainty in the fitting.

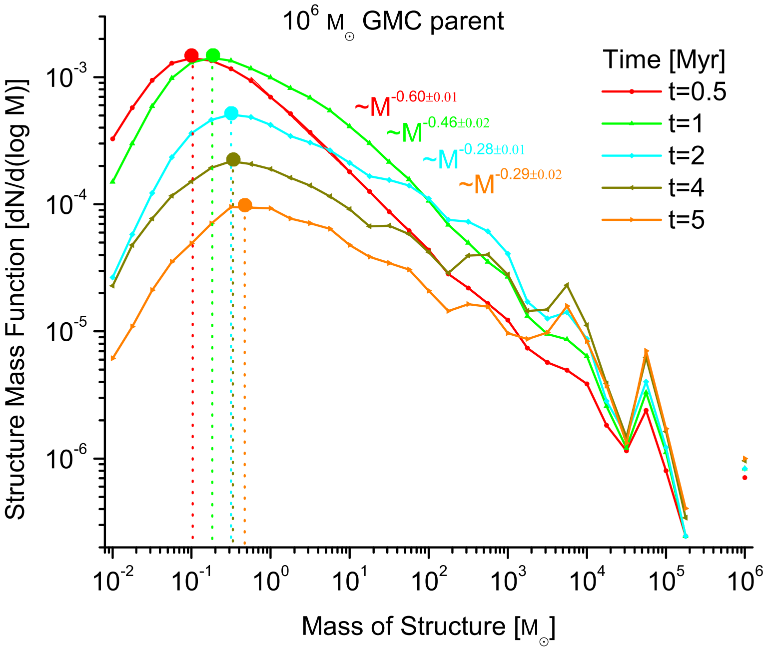

Figure 3.4: Time evolution of number of bound structures of different masses in a parent GMC of $10^6\,\mathrm{M}_\odot$. Here we count *all* self-gravitating structures, including clouds embedded in other clouds, cores etc. The plot is normalized so that integrated mass ($\int M \frac{\mathrm{d}N}{\mathrm{d}\log M} \mathrm{d}\log M$) corresponds to the mass of gas bound in self gravitating clouds relative to the total mass of the parent GMC, which explains the decreasing trend with time as more and more gas ends up in either protostars or becomes unbound. The upper end cuts off close to the parent GMC mass. The high mass power law fitting is done according to Footnote 3.

($\sim M^{-1.15}$) than the canonical Salpeter result of $\sim M^{-1.35}$ for the IMF (see Offner et al. 2014).

Fig. 3.6 clearly shows that there is very small difference between the CMF turnover masses and high mass slopes between GMCs of different sizes after 1 Myr. This is because early collapse is roughly isothermal so these clouds all have the same characteristic fragment mass (M_{crit}, see Eq. 3.20 for details). Systems which are on the same linewidth-size relation (i.e. they form out of the same turbulent cascade) will always have the same M_{sonic}, M_{crit} (see Hennebelle & Chabrier 2008; Hopkins 2012b). During later evolution the GMCs heat up at a different pace as the dynamical times are different. Meanwhile Fig. 3.7 shows that there is a clear trend of increasing turnover mass with time in

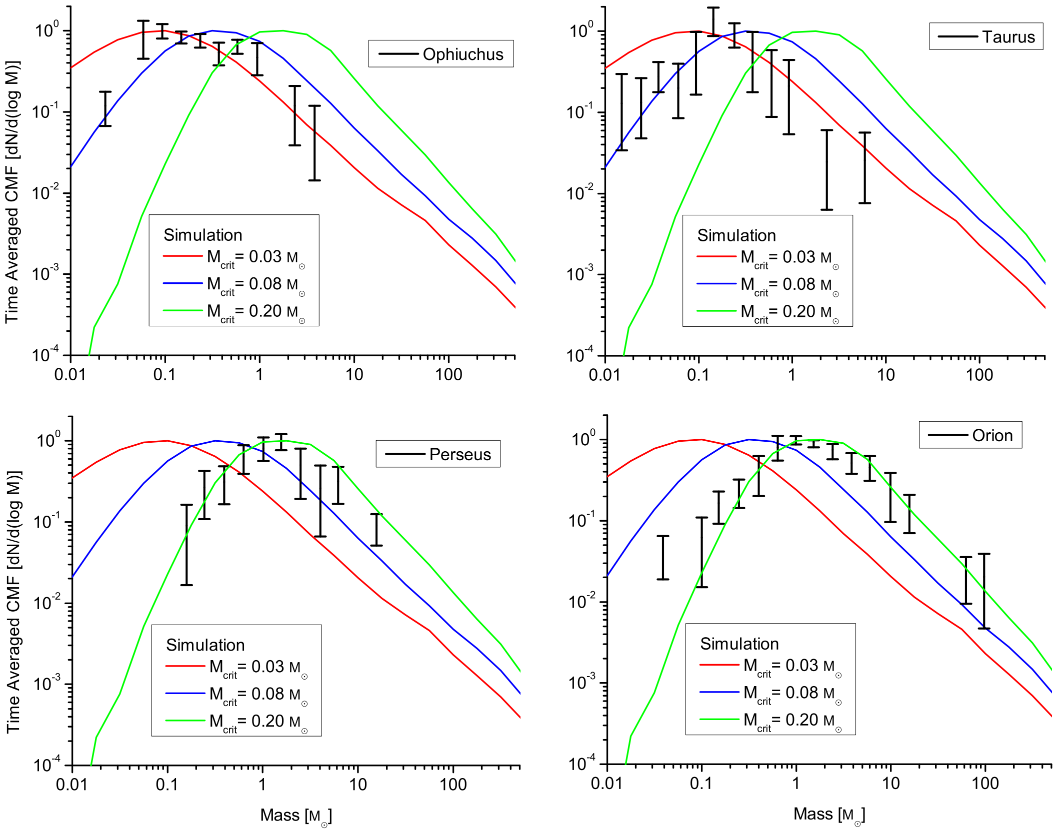

Figure 3.5: Comparison of the average simulated CMF with the observed CMF by Sadavoy et al. (2010) in different clouds in the Milky Way (the plot is normalized so that the peak of the CMF is set to unity). Note that observations which are below the completeness limit are also included (see the original paper for details). The simulated CMFs are averaged both over time (assuming the age of GMCs is uniformly distributed in the [0,5] Myr range) and the GMC mass function (following Fig. 3.3). The different initial critical masses in this case reflect having different T/Q_{coll} values, for definition see Eq. 3.20.

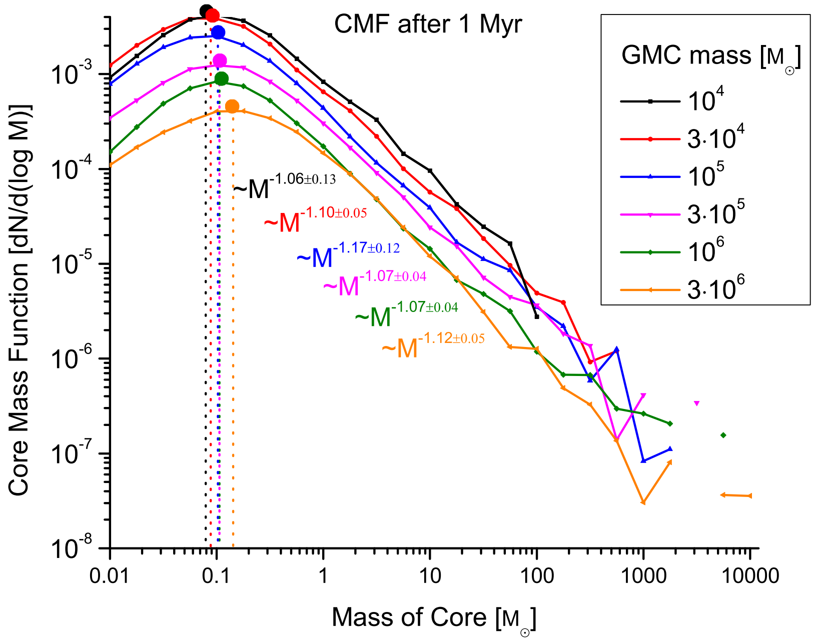

Figure 3.6: The CMF in GMCs of different masses 1 Myr after collapse starts for each cloud (using EOS of Eq. 3.7). The plot is normalized so that integrated mass corresponds to the relative mass of gas bound in cores, the peaks are denoted with solid circles. The high mass power law fitting is done according to Footnote 3. Both the turnover mass and the high mass slope exhibit very little sensitivity to the mass of the parent GMC similar to what was found by Hennebelle (2012); Hennebelle & Chabrier (2008).

each cloud. This phenomenon and its possible cause is further investigated in Sec. 3.3.2. This trend is not visible in case of the physical EOS of Eq. 3.6 as the peak is well below the stellar mass scales (see Fig. 3.9). Nevertheless, this scenario shows that in the absence of a dominant M_{crit} the initial CMF turns over around the sonic mass scale (as shown by previous analytical works e.g. Hennebelle & Chabrier 2008; Hopkins 2012b), but this mass scale gets "forgotten" during the fragmentation cascade.

3.3.2 Evolution of the PSMF

We now examine the mass function of the final collapsed objects: the protostellar system mass function (PSMF).

In Fig. 3.8 we show that parent clouds of all masses produce Salpeter-like

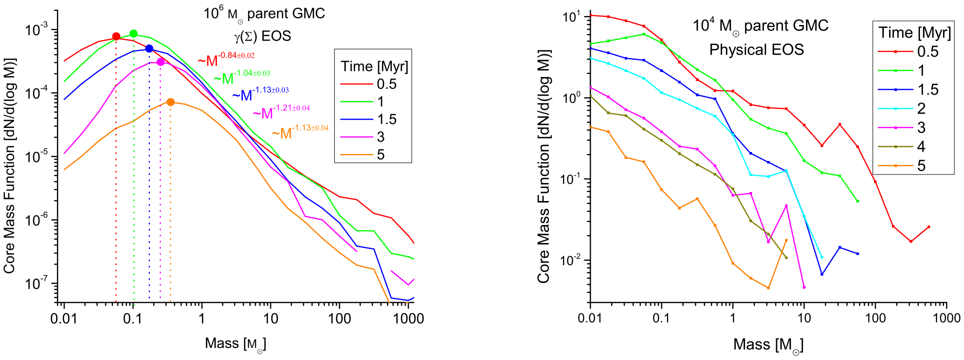

Figure 3.7: **Left**: Time evolution of the CMF in a $10^6\,\mathbf{M}_\odot$ parent GMC using the $\gamma(\Sigma)$ EOS of Eq. 3.7. The plot is normalized so that integrated mass corresponds to the mass of gas bound in self gravitating clouds relative to the total mass of the parent GMC, which explains the downwards trend since less and less gas is bound in cores as more protostars are produced and the cloud gets heated by contraction. The high mass power law fitting is done according to Footnote 3. There is a clear trend in the turnover mass (the peaks are denoted with solid circles) which increases significantly while preserving the overall shape of the function (e.g. high mass slope). **Right**: Time evolution of the CMF in a $10^4\,\mathbf{M}_\odot$ parent GMC using the physically motivated EOS of Eq. 3.6 (a density dependent EOS where the transition point to the $\gamma > 1$ regime is calculated from cooling physics). As expected the CMF has a peak around the sonic mass at early times; however, that feature gets "washed out" by the fragmentation cascade which is not arrested by this EOS until very small scales.

scalings at the high mass end with lower mass clouds producing slightly steeper slopes. Also, there is a clear trend of increasing turnover mass with increasing parent mass, unlike the case of the CMF (See Fig. 3.6). It is worth noting that the GMC mass function is top heavy, which means that the high mass clouds dominate the integrated mass function. If we accept this result then it suggests a possible observational bias of the IMF as most observations focus on smaller clouds in the Milky Way. Also, turbulent fragmentation does not produce a cloud mass dependent "maximum stellar mass".

The increasing turnover mass for both PSMF and CMF is related to the equation of state. In a turbulent cloud, self gravitating fragments of different sizes form, which (according to the EOS of Eq. 3.7) have different effective polytropic indices. According to the EOS there exists a threshold in the surface density (Σ_{crit}) above which $\gamma > 4/3$, stabilizing the cloud against further fragmentation. Thus it is instructive to find the critical mass (M_{crit}) corresponding

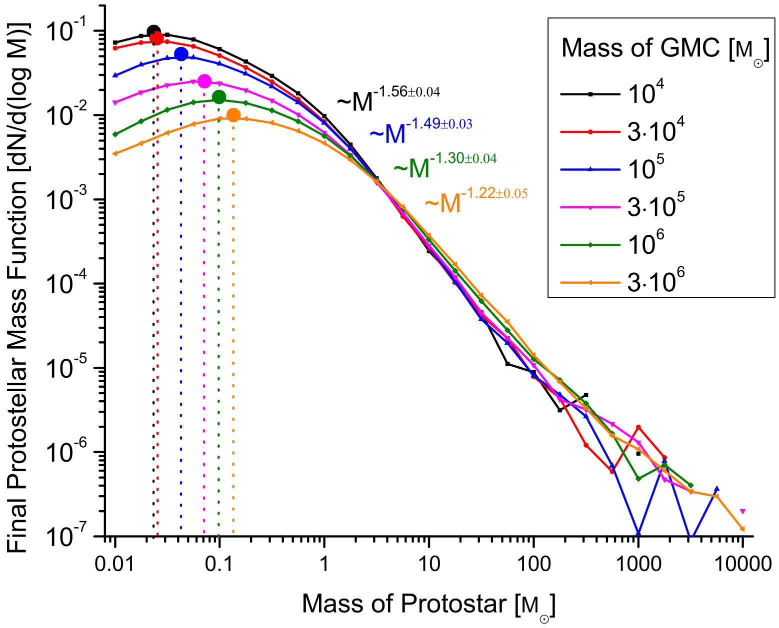

Figure 3.8: Protostellar system mass function (PSMF) after collapse ends in parents of different masses assuming our simple equation of state. The Salpeter slope is always present (the high mass power law fitting is done according to Footnote 3). For these assumptions there appears to be "too many" brown dwarfs, and too much dependence on the parent GMC mass. These are the direct consequences of the EOS of the gas.

to $\Sigma_{\rm crit}$. Using the collapse condition of Eq. 3.8 and expanding up to linear order in γ around 1 (this is a good approximation during most of the cloud's lifetime as the collapse starts at close to isothermal conditions) yields that $\Sigma > \Sigma_{\rm crit}$ requires that

$$R < R_{\rm crit} = R_0 \frac{\gamma \left(\frac{\Sigma_{\rm crit}}{\Sigma_0}\right)^{\gamma-1}}{\frac{\Sigma_{\rm crit}}{\Sigma_0}\left(1+\mathcal{M}_{edge}^2\right) - \mathcal{M}_{edge}^2 + \gamma - 1}, \tag{3.18}$$

where R is the fragment radius and R_0, Σ_0, $\gamma = \gamma\left(\Sigma_0\right)$ are the radius, surface density and the effective polytropic index of the parent cloud. From Eq. 3.18 we can find the critical mass $M_{\rm crit} = 4\pi R^2 \Sigma_{\rm crit}$ below which fragments are unlikely to collapse (note: according to the EOS of Eq. 3.7 the critical surface density $\Sigma_{\rm crit} \approx 2400\,\mathrm{M_\odot/pc^2}$). These formulas can be simplified by assuming isothermal collapse ($\gamma \simeq 1$) and that the parent GMC is highly supersonic ($\mathcal{M}_{edge}^2 \gg 1$); Eq. 3.11 then yields:

$$R_{\rm crit} \approx \frac{R_0 \Sigma_0}{\mathcal{M}_{edge}^2 \Sigma_{\rm crit}} = R_{\rm sonic} \frac{\Sigma_0}{\Sigma_{\rm crit}}. \tag{3.19}$$

Using the mass-size relation of Eq. 3.10 and that $R_0 \gg R_{\rm sonic}$ we obtain

$$M_{\rm crit} \approx \frac{4\pi R_{\rm sonic}^2 \Sigma_0^2}{\Sigma_{\rm crit}} = \frac{M_{\rm sonic}^2}{16\pi R_{\rm sonic}^2 \Sigma_{\rm crit}} = \frac{c_s^4}{4\pi G^2 Q_{coll}^2 \Sigma_{\rm crit}} \propto \frac{T^2}{\Sigma_{\rm crit}}. \tag{3.20}$$

The critical mass only depends on the cloud temperature and the equation of state. A similar sensitivity to the initial temperature has been found by Bate (2009c) using a Jeans mass argument. Assuming that there exists a critical density $\rho_{\rm crit}$ where some physics terminates the fragmentation cascade the corresponding Jeans mass will simply be $\propto T^{3/2}$. It is easy to see that this is the same result one would get when trying to find the critical mass using a $\gamma(n)$ EOS.

Fig.3.9 shows the time evolution of the time and ensemble averaged PSMF for different initial $M_{\rm crit}$ values (the different critical masses in these cases arise from having different $\sigma/Q_{coll}\Sigma_{\rm crit}$, where we fix Q_{coll} and $\Sigma_{\rm crit}$ and vary T_{init}, for definition see Eq. 3.20) which all produce a shape similar to the IMF but with different peak masses. If we compare the results to the canonical IMF fitting functions of Kroupa (2002) and Chabrier (2005), then it is clear that the average PSMF always reproduces the Salpeter scalings, however the turnover point is heavily influenced by $T/Q_{coll}\Sigma_{\rm crit}$. Since Q_{coll} is a constant this implies that the average temperature of the cloud could have a significant effect on the turnover point if $\Sigma_{\rm crit}$ is constant. Meanwhile, Fig.3.9 also shows that the physical EOS of Eq. 3.6 has such a low characteristic mass that the resulting PSMF in the stellar mass range is just a power law. Nevertheless, the position of the peak is still sensitive to the initial conditions ($\propto T^{3/2}$), if one extends the plot to substellar mass scales.

Fig. 3.10 shows how this critical mass evolves in time for our default model assumptions ($\Sigma_{\rm crit} = \rm const.$). It is clear that $M_{\rm crit}$ correlates well with the peaks of the PSMF of the corresponding time interval.

This increase of the critical mass with time has an interesting consequence. Fig. 3.11 shows that the average time of formation monotonically increases

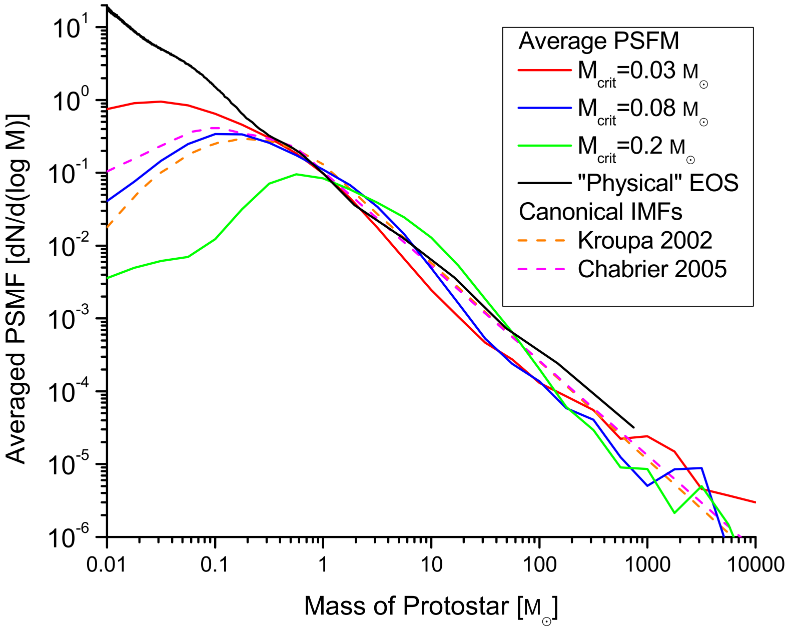

Figure 3.9: Evolution of the averaged PSMF (normalized to integrated mass) for different initial critical masses (set by having different $T/Q_{coll}\Sigma_{\rm crit}$ values, for definition see Eq. 3.20) compared to results using the "traditional" EOS of Eq. 3.6 and the canonical IMF of Kroupa (2002) and Chabrier (2005). The PSMF is averaged both over time (assuming the age of GMCs is uniformly distributed in the [0,5] Myr range) and the GMC mass function (following Fig. 3.3). We included the standard $M_{\rm crit} = 0.03\,\mathrm{M}_\odot$ (solid red), an $M_{\rm crit} = 0.08\,\mathrm{M}_\odot$ (solid blue) and an $M_{\rm crit} = 0.2\,\mathrm{M}_\odot$ (solid black) scenarios with the $\gamma(\Sigma)$ EOS along with a run which had the physically motivated $\gamma(n)$ EOS of Eq. 3.6. For realistic temperatures ($10-30\,\mathrm{K}$) the critical mass of the latter is well below the stellar mass range so the PSMF becomes a pure power law. Meanwhile, for the $\gamma(\Sigma)$ EOS case the PSMF shape is similar for different critical masses, and there is a clear shift of the peak to higher masses with increasing $M_{\rm crit}$. In all cases the high mass end is close to the Salpeter result.

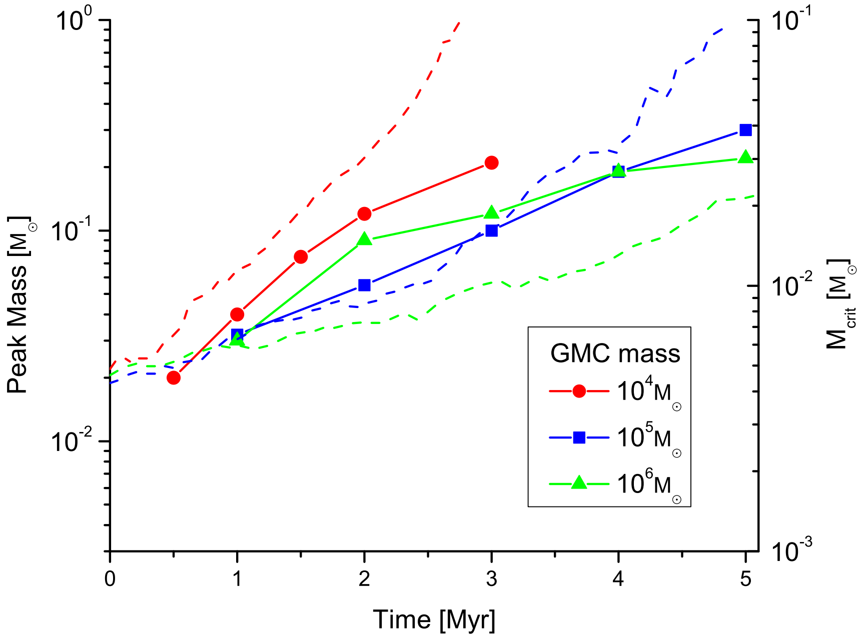

Figure 3.10: The peak masses of the PSMF of different time intervals (solid line with symbols) and the critical mass (dashed lines) for different parent GMC masses according to Eq. 3.18. The critical mass correctly predicts the qualitative evolution of the peak mass.

with the protostellar system mass.

So, if the equation of state does not depend on temperature (e.g. our $\gamma(\Sigma)$ is invariant) then the turnover mass shows a strong ($\propto T^2$) dependence on the initial conditions which would likely lead to a non-universal IMF ($\propto T^{3/2}$ in the $\gamma(n)$ case). A possible solution to this issue is if Σ_{crit} from Eq. 3.20 has a temperature dependence. This perfectly plausible, just recall that the effective EOS is just a crude approximation of complex cooling physics. Bate (2009c) argues that radiative feedback effectively weakens the dependence of the Jeans mass on density, making the turnover mass less sensitive to initial conditions. A similar example is provided by Krumholz (2011), where the initially formed protostar “seed” heats up its environment, preventing it from collapsing. This dense cloud is heated up to $T_{heating} \propto M^{3/8}R^{-7/8} \approx \Sigma^{3/8}$ by the accretion luminosity from the protostar[4], which, using our EOS language,

---

[4] One can derive this temperature by assuming an optically thick cloud in equilibrium that is heated by accretion luminosity $L_{acc} \sim \dot{M}\Psi \sim M/t_{ff}\Psi \propto M^{3/2}R^{-3/2}$ and cooled by

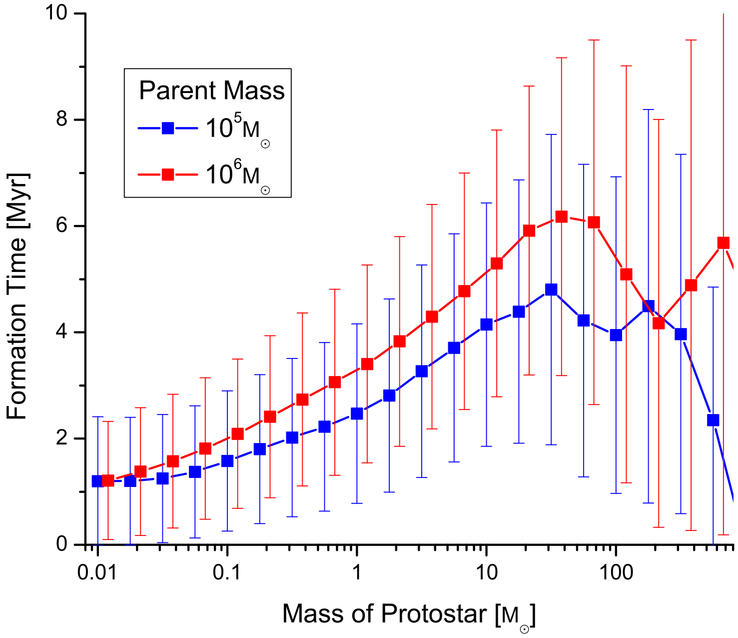

Figure 3.11: Average time of formation for protostars of different masses (the error bars represent the standard deviation) in a model with an *invariant* EOS. There is a clear trend of more massive protostars forming at later times (which is consistent with the shifting of the turnover mass in Fig. 3.10), however the scatter is comparable to this difference. Nevertheless it is clear that most massive stars only start forming after roughly a Myr after the cloud starts collapsing. Changing this requires additional physics beyond turbulence, gravity and cooling.

roughly translates to $\Sigma_{\mathrm{crit}} \propto T^2$, which would produce a constant M_{crit}, and thus a universal IMF.

In a paper in preparation we will explore this feedback model in a fully spatially-dependent framework. For now, let us consider a simple experiment where $\Sigma_{\mathrm{crit}} \propto T^2$.

Fig. 3.12 compares the results of two simulations, one with $\Sigma_{\mathrm{crit}} = \mathrm{const.}$ and one with $\Sigma_{\mathrm{crit}} \propto T^2$. Although the latter still shows some time dependence, the shifting of the peak is greatly reduced, making it more consistent with observations, even though the only assumption about feedback was that it prevents collapsed cores from accreting from their surroundings. Note that

---

thermal radiation $L_{cool} \sim 4\pi R^2 \sigma_{SB} T_{\mathrm{heat}}^4$.

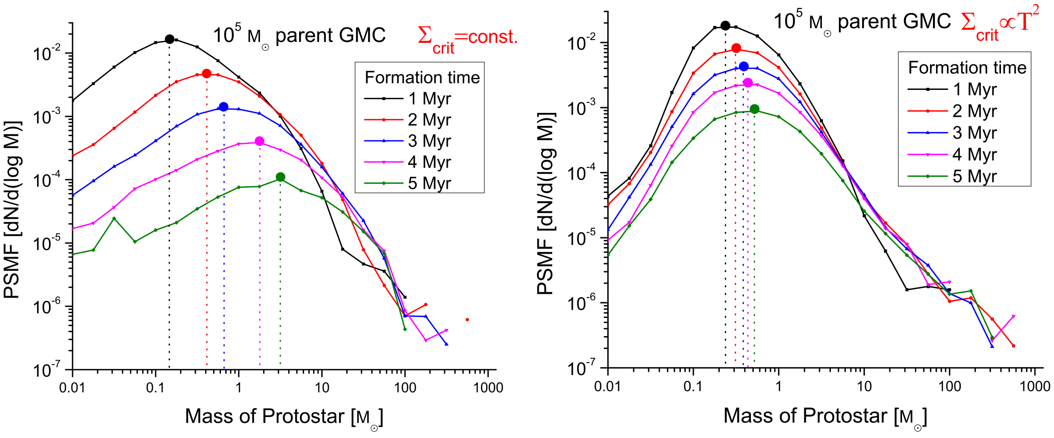

Figure 3.12: PSMF for protostars in a parent GMC of $10^5\,\mathrm{M}_\odot$ for an EOS with $\Sigma_{\rm crit} = \mathrm{const.}$ (left) and for an EOS with $\Sigma_{\rm crit} \propto T^2$ (right). The solid circles show the peaks, which move considerably less for the $\Sigma_{\rm crit} \propto T^2$ case. As implied by Eq. 3.20, if $\Sigma_{\rm crit} \propto T^2$ then $M_{\rm crit} \sim \mathrm{const}$, and the IMF becomes invariant.

our aim with this experiment was only to demonstrate what would be required from a purely EOS based model to produce an invariant IMF; any other physics that sets the critical mass of the EOS constant would achieve similar results.

An important question of star formation is what fraction of the gas ends up in stars. The analytical excursion set models like in Paper I could not answer that question as they assume by default that 100% of the mass ends up in bound structures similar to the Press-Schecter model (Press & Schechter 1974) of dark matter halos which they are based on). However, our semi-analytic framework here allows us to explore different assumptions for the time-dependent behavior of both bound and unbound gas, and thus (in principle) to make predictions for this quantity.

In the “basic” models presented in this paper, we assume that whenever a core collapses and forms a star, any remaining mass in its parent cloud which is no longer self-gravitating (once the core is fully collapsed) is simply thrown out of the system. This is meant to represent a very crude toy model for the effects of feedback (from e.g. protostellar jets) on the parent sub-clumps from which the stars form. With this assumption, we find an integrated star-formation efficiency (after all mass either turns into stars or is unbound) of $\sim 5-10\%$ for GMCs of all sizes. Interestingly, this is almost completely independent of the EOS we assume (either constant $\Sigma_{\rm crit}$ or $\Sigma_{\rm crit} \propto T^2$), as long as it terminates the fragmentation cascade at roughly the same point. Of course, if we assume this gas remains bound to the total system, so it is simply recycled back to the "top level" of the original fragmentation hierarchy until it is consumed (which obviously corresponds to a no-feedback case), then we trivially predict that eventually all gas turns into stars. Of course, the effects of realistic feedback are much more complex than these simplistic assumptions, and we could adopt arbitrarily complex models (for example, evolving each protostar and tracking explicitly location-dependent photo-ionization feedback, which we then use to explicitly calculate whether gas is unbound from the system). We note this result simply to demonstrate the utility of these semi-analytic models for rapidly exploring different assumptions regarding the effects of feedback.

3.4 Conclusions

The aim of this paper is to provide a general framework for the modeling of star formation through turbulent fragmentation from the scale of GMCs to the scale of stars in order to quickly test the effects of different assumptions and new physics. Such a tool could allow theorists to explore different models and parameters before committing significant resources towards a detailed numerical simulation. We propose a semi analytical extension of the model of Guszejnov & Hopkins (2015b) (Paper I) that we believe is detailed enough to capture the physics essential for modeling the formation of stars without being too demanding numerically. Just like the analytical excursion set models it does not simulate turbulence directly; instead it assumes that the density follows a locally random field distribution whose parameters evolve in time so that virial equilibrium is satisfied. This is an assumption about turbulent collapse that needs to be tested in future work. The density field is directly resolved on a grid which preserves spatial and time information, allowing the implementation of more detailed physics (e.g. proper checking for self gravitation, time dependent cloud collapse) and the analysis of the spatial structure. This is not possible in the excursion set formalism which describes the density field around a random Lagrangian point. This also means that unlike the analytical models not 100% of the mass ends up in protostars.

The presented form of the model contains only the minimally required physics (turbulence, self gravity, some equation of state). It is however possible to integrate more sophisticated models to provide a more accurate description of these processes. Also, since the output of our model contains the time dependent evolution of the CMF and the PSMF, one can easily apply corrections during post processing to account for effects like protostellar fragmentation or supernova feedback (stop the evolution when enough SNe exploded).

By applying this framework to modeling the collapse of giant molecular clouds, we found that even the basic model qualitatively reproduces the observed core mass function. The CMF evolution has little dependence on the mass of the parent GMC mass.

Another result of the simulation is the mass distribution of all bound structures in the cloud. This appears to have the same shape as the CMF with a shallower slope of roughly $M^{-0.3}$ at the massive end. These clearly show the hierarchy of bound structures.

One of the main results of our basic model is the protostellar system mass function (PSMF) which is obtained by following the collapse of an ensemble of GMCs following a GMC mass function determined by Hopkins (2012b). As in Paper I we found that the PSMF is qualitatively very similar to the observed IMF: it exhibits a close to Salpeter slope almost independent of the initial conditions, while the turnover mass is mainly set by the equation of state and the initial temperature.

Due to the minimalistic nature of the model we managed to pinpoint the physical quantities influencing the different features of the PSMF and thus the IMF. We found that the Salpeter slope at the high mass end is a clear consequence of turbulence (as shown before in Paper I) where the inclusion of extra physics only causes slight deviation from the pure power law behavior. Furthermore we found that in a medium with a stiff equation of state the actual turnover point in leading order is set by the local temperature ($M_{\rm crit} \propto T^2/\Sigma_{\rm crit}$).

We found that if we assume a $\gamma(\Sigma)$ equation of state then the PSMF for protostars of the same age changes as the parent cloud collapses: the turnover mass increases with time. This can be explained by the increase of $M_{\rm crit}$. This leads to a quadratic dependence of the turnover mass on the initial temperature which is inconsistent with the observed universality of the IMF. This means that it is not possible to derive a universal IMF with an equation of state that has no temperature dependence. One way to “fix” the model is by implementing the feedback from protostars. Using the assumptions of Krumholz (2011) in leading order the heating from the protostars cancels the aforementioned quadratic scaling (due to $\Sigma_{\rm crit} \propto T^2$), leading to a close to universal turnover mass.

3.A Basic Simulation Algorithm

In this appendix we detail step-by-step how the basic version of the simulation works (see flowchart of Fig. 3.13), but note that it can be greatly expanded with new physics, as long as the fundamental assumption (locally random density modes) is kept.

(1) We begin with a GMC sized cloud whose initial parameters (mass, radius, temperature, density, edge Mach number, sound speed etc.) are derived from its mass (M), the sonic mass ($M_{\rm sonic}$) and length ($R_{\rm sonic}$), using the mass-size relation of Eq. 3.10 and linewidth-size relation of Eq. 3.9. These are all initialized on a 3D spatial grid, of resolution $N \times N \times N$ chosen such that the final statistics converge (we found this happens at $N \geq 16$). The density field is initialized assuming that it is lognormal (variance set according to Eq. 3.3) using the full density power spectrum model (transforming to Fourier space and back), while the temperature field follows the density according to the desired equation of state.

(2) We take timestep Δt ($\Delta t \ll t_{\rm dyn}$ and $\Delta t \ll t_{cross}(d)$, where $d = 2R/N$ is the spatial resolution of the grid). This means:

   (a) Global contraction of the cloud (all scales shrink, density uniformly increases) according to Eq. 3.14.

   (b) The density perturbation power spectrum $\delta(\mathbf{k})$ is updated following Eq. 3.4, which assumes density mode statistics obey a local "random walk" in phase space. The actual density field is calculated by Fourier transforming to real space and normalizing the field with the cloud mass (this way mass is conserved).

   (c) The temperature field is updated according to new densities and the chosen EOS (see Eq. 3.5).

   (d) The cloud scale Mach number is updated according to our assumption that the virial parameter is constant during collapse.

(3) We now check whether any self-gravitating substructures have formed by using a Monte Carlo method that involves placing spheres of all possible sizes at random positions and testing them using the collapse criterion of Eq. 3.8.

(4) If such a region is found it is "removed" temporarily and expanded into its own grid. This new grid will have a higher spatial resolution than its

parent, and thus density modes on the newly available small scales need to be initialized (larger modes are inherited from the previous grid). We then repeat steps (2)-(4) on this new grid. This means that during the evolution of its fragments the parent cloud is "frozen" in time. This is motivated by the fact that the dynamical time of fragments is smaller, as $t_{\mathrm{d}yn} \propto 1/\sqrt{\rho}$, so they evolve "fast" compared to their parents. Note that all clouds keep track of physical time, so it is possible to properly date the formation times of protostars and clouds.

(5) The time evolution of each cloud/grid continues until:

  (a) The cloud reaches the protostellar size scale ($R < R_{\mathrm{m}in}$), below which it is assumed to have formed a protostar.

  (b) The cloud is still self gravitating after a number of dynamical times ($t > t_{\mathrm{m}ax}$)[5]. After this limit is reached the cloud is assumed to have cooled and collapsed through other means. Essentially, this represents non-fragmenting cores.

  (c) The cloud stops being self-gravitating. This can happen if a cloud loses enough of its mass that it becomes unbound. Since virial equilibrium is enforced this means no turbulence, which means no more fragmentation. In the model presented above these clouds are *not* forming stars or contributing to the mass of the protostars forming from their fragments, instead this material is "thrown away" (this represents "feedback" in some sense, see Sec. 3.2.3). Note that it is possible within the framework to return this unbound material to the parent GMC where it may form stars, but for simplicity in the presented model we chose not to do that.

(6) Clouds that formed protostars are removed the properties of the protostars are cataloged. We then return to the parent cloud and continue its evolution from Step (4).

(7) This continues until 100% of the original original mass of the cloud is either in protostars or unbound. The final output is the catalog of protostars. Note that it is also possible to get the CMF by exporting the properties of bound structures at a specified time. The whole process

---

[5] This can happen if $\gamma > 1$, as $\tilde{r}$ in Eq. 3.14 does not reach zero in a finite amount of time.

is repeated for a large number of initial GMCs (with different random seeds) to gain adequate statistics.

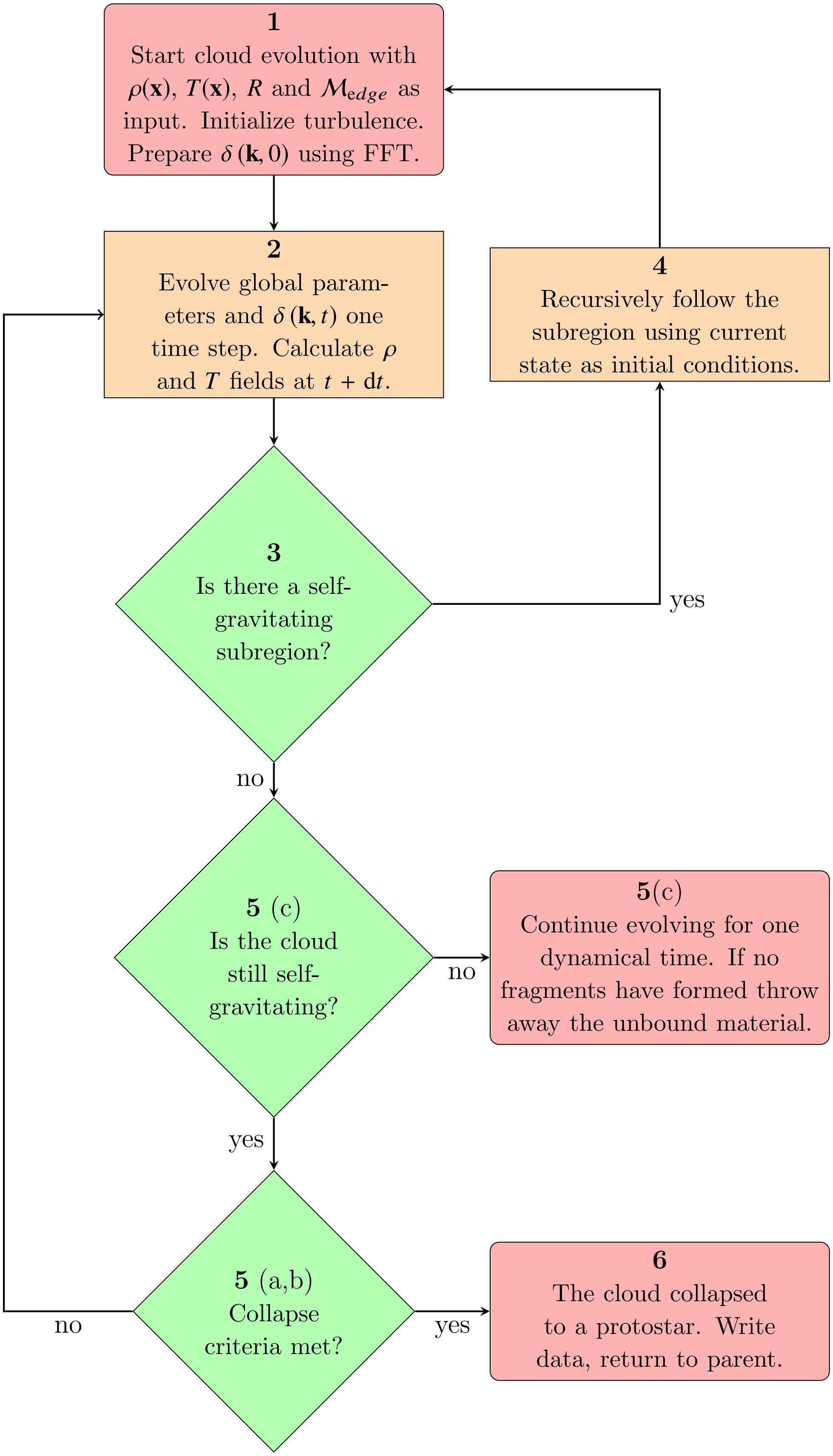

Figure 3.13: Basic algorithm of fragmentation code. The bold numbers in each box show which step from Sec. 3.A they represent. See Sec. 3.A for a more detailed description.

Chapter 4

THE NECESSITY OF FEEDBACK PHYSICS IN SETTING THE PEAK OF THE INITIAL MASS FUNCTION

Guszejnov D., Krumholz M. R., Hopkins P. F., 2016, MNRAS, 458, 673

Abstract

A popular theory of star formation is gravito-turbulent fragmentation, in which self-gravitating structures are created by turbulence-driven density fluctuations. Simple theories of isothermal fragmentation successfully reproduce the core mass function (CMF) which has a very similar shape to the initial mass function (IMF) of stars. However, numerical simulations of isothermal turbulent fragmentation thus far have not succeeded in identifying a fragment mass scale that is independent of the simulation resolution. Moreover, the fluid equations for magnetized, self-gravitating, isothermal turbulence are scale-free, and do not predict any characteristic mass. In this paper we show that, although an isothermal self-gravitating flow does produce a CMF with a mass scale imposed by the initial conditions, this scale changes as the parent cloud evolves. In addition, the cores that form undergo further fragmentation and after sufficient time forget about their initial conditions, yielding a scale-free pure power-law distribution $\mathrm{d}N/\mathrm{d}M \propto M^{-2}$ for the stellar IMF. We show that this problem can be alleviated by introducing additional physics that provides a termination scale for the cascade. Our candidate for such physics is a simple model for stellar radiation feedback. Radiative heating, powered by accretion onto forming stars, arrests the fragmentation cascade and imposes a characteristic mass scale that is nearly independent of the time-evolution or initial conditions in the star-forming cloud, and that agrees well with the peak of the observed IMF. In contrast, models that introduce a stiff equation of state for denser clouds but that do not explicitly include the effects of feedback do not yield an invariant IMF.

4.1 Introduction

New stars form in dense molecular clouds as self-gravitating subregions collapse. Turbulent fragmentation is thought to be the main driving force of this process: turbulence compresses the gas, creating local density fluctuations that may be large enough to become self-gravitating. The appeal of this model comes from the fact that supersonic turbulence naturally produces a power-law relationship between velocity dispersion and size scale that is in good agreement with observations of molecular clouds (Bolatto et al. 2008; Kritsuk et al. 2013; Larson 1981). A second advantage of a turbulence-based model is its universality. The initial mass function (IMF) of stars is observed to be close to universal (Bastian et al. 2010; Offner et al. 2014), with a high-mass end that is well described by a power-law with a slope of roughly $M^{-2.35}$ (Salpeter 1955) and a turnover at a few tenths of a Solar mass[1]. The mass at which this turnover occurs is robustly determined to be a few tenths of a Solar mass in all resolved stellar populations in the Milky Way (e.g., Figure 2 of Offner et al. 2014) and in nearby galaxies (e.g., Geha et al. 2013). Only a few resolved systems show even minor deviations in the location of the peak, and even then only by a factor of ~ 2 (e.g., $0.6 - 0.8\,\mathrm{M}_{\odot}$ in Taurus – Luhman et al. 2009). This lack of variation is remarkable, given that the star-forming systems over which it is measured span many orders of magnitude in mass and density. Even in the most extreme environments, such as the cores of giant elliptical galaxies, the IMF turnover mass differs from the one found locally by at most a factor of a few (Cappellari et al. 2012; Geha et al. 2013; van Dokkum & Conroy 2010). Such a universal distribution is most naturally explained by simple, universal physics that is independent of galactic environment, and the physics of turbulence is an obvious candidate.

There have been many attempts to formulate an analytic theory for the IMF, and for its turnover in particular, based on turbulence. Most are based on the random field approach first used in cosmology by Press & Schechter (1974). This method was first applied to explain the IMF by Padoan et al. (1997) and Padoan & Nordlund (2002), then made more rigorous by Hennebelle & Chabrier (2008, 2009, 2013a) and Hopkins (2012a). Using such a model Hopkins (2012b) calculated the mass function of non-fragmented bound structures at a fixed time instant, a real life equivalent of which would be the core mass function (CMF), as opposed to the IMF. The observed CMFs of nearby star-forming regions have functional forms similar to that of the IMF (Alves et al. 2007; Rathborne et al. 2009; Sadavoy et al. 2010), with a Salpeter-like power-law at high masses and a turnover at lower masses, though the existence and the exact location of the CMF turnover are both quite uncertain due to issues of completeness and confusion – see Offner et al. (2014) and Krumholz (2014) for

---

[1] Due to the high uncertainty of measurements of brown dwarfs the functional form of the turnover is not obvious from the data (Krumholz 2014; Offner et al. 2014). The most common fits are either a broken power law (Kroupa 2002) or a lognormal (Chabrier 2005).

more discussion. The CMF derived by Hopkins (2012b) shares these features. The turnover mass in this model is set by the sonic mass $M_{\mathrm{sonic}} \sim c_s^2 R_{\mathrm{sonic}}/G$ that corresponds to the scale below which self-gravitating structures are subsonic; a similar mass scale arises in the Hennebelle & Chabrier model, and one can show that the Hennebelle & Chabrier and Hopkins mass scales are in fact identical up to constants of order unity (Krumholz 2014). However, this scale is not universal, as it depends on the initial conditions in the star-forming cloud, which calls into question whether such a model can truly explain the near-universality of the IMF.

The proposition that the IMF is determined by the CMF, which in turn is set by the physics of isothermal gravito-turbulent fragmentation, has the appeal of simplicity. However, there remains an obvious question: once a core forms, why should one assume that it will collapse to form a single star, rather than fragmenting further? Simulations of isolated isothermal cores suggest exactly the latter (fragmented) outcome (e.g., Dobbs et al. 2006; Goodwin et al. 2004; Walch et al. 2012a). In principle, the question of the fate of isothermal cores should be resolvable by simulations. In practice, however, this turns out to be a formidable technical challenge. Isothermal turbulence is scale-free (Krumholz 2014; McKee et al. 2010), and thus it is not obvious what dynamic range is required to obtain a converged numerical result. To date, *no* published simulation of isothermal gravito-turbulent fragmentation has demonstrated that the spectrum of point masses it produces is numerically converged, and those few authors who have attempted convergence studies (Kratter et al. 2010; Martel et al. 2006) report non-convergence to the highest numerical resolutions probed. One possible explanation, advanced by Krumholz (2014), is that the characteristic structures created by isothermal turbulence are not singular points but singular filaments. Simulations produce filaments down to the smallest size scales they reach, and then the sink particle algorithm they use to represent collapsing regions breaks those filaments up into points at the grid scale.

Given these problems with purely isothermal fragmentation, a number of authors have proposed that the fragmentation cascade is arrested when the gas begins to heat up, in which case the characteristic stellar mass is determined by whatever physics causes the deviation from isothermality. The most common approach to this problem has been to adopt an equation of state that "stiffens" (i.e., the temperature begins to rise) above some characteristic density or surface density. Since super-isothermal gas is resistant to further fragmentation, one then identifies the IMF peak with the Jeans mass at this "stiffening density", on the basis that fragmentation will be suppressed beyond that point (Larson 2005; Whitworth et al. 1998).

Stiffening of the equation of state can be caused by a diverse range of processes, including the inability of radiative cooling to keep up with adiabatic heating at a density $n \sim 10^{10}$ cm^{-3} (e.g., Masunaga et al. 1998) or a surface density $\Sigma \sim 5000\ \mathrm{M}_\odot\ \mathrm{pc}^{-2}$ (e.g., Glover & Mac Low 2007), the onset of dust-gas coupling at a density $n \sim 10^5$ cm^{-3} (Elmegreen et al. 2008; Larson 2005), or combinations of the above (e.g., Spaans & Silk 2000). Numerical simulations based on these equations of state do find a converged mass scale that can plausibly be identified as a characteristic mass for the IMF (e.g., Bate 2009b; Bonnell et al. 2006). However, it is not clear that the mass scale introduced by those models is actually universal (as opposed to set by initial conditions). Moreover, a number of authors have pointed out that radiative feedback is likely to be more important than any of these processes in setting the gas temperature in an actively star-forming region, and that this process is not well-described by an equation of state (Krumholz 2006; Krumholz et al. 2007; Offner et al. 2009b; Urban et al. 2010). Simulations of star cluster formation including radiative feedback suggest that it is capable of producing an IMF peak that is numerically converged and relatively insensitive to changes in interstellar conditions (Bate 2009c, 2012a, 2014; Krumholz et al. 2011, 2012; Myers et al. 2011).

While these developments are promising, the numerical expense of large-scale simulations including radiative feedback means that only a very small number of calculations have been performed. Moreover, analytic models of fragmentation with radiative feedback have, up to this point, been quite simple (e.g., Krumholz & McKee 2008; Krumholz et al. 2011), and have not been linked to an analytic theory for the full IMF. Recently, Guszejnov & Hopkins (2015a) introduced a new method for performing semi-analytic calculations of turbulent fragmentation. Crucially, this method retains spatial information about how gas fragments, making it possible to include localized feedback mechanisms like stellar radiative heating. These calculations are rapid, enabling a much broader exploration of parameter space than can yet be accomplished with full three-dimensional radiation-hydrodynamic simulations.

In this paper we combine the Guszejnov & Hopkins (2015a) fragmentation model with the Krumholz (2011) model for stellar radiative feedback (henceforth referred to as GH15 and K11 respectively). We also explore alternative treatments of gas thermodynamics, including both isothermal and stiff equation of state models. We use these method to study the predicted IMF in a wide variey of star-forming environments. The remainder of this paper is laid out as follows. First, in Sec. 4.2 we introduce the semi-analytical framework we use to test different models of star formation. In Sec. 4.3.1 we show that isothermal turbulent fragmentation leads to a scale-free IMF. In Sec. 4.3.2 we show that models with a stiffened equation of state are inherently sensitive to the initial conditions so they cannot provide an invariant mass scale. In Sec. 4.3.3 we provide a simple model for protostellar heating that leads to an IMF with remarkably little sensitivity to initial conditions. Finally, in Section 4.4 we discuss the implications of our findings, and conclude.

4.2 Model and Methodology

4.2.1 Model Overview

In order to test the different models we are using the semi-analytical framework of GH15. This takes advantage of the fact that the density fluctuations in a highly turbulent medium locally obey approximately lognormal random field statistics, thereby avoiding the need for computationally expensive hydrodynamical simulations while still preserving spatial information (unlike analytical excursion set models like Guszejnov & Hopkins 2015b; Hopkins 2012b). The present version of the model only includes the bare essential physics: turbulence (pumped by the collapse of the cloud), collapse (at constant virial parameter, motivated by Robertson & Goldreich 2012b and Murray et al. 2015), an equation of state (EOS) and a simple feedback prescription.

The initial conditions of clouds are defined by their mass, the sonic length (R_{sonic}, scale at which the turbulent velocity dispersion is equal to the sound speed) and the sonic mass (M_{sonic}), from which other parameters (e.g. temperature, Mach number) can be derived. For details about initial conditions see GH15 (a detailed step-by-step guide to the model is provided in Appendix A).

Our simulations start from a giant molecular cloud (GMC) with fully developed turbulence and follow its collapse. Every time a new self-gravitating substructure appears (i.e., the cloud fragments) the code is run recursively for each substructure. When a cloud reaches the protostellar size scale ($\sim 10^{-4}\mathrm{pc}$) it is considered to be fully collapsed into a protostar and the simulation stops. This means that the final output of the code is the protostellar system mass function (PSMF) which we will assume to be identical to the IMF throughout this paper. This assumption is not quite accurate, particularly in the brown dwarf regime, as it neglects the production of brown dwarfs via disk fragmentation. We also neglect the growth of stars by Bondi-Hoyle accretion of gas that was not initially part of their collapsing core, though this effect is likely negligible (Krumholz et al. 2005). The leftover unbound material is assumed to escape. All the simulations we present here start from $10^4\,\mathrm{M}_\odot$ GMCs, as the results are completely insensitive to the size of the parent cloud (for demonstration see GH15).

4.2.2 Equation of State Models

In this paper we consider a series of models that include increasingly sophisticated treatments of gas thermodynamics. The simplest, which correspond to the usual assumption in turbulent fragmentation models, is that the gas is isothermal, corresponding to an adiabatic index $\gamma = 1$. The next level of complexity is simulations with a non-constant γ. The simulation allows for arbitrary equations of states which are taken into account as effective polytropes:

$$T(\mathbf{x}, t+\Delta t) = T(\mathbf{x}, t)\left(\frac{\rho(\mathbf{x}, t+\Delta t)}{\rho(\mathbf{x}, t)}\right)^{\gamma(t)-1}, \tag{4.1}$$

where $\gamma(t)$ is the effective polytropic index at the time t. To explore models in which the key physical process is a stiffening of the equation of state, we consider two possible formulations. Some authors have proposed that stiffening occurs at a characteristic surface density Σ_{crit}, and we refer to models of this form as $\gamma(\Sigma)$ equations of state (EOS's). The particular parameterization we explore in this work is similar to that that proposed by Glover & Mac Low (2007), which is

$$\gamma(\Sigma) = \begin{cases} 1.0 & \Sigma < \Sigma_{\mathrm{crit}} \\ 31/24 & \Sigma > \Sigma_{\mathrm{crit}} \end{cases}, \tag{4.2}$$

where $\Sigma = M/(4\pi R^2)$ for a cloud of mass M and radius R[2]. GH15 shows that using the standard value of $\Sigma_{\mathrm{crit}} = 5000\,\mathrm{M}_\odot/\mathrm{pc}^2$ leads to a turnover mass of $\sim 0.01\,\mathrm{M}_\odot$, much too low compared to the observed IMF; indeed, the mass picked out by this choice is simply the opacity limit for fragmentation (Rees 1976). For this reason, we set Σ_{crit} so that it is equal to critical surface density

---

[2] Note that the value of 31/24 was chosen to allow the comparison of models with protostellar heating and $\gamma(\Sigma)$ EOSs (see Sec. 4.3.3). The choice of this value has no effect on the sensitivity of the results to initial conditions.

of the protostellar heating model (Σ_{heat}, see Sec. 4.3.3) in the standard ($T_0 = 10\,\mathrm{K}$) scenario. This means $\Sigma_{\mathrm{crit}} \sim 130\,\mathrm{M_\odot pc^{-2}}$. Using a higher surface density would only shift the turnover mass scale to lower values, but would not affect its sensitivity to initial conditions (see GH15 for results with such an EOS). In other words, we are giving these models their "best chance" to fit the data.

Another formulation we consider is one where the stiffening occurs at a characteristic volume density ρ_{crit}, which we refer to as a $\gamma(\rho)$ EOS. The form we adopt for this EOS is equivalent to the one used by Bate (2009b):

$$\gamma(\rho) = \begin{cases} 1.0 & \rho < \rho_{\mathrm{crit}} \\ 1.4 & \rho > \rho_{\mathrm{crit}} \end{cases}, \tag{4.3}$$

where $\rho = 3M/4\pi R^3$. Once again we chose the critical value so that it is convenient to compare with the other models so we set $\rho_{\mathrm{crit}} = 15000\,\mathrm{M_\odot/pc^{-3}}$ corresponding to $n_{H_2,\mathrm{crit}} \approx 2.6 \times 10^5\,\mathrm{cm^{-3}}$.

For reference we also include a scenario with a more physically-motivated EOS based on the works of Masunaga & Inutsuka (2000) and Glover & Mac Low 2007:

$$\gamma_{\mathrm{phys}}(\rho) = \begin{cases} 0.8 & \rho < \rho_{\mathrm{crit,1}} \\ 1.0 & \rho_{\mathrm{crit,1}} < \rho < \rho_{\mathrm{crit,2}} \\ 1.4 & \rho > \rho_{\mathrm{crit,2}} \end{cases}, \tag{4.4}$$

where we set $\rho_{\mathrm{crit,1}} = 5000\,\mathrm{M_\odot/pc^{-3}}$ and $\rho_{\mathrm{crit,2}} = 5\times10^8\,\mathrm{M_\odot/pc^{-3}}$ corresponding to $n_{H_2,\mathrm{crit,1}} \approx 10^5\,\mathrm{cm^{-3}}$ and $n_{H_2,\mathrm{crit,2}} \approx 10^{10}\,\mathrm{cm^{-3}}$.

While these are only three of the EOS's that have been proposed in the literature, they serve as representative examples of the outcomes produced by such an approach.

4.2.3 Radiation Feedback Models

The final class of models we consider are those with a simple treatment of protostellar radiative feedback. In these we assume that the center of self-gravitating clouds collapses first, forming a protostellar seed, and then the rest of the cloud collapses onto it. The energy of the matter accreted by this seed is radiated within the optically thick core. The temperature of the material depends on the accretion rate onto the protostar (and thus the mass and dynamical time of the gas around it), and on the energy yield per unit mass from accretion, which we denote Ψ. The value of Ψ is set by the protostellar mass-radius relation, and K11 shows that it is determined primarily by the effects of deuterium burning, which thermostats the central temperatures of protostars. Because deuterium burning begins when protostars are only a few $\times 10^{-2}\,\mathrm{M}_{\odot}$, and, for low mass protostars, continues for ~ 10 Myr, it is the dominant factor in setting Ψ during the bulk of a molecular cloud's star-forming history. Comparing with detailed protostellar evolution calculations, K11 finds $\Psi \approx 2.5\times 10^{10}\,\mathrm{J/kg}$ to better than half a dex accuracy for all protostellar masses in the range $0.05-1\,\mathrm{M}_{\odot}$, and to better than a dex accuracy from $0.01-0.05\,\mathrm{M}_{\odot}$. We therefore adopt this value of Ψ throughout the remainder of this paper. Following K11, this heats any core harboring an accreting protostar up to a temperature

$$T_{\mathrm{heat}}^{4} \approx \frac{\Psi\sqrt{G}}{4\pi\sigma_{SB}} M^{3/2} R^{-7/2}. \tag{4.5}$$

Crudely, this scaling reflects energy conservation as $L = 4\pi R^2 \sigma_{SB} T_{\mathrm{heat}}^4$ for the opaque cloud. Combined, internal heating and the physical processes captured by the EOS models set the temperature as

$$T^4 = T_{\mathrm{EOS}}^4 + T_{\mathrm{heat}}^4, \tag{4.6}$$

where T_{EOS} is the temperature of the cloud if only EOS effects are taken into account. Note that this is an extremely simplistic treatment of protostellar heating, where each cloud is assumed to have a protostar "seed" at its center which heats (uniformly) only its own cloud. This heating is assumed to be "turned on" as soon as the cloud forms. However, since the temperature depends on Ψ only to the $1/4$ power, even a factor of ~ 10 error in its value, as can happen for $0.01\,\mathrm{M}_{\odot}$ protostars, corresponds to a relatively modest error in T. For stars near the peak of the IMF, which we shall see this model places at $\sim 0.3\ M_{\odot}$, the error is even smaller.

To easily identify the results for different models and initial conditions we use the labels shown in Table 4.1. The *T10* label refers to initial conditions similar to MW GMCs, *T20* and *T75* have enhanced temperatures as are typically found in regions of very active star formation or in the Galactic center, *hiDens* has enhanced temperature and density, similar to a dense, massive star-forming region in the MW, while *ULIRG* runs have the very high temperature and strong turbulence characteristic to the clouds of Ultra Luminous Infrared Galaxies (ULIRGs). Finally, the *hiMach* model has an enhanced Mach number but fixed temperature; we are unaware of a physical analog for this case, but we include it because it provides useful insight into the physics of the model.

4.3 Source of Invariant Mass Scale

One of the key features of the IMF is the turnover mass which appears to be close to universal. In this section we investigate different models of turbulent fragmentation – starting from the simplest – to test whether they are capable of producing a nearly-invariant turnover mass, as demanded by the observations.

4.3.1 Failure of Isothermal Fragmentation

We first examine our isothermal case, *IsoTherm_T10*, the results for which are shown in Fig. 4.1. As the Figure shows, the IMF we obtain in the isothermal case is a pure power-law, with no visible turnover. Although not shown in Figure 4.1, we obtain a similar scale-free result for the IMF produced by purely isothermal fragmentation independent of our choice of initial conditions. It is important to note that, in the isothermal case, the core mass function (CMF) does have a turnover, at the sonic mass $M_{\rm sonic} \sim c_s^2 R_{\rm sonic}/G$, which is set by the initial conditions (see GH15). However, this does not result in an IMF with a turnover.

This result might at first seem surprising, but we can understand it through a simple analytic argument. In a number of analytical studies (e.g. Hopkins 2012b) the IMF is inferred from the CMF by shifting the mass scale by a factor of 1/3 (rule of thumb: "a third of the bound mass ends up in the star"), which is not physically correct, as cores undergo gravitational collapse which takes a finite amount of time, allowing them to further fragment into a spectrum of submasses (Guszejnov & Hopkins 2015b).

This means that a single initial core forms its own sub-cores starting from different initial conditions, so the distribution of subfragments (CMF of "second generation" fragments) will have its turnover at a different scale than the parent population. The collapse of highly supersonic clouds is self-similar, so every factor of 2 contraction takes about a dynamical time (see Sec. 9.2 in Hopkins (2013c)). This means that the cloud can fragment at any scale, and thus there is the same "amount of fragmentation" at each scale, producing an infinite fragmentation cascade[3]. This explains why numerical studies have

---

[3] Note that to have finite mass in any mass bins the cascade cannot be infinite, it has to be terminated at some finite scale by additional physics. So our isothermal model still has two mass scales: 1) the outer scale set by initial conditions (e.g. GMC mass) and 2) the cascade termination scale. If these scales are sufficiently far, a scale-free regime forms between them (similar to the inertial range in turbulence). Assuming that the stellar mass

Label	Input Parameters		Derived Parameters					Thermodynamics
	$\mathbf{M}_{\text{sonic}}$ [$M_\odot$]	$\mathbf{R}_{\text{sonic}}$ [pc]	$\mathbf{T}_0$ [K]	$\mathbf{R}_0$ [pc]	$\mathcal{M}_0$	Σ_0 [$M_\odot pc^{-2}$]	$\mathbf{n}_{H_2,0}$ [cm^{-3}]	
IsoTherm_T10	2.3	0.1	10	9.3	9.6	9.3	50	Isothermal
EOSΣ_T10	2.3	0.1	10	9.3	9.6	9.3	50	$\gamma(\Sigma)$ EOS
EOSΣ_T20	4.6	0.1	20	6.5	8.1	18.6	150	$\gamma(\Sigma)$ EOS
EOSΣ_T75	17.25	0.1	75	3.4	5.8	70.7	1100	$\gamma(\Sigma)$ EOS
EOSΣ_hiMach	0.09	0.004	10	1.88	21.7	224	6200	$\gamma(\Sigma)$ EOS
EOSΣ_ULIRG	0.42	0.0026	75	0.57	14.75	2480	2.3×10^5	$\gamma(\Sigma)$ EOS
EOSρ_T10	2.3	0.1	10	9.3	9.6	9.3	50	$\gamma(\rho)$ EOS
EOSρ_T20	4.6	0.1	20	6.5	8.1	18.6	150	$\gamma(\rho)$ EOS
EOSρ_T75	17.25	0.1	75	3.4	5.8	70.7	1100	$\gamma(\rho)$ EOS
EOSρ_hiMach	0.09	0.004	10	1.88	21.7	224	6200	$\gamma(\rho)$ EOS
EOSρ_ULIRG	0.42	0.0026	75	0.57	14.75	2480	2.3×10^5	$\gamma(\rho)$ EOS
EOSPhys_T10	2.3	0.1	10	9.3	9.6	9.3	50	$\gamma_{\text{phys}}(\rho)$ EOS
Heated_T10	2.3	0.1	10	9.3	9.6	9.3	50	Protostellar Heating
Heated_T20	4.6	0.1	20	6.5	8.1	18.6	150	Protostellar Heating
Heated_T75	17.25	0.1	75	3.4	5.8	70.7	1100	Protostellar Heating
Heated_hiMach	0.09	0.004	10	1.88	21.7	224	6200	Protostellar Heating
Heated_hiDens	0.46	0.01	20	2.08	14.4	183	5400	Protostellar Heating
Heated_ULIRG	0.42	0.0026	75	0.57	14.8	2480	2.3×10^5	Protostellar Heating

Table 4.1: Initial conditions of the different simulation runs presented in this paper. The actual input parameters of the code are the sonic mass M_{sonic} and length R_{sonic}, from which more physical parameters like initial temperature (T_0), radius (R), Mach number ($\mathcal{M}_0$), surface density (Σ_0) and number density ($n_{H_2,0}$) can be derived. All runs were performed for a large statistical ensemble (~ 500) of $10^4\,M_\odot$ GMCs.

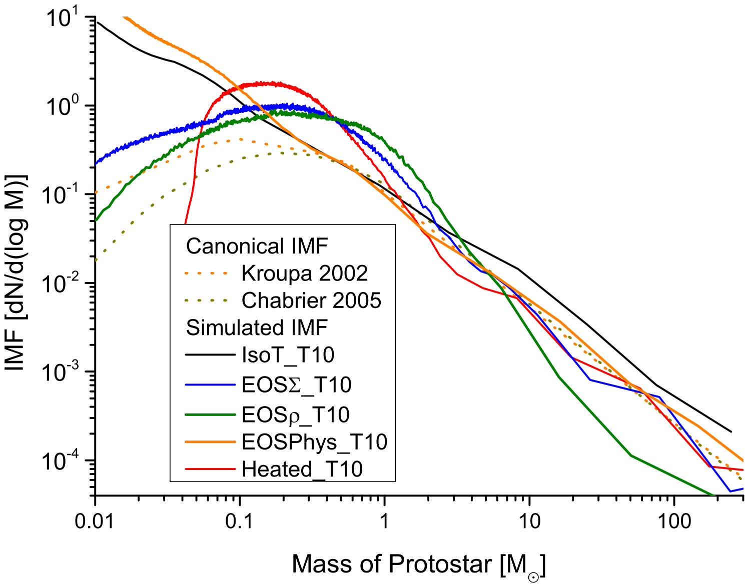

Figure 4.1: The IMF in the case of purely isothermal equation of state (model *IsoTherm_T10*, solid black), a surface density dependent "stiff" EOS (*EOSΣ_T10*, solid blue), a volume density dependent "stiff" EOS (*EOSρ_T10*, solid green), a physically motivated "stiff" EOS (*EOSPhys_T10*, solid orange) and a protostellar heating (*Heating_T10*, solid red) model. We compare these to the canonical IMFs of Kroupa (2002) and Chabrier (2005). Isothermal collapse leads to a featureless power-law close to $\mathrm{d}N/\mathrm{d}M \propto M^{-2}$ while both protostellar heating and the EOS introduce a turnover at lower masses while having close to canonical behavior at higher masses. Although the physically motivated EOS of Eq. 4.4 does create a turnover, it is at such a low mass that the resulting IMF looks like a power law in the stellar mass range.

been unable to get converged results, as higher resolution leads to fragmentation on even smaller scales.

We will now attempt to illustrate the qualitative behavior we might expect from a self similar fragmentation cascade, by calculating the IMF in a special case. First, let us assume that a self gravitating cloud has λ chance of collapsing without fragmentation and forming a star. Because the process is self-similar, λ must be independent of cloud mass. Let us further assume that when a cloud of M mass fragments, the newly formed clouds have an average mass of αM. For convenience let us further simplify the model by assuming that a

---

scale is much higher than the termination scale, the distribution in the that range must be close to the self similar.

cloud either collapses to a star or breaks up into fragments of α relative mass.

In this simplified model, calculating the mass budget is very easy. The ith generation of fragmentation produces clouds of mass $M_i = \alpha^i M_0$, where M_0 is the mass of the initial cloud. The total mass of these clouds is $M_0(1-\lambda)^i$, where the second factor is simply the fraction of the mass not collapsed to stars yet in the previous $i-1$ generations. Since a fraction λ of these clouds will collapse to stars without fragmenting further, the total mass of stars of mass M_i is just $f_i = M_0\lambda(1-\lambda)^i$. As mentioned in Sec. 1, the results from numerical simulations show a large degree of fragmentation, so we expect $\lambda \ll 1$. In this limit, $f_i \approx M_0\lambda(1-i\lambda)$, and f_i will therefore be approximately constant for all $i \ll 1/\lambda$. Since $1/\lambda \gg 1$, this means that f_i is nearly constant over a very large number of generations of fragmentation. Further recall that, since the generations of of fragments are separated logarithmically in mass (i.e., $\log(M_i/M_{i+1}) = \log\alpha$ is constant), a constant value of f_i corresponds to constant mass per logarithmic interval in object mass. In terms of number of objects per unit mass (as opposed to per unit log mass), this is $dN/dM \propto M^{-2}$, which is close to what we find. Our actual model is considerably more complex, in that clouds can produce variable numbers of fragments with variable masses, but this simple illustration captures the essence of the isothermal result.

In summary: although isothermal models like Hopkins (2012b) recover the CMF shape, they are unable to explain the shape of the IMF. In the case of isothermal fragmentation, independent of the form of the CMF, the IMF becomes a power-law of M^{-2} as the initial conditions are "forgotten" during the fragmentation cascade. This means that to produce an IMF that is not a pure power-law, as observed, an extra physical process is required that would stop the cascade at a mass scale invariant to the initial conditions.

4.3.2 Can a Universal Mass Scale Come from the Equation of State?

One mechanism to imprint a mass scale onto the process of turbulent fragmentation is to have the equation of state deviate from isothermality, either because the gas becomes optically thick to its own cooling radiation, or due to a change in the cooling process such as the onset of grain-gas coupling. We investigate this approach in our EOS models.

Figure 4.2 shows the results of simulations using our $\gamma(\Sigma)$ (surface density-dependent) EOS (*EOSΣ* models), for a variety of initial conditions. We see that, with an appropriate choice of Σ_{crit}, one can obtain a stellar mass function that agrees reasonably well with the observed IMF. However, one can do so only for a particular choice of initial conditions. As shown in GH15, an EOS with stiffening suppresses fragmentation below mass scale $M_{\text{crit}} \sim \frac{c_s^4}{\Sigma_{\text{crit}} G^2} \propto T^2/\Sigma_{\text{crit}}$, which is clearly shown by the figure. Also, stronger turbulence leads to more fragmentation and thus more brown dwarfs (see *EOSΣ_T75* and *EOSΣ_ULIRG*) in accordance with predictions (e.g. Hopkins 2013e). At first *EOSΣ_hiMach* might seem to contradict that as it has more large protostars than the standard case. This, however, is caused by the interaction of the initial conditions with the adopted EOS. In this scenario the initial surface density $\Sigma_{init} \sim M_{\text{sonic}}/\left(R_{\text{sonic}}^2 8\pi\right) \propto T/R_{\text{sonic}}$ is already above the stiffening transition surface density Σ_{crit}. As a result, there is very little fragmentation because the EOS is always "stiff". It is also worth noting that the EOS model always has a slow cut-off at low masses despite the fact that protostellar disk fragmentation (a potential source of brown dwarfs) is neglected, so it is likely to overproduce brown dwarfs,

We have similarly tested an EOS that becomes stiff at a critical volume density ρ_{crit} (see Eq. 4.3). Fig. 4.3 shows that, as in the case for the $\gamma(\Sigma)$ models, the volume density dependent EOS is also very sensitive to initial conditions. This can be easily understood using a similar arguments as the ones used by GH15 in the $\gamma(\Sigma)$ case: using the collapse condition and size-mass relations (see Sec. 2.2 in GH15) one can find the size and mass of a self gravitating fragment whose density is ρ_{crit}, which leads to the corresponding turnover mass scale $M_{\text{crit}} \approx M_{Jeans}(\rho_{\text{crit}}) \propto T_0^{3/2} \rho_{\text{crit}}^{-1/2}$ (this is also shown by Bate 2009c).

We have therefore shown that, while it is possible to choose critical values Σ_{crit} or ρ_{crit} such that a stiffened equation of state produces an IMF peak that is qualitatively consistent with observations, such a choice works for only one particular set of initial conditions (see Figures 4.2-4.3). Substantially different initial temperatures necessitate different choices to keep the IMF peak fixed, and there is no obvious physical reason why the critical parameters should vary in such a manner. Indeed, we remind readers that even the values we have used for the standard MW case ($T_0 = 10\,\text{K}$) have been optimized to fit the observations, and are not motivated by any plausible physical model. Choosing the values of Σ_{crit} or ρ_{crit} that one would naturally predict based on considerations of gas thermodynamics would make the agreement with observations very poor even in the Milky Way-like case (see *EOSPhys_T10* in Fig. 4.1).

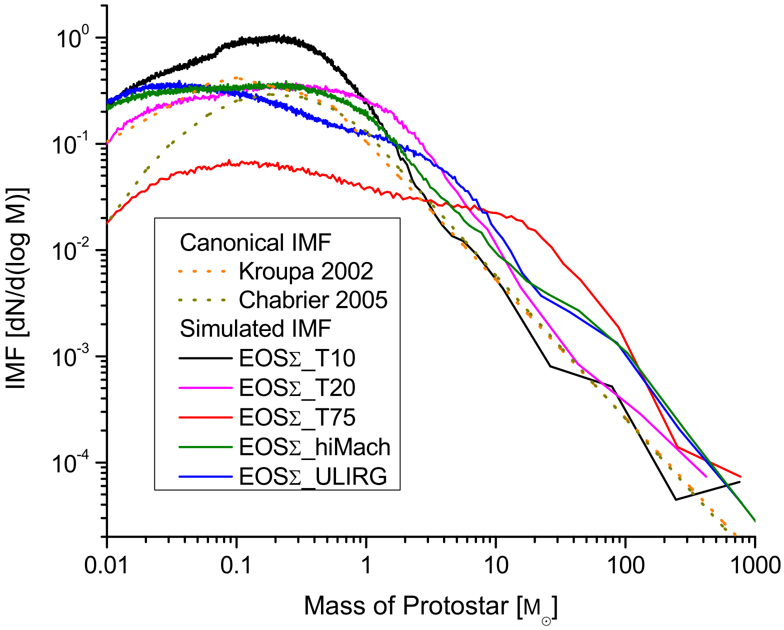

Figure 4.2: The IMF of the surface density dependent EOS model (*EOS*Σ) for standard (*EOS*Σ*_T10*: $T = 10\,\mathrm{K}$, $R_{\mathrm{sonic}} = 0.1\,\mathrm{pc}$), high temperature (*EOS*Σ*_T20*: $T = 20\,\mathrm{K}$), extreme turbulence (*EOS*Σ*_hiMach*: $R_{\mathrm{sonic}} = 0.0026\,\mathrm{pc}$), extreme temperature (*EOS*Σ*_T75*: $T = 75\,\mathrm{K}$) and ULIRG (*EOS*Σ*_ULIRG*: $T = 75\,\mathrm{K}$, $R_{\mathrm{sonic}} = 0.0026\,\mathrm{pc}$) initial conditions (see Table 4.1). There is a clear trend of increasing turnover mass with initial temperature, consistent with our expectation that, for these EOS models, the turnover should scale as $M_{\mathrm{crit}} \propto T_0^2$.

4.3.3 Effects of Protostellar Heating

Another proposed origin of a universal mass scale is stellar feedback, including protostellar heating, outflows, accretion, photo-ionization heating and supernovae, none of which are scale-free processes. Thus they all have the capability to imprint a mass scale. In this paper we only concentrate on protostellar heating as it is the earliest and strongest feedback mechanism during the evolution of protostellar cores. Most of the other mechanisms act *after* the stars form, which can therefore only alter the IMF of "second generation" stars.

Figure 4.4 shows the results of our calculation including protostellar heating. Similar to the EOS models, at very high masses the additional physics (protostellar heating) has no significant effect, and thus the IMF looks similar to the

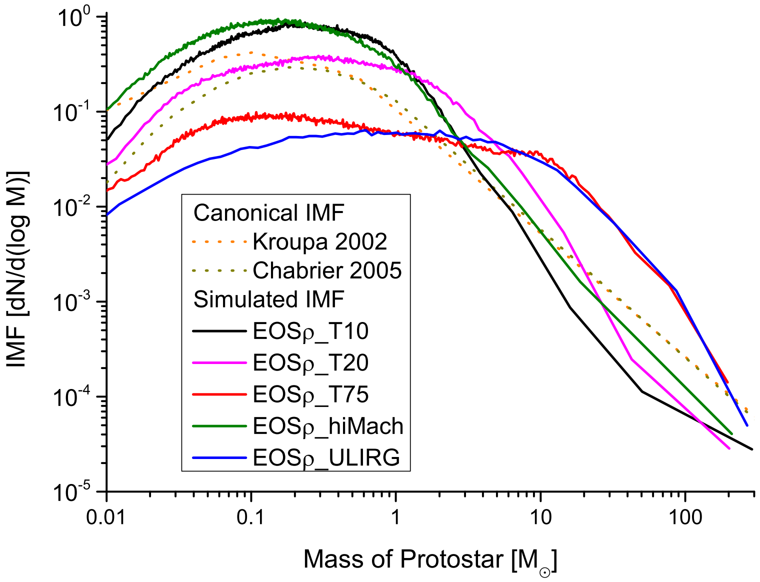

Figure 4.3: The IMF of the volume density dependent EOS model (*EOSρ*)for standard (*EOSρ_T10*: $T = 10\,\mathrm{K}$, $R_{\mathrm{sonic}} = 0.1\,\mathrm{pc}$), high temperature (*EOSρ_T20*: $T = 20\,\mathrm{K}$), extreme turbulence (*EOSρ_hiMach*: $R_{\mathrm{sonic}} = 0.0026\,\mathrm{pc}$), extreme temperature (*EOSρ_T75*: $T = 75\,\mathrm{K}$) and ULIRG (*EOSρ_ULIRG*: $T = 75\,\mathrm{K}$, $R_{\mathrm{sonic}} = 0.0026\,\mathrm{pc}$) initial conditions (see Table 4.1). There is a clear trend of increasing turnover mass with initial temperature, consistent with $M_{\mathrm{crit}} \propto T_0^{3/2}$. Despite having stronger turbulence *EOSρ_ULIRG* seems to produce more top heavy IMF than *EOSρ_T75*. This occurs because in this model the initial density starts out very close to the critical density.

isothermal result of M^{-2}. The isothermal fragmentation cascade is terminated around the characteristic mass of the model, creating a "pile up". Note that the current model underproduces brown dwarfs as it neglects disk fragmentation, and more generally any fragmentation process that depends on angular momentum. As the figure shows, inclusion of heating produces a peak that is consistent with the observed peak of the IMF, and that is remarkably insensitive to changes in the star-forming environment. The only changes in the position of the peak visible in Figure 4.4 are in the *ULIRG* and *hiMach* runs, where the peak is shifted to lower masses by a factor of ~ 2. The *hiDens* run, which is set up to emulate a dense star forming region in the Milky Way, is intermediate between these two cases and the normal Milky Way case, with a peak that is shifted by a tens of percent slightly relative to *T10*. We emphasize that, unlike the $\gamma(\Sigma)$ and $\gamma(\rho)$ cases where we explicitly tuned model parameters to produce the correct peak mass, the protostellar heating model is not tuned, and has no free parameters. Its only parameter is the value of Ψ, which is determined entirely by the physics of stellar structure and deuterium burning. Thus both the location and the invariance of the IMF peak in this model are independent predictions.

It is worth noting that this model does seem to produce too few brown dwarfs and an excess of M dwarf stars. However, it also neglects protostellar disk fragmentation and other "sources" of brown dwarfs, which would reduce the excess between $0.1-1\,\mathrm{M}_\odot$ and enhance the number of objects at lower masses. Whether including these processes leads to the correct proportion of brown dwarfs remains an open question, though the radiation-hydrodynamic simulations of Bate (2009b, 2014) and Krumholz et al. (2012) suggest this is in fact the case.

It is also instructive to compare the results of the protostellar heating models to the EOS models, in order to understand why the results are so different. We use a simple model that assumes the cloud behaves "isothermally" except for a global heating term. This means that $T_{\mathrm{EOS}} = T_0$ (from Eq. 4.6), which is the initial temperature of the cloud (set by external heating like cosmic rays). At first glance the protostellar heating model proposed above seems very much like an opacity limit EOS model, as $T_{\mathrm{heat}} \propto M^{3/8}R^{-7/8} \approx \Sigma^{3/8}$ so the collapse of the cloud is isothermal until a characteristic Σ_{heat} is reached where $T_{\mathrm{heat}} = T_0$. From that point on $T \approx T_{\mathrm{heat}}$, which means that the temperature increases as if we had a polytropic index of $\gamma = 31/24$ (see Eq. 4.2). Similar to the EOS models we can find the characteristic fragment mass M_{crit} where this transition happens. Using the above relations, the collapse threshold $\frac{M}{R}\frac{1}{T}\frac{1}{1+\mathcal{M}^2} = \mathrm{const.}$ and assuming a subsonic, fragment ($\mathcal{M} \ll 1$) we get $M_{\mathrm{crit}}T_0^{1/4} = \mathrm{const.}$ which means that there is remarkably weak sensitivity to the initial temperature (K11 includes a more rigorous derivation which yields $M_{\mathrm{crit}} \propto T_0^{-1/18}$). Comparing Fig. 4.4 with Fig. 4.2 makes the difference this produces in the resulting IMF abundantly clear.

4.4 Conclusions

The aim of this paper is to investigate what physical processes can explain the origin of the IMF, and in particular the fact that the IMF is not a powerlaw, and that its characteristic mass scale is remarkably insensitive to variations in the star-forming environment. To this end, we have considered three classes

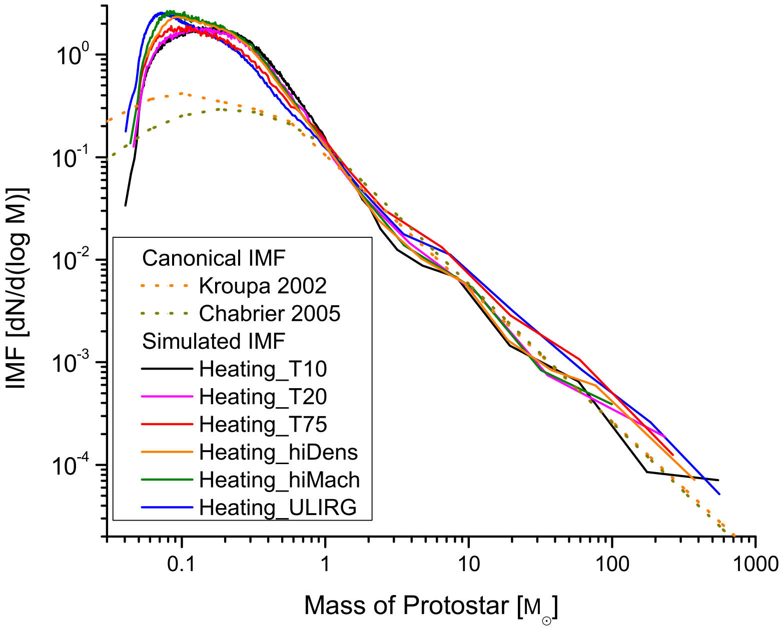

Figure 4.4: The IMF of the protostellar heating model with standard (*Heating_T10*: $T = 10\,\mathrm{K}$, $R_{\mathrm{sonic}} = 0.1\,\mathrm{pc}$), high temperature (*Heating_T20*: $T = 20\,\mathrm{K}$), high density and temperature (*Heating_hiDens*: $T = 20\,\mathrm{K}$, $n = 5000\,\mathrm{cm}^{-3}$), extreme turbulence (*Heating_hiMach*: $R_{\mathrm{sonic}} = 0.0026\,\mathrm{pc}$), extreme temperature (*Heating_T75*: $T = 75\,\mathrm{K}$) and ULIRG (*Heating_ULIRG*: $T = 75\,\mathrm{K}, R_{\mathrm{sonic}} = 0.0026\,\mathrm{pc}$) initial conditions (see Table 4.1). The predicted IMF is remarkably invariant to initial conditions. The turnover point does shift slightly to lower masses for both very strong turbulence and high temperature (stronger turbulence makes fragmentation easier and a higher initial temperature means that protostellar heating becomes dominant at a smaller size scale).

of models for gas thermodynamics: purely isothermal models, models with an equation of state that stiffens at a characteristic volume or surface density, and models containing a simple analytic estimate for the effects of protostellar heating.

We find that purely isothermal models categorically fail to reproduce the IMF. Although the initial conditions do imprint a mass scale (the sonic mass), which is apparent in the distribution of bound structures (i.e., the CMF), due to the lack of mass scale in the equations of motion this scale is "forgotten" during the fragmentation cascade, leading to an M^{-2} power-law solution for the IMF (consistent with the lack of convergence reported thus far in numerical studies). This means that isothermal gravito-turbulent fragmentation cannot explain the existence or universality of the turnover scale in the IMF. Some other physics is needed for that.

An often invoked expansion of the fragmentation model is to have the clouds transition from an isothermal to a "stiff" equation of state when they reach a critical surface or volume density and become thick to their own cooling radiation. This does provide a mass scale for the system, and by tuning the parameters of the model appropriately one can reproduce the observed IMF turnover. However, we find that this approach results in a mass scale that is extremely sensitive to initial conditions ($M_{\mathrm{crit}}[\gamma\,(\Sigma)] \propto T^2$ and $M_{\mathrm{crit}}[\gamma\,(\rho)] \propto T^{3/2}$), rendering these models unable to provide a universal mass scale as is observed. Moreover, producing agreement with the observed mass scale even for initial conditions similar to those found in Solar neighborhood star-forming regions requires parameter choices that are very far from what one would have estimated based on any first-principles physical argument.

We argue instead that feedback physics can provide a mass scale that is both in good agreement with observations and insensitive to the conditions in the star-forming region. As an example, based on Krumholz (2011), we have formulated a simple prescription for protostellar heating. This alone of all the analytical models we consider is able to provide a *universal* IMF turnover, despite large variations in initial gas temperature, densities, Mach number and masses of star forming clouds.

4.4.1 Caveats and Future Work

We close with a discussion of the limitations of our model, and how we plan to improve it in future work. We utilize the semi-analytical framework of Guszejnov & Hopkins (2015a) which makes strong approximations. Motivated by Robertson & Goldreich (2012b) we assume collapse at constant virial parameter as turbulence is pumped by gravity. While this assumption has empirical support, it has not been rigorously demonstrated (although simulations so far seem to confirm this, see Murray et al. 2015). Furthermore, the simulation only follows the evolution of self gravitating structures until they reach the size scale where angular momentum becomes important (which is not treated in the current models), and thus processes that act on the scales of disks or smaller (e.g. disk fragmentation) are neglected. This could have a significant effect on the low mass end of the resulting IMF. Also, fragments are assumed to evolve independently, so mergers and other interactions are neglected[4]. Finally, the protostellar heating model assumes instantenous, isotropic, steady state heating and neglects other forms of feedback (e.g. outflows).

Some of these limitations will be easier to remove than others. The assumption that collapse occurs at constant virial parameter can be investigated by simulations, as can be the fragmentation of disks, and in principle results from these calculations could be incorporated into our model. Similarly, a number of authors have proposed more complex models for the protostellar heating, including the effects of fluctuations in time (e.g., Lomax et al. 2014) that was found to have significant effect on the statistics of star formation (Lomax et al. 2015; Stamatellos et al. 2012), and these could be included as well. Furthermore, it is possible to include angular momentum (like in Hopkins 2012b) and interaction between fragments with significant extension of the model. The entire framework can also be checked against radiation-hydrodynamic simulations such as those of Krumholz et al. (2012) or Myers et al. (2014).

In addition to these improvements in the model itself, an obvious next step is to identify predictions of the model that can be compared with real data. We mention here two obvious, first order predictions that we plan to investigate in future work. First, using the output of cosmological simulations or semi-analytic models, we can investigate the extent to which the small amount of variation we do find in the protostellar heating model produces significant variations in the IMFs of elliptical galaxies over cosmological times. These predictions can then be compared to observations (e.g., Cappellari et al. 2012;

---

[4] This is actually a fairly good assumption. The timescale for two clouds of R radius to merge in this framework is $t_{merger} \sim d/v$, where d is the separation between clouds and v is their relative velocity towards each other. It is easy to show that $t_{merger}/t_{freefall} \sim \sqrt{d/R\,(1+R_{\rm sonic}/R)} > \sqrt{d/R}$. This means that the timescale for merging is only comparable to the freefall time if the clouds initially form right next to each other ($d \sim 2R$).

van Dokkum & Conroy 2010). Second, because our model retains spatial information, it makes predictions for the clustering of stars as well as for their mass distribution. This too can be checked against the spatial distribution of stars in nearby star-forming regions, a test that has been performed before using both analytic (Hopkins 2013a) and numerical (Hansen et al. 2012a; Myers et al. 2014) models. It should be noted, however, that without accounting for protostellar disk fragmentation most results (e.g. correlation function, binarity) will only be valid on scales larger than the typical protostellar disk size.

Chapter 5

COMPARING MODELS FOR IMF VARIATION ACROSS COSMOLOGICAL TIME IN MILKY WAY-LIKE GALAXIES

Guszejnov D., Hopkins P. F., Ma X., 2017, MNRAS, 472, 2107

Abstract

One of the key observations regarding the stellar initial mass function (IMF) is its near-universality in the Milky Way (MW), which provides a powerful way to constrain different star formation models that predict the IMF. However, those models are almost universally "cloud-scale" or smaller – they take as input or simulate single molecular clouds (GMCs), clumps, or cores, and predict the resulting IMF as a function of the cloud properties. Without a model for the progenitor properties of all clouds which formed the stars at different locations in the MW (including ancient stellar populations formed in high-redshift, likely gas-rich dwarf progenitor galaxies that looked little like the Galaxy today), the predictions cannot be fully explored, nor safely applied to "live" cosmological calculations of the IMF in different galaxies at different cosmological times. We therefore combine a suite of high-resolution cosmological simulations (from the Feedback In Realistic Environments project), which form MW-like galaxies with reasonable star formation properties and explicitly resolve massive GMCs, with various proposed cloud-scale IMF models. We apply the models independently to *every* star particle formed in the simulations to synthesize the predicted IMF in the present-day galaxy. We test models where the IMF depends on Jeans mass, sonic or "turbulent Bonner-Ebert" mass, fragmentation with a polytropic equation-of-state, or where it is self-regulated by protostellar feedback. We show that all of these models, except the feedback-regulated ones, predict far more variation ($\sim 0.6-1\,$dex $1\,\sigma$ scatter in the IMF turnover mass) in the simulations than is observed in the MW.

5.1 Introduction

The (instantaneous) mass distribution of stars at their formation time, also known as the initial mass function (IMF), is one of the key predictions of any star formation model. This governs essentially all observable and theoretical aspects of star formation and stellar populations – observable luminosities and colours; effects on stellar environments via feedback in the form of stellar winds, radiation and supernovae; nucleosynthesis and galactic chemical evolution, and so on. The IMF has been well-studied within the MW, and appears to be well-fit by a simple function with a Salpeter (1955) power-law slope at high masses and lognormal-like turnover at low masses (Chabrier, 2005; Kroupa, 2002). Perhaps the most interesting feature of the IMF is its universality: it has been found that there is quite weak variation within the MW (for recent reviews, see Bastian et al., 2010; Chabrier, 2003; Krumholz, 2014; Offner et al., 2014, and references therein), albeit with a few possible outliers (e.g. Kraus et al., 2017; Luhman et al., 2009). As Offner et al. (2014) emphasize, this universality includes both very young ($\sim$Myr-old) and very old ($\sim 10\,$Gyr-old) stellar populations; stars forming in small, nearby GMCs with masses $\sim 10^4 - 10^6\,\mathrm{M}_\odot$ and massive complexes with masses $\sim 10^6 - 10^7\,\mathrm{M}_\odot$; the solar neighbourhood at $\sim 10\,$kpc from the galactic centre (where the gas disk surface density is $\sim 10\,\mathrm{M}_\odot\,\mathrm{p}c^{-2}$) and the central molecular zone at sub-kpc and $\sim 100\,$pc scales (where gas surface densities are order-of-magnitude larger).

In other galaxies, the IMF usually must be *assumed*, and with an IMF assumption, physical properties of the stellar populations and galaxies (e.g. their stellar masses) are derived from observables (e.g. light, colours). This makes it critical to understand the IMF, in order to understand galaxy formation. Likewise it is critical for models of galaxy formation to predict or assume *some* IMF model, in order to make any meaningful predictions for observable quantities. The universality of the IMF in old stellar populations in the MW is widely taken as a suggestion that it may be near-universal in other galaxies, because older populations in the MW formed when the galaxy was much younger and very different, likely a typical high-redshift gas-rich, metal-poor dwarf galaxy. There are indirect constraints on the IMF both from spectral features and integrated mass-to-light constraints in nearby galaxies: these mostly also favor a universal IMF (e.g. Andrews et al., 2013, 2014; Fumagalli et al., 2011; Koda et al., 2012; Weisz et al., 2015). More recently there have been more interesting hints of variation in the centres of massive elliptical galaxies (Cappellari et al., 2012; Conroy & van Dokkum, 2012; Martín-Navarro et al., 2015a,b,c; Posacki et al., 2015; Sonnenfeld et al., 2015; Treu et al., 2010; van Dokkum & Conroy, 2010, 2011), and perhaps also in faint dwarf galaxies (Brown et al., 2012; Geha et al., 2013; Hoversten & Glazebrook, 2008). Even so, it is worth stressing that the implied variation is not radical: it implies variation of a factor < 2 in the stellar mass-to-light ratio.

As a result, there is a long history of both theoretical and empirical models for galaxy formation which have attempted to predict the IMFs that should arise in different galaxy populations, either as a function of either galaxy-scale or ~kpc-scale properties (what can be resolved in most previous calculations) within the galaxies (see e.g. Baugh et al., 2005; Blancato et al., 2016; Davé et al., 2012; Hopkins, 2013e; Lacey et al., 2016; Narayanan & Davé, 2012; Recchi & Kroupa, 2015; van Dokkum, 2008). At the same time, the specific hints of galaxy-to-galaxy variation discussed above have prompted a new wave of theoretical models which argue the IMF could vary under certain conditions at the GMC or sub-GMC scale, in a way that may connect to the systematic variation inferred in different galaxies (e.g. Bekki 2013; Chabrier et al. 2014; Ferreras et al. 2015; Weidner et al. 2013).

However, these models in every case rely on very strong simplifying assumptions – the IMF is predicted as a function of the cloud properties out of which the stars form, such as its temperature, density, turbulent velocity dispersion, virial parameter, etc. (from which properties like the Jeans mass, or the turbulent Bonner-Ebert mass, or the IGIMF turnover mass, are determined). It is impossible at present to know this empirically for all the clouds that formed the old stellar populations today in a galaxy (or even for most clouds within a galaxy at present day), so instead some strong additional assumptions are usually applied. For example, authors assume isothermal gas with $T = 10\,\mathrm{K}$ (or some other temperature) at all densities, a universal linewidth-size relation across all galaxies, redshifts, and regions within galaxies, or a Jeans or sonic mass within clouds that somehow scales proportionally to that measured from the gas at the $\gtrsim$kpc scales resolved in the cosmological calculations. But if these properties vary across cosmic time, or cloud-to-cloud, then any such model will produce variation in the predicted IMF which can be compared to the observational limits within the MW.

In this paper we therefore investigate the predicted variation in the IMF peak imprinted by these physics in a number of IMF models. We combine high-resolution simulations of MW-like galaxies (where the cloud-scale properties can be at least partially resolved) with the relevant small-scale models for IMF variation as a function of cloud properties.

5.2 Model and Methodology

5.2.1 Simulation

We utilize a set of numerical simulations of MW-like galaxies (see Table 5.1) presented in Hopkins et al. (2017a), from the Feedback in Realistic Envi-

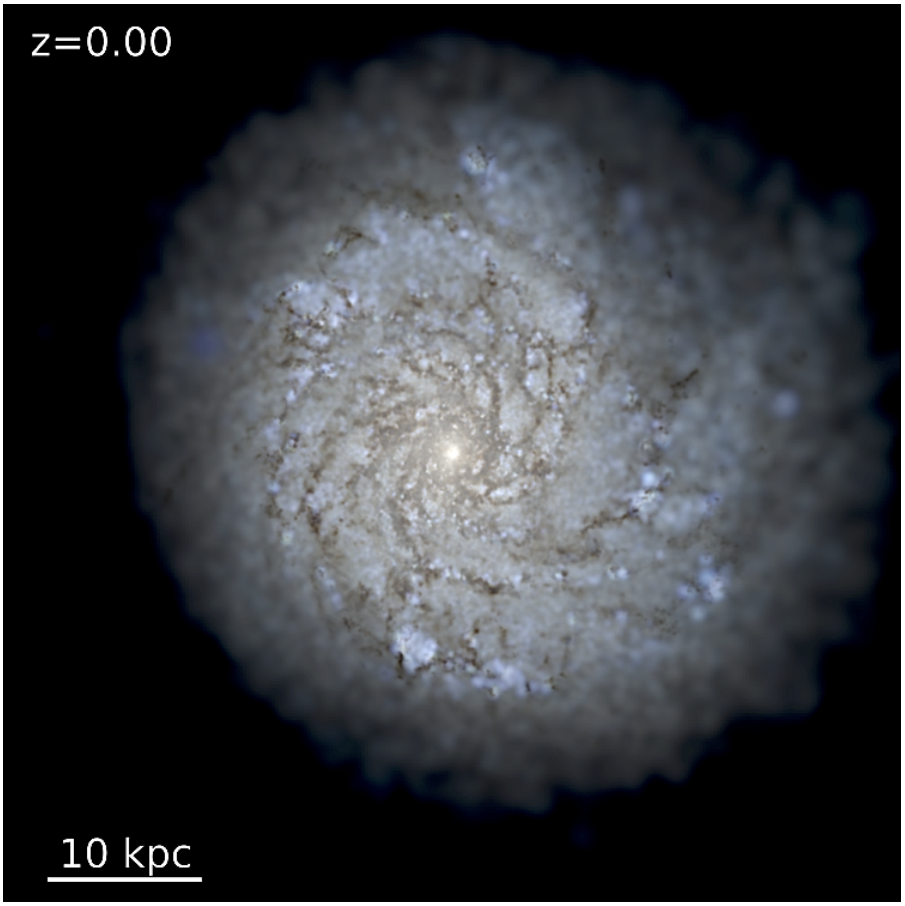

Figure 5.1: Visualization of the starlight (mock *ugr* composite image, accounting for each stellar sink-particle's age and metallicity and ray-tracing including dust obscuration) from one of the simulated MW-like galaxies (see Table 5.1) we use in our calculations (galaxy **m12i** from Hopkins et al. 2017a with $56000, \mathrm{M}_{\odot}$ resolution). Note that resolved molecular clouds and arms are evident. See Fig. 5.2 for the other galaxies from Table 5.1.

ronments (FIRE) project (Hopkins et al. 2014).[1] The simulations are fully cosmological "zoom-in" simulations (where resolution is concentrated on one galaxy in a large cosmological box, run from redshift $z > 100$ to today) and are run using GIZMO (Hopkins 2015)[2], with the mesh-free Godunov "MFM" method for the hydrodynamics (Hopkins, 2015). Self-gravity is included with fully-adaptive force and hydrodynamic resolution; the simulation mass resolution is fixed at 7000 or $56000\,\mathrm{M}_{\odot}$ (Table 5.1). The simulations include detailed metallicity-dependent cooling physics from $T = 10 - 10^{10}\,\mathrm{K}$, including photoionization/recombination, thermal bremsstrahlung, Compton, photoelectric,

---

[1] `http://fire.northwestern.edu`

[2] `http://www.tapir.caltech.edu/~phopkins/Site/GIZMO.html`

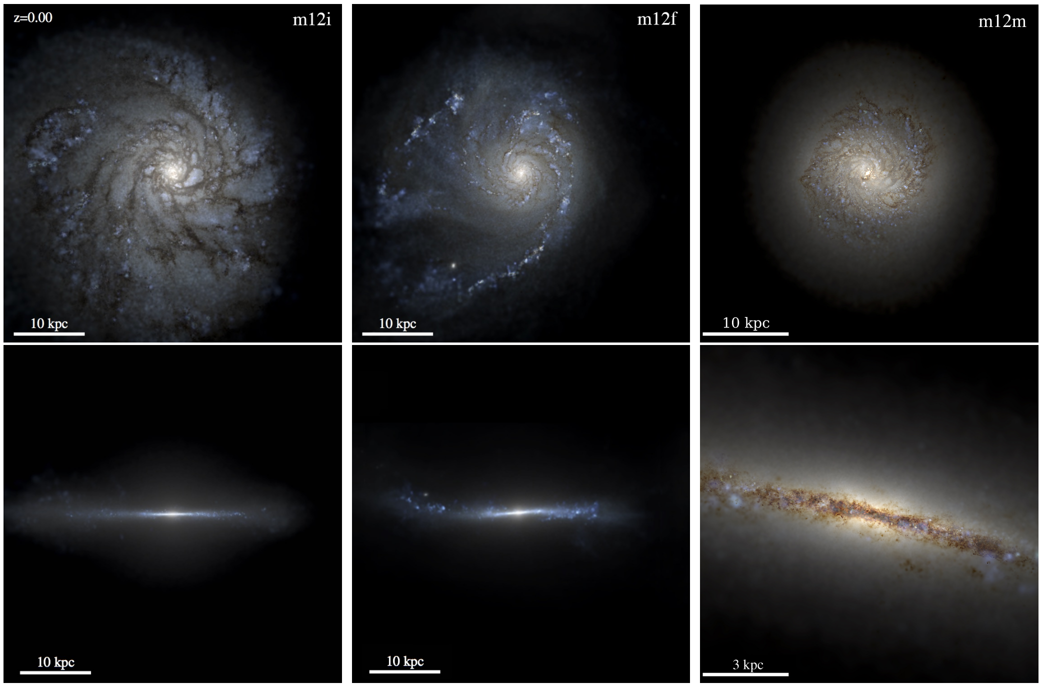

Figure 5.2: Face on (top) and edge on (bottom) visualizations of starlight (mock *ugr* composite image, accounting for each stellar sink-particle's age and metallicity and ray-tracing including dust obscuration) for the simulated MW-like galaxies from Table 5.1. Unlike Fig. 5.1 the m12i example shown here is from the high resolution ($7000\,\mathrm{M}_\odot$) run. The MHD run is not shown as it gives virtually identical results as the non-MHD runs (see Su et al., 2016). Note the edge-on images of **m12i** and **m12f** are a mock Galactic (Aitoff) projection from a random star at $\sim 10\,$kpc from the galactic center. For more details on the individual runs see Hopkins et al. 2017a.

metal line (following Wiersma et al. 2009), molecular, fine structure (following Ferland et al. 2013), dust collisional and cosmic ray processes, including both a meta-galactic UV background and each star in the simulation as a local source.

Individual stars are not resolved in the simulations; but star formation is approximated from resolved scales via a sink-particle method. Gas which is locally self-gravitating, self-shielding, Jeans unstable, and exceeds a minimum density $n > n_{\rm crit} = 1000\,{\rm cm}^{-3}$ (Table 5.1) is transformed into "star cluster sink particles" on its dynamical time. Each such particle represents an IMF-averaged single stellar population of the same age and metallicity, with mass equal to the mass resolution.

Once formed, the simulations include feedback from these star particles via OB & AGB mass-loss, SNe Ia & II, and multi-wavelength photo-heating and

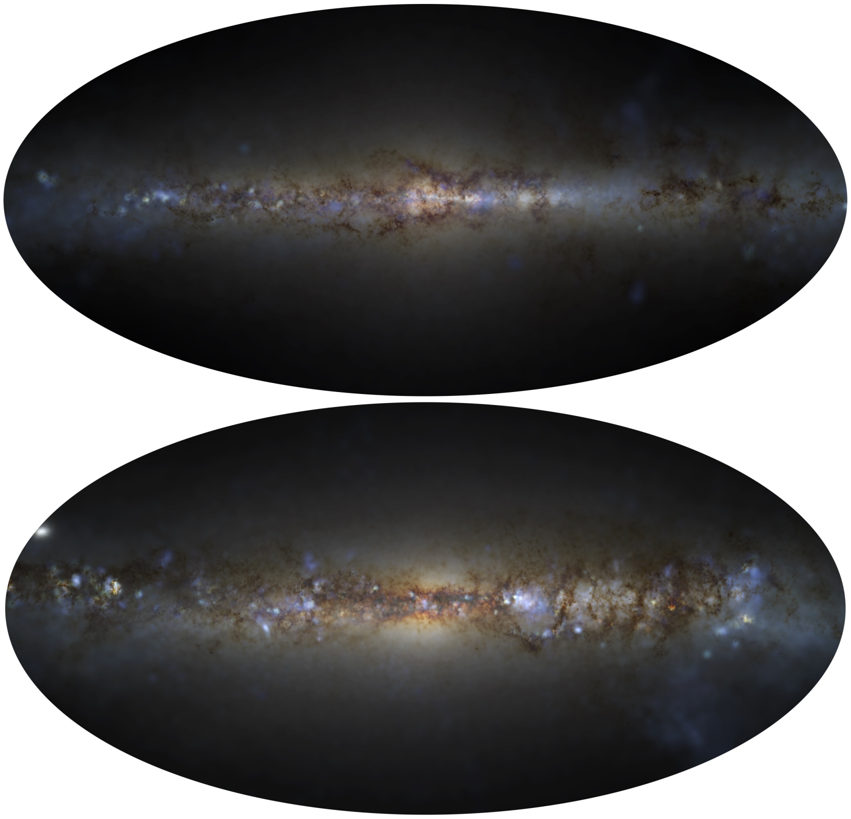

Figure 5.3: Mock Galactic (Aitoff) projection from a random star at $\sim 10\,$kpc from the galactic center, for **m12i** (*top*) and **m12f** (*bottom*). For more details on the individual runs see Hopkins et al. 2017a.

radiation pressure; with inputs taken directly from stellar evolution models (Leitherer et al., 1999), assuming (in-code) a universal IMF (Kroupa, 2002).

There are two reasons for using cosmological simulations instead of present-day observational data or a more localized cloud simulation. (1) We wish to test and validate the approach of using cloud-scale IMF models *dynamically* in next-generation cosmological simulations. Because stellar feedback and observable properties depend on the IMF, truly self-consistent predictions should include some sub-grid IMF model. These cosmological simulations were run assuming a universal IMF, but others (see references in § 5.1) adopt a dynamical IMF model based on resolution-scale properties. But it has not been asked whether the models they considered violate observational constraints in the MW. (2) Stars at a given present-day position in a galaxy can form at wildly different times/places (some even in other dwarf galaxies). This is especially true for the stars in old MW clusters, which appear to have formed at high redshifts, probably in distinct dwarf galaxies with entirely distinct radiation fields, turbulent velocity dispersions, gas masses, etc. It is impossible to know the distribution of progenitor cloud properties *at star formation for old stars* (needed for a given IMF model to make predictions) from observations (or localized simulations) alone.

The galaxies studied here, shown in Figs. 5.1-5.2 – have been studied extensively in previous work: they are similar to the MW in their stellar mass, present-day gas fractions and SFRs (Hopkins et al., 2014), and metallicity (Ma et al., 2016b). Our "fiducial case" **m12i** is also similar to the MW in its stellar kinematics, thin+thick disk morphology, metallicity gradient and metal abundance ratio gradients (in both vertical and radial directions) stellar age distribution (Ma et al., 2016a, 2017), ***R***-process element distribution (van de Voort et al., 2015) and galactic stellar halo and satellite dwarf population (Wetzel et al., 2016). The other two examples represent a slightly later-type (**m12f**) and earlier-type (**m12m**) galaxy, at the same stellar mass and SFR. This is particularly useful because of course no simulation will exactly match the formation history of the MW, so it is important to understand whether our predictions are sensitive to this.

These and other FIRE simulations have also been shown to reproduce the observed Kennicutt-Schmidt relation (Orr et al., 2017; Sparre et al., 2015), properties of galactic outflows (Muratov et al., 2015) and (in higher resolution, non-cosmological simulations) the observed mass function (and CO luminosities), size-mass, and linewidth-size distributions of GMCs (Hopkins et al., 2012, 2013b). One might reasonably worry that this cannot be captured at the lower resolution necessary in cosmological simulations. Therefore in Fig. 5.4 we plot the mass function and linewidth-size relation of GMCs identified at present-day in the actual simulations studied here. They appear to agree at least plausibly with observed properties (Dobbs et al., 2014; Heyer & Dame, 2015). Note that our mass resolution introduces a cut-off at the low mass end of the GMC mass function because these clouds cannot be resolved by the simulation. However, all simulations included in this paper do resolve the most massive GMCs ($> 10^6\,\mathrm{M}_\odot$), in which most of the mass is concentrated (owing to the shape of the GMC mass function), allowing us to recover galactic properties even at lower resolutions. This is clearly apparent in the linewidth-size relation which shows a good agreement with Bolatto et al. (2008). All of this is not to say that the simulations are perfect analogues to the MW; however they are at least a reasonable starting point (see Fig. 5.4 for details).

Our choice of $n_{\rm crit} = 1000\,cm^{-3}$ (at mass resolution $7000 - 56000\,{\rm M}_{\odot}$) can be justified by assuming that GMCs follow the mass-size relation of Bolatto et al. (2008) ($M_{cloud} \sim \pi\,(85\,{\rm M}_{\odot}\,{\rm pc}^{-2})\,R_{cloud}^{2}$), which implies the density threshold for star formation is slightly higher than the mean density of the most-dense resolved clouds. More specifically, we chose the density threshold to correspond to the typical density where the Jeans/Toomre fragmentation scale falls below our mass resolution. In either case the GMC mass function and SFR is dominated by the most massive (hence well-resolved) clouds. This is evident in Fig. 5.4, where we show the GMC mass function and linewidth-size relation predicted at present-day in the galaxy both (a) agree reasonably well with observations (within a factor ~ 2 at all cloud sizes/masses resolved), and (b) are insensitive to resolution (except, of course, that at higher resolution they extend to smaller GMCs). This gives us some confidence that our predictions are not strongly resolution-dependent. In Table 5.1 we show that varying resolution and physics (in an otherwise identical run including magnetic fields, **m**12i+MHD) do not significantly alter our predictions.

Because the simulations resolve down to cloud scales, but no further, we treat each star-forming gas element as an independent "parent cloud", which sets the initial conditions for its own detailed IMF model (in accordance with the IMF models we investigate). Specifically, whenever a sink particle is spawned, we record all properties of the parent gas element from which it formed, and use these in post-processing to predict the IMF. Fig. 5.5 shows the properties of gas elements at one instant, $z = 0$, weighted by star formation rate. Integrating over all times and all galaxies which form stars that ultimately reside in the final galaxy, Fig 5.6 shows the density and temperature distribution of these "star forming particles" (gas at the moment the simulation assigned its mass to a sink particle) at the time of their formation, from our high-resolution **m12i** run. Not surprisingly most sinks form around the simulation density threshold from this particular run ($\sim 1000\,cm^{-3}$). This choice has no effect on the scatter in both n_{cloud} and T_{cloud}, which are the relevant parts to our study. Scatter in these quantities translate to a scatter in the local IMF according to the IMF models we are studying. Note that Narayanan & Hopkins (2013) show the inferred temperature range from mock CO-ladder observations will tend to be significantly smaller than the range plotted here. We wish to emphasize that what is plotted in Fig. 5.6 is not the density/temperature of the core or proto-stellar gas that which directly collapses and forms stars; that is not resolved in these simulations. Instead these are the properties of the progenitor molecular clouds, measured at the smallest resolved scales, which will (and must, physically) fragment into denser sub-clumps that can directly form stars. Also, the width in this distribution is expected to be higher than in present day clouds because of the longer lifetime of stars which preserves the progenitor cloud properties in their IMF for cosmological timescales.

5.2.2 From Parent Cloud to IMF Properties

From this point we infer the IMF turnover mass from the initial conditions of these parent clouds. This exercise has been done in detail by Guszejnov et al. (2016) where the semi analytical framework of Guszejnov & Hopkins (2016) was utilized to create a mapping between GMC properties and the IMF. Fig. 5.7 shows how the IMF peak scales with initial temperature in an equation of state (EOS) and a protostellar feedback based IMF model. Such scaling relations can be analytically derived for other IMF models (e.g. Jeans mass) as well – we focus here on how each model predicts the turnover or "critical" mass $M_{\rm crit}$ scale, because this is the most identifiable feature of the IMF (it sets the mass-to-light ratio, and varies significantly between models). In contrast the bright-end slope varies negligibly between models[3], so it is not useful as a diagnostic.

In this paper we investigate the sensitivity to initial conditions for the following classes of IMF models (summarized in Table 5.1):

- **Jeans mass models:** The Jeans instability is the primary mechanism for the collapse of gas clouds into stars, so these models assume that IMF properties are set by local mean Jeans mass of the parent molecular cloud complex (e.g. Bate & Bonnell 2005). Therefore, the critical mass is

  $$M_{\rm crit,\mathit{J}} \sim \frac{\pi c_s^3}{6G^{3/2}\rho^{1/2}}. \tag{5.1}$$

  Note that the models may still assume sub-fragmentation to smaller scales, but the key assumption (for our purposes) is simply that the turnover mass somehow scales proportional to the parent cloud Jeans mass.

---

[3] Note that observations do indicate variations in the IMF slopes in extra-galactic populations (e.g. Cappellari et al., 2012; Shu et al., 2015; Spiniello et al., 2012) but these measurements only sample the relatively low mass region of the IMF ($< \mathrm{M}_\odot$). The IMF in the MW, however, is well sampled at higher masses and appears to be consistent with a near-universal power-law tail (Offner et al., 2014), which most IMF models are able to roughly reproduce (see references in Table 5.1 for specifics in each case).

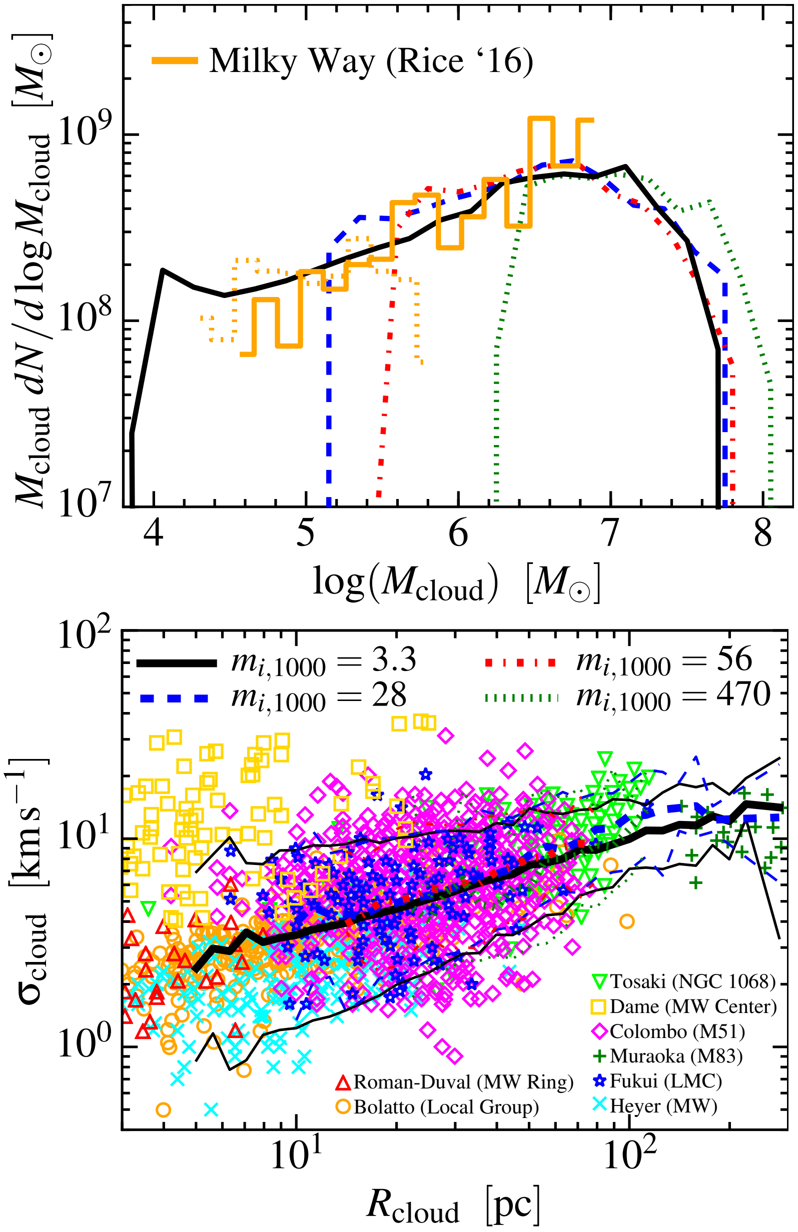

Figure 5.4: *Top:* Mass function (MF) of GMCs in the fiducial simulation (Fig. 5.1) at $z \approx 0$, at different mass resolution (baryonic particle mass $m_i = 1000\,m_{i,\,1000}\,{\rm M_\odot}$). We restart the fiducial simulation from Fig. 5.1 (with $m_{i,\,1000} = 56$) at $z = 0.1$, after re-sampling the particles to raise/lower the mass resolution. We then evolve it for $\sim 1\,$Gyr to $z = 0$, and measure the MF of dense cold-gas clouds (identified in post-processing with a friends-of-friends group-finder) time-averaged over the last $\sim 100\,$Myr inside $< 20\,$kpc of the galaxy center. All details of the resampling and group-finding method are in Hopkins et al. (2017a). We compare the observed MW GMC MF from Rice et al. (2016), normalized to the same total mass, measured inside (*solid*) and outside (*dotted*) the solar circle. At all resolutions, a GMC MF similar to that observed is recovered. The most massive GMCs contain most of the mass/star formation and are the first-resolved. At higher resolution we extend to smaller GMCs. *Bottom:* Linewidth-size relation for the same clouds (median in thick lines; $5-95\%$ intervals in thin lines), vs. observations in nearby galaxies (Bolatto et al., 2008; Colombo et al., 2014a; Fukui et al., 2008; Heyer & Dame, 2015; Heyer et al., 2009; Muraoka et al., 2009; Roman-Duval et al., 2010; Tosaki et al., 2017); note our definition of R_{cloud} is equivalent to their σ_r). The predicted normalization and $1\,\sigma$ dispersion ($\approx 0.12\,$dex, although it increases slightly to ≈ 0.2 dex at the lowest masses) are consistent with observations (compare e.g. Kauffmann et al. 2013). There is no systematic resolution dependence (other than sampling smaller clouds at higher resolution).

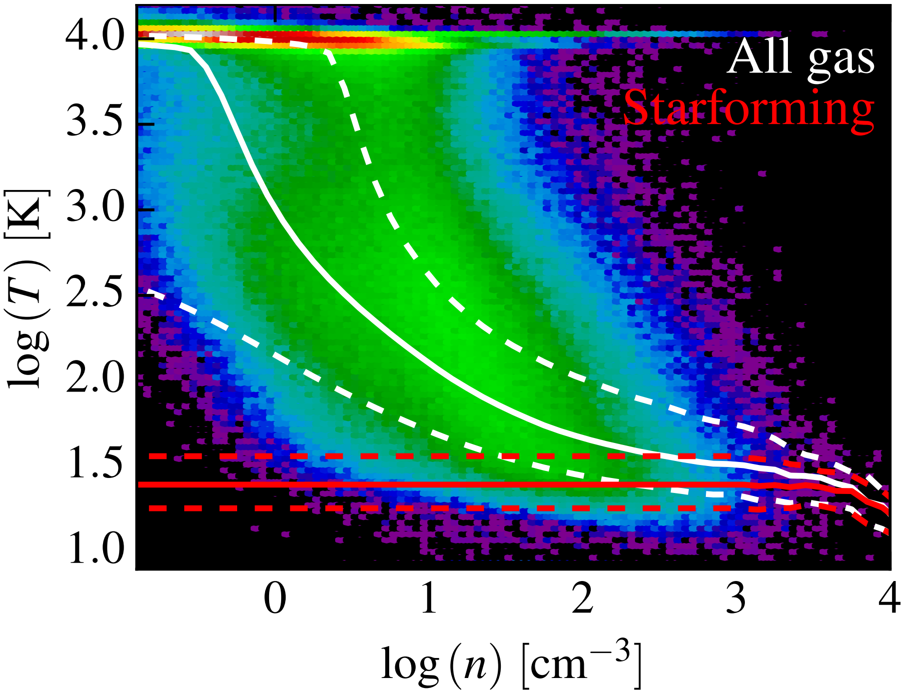

Figure 5.5: Density-temperature diagram for gas at *present-day* ($z = 0$) in our high-resolution **m12i** simulation (others are similar). Colors show a 2D histogram colored by the gas-mass per-pixel (log-weighted, increasing black-blue-green-red with a ~ 6 dex stretch), so this is peaked where there is significant mass in a narrow temperature range. HII regions, warm ionized medium, and warm and cool neutral phases are evident (we do not show lower densities where hot gas is prevalent). Solid (dashed) lines show the median (interquartile) temperature of all gas denser than $> n$, weighted by mass (*white*) or star formation rate (*red*). The latter converges rapidly because SF is restricted to high-n gas. At $z = 0$ in the simulation, most SF occurs in gas with $n > 1000\,cm^{-3}$ and $T \approx 20 - 30\,$K.

- **Opacity limit equation of state (EOS) models:** As the molecular gas becomes denser it reaches the point where it becomes opaque to its own cooling radiation, leading to a transition from isothermal to adiabatic behavior, terminating fragmentation at the Jeans mass at this density. This can occur at a critical volume density $\rho_{\rm crit}$ (e.g. Glover & Mac Low 2007; Jappsen et al. 2005a; Larson 2005; Low & Lynden-Bell 1976; Masunaga & Inutsuka 2000; Whitworth et al. 1998). Motivated by radiation transfer simulations like Bate 2009c we also investigated the case where the transition occurs at a critical surface density $\Sigma_{\rm crit}$. The

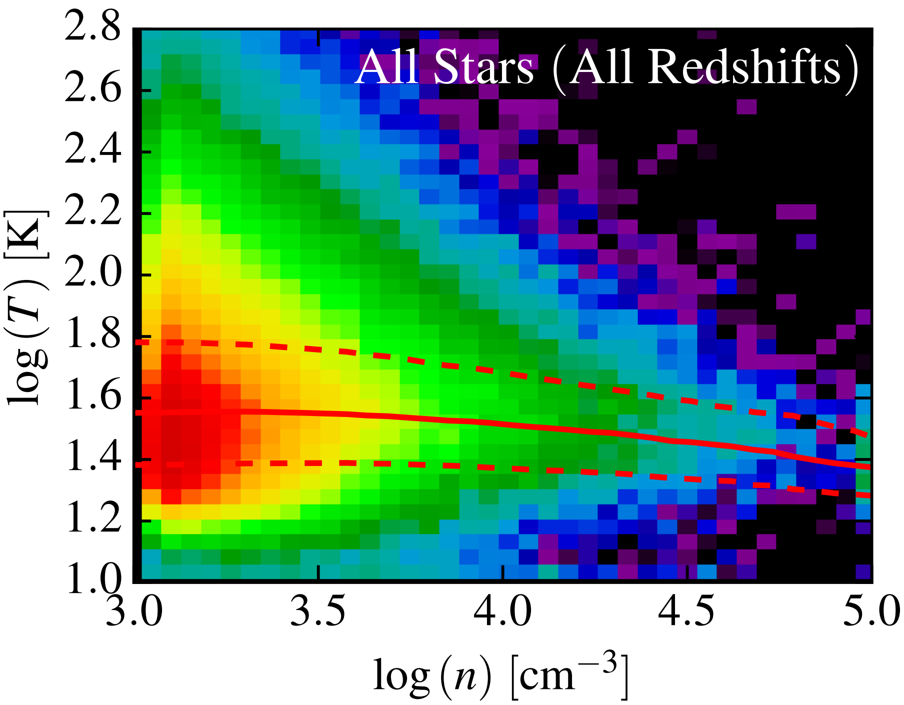

Figure 5.6: Density-temperature diagram (as Fig. 5.5; same galaxy), but for the progenitor clouds (gas elements which formed a stellar sink particle) of *all* stars which reside in the $z = 0$ galaxy (integrated over all cosmic time). Note these are the cloud properties *at the moment the sink formed*, weighted by mass in stars today (colors use ~ 3 dex stretch). As expected, most sinks form a factor of a few above our minimum threshold ($n_{\rm crit} = 1000\,{\rm c}m^{-3}$), though some gas reaches much higher densities. Lines again show the median and inter-quartile range for stars formed at resolved densities $> n$. Accounting for different times and progenitor galaxies, the dispersion in temperatures at a given density is a factor $\sim 3-4$ larger here than for star-forming gas just at $z = 0$.

critical masses in these cases are

$$M_{\rm crit,\rho} \sim \frac{\pi c_s^3}{6G^{3/2}\rho_{\rm crit}^{1/2}}, \quad M_{\rm crit,\Sigma} \sim \frac{c_s^4}{G^2\Sigma_{\rm crit}}, \tag{5.2}$$

where $\rho_{\rm crit}$ and $\Sigma_{\rm crit}$ are the critical densities for the isothermal-adiabatic transition.

- **Turbulent/sonic mass models:** A number of analytical theories derive the CMF and IMF from the properties of the turbulent medium, in which they form (e.g. Hennebelle & Chabrier 2008, 2013a; Hopkins 2012b; Padoan & Nordlund 2002). In these models, both the CMF and IMF peaks are set by the "sonic mass" $M_{\rm sonic}$, namely the turbulent Jeans

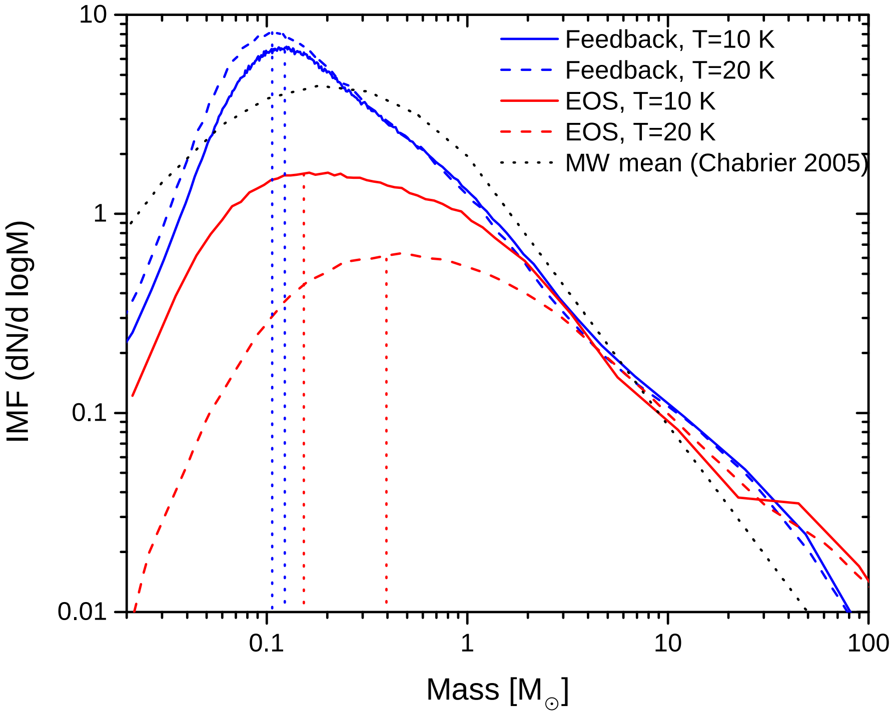

Figure 5.7: Predicted IMF using the framework of Guszejnov & Hopkins (2016), within progenitor clouds with different initial temperatures T_{cloud} = 10 K or 20 K. We compare two IMF models from Table 5.1: (1) accounting for proto-stellar heating, and (2) ignoring heating and treating the gas with a polytropic equation-of-state until some it reaches the opacity limit. We compare the standard fit to the observed IMF from Chabrier (2005). Differences in temperature produce different model shifts, per the scalings in Table 5.1.

or Bonner-Ebert mass at the sonic scale ($R_{\rm sonic}$) below-which the turbulence becomes sub-sonic and therefore fails to generate large fluctuations (which seed fragmentation). The critical mass is

$$M_{{\rm crit},S} = M_{\rm sonic} \sim \frac{2c_s^2 R_{\rm sonic}}{G}, \tag{5.3}$$

where $R_{\rm sonic}$ is defined through the linewidth-size relation

$$\sigma^2_{turb}(\lambda) = c_s^2 \frac{\lambda}{R_{\rm sonic}}. \tag{5.4}$$

In our calculations σ^2_{turb} is estimated from the simulations when a star particle forms by measuring the velocity dispersion (after subtracting the mean shear) between neighboring particles in a sphere of radius λ (taken to be that which encloses the nearest ~ 32 gas neighbours).

- **Protostellar feedback models:** Although there are a number of ways newly-formed stars can regulate star formation, most studies have concluded that at the scale of the IMF peak (early protostellar collapse of $\sim 0.1\,\mathrm{M}_\odot$ clouds) the most important self-regulation mechanism is radiative feedback from protostellar accretion (Bate, 2009c; Guszejnov et al., 2016; Krumholz, 2011). This sets a unique mass and spatial scale within which the protostellar heating has raised the temperature to make the core Jeans-stable, terminating fragmentation. The resulting critical masses are

$$M_{\mathrm{crit},B} \sim 0.5 \left(\frac{\rho}{1.2\times 10^{-19}\,\mathrm{g/cm^3}}\right)^{-1/5} \left(\frac{L_*}{150\,\mathrm{L}_\odot}\right)^{3/10} \mathrm{M}_\odot, \tag{5.5}$$

$$M_{\mathrm{crit},K} \sim 0.15 \left(\frac{P/k_B}{10^6\,\mathrm{K/cm^3}}\right)^{-1/18} \mathrm{M}_\odot \tag{5.6}$$

where L_* is the average luminosity of accreting protostars and P is the pressure. These different formulas come from Bate (2009c) and Krumholz (2011), respectively; the differences are due to the detailed uncertainties treating radiation. However for our purposes they give *nearly identical* results, so we will focus on the model from Krumholz (2011).

5.3 Results and Discussion

Fig. 5.8 shows that there is significant variation in the properties of the progenitor GMC complexes which formed stars that ultimately end up at a specific galacto-centric radius. We stress that this is not the variation of properties in *present-day* star-forming clouds, but includes all variations in time as well: if the galaxy progenitor was gas-rich (gas fraction $\sim 1/2$) at $z \sim 1-2$ for example, then the midplane gravitational pressure ($\sim G\,\Sigma_{gas}^2$) would have been a factor ~ 100 larger than in the galaxy today. Fig. 5.9 shows that this, in turn, produces large IMF variations in all models here except those accounting for protostellar heating. Such variations (> 0.5 dex in $M_{turnover}$) are strongly ruled-out by observations (Bastian et al., 2010). Note that these results are robust to variations in simulation parameters (see Table 5.1).

The variations in the IMF predicted by some of the simple models here (e.g. the Jeans-mass models) have often been substantially underestimated in previous work in the literature. In analytic models of the IMF (see references in Sec. 5.1) or galaxy-scale models which fail to resolve individual "parent clouds", but post-process the entire galaxy (with $>$ kpc-scale resolution) to determine

Model	$M_{\rm crit}$	**Reference**	**Galactic IMF variation ($\sigma_{M_{\rm crit}}$) [dex]**				
			m12i ($56000\,{\rm M}_\odot$) ($1000\,cm^{-3}$)	**m12i** ($7000\,{\rm M}_\odot$) ($1000\,cm^{-3}$)	**m12i+MHD** ($7000\,{\rm M}_\odot$) ($1000\,cm^{-3}$)	**m12f** ($7000\,{\rm M}_\odot$) ($1000\,cm^{-3}$)	**m12m** ($7000\,{\rm M}_\odot$) ($1000\,cm^{-3}$)
Jeans Mass	$\propto T^{3/2}\rho^{-1/2}$	Bate & Bonnell 2005	0.60	0.54	0.61	0.56	0.65
Turbulent/Sonic Mass	$\propto T R_{\rm sonic}$	Hopkins 2012b	0.91	0.96	0.86	0.91	0.84
Opacity-limited, $\rho_{\rm crit}$	$\propto T^{3/2}$	Jappsen et al. 2005a	0.63	0.53	0.58	0.54	0.61
Opacity-limited, $\Sigma_{\rm crit}$	$\propto T^2$	Bate 2009c	0.81	0.70	0.75	0.73	0.81
Protostellar Heating	$\propto (\rho T)^{-1/18}$	Krumholz 2011	0.030	0.026	0.031	0.027	0.031

Table 5.1: Rows: Different IMF models compared in this paper, each with the predicted scaling of the IMF turnover mass $M_{\rm crit}$ with initial parent cloud properties (§ 5.2.2), reference, and the predicted 1σ dispersion in $\log_{10}(M_{\rm crit})$ across the galaxy at present-day (averaging Fig. 5.8 over all galacto-centric radii). We measure $\sigma_{M_{\rm crit}}$ from five simulations: galaxies **m12i**, **m12f**, and **m12m** are three distinct Milky Way-mass ($\sim 10^{12}\,{\rm M}_\odot$) halos which produce similar disky, Milky Way-like galaxies (stellar mass $\sim 0.5-1\times10^{11}\,{\rm M}_\odot$), but have different formation histories (see Fig. 5.2 for visualizations and Hopkins et al. 2017a for details). For each we label the mass resolution (in ${\rm M}_\odot$) and minimum density $n_{\rm crit}$ for creation of stellar sink particles. For **m12i**, we compare two alternative runs: one at lower resolution, and one including magnetic fields (**m**12i+MHD). The predicted IMF variation is remarkably robust across all these simulations.

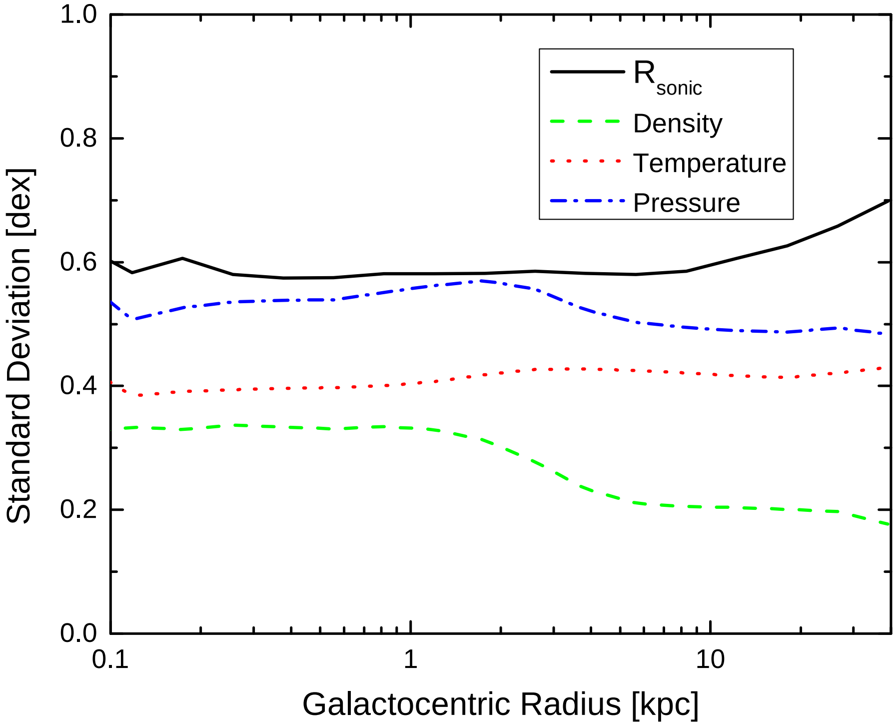

Figure 5.8: Standard deviation in star-forming progenitor cloud properties (measured *at the time of star formation*, as in Fig. 5.6), across the progenitor clouds of all stellar sink particles which reside at a given present-day galactocentric radius (in our fiducial *m12i* run with $56000\,\mathrm{M}_\odot$ resolution; however the dependence on radius is weak and all our simulations in Table 5.1 give similar results). Note that this is *not* the variation of present-day star forming clouds at different radii, as stars at some present-day radius could have formed at wildly different times and positions (for example, at high redshift in a more gas-rich disk with much larger pressures and densities). Thermodynamic and turbulent progenitor-cloud properties vary by $\sim 0.3 - 0.5\,$dex; this implies large IMF variations for any model which has a strong dependence on these quantities.

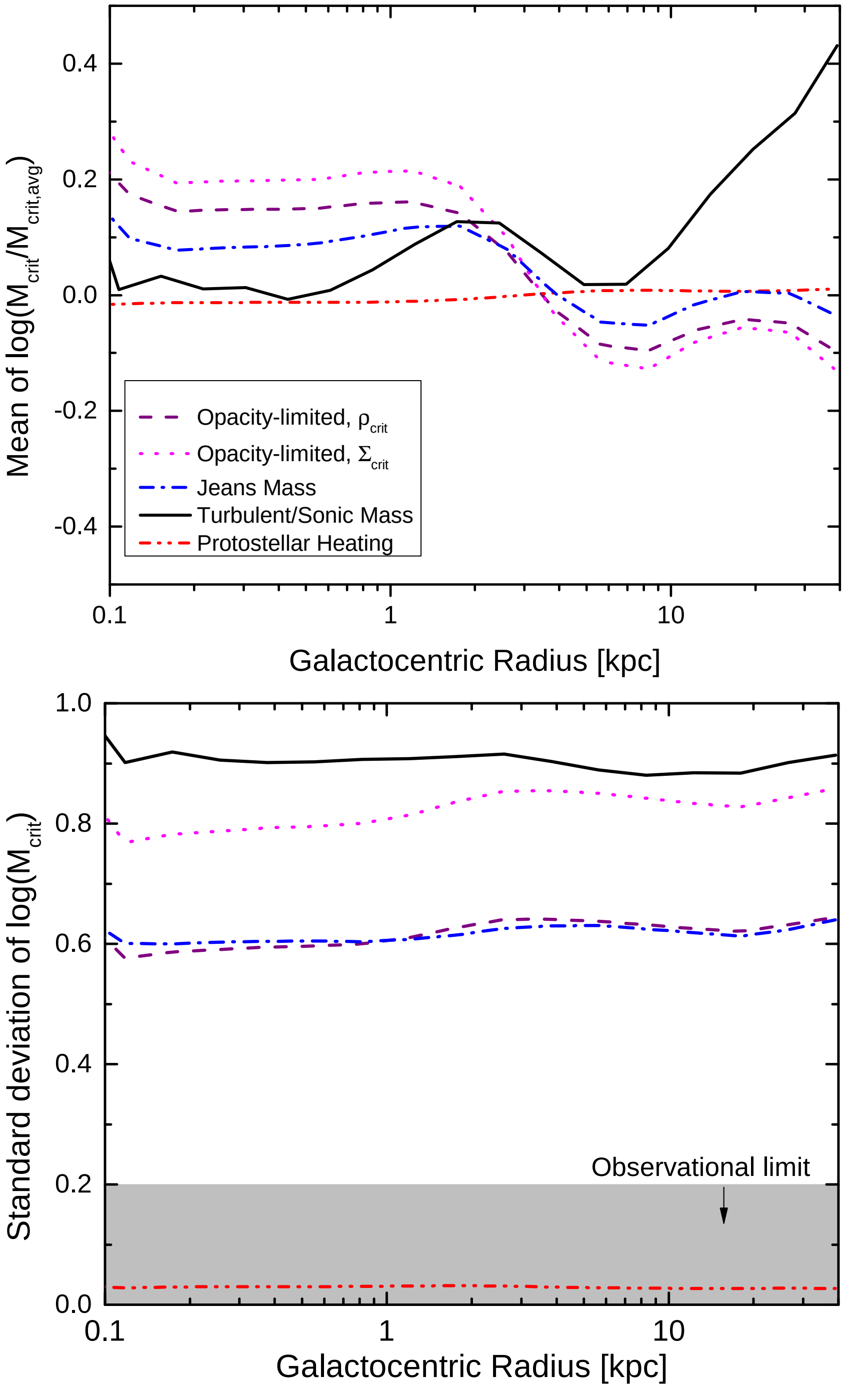

Figure 5.9: Mean (top) and standard deviation (bottom) of the IMF turnover mass $M_{\rm crit}$ normalized its galactic average ($M_{{\rm crit},avg}$) at different galacto-centric radii (in our fiducial *m12i* run with $56000\,\mathrm{M}_{\odot}$ resolution). We compare the IMF models in Table 5.1 and the observationally allowed range of scatter in the IMF across the Milky Way, from Bastian et al. (2010). In these simulations, only models accounting for protostellar heating avoid strongly over-predicting the scatter in MW IMFs. The models are shown here for the same example galaxy in Fig. 5.8, but we obtain very similar results for each of the five simulated galaxies in Table 5.1.

an IMF (Blancato et al., 2016; Hopkins, 2013e; Narayanan & Davé, 2012), it is commonly assumed that all star-forming clouds are uniformly at the same isothermal temperature (e.g. $T = 10\,\mathrm{K}$ at *all* densities), virial parameter, and lie exactly on the same linewidth-size relation. For example, if the gas *at all densities and all cosmic times* had exactly the same temperature, then the variation in the IMF for the opacity-limited EOS models would vanish (all clouds and cores lie on exactly one adiabat). This assumption is not correct, however, as even in the present-day MW (e.g. fixed redshift and galaxy properties) both GMC and clump temperatures (e.g. Bergin & Tafalla, 2007; Mills & Morris, 2013; Nishimura et al., 2015; Ott et al., 2014; Sánchez-Monge et al., 2014)[4] and virial parameters (e.g. Kauffmann et al., 2013; Svoboda et al., 2016) vary substantially. As expected variations are more pronounced in other nearby dwarf or star-forming galaxies (Gorski et al., 2017; Tang et al., 2017) or redshift $z \gtrsim 1-2$ galaxies and starburst systems (see e.g. González-Alfonso et al., 2012; Mangum et al., 2013; Miyamoto et al., 2015; Narayanan & Krumholz, 2014; Ott et al., 2011; Zschaechner et al., 2016), which are better analogues to the progenitors where many of the stars in the present-day Galaxy formed.

It is certainly possible that we (and these observations) have over-estimated the range of temperatures of GMCs in different environments. But the strong temperature sensitivity of the EOS models (e.g. $\propto T^2$) means that the temperature of *all* progenitor clouds, at all redshifts and in all progenitor galaxies, which formed stars in today's MW, would have to lie within a scatter of just $\sim 20\%$ in temperature (smaller than that observed in just solar-neighborhood clouds) in order to avoid exceeding the allowed IMF variation in the MW.

Moreover the linewidth-size relation is observed to vary systematically, both within the MW and galaxy-to-galaxy, with high-redshift galaxies (the progenitors of the MW) differing by more than an order of magnitude (see e.g. Canameras et al., 2017; Swinbank et al., 2011, 2015, and references therein). Even if temperature variations are neglected entirely, in the "Turbulent/Sonic Mass" models the turnover mass is proportional to the *square* of the deviation $((\sigma_{cloud}/\langle\sigma[R]\rangle)^2)$ of each cloud from the linewidth-size relation (Hennebelle & Chabrier, 2008; Hopkins, 2012b), but these deviations are observed to be

---

[4] Note that Nishimura et al. (2015) only focuses on Orion A and B so these results are not necessarily representative of the entire MW. Also, as our stars form primarily around $n_{\mathrm{crit}} = 1000\,cm^{-3}$, the average temperature of the progenitor clouds is higher than the observed GMCs because they have not reached the cooler, higher-density fully-molecular phases (see Figs. 5.5-5.6).

$\sim 0.3 - 0.5$ dex even within the MW at present-time (Bolatto et al., 2008) implying > 0.6 dex scatter. Likewise the density dependence in "Jeans Mass" models predicts > 0.3 dex scatter even if all temperature variations, time variations, and progenitor-galaxy variations are neglected (e.g. if we use only the scatter in cloud densities observed in the solar neighborhood of the MW at the present instant).

Recall, the cloud properties we use to predict the IMF are measured at a density scale of $\sim 1000\,cm^{-3}$ and mass scale $\sim 7000 - 56000\,\mathrm{M}_{\odot}$. Obviously the clouds must continue to evolve and fragment to form actual stars – this is what our cloud-scale IMF models attempt to model. One might wonder, however, whether during this process some of the scatter might be reduced (if, for example, the clouds all converged to the same temperature eventually, owing to some additional physics). In the opacity-limited models, the equation of state (EOS) is specified (generally the cloud cools with $T \propto \rho^{-0.3}$ to some density, becomes approximately isothermal, then becomes adiabatic above the opacity-limit density), so this is already built into the model explicitly. In the "Jeans Mass" or "Turbulent/Sonic Mass" models, we have implicitly assumed an isothermal EOS within each cloud so their temperature was assumed to be constant throughout their evolution and set by the initial conditions. One might, therefore, consider a more complicated version of these models (different from the simple scalings used thus far). Let us assume star formation occurs above some critical density ρ_{crit} and the gas follows a polytropic EOS with index γ. The critical mass (Table 5.1) will then depend on $T_{\mathrm{crit}}(\rho = \rho_{\mathrm{crit}}) = T_{cloud}\,(\rho_{\mathrm{crit}}/\rho_{cloud})^{\gamma-1}$, as $M_{\mathrm{crit}} \propto T_{\mathrm{crit}}^{\alpha}$ where $\alpha = 3/2,\ 1$ for the Jeans and Turbulent/Sonic models, respectively. Some simple algebra then gives us logarithmic variance in M_{crit}, $S_{\log M_{\mathrm{crit}}} = \alpha\,(S_{\log T_{cloud}} + [\gamma - 1]\,S_{\log \rho_{cloud}})$. Putting in the actual values (Fig. 5.8) this gives a dispersion $\sigma_{\log M_{\mathrm{crit}}} \approx 0.6,\ 0.4$ dex for the Jeans and Turbulent/Sonic models (for any $\gamma \sim 0.5 - 1.5$). This reduces the predicted IMF variation, but still leaves it far larger than observed.

Thus we have shown that *some* additional physics on cloud or sub-cloud scales must be accounted for to reconcile the predictions of the "no-feedback" IMF models with the (weak) IMF variations observed in the MW. The "protostellar heating" models represent one physically-motivated class of models that do exactly this. Of course there may be others, but, broadly-speaking, they would need to either (a) strongly reduce the level of dependence of the predicted IMF on cloud properties (as the protostellar heating models do), or (b) strongly reduce the variation in GMC-scale properties predicted across cosmic time in the progenitor galaxies that form the MW. The latter is not impossible but seems to contradict the direct observations cited above, showing large variations in cloud properties in distant galaxies.

5.3.1 Caveats

Of course detailed, complex simulations (like the cosmological FIRE runs we are using) employ a large number of approximations to make problems numerically tractable. Although these simulations have been extensively vetted numerically (for details see Hopkins et al., 2017a) some caveats worth noting include:

- Our analysis uses a somewhat arbitrary $n_{\rm crit} = 1000\,cm^{-3}$ minimum density threshold for star formation, based on numerical considerations. Using a much higher threshold would require much greater mass resolution (or else it would introduce severe numerical artifacts), which is not computationally feasible (these are the highest-resolution cosmological simulations of MW-mass galaxies ever run, at present). However, within the range we can probe, our results do not appear to depend sensitively on the density threshold or other numerical criteria for star formation.[5]

- In the simulations, gas elements are replaced by star particles instantaneously once all star formation criteria and timescales are satisfied, so star formation happens in discrete steps. In the large GMCs where most stars form ($\sim 10^6 - 10^7\,\mathrm{M}_\odot$), this means that the first generation of stars formed can continue to alter the GMC properties while subsequent star formation occurs. However star formation in the smallest GMCs will be artificially "abrupt" (although GMCs with masses this low contribute negligibly to the variation in the IMF).

- Feedback processes from low-mass stars, e.g. proto-stellar outflows, are not explicitly included in the simulations. We only consider the effects of massive stars, which dominate on GMC scales provided there are sufficient stars to sample the IMF.

---

[5] In Orr et al. (2017), we show the results of a number of simulations where we re-run our **m12i** galaxy from $z \approx 0.1 - 0.0$, as in Fig. 5.4, but vary the numerical SF criteria. This includes changing the minimum SF density (from $\sim 10 - 1000\,cm^{-3}$), removing requirements that the gas be molecular and/or self-gravitating, and changing the efficiency per free-fall time with which gas that meets this criteria will turn into stars (from $\sim 1 - 100\%$). We have re-run our analysis, restricted to just those stars formed over the period the simulations were re-run, and find these changes do not significantly influence the predicted IMF variations.

- The turbulent velocity dispersion in the code is calculated from using a kernel interpolation over the the relative velocities between the nearest ~ 32 resolution elements, after subtracting the coherent shear and contraction/expansion terms. This means that for very small GMCs with masses $\lesssim 10$ times the resolution, internal motions are not well-resolved. In this limit the general tendency is to *under*-estimate the turbulent velocity dispersions (see e.g. the detailed turbulence studies in Hopkins 2015). But again, these do not contribute significantly in our predictions.
- The simulations do not explicitly follow non-equilibrium chemistry (e.g. molecular hydrogen formation/destruction), instead relying on pre-tabulated equilibrium cooling rates as a function of density, temperature, metallicity, and the strength of the local radiation field in several bands. It was shown by Hopkins et al. (2012) that these approximations have little to no effect on galactic star formation properties, but they could conceivably alter the scatter in small-scale cloud properties.

5.4 Conclusions

In this paper we explore the application of broad classes of IMF models to high-resolution fully-cosmological galaxy formation simulations. Stars at a some present-day location might have formed at very different times and places, in an environment radically different from today's MW: only by using a cosmological simulation instead of local simulations or observations can we predict the properties of their progenitor star-forming clouds at these times and places, and therefore use these models to predict, for example, the variations in the IMFs of old stellar populations in the present-day galaxy. This also provides an important consistency and validity check for future attempts to incorporate these IMF models into such simulations *dynamically*, as stellar feedback plays a critical role in the simulations and it, obviously, depends on the IMF.

In summary, we find that only models accounting for protostellar heating produce sufficiently weak IMF variations, in these simulations, to be compatible with observations. This discrepancy is not obvious in many previous studies (either analytic or idealized single-cloud simulations) as they artificially assume all clouds (at all locations and cosmic times) have the same temperature and obey the same linewidth-size relation (without scatter or systematic variation), whereas observations find significant variations in molecular gas temperatures and velocity dispersions (both within the MW and in nearby and high-redshift star-forming galaxies, which may more closely resemble the MW progenitors where these stars formed).

The protostellar heating models, on the other hand, actually predict IMF variations significantly below the observational upper limits (see Fig. 5.9). Additional sources of variance are therefore easily accommodated in these models, such as those that should come from a combination of (a) stochastic statistical sampling effects (see Bastian et al. 2010; these may be especially important in small clouds such as Taurus which are not resolved by our simulations, see Kraus et al. 2017), (b) measurement uncertainties, or (c) additional physics not accounted for by the model (e.g. bursty accretion or other physics may modify the radiative efficiency and heating effects of protostars, introducing some IMF variation).

In future work, we will examine whether the protostellar heating models considered in this study should produce observably-large IMF variation under more extreme conditions. Preliminary comparison of single-cloud conditions in Guszejnov et al. (2016) suggests these models can produce as much as factor ~ 2 shifts in the turnover mass under extreme starburst conditions analogous to Arp220, but this needs to be explored in more detail. We will also explore in more detail IMF shape variations, the predicted IMF in different sub-regions of the galaxy (e.g. the galactic nucleus), and the IMF in specific populations (e.g. metal-poor globular clusters versus present-day stellar populations).

Chapter 6

PROTOSTELLAR FEEDBACK IN TURBULENT FRAGMENTATION: CONSEQUENCES FOR STELLAR CLUSTERING AND MULTIPLICITY

Guszejnov D., Hopkins P. F., Krumholz M. R., 2017, MNRAS, 468, 4093

Abstract

Stars are strongly clustered on both large ($\sim$ pc) and small ($\sim$binary) scales, but there are few analytic or even semi-analytic theories for the correlation function and multiplicity of stars. In this paper we present such a theory, based on our recently-developed semi-analytic framework called MISFIT, which models gravito-turbulent fragmentation, including the suppression of fragmentation by protostellar radiation feedback. We compare the results including feedback to a control model in which it is omitted. We show that both classes of models robustly reproduce the stellar correlation function at > 0.01 pc scales, which is well approximated by a power-law that follows generally from scale-free physics (turbulence plus gravity) on large scales. On smaller scales protostellar disk fragmentation becomes dominant over common core fragmentation, leading to a steepening of the correlation function. Multiplicity is more sensitive to feedback: we found that a model with the protostellar heating reproduces the observed multiplicity fractions and mass ratio distributions for both Solar and sub-Solar mass stars (in particular the brown dwarf desert), while a model without feedback fails to do so. The model with feedback also produces an at-formation period distribution consistent with the one inferred from observations. However, it is unable to produce short-range binaries below the length scale of protostellar disks. We suggest that such close binaries are produced primarily by disk fragmentation and further decrease their separation through orbital decay.

6.1 Introduction

Star formation (SF) is complex problem that involves nonlinear physics (turbulence, chemistry, gravity, radiation, etc.) on a vast dynamic range. To achieve a deeper understanding of this process a number of simplified theoretical models have been proposed that try to pinpoint the physical processes responsible for individual qualitative features. The most common test of these models is a comparison to the initial mass function (IMF), but that is just one aspect of star formation. It has been long proposed that the stellar clustering and multiplicity properties carry the imprints of the physical processes of star formation (Kuiper 1935), making them an ideal secondary test for different star formation models.

It is well known that star-forming regions are highly structured, with stellar positions correlated on a wide range of scales Bressert et al. (2010); Gouliermis et al. (2015); Lada & Lada (2003); Portegies Zwart et al. (2010). The stellar correlation function has been measured in a wide range (about 5 orders of magnitude in radius) and is found to be rising monotonically on smaller scales in all star clusters (Hartmann 2002; Hennekemper et al. 2008; Kraus & Hillenbrand 2008; Nakajima et al. 1998; Simon 1997). Despite the overwhelming observational data and statistical analysis (Bate et al., 1998; Cartwright & Whitworth, 2004) there has been little effort to formulate a theoretical understanding of why star formation is clustered. A number of authors have measured the clustering of the stars produced in numerical simulations (e.g., Hansen et al. 2012b; Klessen & Burkert 2000; see the review by Krumholz 2014 for further references) and found reasonable agreement with observations, but the physical origin of the result was not completely clear. Hopkins (2013a) (henceforth referred to as H13) was the first to provide a quantitative explanation in terms of the statistics of turbulence. Using the excursion set formalism H13 showed that the correlation function of "last crossing objects"[1] is remarkably similar to that of observed cores, which itself is similar to the correlation function of stars (Stanke et al. 2006). However, this model has a significant limitation in that it is calculated at a *fixed time*, so the collapse and further fragmentation of cores is not taken into account; it cannot therefore predict the correlation function of stars, nor their multiplicity statistics.

There is similarly an abundance of observational data about the multiplicity properties of stars (e.g. Raghavan et al. 2010 for Solar-type stars, Burgasser et al. 2007 for brown dwarfs; see Duchêne & Kraus 2013 for a more detailed review). It is generally understood that most multiple star systems either form during the star formation phase through common core fragmentation and protostellar disk fragmentation (Tohline 2002) or during the cluster dissolution phase (Kouwenhoven et al., 2010; Parker & Meyer, 2014). Most theoretical work is focused on modeling these processes in detailed numerical studies. Hydrodynamical simulations (e.g. Bate 2009b, 2012a; Krumholz et al.

---

[1] Smallest self-gravitating structures in a fully developed turbulent medium at a fixed time. They are considered to be the analogues of protostellar cores.

2012; Offner et al. 2010) have shown good agreement with observed multiplicity statistics and found that radiation feedback is essential. However, these simulations necessarily have limited dynamical range and statistics, of key importance for high-mass stars and long range binaries, and pinpointing the key physics in them is quite challenging.

There has also been significant effort to infer *at-formation* multiplicity properties from observations. Both observations (Duchêne 1999; Kraus et al. 2008, 2011) and simulations have shown that stars are born in complex, multiple systems that are broken up by dynamical effects (e.g., ejection of stars), causing multiplicity to drop (Goodwin et al. 2007; Kaczmarek et al. 2011) and the period distribution (commonly referred to as the *binary distribution function*) to shift to shorter periods (Kroupa 1995; Marks et al. 2011). This can be understood as the result of long range binaries being preferentially broken up by ejection events, which also increase the binding between leftover stars ("hardening"). This means that to reproduce the present day multiplicity and binary distribution functions the at-formation multiplicity should be of order unity for massive stars, and their period distribution should be flat. These findings, however, have recently been called into question. Parker (2014) showed that the densities of star forming regions are constant or increasing with time, while Parker & Meyer (2014) found that an initial distribution of stars with unit multiplicity and an excess of wide binaries will not evolve through N-body processes into a distribution consistent with that observed in field stars.

The aim of this paper is to expand upon the work of H13 by investigating the features imprinted by isothermal fragmentation and protostellar heating through common core fragmentation in the stellar correlation and multiplicities. This is accomplished by utilizing the MISFIT (Minimalistic Star Formation Including Turbulence) semi-analytical framework described by Guszejnov et al. (2016) (hereafter referred to as GKH16), which combines the fragmentation formalism of Guszejnov & Hopkins (2015a) and the protostellar heating model of Krumholz (2011) (henceforth referred to as GH15 and K11) to follow the evolution and collapse of a statistical ensemble of giant molecular clouds (GMCs) down to the protostellar size scale.

The remainder of this paper is organized as follows. First, in Sec. 6.2 we briefly outline the MISFIT framework that we use. In Sec. 6.3.1 we show that the stellar correlation function is insensitive to both initial conditions and underlying physics and that the predicted 2D correlation function agrees well with observations. In Sec. 6.3.2 we show that for low mass stars, turbulent fragmentation mediated by radiation feedback can roughly reproduce the observed multiplicities and mass ratio distribution, and provides qualitative agreement with the expected binary distribution function. However, we also show that protostellar disk fragmentation is necessary to explain the short period tail of the distribution. Finally, in Sec. 6.4 we summarize our findings and conclude.

6.2 Model and Methodology

6.2.1 Semi-Analytic Framework

In this study we use an improved version of the MISFIT semi-analytical framework introduced in GH15 and GKH16 (see Sec. 6.A for a detailed description of all changes from the previously published version) which allows us to simulate the evolution and fragmentation of GMC sized clouds at a modest computational cost (compared to full radiation-hydro simulations). This not only allows the rapid exploration of different initial conditions and underlying physics but also enables a statistical analysis as we are able to simulate an ensemble of clouds.

This, of course, comes at the cost of some simple approximations. The main assumption of MISFIT is that density fluctuations in collapsing GMCs are created by turbulence and thus obey "random walk" statistics (see e.g. Hopkins 2013d). As the cloud collapses it pumps energy into turbulence (so that virial equilibrium is maintained) as motivated by Robertson & Goldreich (2012b) and Murray et al. (2015). Unlike most analytical models MISFIT preserves spatial and temporal information and can be easily expanded with additional physics (e.g. equation of state, angular momentum etc.). We show in Sec. 6.B that, despite these strong assumptions, our results are roughly in agreement with the detailed radiation hydrodynamical simulation of Bate (2012a).

The simulation starts from a GMC with fully developed turbulence and follows its collapse. The density field of the cloud is resolved on a grid with N^3 points and is evolved in Fourier space following a Fokker-Planck equation (see Hopkins 2013c and GH15). For the bulk of this paper we use $N = 32$, and in Sec. 6.C we show that this is sufficient to achieve convergence. Every time a new self-gravitating substructure appears (i.e., the cloud fragments) the code is run recursively for each substructure. When the cloud size reaches the pre-defined relative size scale $R_{\mathrm{m}in}/R_0$ (the *relative termination scale*) the simulation stops. This termination scale represents the length scale where the initial assumptions break down and the self-similar fragmentation cascade is terminated.

The primary effect that breaks self-similarity and imposes a scale in our calculations is angular momentum, which leads to the formation of a disk once the object has contracted a certain amount. Disk formation is the natural termination scale. In our model the source of angular momentum is random turbulent motion, which in the supersonic limit means that the distribution of the rotational kinetic energy fraction $\beta = E_{rot}/E_{pot}$ is strongly peaked around a few percent (Burkert & Bodenheimer, 2000), consistent with the observed distribution of protostellar core rotation rates (Goodman et al., 1993). If one translates this into an angular momentum and assumes that the specific angular momentum of fluid elements is conserved during collapse, the characteristic radius of disk formation is $R_{min} \approx \beta R_0$. In this paper we adopt $R_{min}/R_0 = 0.01$ as our fiducial value for most calculations, and we explore the sensitivity of the results to our choice in Sec. 6.C.

The initial conditions of the parent clouds are defined by their mass M_{GMC}, the sonic length $R_{\rm sonic}$ (the scale at which the turbulent velocity dispersion is equal to the sound speed), the sonic mass $M_{\rm sonic}$ (the minimum self-gravitating mass at the sonic scale), and the termination scale R_{min}. All other parameters (e.g. temperature, Mach number) can be derived from these. Moreover, the total mass only affects our results by changing the outer scale of the turbulent cascade, a result we demonstrate in Sec. 6.C, so we shall not discuss it further here. For details about initial conditions and the detailed algorithm see GH15 in which a detailed step-by-step guide to the model is provided in Appendix A.

The final output of the simulation is a list of protostars and their initial properties (e.g. mass, velocity, position). As we are not accounting for later dynamical processes, our results only apply *at the time of formation*. The leftover unbound material is assumed to escape.

6.2.2 Implementation of Stellar Feedback

In this paper we investigate the clustering properties of two classes of models: the case of pure isothermal fragmentation and a model with feedback from protostellar heating based on K11. Isothermal turbulence is scale-free (Krumholz 2014; McKee et al. 2010), so we expect no absolute scales in any results (although scales from initial conditions may appear), while the heated model imprints a mass scale that is insensitive to initial conditions (hence there is a peak in the IMF, as shown in GKH16). For comparison we also include some runs where in addition to protostellar heating the gas has a “stiffening” equation of state (EOS). This means that the gas reacts to compression as a sub-isothermal medium at very large scales, isothermally at intermediate scales and transitions to an adiabatic behavior after reaching a threshold volume density where it becomes opaque to its own cooling radiation. We model this effect using a physically motivated EOS based on Masunaga & Inutsuka (2000) and Glover & Mac Low (2007). In this case the effective polytropic index depends on the local volume density as

$$\gamma_{\mathrm{phys}}(\rho) = \begin{cases} 0.8 & \rho < \rho_{\mathrm{crit,1}} \\ 1.0 & \rho_{\mathrm{crit,1}} < \rho < \rho_{\mathrm{crit,2}} \\ 1.4 & \rho > \rho_{\mathrm{crit,2}} \end{cases}, \tag{6.1}$$

where we set $\rho_{\mathrm{crit,1}} = 5000\,\mathrm{M_\odot/pc^{-3}}$ and $\rho_{\mathrm{crit,2}} = 5\times10^8\,\mathrm{M_\odot/pc^{-3}}$ corresponding to $n_{\mathrm{H_2,crit,1}} \approx 10^5\,\mathrm{cm^{-3}}$ and $n_{\mathrm{H_2,crit,2}} \approx 10^{10}\,\mathrm{cm^{-3}}$. See GKH16 for more details.

Our treatment of protostellar radiative feedback is a fairly crude approach motivated by K11, and supported numerically by Krumholz et al. (2016). We assume that the center of self-gravitating clouds collapses first, forming a protostellar seed, then the rest of the cloud accretes onto it. The energy of the matter accreted by this seed is radiated within the optically thick core. The temperature of the material depends on the accretion rate onto the protostar (and thus the mass and dynamical time of the gas around it), and on the energy yield per unit mass from accretion, which we denote Ψ. The value of Ψ is set by the protostellar mass-radius relation, and K11 shows that it is determined primarily by the effects of deuterium burning, which regulates the central temperatures of protostars. Because deuterium burning begins when protostars are only a few $\times 10^{-2}\,\mathrm{M_\odot}$, and, for low mass protostars continues for ~ 10 Myr, it is the dominant factor in setting Ψ during the bulk of a molecular cloud's star-forming history. Comparing with detailed protostellar evolution calculations, K11 finds that $\Psi \approx 2.5\times10^{14}$ erg g^{-1} to better than half a dex accuracy for all protostellar masses in the range $0.05 - 1\,\mathrm{M_\odot}$, and to better than a dex accuracy from $0.01 - 0.05\,\mathrm{M_\odot}$. We therefore adopt this value of Ψ throughout the remainder of this paper. If we assume a spherically symmetric system then, following K11, the gas at R distance from an accreting protostar is heated up to a temperature of

$$T_{heat}^4 \approx \frac{\Psi\sqrt{G}}{4\pi\sigma_{SB}} M^{3/2} R^{-7/2}, \tag{6.2}$$

where M is the mass enclosed in radius R, while G, $\sigma_{\mathrm{S}B}$ are the gravitational and Stefan-Boltzmann constant respectively. Crudely, this scaling reflects energy conservation as $L = 4\pi R^2 \sigma_{\mathrm{S}B} T_{\mathrm{h}eat}^4$ for the opaque cloud (see K11 for more details). Combined, internal heating and the physical processes captured by the EOS of the model set the temperature as

$$T^4 = T_{\mathrm{E}OS}^4 + T_{\mathrm{h}eat}^4. \tag{6.3}$$

Note that in the feedback only case we use an isothermal EOS, which means that $T_{\mathrm{E}OS} = T_0$ where T_0 is the initial temperature of the cloud.

It is important to note that protostellar feedback is not scale-free. By using Eq. 6.2 and assuming virial equilibrium we can find the length scale $\lambda_{\mathrm{h}eat}$ around a protostar below which heating becomes important ($T_{\mathrm{h}eat} \geq T_0$):

$$\lambda_{\mathrm{h}eat} = \left(\frac{\Psi\sqrt{G}}{4\pi\sigma_{SB}}\right)^{1/2} \left(\frac{k_B}{G\mu m_{\mathrm{H}}}\right)^{3/4} T_0^{-5/4} \approx 0.02\,\mathrm{pc} \left(\frac{T_0}{10\,\mathrm{K}}\right)^{5/4}, \tag{6.4}$$

where μ is the mean molecular weight measured in units of m_{H} and k_B is the Boltzmann constant. For our numerical calculations we adopt $\mu = 2.3$, appropriate for fully molecular H_2 with 1 He per 10 H nuclei. We can similarly find the characteristic mass scale

$$M_{\mathrm{h}eat} \approx 0.5\,\mathrm{M}_{\odot} \left(\frac{T_0}{10\,\mathrm{K}}\right)^{-1/4} \tag{6.5}$$

that sets the peak of the IMF (see K11 for a more detailed calculation that leads to $M_{\mathrm{h}eat} \propto T_0^{-1/18}$).

To easily identify the results for different models and parameters we use the labels shown in Table 6.1. The *STD* label refers to initial conditions similar to Milky Way GMCs, while *ULIRG* runs have the very high temperature and strong turbulence characteristic to the clouds of Ultra Luminous Infrared Galaxies (ULIRGs). There are also a number of runs where the physical parameters are not varied but the numerical ones are, so that we can identify numerical artifacts in our results.

6.2.3 Clustering and Multiplicity Statistics

For each simulation we have as output a list of stellar masses and positions. From these, we compute several statistical quantities describing the stellar

Label	**Input Parameters**					**Derived Parameters**			**Thermodynamics**
	$\mathbf{M}_{GMC}$ [$\mathrm{M}_\odot$]	$\mathbf{R}_{min}/R_0$	**N**	$\mathbf{M}_{\mathrm{sonic}}$ [$\mathrm{M}_\odot$]	$\mathbf{R}_{\mathrm{sonic}}$ [pc]	$\mathbf{T}_0$ **[K]**	$\mathbf{R}_0$ [pc]	$\mathcal{M}_0$	
Isohermal - MW	10^4	10^{-2}	32	1.6	0.1	10	11.1	10.5	Isothermal
Isothermal_SmallR	10^4	10^{-3}	32	1.6	0.1	10	11.1	10.5	Isothermal
Isohermal - ULIRG	10^4	10^{-2}	32	0.31	0.0026	75	0.66	13.1	Isothermal
Heating - MW	10^4	10^{-2}	32	1.6	0.1	10	11.1	10.5	Protostellar Heating
Heating - ULIRG	10^4	10^{-2}	32	0.31	0.0026	75	0.66	13.1	Protostellar Heating
Heating_N16	10^4	10^{-2}	16	1.6	0.1	10	11.1	10.5	Protostellar Heating
Heating_N64	10^4	10^{-2}	64	1.6	0.1	10	11.1	10.5	Protostellar Heating
Heating_M1E3	10^3	10^{-2}	32	1.6	0.1	10	3.5	5.2	Protostellar Heating
Heating_M1E5	10^5	10^{-2}	32	1.6	0.1	10	35.4	16	Protostellar Heating
Heating_SmallRmin	10^4	10^{-3}	32	1.6	0.1	10	11.1	10.5	Protostellar Heating
Heating_LargeRmin	10^4	10^{-1}	32	1.6	0.1	10	11.1	10.5	Protostellar Heating
Heating+EOS - MW	10^4	10^{-2}	32	1.6	0.1	10	11.1	10.5	Heating+EOS
Heating+EOS - ULIRG	10^4	10^{-2}	32	0.31	0.0026	75	0.66	13.1	Heating+EOS

Table 6.1: Initial conditions of the different models presented in this paper. The actual input parameters of our models are the GMC mass M_{GMC}, sonic mass M_{sonic} and length R_{sonic}, from which more physical parameters like initial temperature (T_0), radius (R) and Mach number ($\mathcal{M}_0$) at the cloud scale ($R = R_{GMC}$) can be derived. The resolution of each "refinement level" of our semi-analytic calculation is set by N^3, but each structure is continuously followed and sub-refined. This cascade is terminated when a cloud reaches $R_{\mathrm{m}in}/R_0$ relative size (the cascade "termination scale"), without fragmentation. All calculations were performed for a statistical ensemble $(20 - 200)$ of GMCs.

distribution. Our first quantity of interest is the correlation function. In this paper we adopt the usual definition of the 3D correlation function $\xi(r)$,

$$\begin{aligned} P(r, dr) &= \frac{\langle N(r, \mathrm{d}r)\rangle}{\langle n\rangle \, \mathrm{d}V} \\ 1+\xi(r) &= \lim_{\mathrm{d}r\to 0} P(r, dr), \end{aligned} \tag{6.6}$$

where $N(r, \mathrm{d}r)$ is the number of objects whose distance is $\in [r, r+\mathrm{d}r]$, n is the density of objects, $\mathrm{d}V = 4\pi r^2 \mathrm{d}r$ and $\langle ...\rangle$ denotes ensemble averaging.

We can similarly define the 2D correlation function $\xi_{2D}(r)$, which is identical to ξ except that one computes the distance only in 2 of the 3 orthogonal directions. Unlike ξ, the stellar $\xi_{2D}(r)$ is measurable and it is easy to show that $\xi_{2D}(r) \propto \Sigma_*(r)$, where $\Sigma_*(r)$ is the mean surface density of stars measured in an annulus at r distance from other stars. For the purpose of generating quantities that can be readily compared to observations, we must also account for sensitivity limits, which make it difficult to detect low mass objects. Since studies of stellar correlation have been performed with a wide range of sensitivities, we simply choose a roughly representative limiting mass $M_{\mathrm{m}in} = 0.5\,\mathrm{M}_\odot$, and compute our correlation function using only stars more massive than this limit.

Our second characteristic of interest is the multiplicity properties of the stars – both the multiplicity fractions and the distribution of periods and mass ratios. Since our calculations involve no dynamical evolution after the protostars are formed, deriving these statistics is not trivial, as the newly formed stars form a fractal-like structure where each star is bound to a number of other stars. Such a configuration is expected for young star clusters based on simulations, and is completely consistent with the observed distribution of newly-formed stars (e.g., Bate, 2009a; Kruijssen, 2009; Krumholz et al., 2012). However, it makes identification of distinct, bound systems difficult, and leads to structures which are very unlikely to survive for even a single cluster crossing time (e.g. non-hierarchical quadruple systems orbiting each other). Thus it is important that we try to correct for this behavior. In this paper we use the hierarchical algorithm introduced by Bate (2009a), which has the following steps:

1. Calculate the binding energy between all pairs of stars.
2. Find the most bound pair and replace it with a single point mass with the same total mass and momentum, located at the center of mass of the

removed pair.

3. Recursively repeat steps 1 and 2 until no more bound stars are left, with the exception that we do not combine pairs of objects if the resulting bound aggregate would consist of more than 4 individual stars. If such an aggregate is the most bound pair at any point, proceed to the next most bound pair, terminating if no other bound pair exists. Also, in order to get stable, hierarchical multiples we require that the period of a newly assigned star is at least ten times higher than that of the original aggregate.

This algorithm provides a list of single, binary, triple and quadruple star systems with which we can calculate the *multiplicity fraction* f, defined as

$$f(M) = \frac{B+T+Q}{S+B+T+Q}, \tag{6.7}$$

where S, B, T, Q are the number of single, binary, triple, quadruple systems within which the most massive star (*primary star*) has mass M. This definition has the advantage that it can be observed fairly robustly (Bate 2009a; Hubber & Whitworth 2005), as this does not differentiate between the classes of multiple star systems, so f does not change if a new companion star is discovered in a binary system. Note that to account for the decreased sensitivity of observations to very low mass stars we neglect companions below $0.01\,\mathrm{M}_{\odot}$.

6.3 Results

6.3.1 The Stellar Correlation Function

Figure 6.1 shows the predicted stellar correlation function for a selection of our models, computed using an ensemble average of the $\sim 20-200$ GMCs we have run for each case. The shape is close to a power-law, $\xi(r) \propto r^{-\gamma}$ with $\gamma \simeq 2$, with a cut-off at the size scale of the parent GMC. These properties are remarkably robust to changes in initial conditions and even to changes in the underlying small scale physics.

Qualitatively, the isothermal pure-power-law behavior can be understood with a simple toy model: small objects form after significant contraction and a number of fragmentation events for which the physics is self-similar in the isothermal case. So imagine that a cloud contracts by a factor of ϵ, and then fragments into two equal-mass fragments. Then each of these two fragments contracts and produces two more fragments, and so on. This prescription is

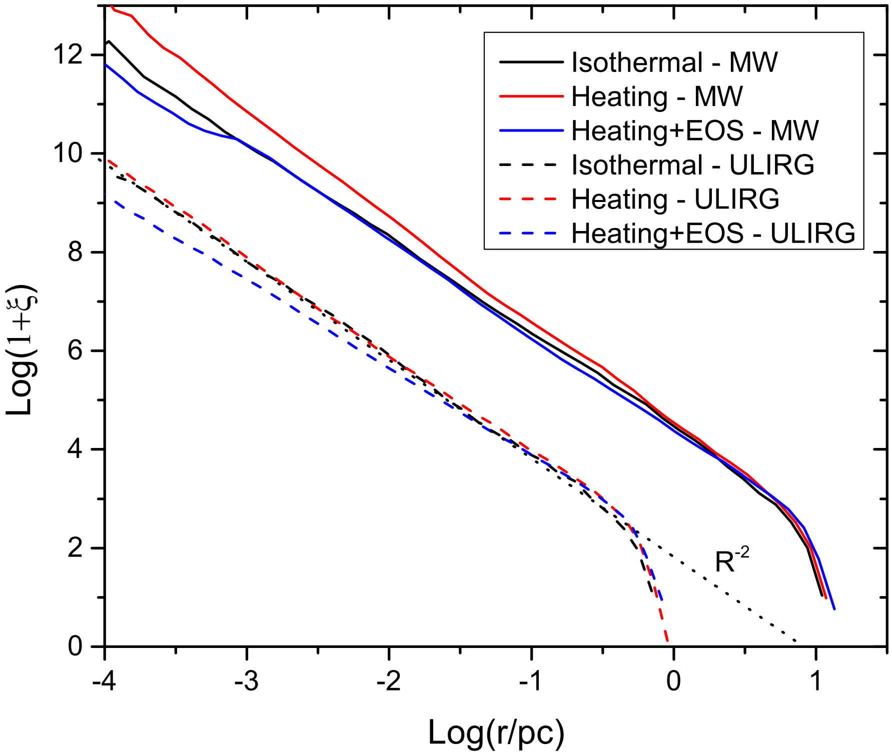

Figure 6.1: Stellar correlation function for star formation models with isothermal physics (*Isothermal*), protostellar heating (*Heating*) and protostellar heating with an artificial EOS (*Heating+EOS*) for two sets of initial conditions: the MW-like *MW* and the more extreme *ULIRG*. It is apparent that the initial conditions and underlying physics have limited effect on the qualitative behavior which is close to a power law (the sub-isothermal regime of the EOS models cause a slight difference in the slope). The different large scale cut-offs are introduced by the different initial cloud sizes, and the different normalization simply results from the different linewidth-size relation between the Milky Way and ULIRG cases.

similar to a well-studied fractal, the Cantor Set (Cantor Dust more specifically). For this, the correlation function is a power-law with slope $f(\epsilon) \sim 2$ for $\epsilon \sim 1/2$ (see Sec. 6.D).

Figure 6.2 compares our predictions to the observed surface density of stars (proportional to the 2D correlation function). In examining this plot, note that the absolute values of the stellar surface densities are not meaningful, since these are just dictated by a our choice of sonic length, and thus can be tuned freely by considering slightly different physical scalings, exactly as one might expect when considering a range of star-forming regions of widely varying density, mass, and velocity dispersion. Instead, the meaningful comparison is the shapes of the functions. In this regard, we see that the simulated correlation functions have a slope quite similar to the observations at scales larger than $\sim 10^{-2}\,\mathrm{pc}$. Below this scale our models cannot reproduce the significant steepening of the correlation function. We show below that this directly manifests in the distribution of short period binaries where the simulation fall short of observations at the same scale. This is the length scale of the largest protostellar disks, which suggests that disk physics (which are neglected in these models) is responsible for the steepening. However, we must stress that dynamical relaxation does affect the observed, finite age systems and is probably responsible for outlier systems like Trapezium and Upper Sco. Both of these systems are *dynamically* older, in the sense that they have existed for more crossing times, than the other systems shown, which supports this conjecture. One should be careful not to draw the false conclusion that this model fully explains the observed stellar spatial distribution simply because it reproduces the correlation function. It has been shown that very different geometries (e.g., fractal vs spherical) can lead to similar correlation function slopes (Gouliermis et al., 2014). Nevertheless we can say that this model is at least consistent with the observed stellar correlation function in the large scale, fractal-like regime.

6.3.2 Multiplicity

After grouping stars into bound systems following the procedure described in Section 6.2.3, we assign each star one of the following labels:

1. *Single*: The star is not bound to any other stars.
2. *Multiple*: The star is the most massive (primary) star of a multiple star system.

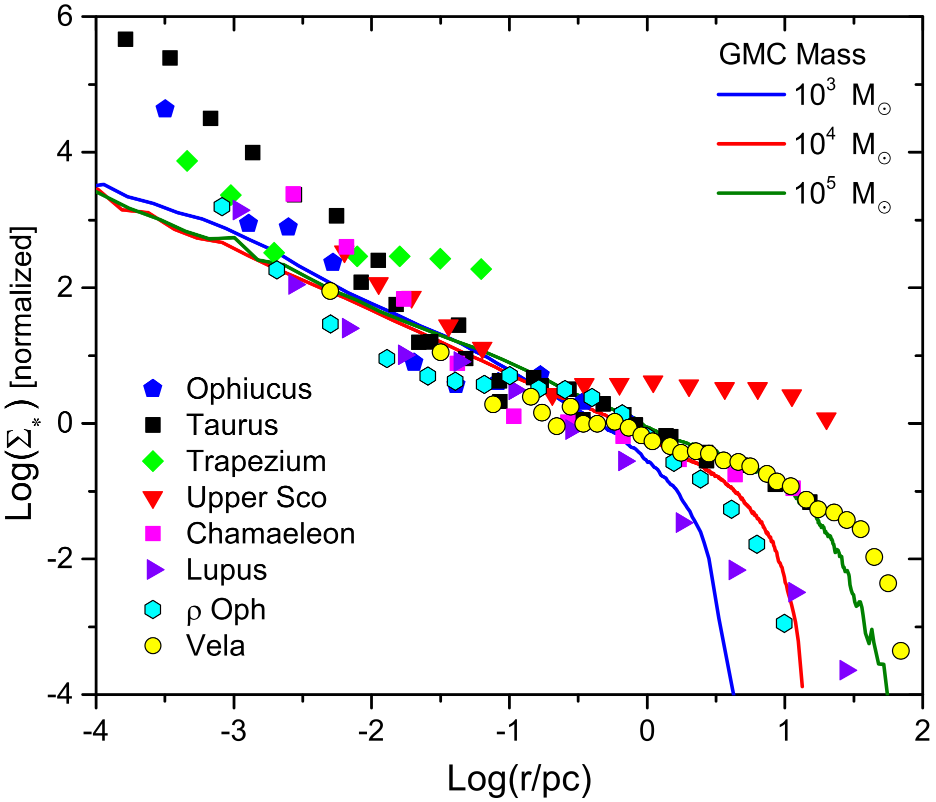

Figure 6.2: Observed surface density of neighboring stars (Σ_*, which is proportional to the projected correlation function ξ_{2D}) for Chamaeleon, Ophiucus, ρ Oph, Taurus, Trapezium, Upper Sco, Lupus and Vela (using data from Hartmann 2002; Hennekemper et al. 2008; Kraus & Hillenbrand 2008; Nakajima et al. 1998; Simon 1997) compared to predicted Σ_* functions for our models including protostellar heating (solid lines, *Heating_M1E3*, *Heating-MW*, *Heating_M1E5*). The absolute values of the observation depend on a number of external factors so they are normalized to roughly match simulations in the 0.1-1 pc range.

3. *Non-primary*: The star is part of a multiple star system, but it is not the primary star.

Not all of the companion stars that emerge from our analysis would be detectable by current techniques. In particular, brown dwarf companions to main sequence stars are quite hard to detect. Therefore we must correct for completeness before comparing to observations. As a guide to the current observational capabilities, we follow the summary given in Table 8 of De Rosa et al. (2014). Based on this summary, we apply the following cuts to our data:

1. For primaries with mass $M > 0.08\ M_{\odot}$, we discard any companions with masses below $0.08\ M_{\odot}$
2. For primaries with mass $M < 0.08\ M_{\odot}$, we discard companions for which the secondary to primary mass ratio is < 0.2.

While these cuts are only an approximate representation to the diversity of observational survey selection functions in the literature, they provide a reasonable approximation to the capabilities of the current state of the art.

Fig. 6.3 shows the fraction of stars in each of the three classes as a function of stellar mass before and after applying the observational bias. Since the isothermal model has no inherent physical scale, in an ideal case we would not expect any mass dependence. However, the finite initial mass $M_{\mathrm{G}MC}$ and the cut-off imposed by observational selection affect the results. The former leads to finite size effects at larger masses. Specifically, since there is a finite total mass, there must be a single most massive star, and for obvious reasons it cannot be non-primary. Similarly, other stars that are near the most massive are also biased against being non-primary. This effect is responsible for the decline in the non-primary curve at high masses. At the other end of the mass spectrum, the fact that brown dwarf companions to hydrogen-burning primaries are difficult to detect explains the sharp decline in the non-primary fraction and sharp rise in the multiple fraction for the lowest mass bin. The sharp change in behaviour above and below $0.1\,\mathrm{M}_{\odot}$ has a simple explanation: for hydrogen-burning stars, multiplicity surveys are primarily conducted in the field, while for brown dwarfs they are mainly conducted in young clusters. Since brown dwarfs are easier to detect in young clusters than in the field, surveys of brown dwarf primaries are much more complete in finding brown dwarf companions than surveys of hydrogen-burning primaries.

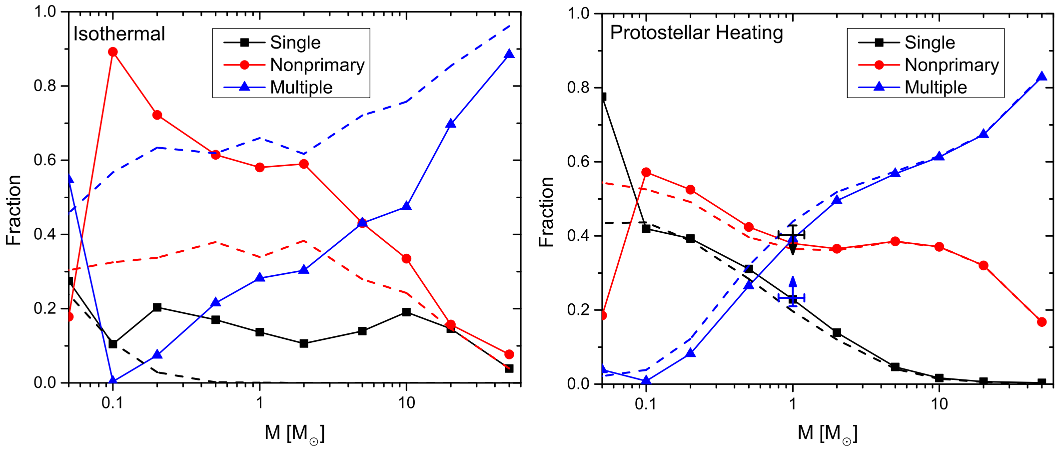

Figure 6.3: Fraction of stars in bound systems as a function of mass in our models of isothermal fragmentation (left; *Isothermal - MW*) and including protostellar heating (right; *Heating - MW*). We assign each star one of the *single*, *multiple* and *nonprimary* labels. The dashed lines show the true distribution predicted by the model, while the solid lines show the results that would be observed given the completeness limits of current surveys. The brackets show the results of Moe & Di Stefano (2016) based on their analysis of the Raghavan et al. (2010) observations. The sudden change around $0.1\,\mathrm{M}_\odot$ is due to the different observational bias for very low mass stars; see the main text for details.

The case including stellar radiation feedback looks qualitatively similar to the isothermal one. In both cases we recover the simple rule that more massive stars tend to be the primary stars of systems while smaller stars tend to be their companions. However, most of the stars in the isothermal model were born in systems of multiple stars, while there is a significant number of single stars in the radiative heating case. The transition from where it becomes more common for stars to be the primaries of multiple systems than to be single is $\sim 1\ M_\odot$, which is a result of the peak in the stellar mass function imposed by heating, which suppresses the formation of stars below the IMF peak at $\sim 0.3\,\mathrm{M}_\odot$. Smaller stars are unlikely to be primaries mainly because there are increasingly few lower mass stars available to be their companions.

We can also compare the results of our models to observations. In Fig. 6.3 we plot in the right panel the results of Moe & Di Stefano (2016), based on analysis of the observations of Raghavan et al. (2010). Compared to these observations, our model slightly overpredicts the multiplicity of solar type stars and underpredicts the fraction that are single.

We compare the stellar multiplicity as a function of primary mass with observations in Figure 6.4. We find that the observed results for the heated and isothermal cases are similar, and both qualitatively reproduce the observational result that the multiplicity fraction is near unity for primaries substantially above 1 $\mathrm{M}_\odot$, dropping to tens of percent for $\sim 0.3\,\mathrm{M}_\odot$ or smaller primaries. However, the apparent similarity between the observed distributions for the isothermal and heated cases is primarily an illusion due to observational completeness effects. In the isothermal case, essentially *every* $\sim 1\,\mathrm{M}_\odot$ primary has an undetected brown dwarf companion, and thus the true multiplicity fraction for primaries of this mass is close to unity. It is only our inability to detect these brown dwarfs that makes the predicted distribution in the isothermal case at all compatible with the observations.

It is also worth investigating how these results would be affected by protostellar disk fragmentation. To do so, we construct a toy model for protostellar disk fragmentation that can be used to post-process our simulation results, based on the works of Kratter et al. (2010) and Offner et al. (2010). They define the thermal parameter of the disk as $\xi = \dot{M}_{\mathrm{in}}G/c_{s,d}^3$, where $\dot{M}_{in}$ is the infall accretion rate onto the disk and $c_{s,d}$ is the sound speed of the disk. Both find that ξ is the main parameter in determining whether a protostellar disk fragments or not. Physically, ξ is just the ratio of the accretion rate $\dot{M}_{\mathrm{in}}$ into the disk to the maximum rate at which a gravitationally stable disk with dimensionless viscosity $\alpha \lesssim 1$ can deliver mass to the central star, which is $\sim c_{s,d}^3/G$.

Using our protostellar heating prescription we can express $c_{s,d}^2 \propto T_d \approx T_{\mathrm{heat}}\,(R_d/R_{\mathrm{core}})^{-1/2}$ where we have used that $T^4 \propto R^{-2}$ in an opaque medium. As noted above, the outer edge of the disk should be found at a radius $R_d \approx \beta R_{\mathrm{core}}$, where β is the rotational kinetic energy divided by the binding energy. Using Eq. 6.2 to evaluate T_d at this radius R_d yields

$$\xi \sim \left(\frac{G^{7/8}\mu m_{\mathrm{H}}(4\pi\sigma_{\mathrm{SB}})^{1/4}}{\Psi^{1/4}k_b}\right)^{3/2}\beta^{3/4}R_{core}^{-3/16}M^{15/16}, \tag{6.8}$$

where we used $c_s^2 = k_B T/\mu m_{\mathrm{H}}$ with μm_{H} as the molecular weight of the gas. ξ has a weak dependence on the radius so we can safely use the $R \sim 10^{-4}\,\mathrm{pc}$ protostellar disk size scale. This leads to $\xi \approx 0.65\,(M/\mathrm{M}_\odot)^{15/16}$. Based on Fig. 2 of Kratter et al. (2010) fragmentation is very likely if $\xi > 1$, which corresponds to collapsing final fragment masses $> 1.5\,\mathrm{M}_\odot$ in our model. Thus, in this crude approximation, the only effect protostellar disk fragmentation

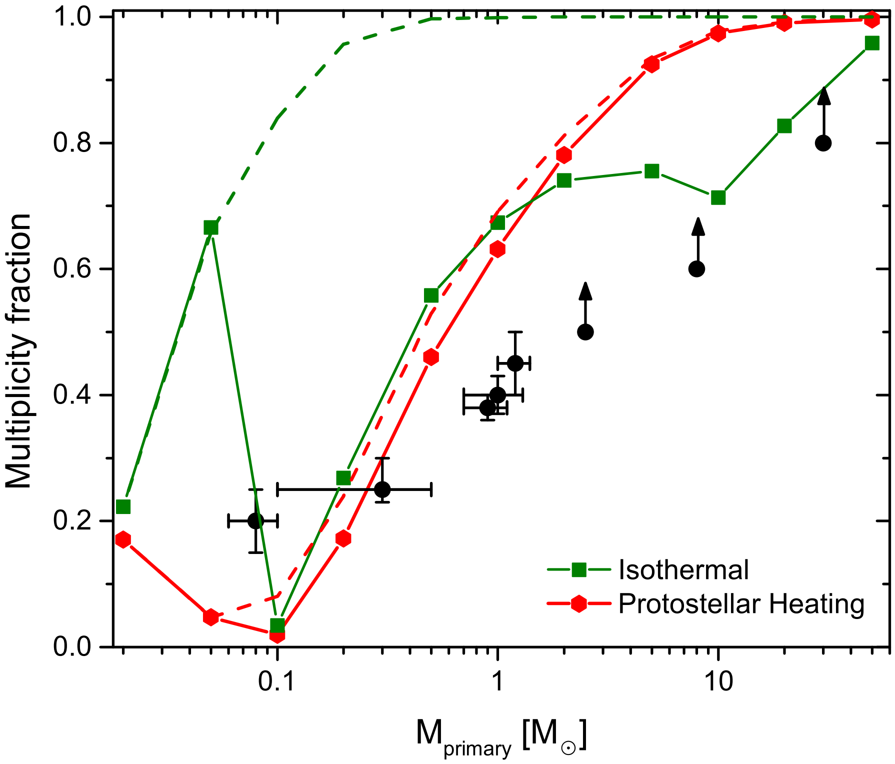

Figure 6.4: The multiplicity of stars of different masses in the isothermal case (*Isothermal - MW*) and the model with protostellar heating (*Heating - MW*) compared to the observed multiplicity fractions (black circles with error bars) from the review of Duchêne & Kraus (2013). The dashed lines show the results without the observational bias. Both models overpredict the multiplicity fraction as dynamical processes are neglected in our simulations, but the effect is far more severe for the isothermal model, particularly at low masses. Note that the sudden change around $0.1\,\mathrm{M}_\odot$ is due to the different observational bias for very low mass stars.

would have on our multiplicity fraction in Fig. 6.4 is that it would reach unity at a somewhat lower stellar mass. Our conclusion that low mass disks are for the most part too warm to fragment, but that disk fragmentation should be common for somewhat super-Solar and larger stars, is consistent with the numerical results of Offner et al. (2010).

6.3.3 Demographics of the Binary Population

6.3.3.1 Mass Ratios and the Brown Dwarf Desert

One of the key observed properties of binaries is the apparent flat mass distribution of companion masses with a cut-off at very low masses (the so-called

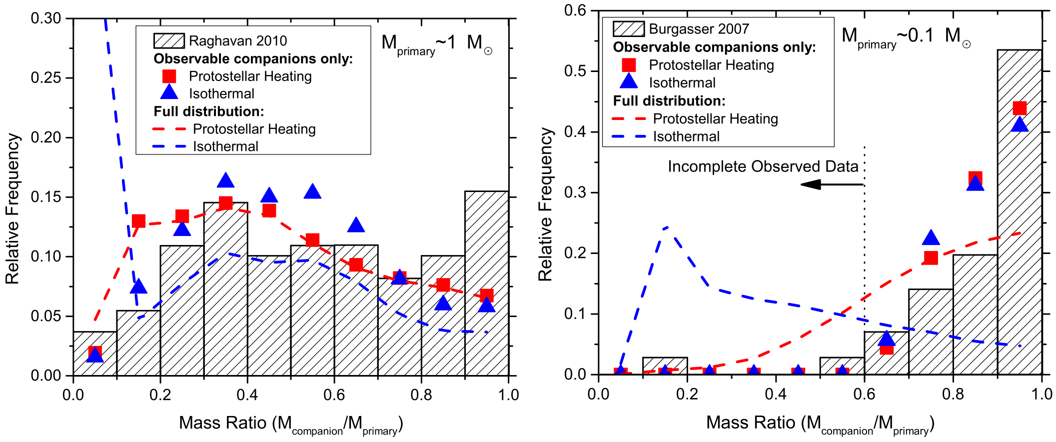

Figure 6.5: The relative frequency of **most massive** companions of Solar type stars (left) and VLM stars (right). Red and blue points and dashed lines show the results of our simulations with and without applying the observational bias, as indicated in the legend, while hatched histograms show the observations of Raghavan et al. (2010) for Solar type stars and Burgasser et al. (2007) for VLM stars. While both the isothermal and radiative models are consistent with observations after applying completeness limits, the isothermal simulations predict the existence of a very large number of currently-unseen low-mass companions that would be detectable in deeper observations. Also, none of our results reproduce the peak at unit relative mass which could be the result of either preferential dynamical hardening/ejection or missing physics in the model (e.g. disk physics).

"brown dwarf desert"). In Fig. 6.5 we test to what extent our models can reproduce this observation by comparing the mass distribution of the *most massive* companions in our simulations with observations of this quantity for Solar type and very low mass (VLM) stars ($M \sim 0.1\,\mathrm{M}_\odot$). Although in principle we could compute other mass ratios (e.g., the mass ratios of all pairs of stars in multiple systems, c.f. Raghavan et al. 2010), we focus on the most massive companions because these are the most robustly determined from observations. It is extremely challenging observationally to identify secondary and tertiary companions of a star in a triple or quadruple system. As a result, observations are most likely to discover the most massive companion rather than all companions, making the primary to secondary mass ratio the most well-determined. This also has the advantage that the most massive companion is the least likely to be ejected by dynamical processes. For our heated models, however, in practice it makes relatively little difference whether we include all companions or just the most massive one.

Examining Figure 6.5, it is clear that the isothermal and heated models are both roughly consistent with observations *after* the observational bias is applied. The primary exception is that both models somewhat underpredict the frequency of near-equal mass companions; such companions can plausibly be attributed to disk fragmentation, which tends to produce mass ratios close to unity (Bate, 2000). It is important to note that without the observational bias the isothermal model predicts an overwhelming number of very low mass ratio companions. Meanwhile the results for Solar type stars in the heated case is only slightly affected by observational bias, which means that the brown dwarf desert is not an observational bias.

To gain further insight into why our heated models are able to reproduce the brown dwarf desert, while our isothermal models fail, let us compare these companion mass distributions with the null hypothesis that that companion masses are randomly drawn from the IMF[2]. Fig. 6.6 compares our measured companion mass ratio distribution with that we would expect under the null hypothesis, again considering only the most massive pair in a given star system[3]. The figure shows that in no case are the results consistent with random sampling of companions from the IMF. In the isothermal case the companion distribution for both Solar and VLM primaries follows the IMF for very low mass companions, but that there is a significant excess of companions at mass ratios $\sim 0.5-1$. In the heated case the situation is qualitatively similar, in that mass ratios near unity are overrepresented compared to the null hypothesis.

Now let us consider the implications of this finding for the brown dwarf desert. The companion mass ratio distribution is a product of two factors: the un-

---

[2] Binaries forming from randomly sampling the IMF has been ruled out (Reggiani & Meyer, 2011), making it an important test for theoretical models.

[3] Computing the null hypothesis distribution requires some care, because for systems with > 2 stars, even if all companions are drawn randomly from the IMF, the mass distribution for the most massive companion does not follow the IMF. Specifically, suppose we have an IMF $dN/dM = p(M)$, so that the cumulative distribution function (CDF) of masses (i.e., the probability that a randomly chosen star has mass $< M$) is $P(M) = \int_0^M p(M)\,dM$. Now consider a system where the primary has mass M_p. Since we require companion masses to be smaller than M_p, they follow the conditional CDF $P(M \mid M_p) \propto \int_0^{\min(M,M_p)} p(M)\,dM$, which for $M < M_p$ has the same shape as the CDF for single stars. However, now consider a system consisting of n stars. The most massive companion has a mass $< M$ only if all $n-1$ companions have mass $< M$, and if the companion masses are independent the probability of this is $P(M \mid M_p)^{n-1}$. This does not have the same shape as the single star CDF. For the purposes of Figure 6.6, we account for this effect by generating our null hypothesis lines as a weighted sum $P_1(M \mid M_p) = \sum_{n>1} w_n(M_p) P(M \mid M_p)^{n-1}$, where both the single star CDFs $P(M \mid M_p)$ and the relative frequencies $w_n(M_p)$ of multiplicity n are measured directly from the simulations for each primary mass M_p.

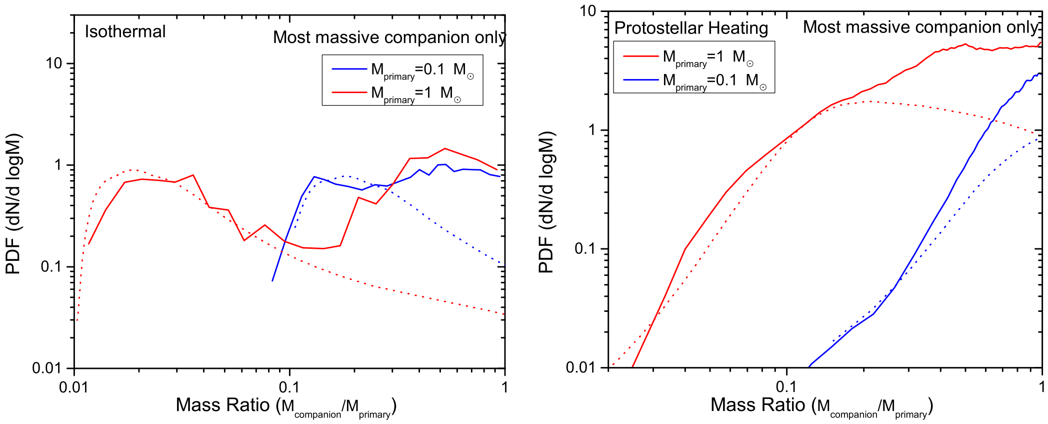

Figure 6.6: The two panels show the PDF of mass ratios between the two most massive stars in a given system, for primary masses $M_{primary} = 0.1$ M$_\odot$ (solid blue) and $M_{primary} = 1$ M$_\odot$ (solid red). We show these quantities both for the isothermal case and the model with protostellar heating, as indicated. For comparison, the dotted lines show the distributions that would result from the null hypothesis that companions are randomly drawn from the IMF. Note that the underlying simulation results shown here are identical to those shown in Figure 6.5, but they have been binned differently here for clarity.

derlying IMF of all stars, and any biases imposed by the fact that the stars whose mass distribution we are computing are non-primaries. With or without heating, we find that mass ratios near unity are favoured compared to a null hypothesis of random IMF sampling. That is, if we collect two samples of stars with the same upper mass limit, and for one sample we randomly select only non-primary stars and for the other we randomly select stars without regard to multiplicity characteristics, the non-primary sample will typically be more massive. For Solar-type primaries, the combination of a bias towards higher mass companions and the overall negative slope of the IMF near 1 M$_\odot$ (so that lower mass stars are more probable overall) yields a relatively flat mass ratio distribution – the IMF shape and the bias nearly cancel.

Now let us consider VLM stars. For VLM primaries, the bias towards equal mass companions is qualitatively similar to that for Solar-type stars. For our isothermal case, and unlike in reality, the IMF slope near 0.1 M$_\odot$ is also about the same as that near 1 $M_\odot$, due to the overall scale-free nature of isothermal fragmentation. Because both the IMF slope and the bias are about the same for Solar and VLM stars, the distribution of companion mass ratios is also qualitatively similar. For our heated case, as in reality, we have a very different situation. The slope of the IMF is negative near 1 $\mathrm{M}_\odot$, but positive (or at least close to flat) near 0.1 $\mathrm{M}_\odot$. As a result, for VLM primaries both the bias towards massive companions and the IMF itself favour more massive objects as companions. The result is a companion mass ratio distribution that is sharply biased towards stellar companions and away from brown dwarfs, producing the observed brown dwarf desert. We therefore find that the brown dwarf desert is a result of the change in the IMF slope between ~ 0.1 and ~ 1 $\mathrm{M}_\odot$, which in turn is imposed by thermal feedback, causing a deviation from scale-free behaviour during gas collapse and fragmentation.

6.3.3.2 Binary Separations

In addition to the mass ratio distribution, our spatially-resolved model allows us to examine the predicted semi-major axis distribution of binaries. We do so in Fig. 6.7 for Solar-type stars. The distribution appears peaked which comes from the peak of the companion mass ratio distribution (Fig. 6.6) with the corresponding length scale of $\sim \frac{GM_p}{c_s^2} \approx 0.05\,\mathrm{pc}$.

Comparing with the observations from Marks et al. (2011) we can see that on large scales our model of common core fragmentation seems to very roughly reproduce the present day observations. Although our results only give the "at-formation" period distribution, the comparison is still meaningful because, as explained in Sec. 6.2, we have attempted to limit the systems we count in our model to hierarchical systems that should be dynamically stable. In any case, it is clear that, similar to the case of the 2D correlation function (Fig. 6.2), turbulent fragmentation is unable to reproduce the observations on small scales. Another source for such binaries is required at $\leq 100\,\mathrm{AU}$, for which protostellar disk fragmentation is a good candidate[4]. Note that decreasing $R_{\mathrm{m}in}/R_0$ would technically improve the fit (see Sec. 6.C), but this would require unphysically low values.

6.4 Conclusions

The aim of this paper is to investigate the origin of the stellar correlation function and multiplicity statistics, and in particular to understand which features of these distributions result from pure scale-free isothermal fragmentation, and

---

[4] It should be noted that disc fragmentation simulations also fail to produce extremely close binaries ($\leq 10\,\mathrm{AU}$). These are likely to have either formed from a wider binary whose separation decreased due to orbital decay (e.g. Korntreff et al. 2012; Stahler 2010), or from exchange interactions in star clusters.

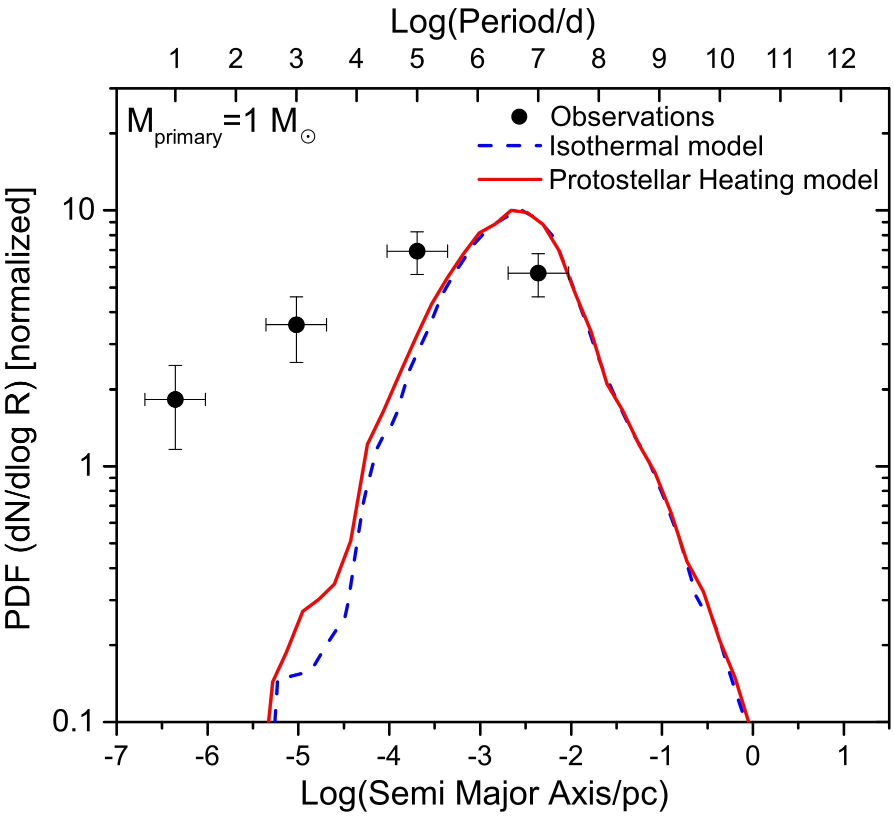

Figure 6.7: Semi-major axis distribution for binaries with fixed primary mass ($\sim 1\,\mathrm{M}_\odot$) in case of the isothermal model (dashed) and the case with protostellar heating (solid). The figure also includes the observed present day distribution from Moe & Di Stefano (2016) for solar type stars. The observed period distribution of solar type stars could plausibly be explained by common core fragmentation at large scales, but there a serious discrepancy for short-range binaries, further implying that protostellar disk fragmentation or dynamical effects play a crucial role.

which bear the imprints of scale-dependent stellar feedback. Using the MISFIT semi-analytical turbulent fragmentation framework of GH15 and GKH16 we find that the shape of the correlation function is almost entirely set by isothermal turbulence. Stellar feedback, which operates primarily on small scales, has little effect. On smaller scales ($\leq 100\,\mathrm{AU}$) both a purely isothermal model and one including stellar radiation feedback underpredict the stellar correlation, suggesting that our turbulent fragmentation models lack certain small scale physics (likely protostellar disk fragmentation). As with the correlation function, we find that our models provide a reasonable match to the observed the binary period distribution at large separations. This is true regardless of whether we include protostellar heating or not, just as they fail to produce enough very close binaries. We again conjecture that these close binaries are a result of disk fragmentation and N-body interaction, which our model does not include.

The situation for the mass ratios and multiplicity fraction of binaries is quite different. Isothermal fragmentation produces far too many multiple stars compared to what is observed, with even $\sim 1\ \mathbf{M}_\odot$ stars predicted to have multiplicities near unity. Adding protostellar heating substantially improves the situation, though the multiplicity fraction is still somewhat too high, likely because our models do not include dynamical evolution that will disrupt unstable systems. These differences, however, are almost completely washed out by the observational biases.

Most interestingly, if we neglect the observational bias we find that while turbulent fragmentation with or without protostellar heating can adequately reproduce the observed companion mass distribution for Solar type stars (except for very low mas companions), but only when protostellar heating is included can we reproduce the mass distribution of companions for low-mass primaries. In particular, only our models including radiative feedback reproduce the "brown dwarf desert", whereby the companions to low mass stars ($\sim 0.1\ \mathbf{M}_\odot$) are overwhelmingly stellar objects (i.e., close to a mass ratio of unity) rather than brown dwarfs. Models that include only scale-free physics predict a companion mass ratio distribution for low mass stars that is qualitatively similar to that for Solar-type stars, a direct consequence of the scale-free nature of these models. In contrast, protostellar heating suppresses the number of brown dwarfs relative to stars, so that the companion mass ratio distribution is very different for Solar-type stars that lie above the IMF peak and low-mass stars that lie at ore below it. We therefore conclude that the brown dwarf desert is a consequence of the physical mass scale imprinted by protostellar heating into the otherwise scale free star formation process.

6.A Improvements to Previous Model

Two papers (Guszejnov & Hopkins 2015a; Guszejnov et al. 2016) have been published so far using the MISFIT (Minimalist Star Formation Including Turbulence) semi-analytical star formation framework as this paper. Since the publication of those results, several improvements have been made to the algorithm, all of which are implemented for this paper. These do not change any of the published qualitative IMF results (e.g. general shape, sensitivity to initial conditions). They include:

- Correction of a bug that suppressed fragmentation at the end of the cloud evolution, violating self-similarity at a weak level. The effects on our previous work are small, but are substantial on the statistics on low mass companions. This is now fixed.

- Fragments are properly tracked and taken into account for the evolution of their parent (e.g. their contribution to the gravitational potential is taken into account as long as the parent has not yet contracted beyond their position). This causes no qualitative difference.

- Instead of using an absolute termination scale (taken to be $R_{\mathrm{m}in} = 10^{-4}\,\mathrm{pc}$ in the previous papers, roughly the size of protostellar disks), the collapse of clouds now terminates once clouds have contracted to a fixed fraction of their initial radius, chosen to be roughly when angular momentum support becomes dominant. This assumes that the source of angular momentum for clouds is from random turbulent motion. The resulting distribution for $\beta = \frac{E_{rot}}{E_{pot}}$ is strongly peaked around a few percent (Burkert & Bodenheimer 2000). If collapse happens at constant virial parameter than the size scale where angular momentum starts dominating is βR_0. This is the scale where the cloud flattens and forms a disk, which we choose as our termination point.[5]

- We set a lower limit of $0.007\,\mathrm{M}_{\odot}$ on fragment masses based on the opacity arguments of Low & Lynden-Bell (1976). This is in fact equivalent to a simplified EOS model, where we terminate the fragmentation once the cloud reaches the adiabatic limit. This provides a natural termination for the fragmentation cascade in our "isothermal" models, otherwise our results would not converge (see GKH16)

6.B Comparison with detailed hydrodynamic simulations

There have been a number of hydrodynamical simulations attempting to find the multiplicity statistics and separation distribution of newly formed stars (e.g. Bate 2009b, 2012a; Delgado-Donate et al. 2004; Goodwin et al. 2004; Krumholz et al. 2012; Offner et al. 2010). The semi-analytical approach we present in this paper has several advantages over these (e.g. faster, no absolute

---

[5] The choice of a relative termination scale instead of an absolute value has the added benefit of imprinting no absolute length scale into the problem, preserving self-similarity.

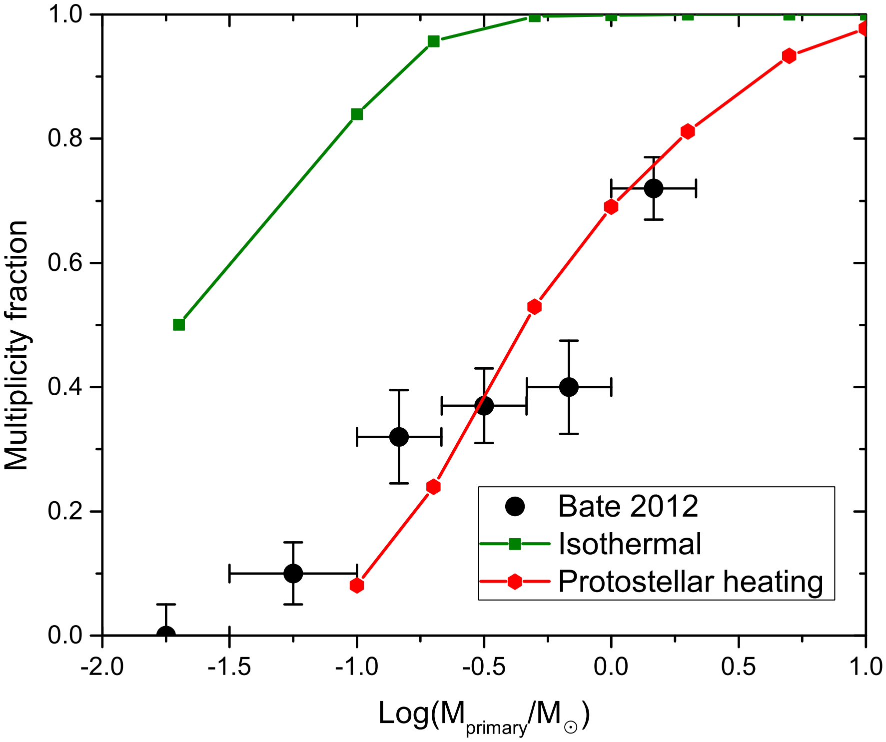

Figure 6.8: The multiplicity of stars of different masses in the isothermal case (*Isothermal - MW*) and the model with protostellar heating (*Heating - MW*) compared to the results of Bate (2012a) (black circles with error bars).

resolution limit, starts from GMC) but at the cost of several strong assumptions, so it is crucial that we compare our results with theirs. We choose to compare with the simulations of Bate (2012a), as these have the largest sample of multiple systems. Since we know the full binary distribution from the simulations, we make this comparison without the observational completeness correction that we apply when comparing to observations in the main text.

Figures 6.8-6.10 show that our results are qualitatively, and in many cases quantitatively, consistent with the simulations of Bate (2012a). An important difference between our current model and the traditional simulations is that MISFIT does not have a finite resolution limit, but it does neglect disk physics. This leads to the discrepancy at small separations shown in Fig. 6.10.

6.C Numerical Tests and Convergence

In this section we show how the GMC massM_{GMC}, the termination scale R_0/R_{min}, and the resolution parameter N affect our results. To explore these

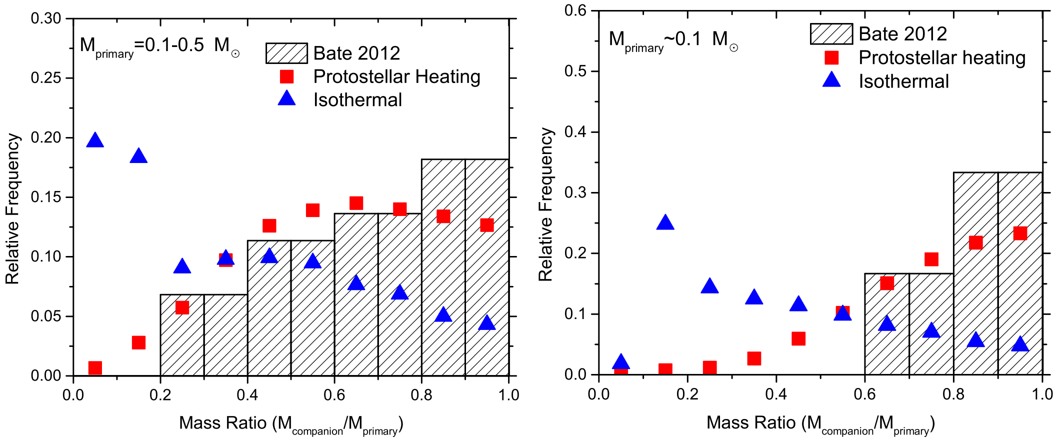

Figure 6.9: The relative frequency of **most massive** companions of small stars (left, $M_{primary} = 0.1 - 0.5\,\mathrm{M}_{\odot}$) and VLM stars (right, $M_{primary} = 0.1\,\mathrm{M}_{\odot}$). Red and blue points show the results of our simulations without applying the observational bias, while hatched histograms show the results of Bate (2012a).

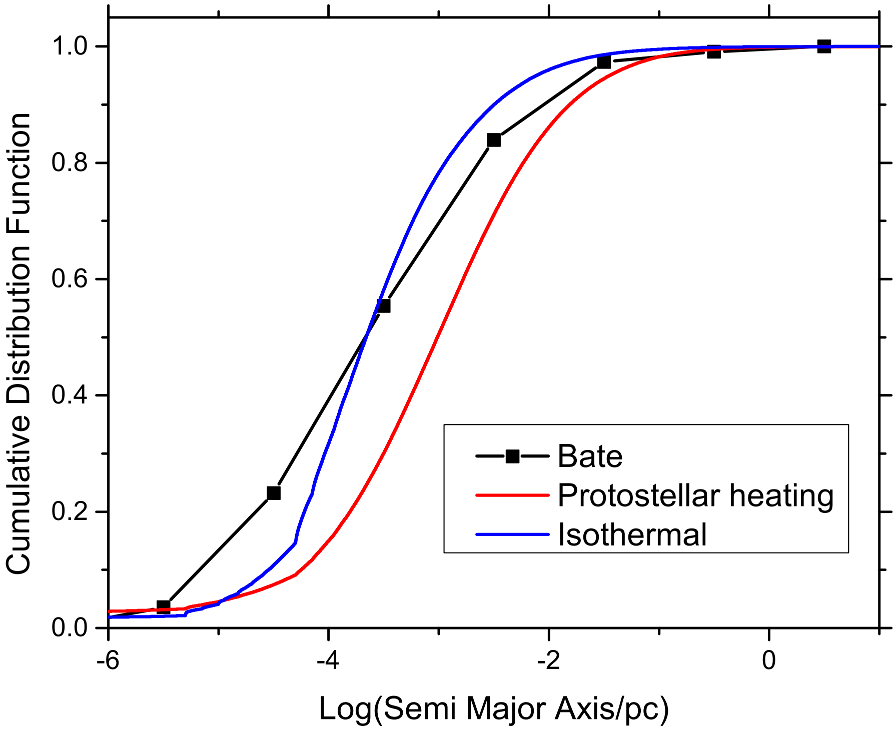

Figure 6.10: Cumulative Semi-major axis distribution for multiple systems where ($M_{primary} > 0.1\,\mathrm{M}_{\odot}$) in case of the isothermal model (blue) and the case with protostellar heating (red) along with the results of Bate (2012a). This includes *all* separations, hierarchical triples and quadruples contribute 2 and 3 values respectively.

questions, we have repeated our fiducial *Heating - MW* run with different resolutions ($N = 16, 32, 64$), GMC masses ($M_{GMC} = 10^4, 10^5, 10^6$ M$_\odot$), and different termination scales ($R_0/R_{\mathrm{m}in} = 10^{-3}, 10^{-2}, 10^{-1}$). The full list of runs performed in given in Table 6.1. Note that unlike the results in the main text these are not modified to account for observational biases.

We first examine how our results affect the same of the IMF produced by our models. Fig. 6.11 shows that the shape of the IMF is robust to changes in N, reaching convergence around $N = 32$. The location of the IMF peak and the high mass slope are also essentially insensitive to the GMC mass; the location of the peak does shift by an extremely small amount as we vary the GMC mass, as a result of its dependence on the Mach number of the turbulence; the two are related thanks to our assumption that clouds have virial ratios $\alpha_{\mathrm{v}ir} \approx 1$. However this shift is only $\sim 10\%$ over a plausible range of GMC masses. The IMF shows its greatest sensitivity to the relative termination scale $R_{\mathrm{m}in}/R_0$, particularly the abundance of brown dwarfs beyond the peak. In reality our choice of a single $R_{\mathrm{m}in}/R_0$ value is an oversimplification, since real turbulence fields produce a distribution of rotational kinetic energies β, and thus a distribution of $R_{\mathrm{m}in}/R_0$ parameters; the real IMF should therefore resemble a weighted average of the curves shown in Fig. 6.11.

Fig. 6.12 shows how variation of our three parameters affects the stellar correlation function. As with the IMF, we find that the correlation function is insensitive to changes in both the resolution parameter N and the initial GMC mass – the former produces no noticeable differences past $N = 32$, while the latter mostly rescales the outer cut-off/size scale. Also, as with the IMF, larger initial masses lead to verly slightly shallower slopes. This is consistent with the discussion in Section 6.3.1 and Sec. 6.D: larger masses mean stronger initial turbulence which in turn means easier fragmentation. However, as with the IMF, the effect is extremely modest. Finally, the bottom panel of Fig.6.12 shows that the relative termination scale has no effect on the correlation function apart from introducing a small-scale cut-off.

Fig. 6.13 shows the peak of the separation distribution converges above $N = 32$, and the parent GMC mass has little effect on it. The relative termination scale $R_{\mathrm{m}in}/R_0$ sets the width of the peak; its position is set by $\frac{GM_{primary}}{c_s^2}$, as discussed in Sec. 6.3.2. Decreasing $R_{\mathrm{m}in}/R_0$ increases the abundance of binaries at small separations, since it pushes the transition between common core fragmentation (which we are modeling) and disc fragmentation (which are

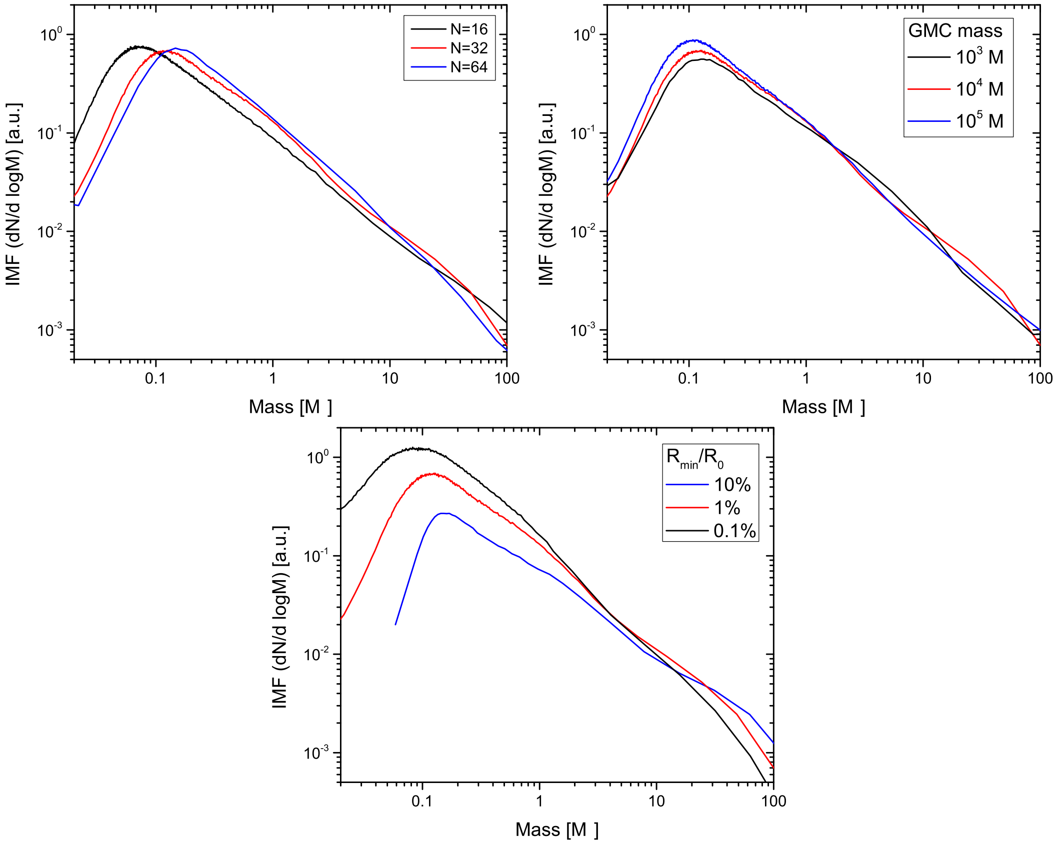

Figure 6.11: Effects of the simulation resolution N (top left), parent GMC mass (top right) and the relative termination scale $R_{\mathrm{m}in}/R_0$ (bottom) on the IMF.

are not) to smaller scales. However, as noted in the main text, only a value of $R_{\mathrm{m}in}/R_0$ that is unphysically small would produce enough short-period binaries to be consistent with the observations.

6.D Cantor-like Model of Fragmentation

One of the most important properties of isothermal fragmentation is that it is scale-free, so we expect self-similar, fractal-like structures to emerge. We can formulate a simple toy model to describe this process where self-gravitating clouds contract to about ϵ relative scale before breaking into two (see Fig. 6.14) along a random axis. The distance of the two fragments is uniformly chosen between 0 and R_{parent}. The fragments then rearrange themselves into spheres at the same density as their parent (meaning their radius is $2^{-1/3}R_{parent}$). This model is very similar to the generalized Cantor dust (3D analogue of the generalized 1D Cantor set) that have the fractal dimensions of $D_{\mathrm{set}} = \frac{\ln 2}{\ln 2 - \ln \epsilon}$ and

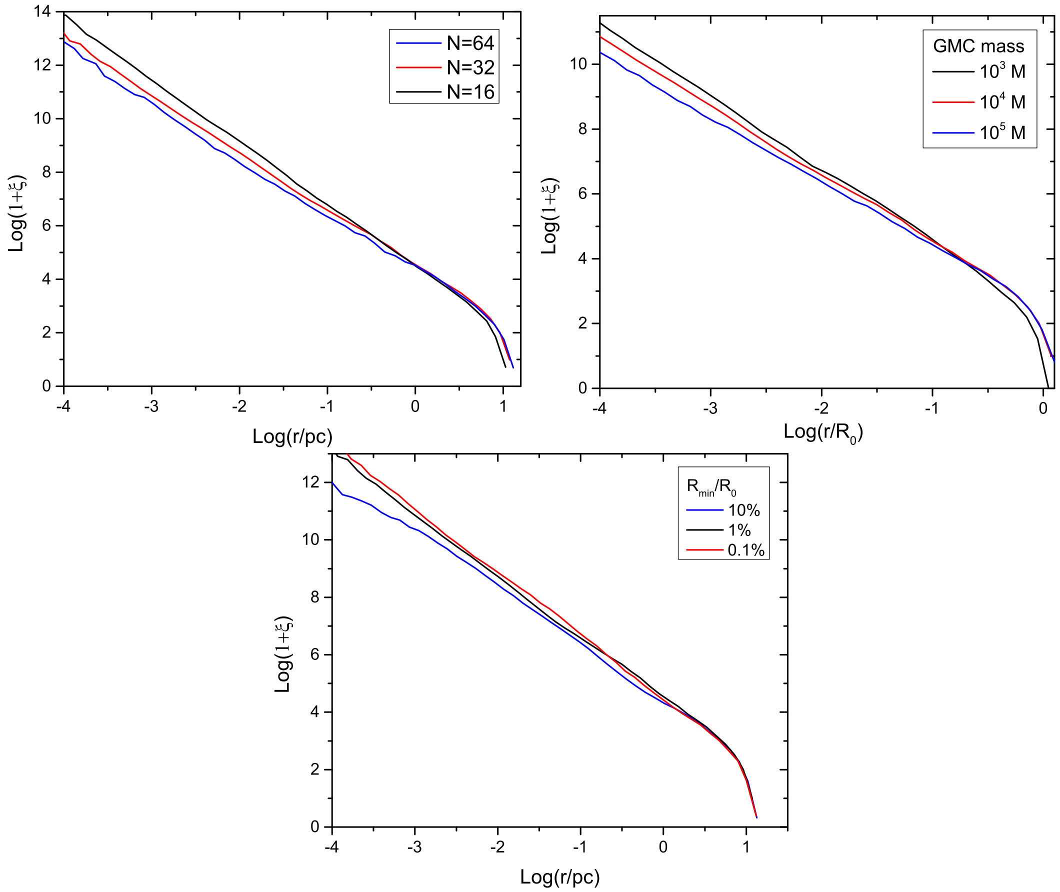

Figure 6.12: Effects of the simulation resolution N (top left), parent GMC mass (top right) and the relative termination scale $R_{\mathrm{m}in}/R_0$ (bottom) on the stellar correlation function.

$D_{\mathrm{d}ust} = \frac{3\ln 2}{\ln 2 - \ln\epsilon}$, leading to a 3D correlation function of r^{D-3}.

We can analytically calculate the fractal dimension of our Cantor-like model if we take the separation between fragments to be the mean value of $R_{parent}/2$. If we take the initial radius of the first sphere to be unity then, after n iterations, the number of the objects is $N = 2^n$ while their size is $R_n = \epsilon^N 2^{-N/3}$. If we choose a random fragment then the number of fragments within an R_m radius is $N_m = 2^{n-m}$, thus

$$D \equiv \frac{\mathrm{d}\ln N_m}{\mathrm{d}\ln R_m} = \frac{\ln 2}{\frac{1}{3}\ln 2 - \ln\epsilon}. \tag{6.9}$$

Fig. 6.15 shows that this result is actually exact. Since isothermal fragmentation is quite similar to this toy model, we expect the predicted stellar correlation function to have a slope between -1 and -3 (for reasonable ϵ values).

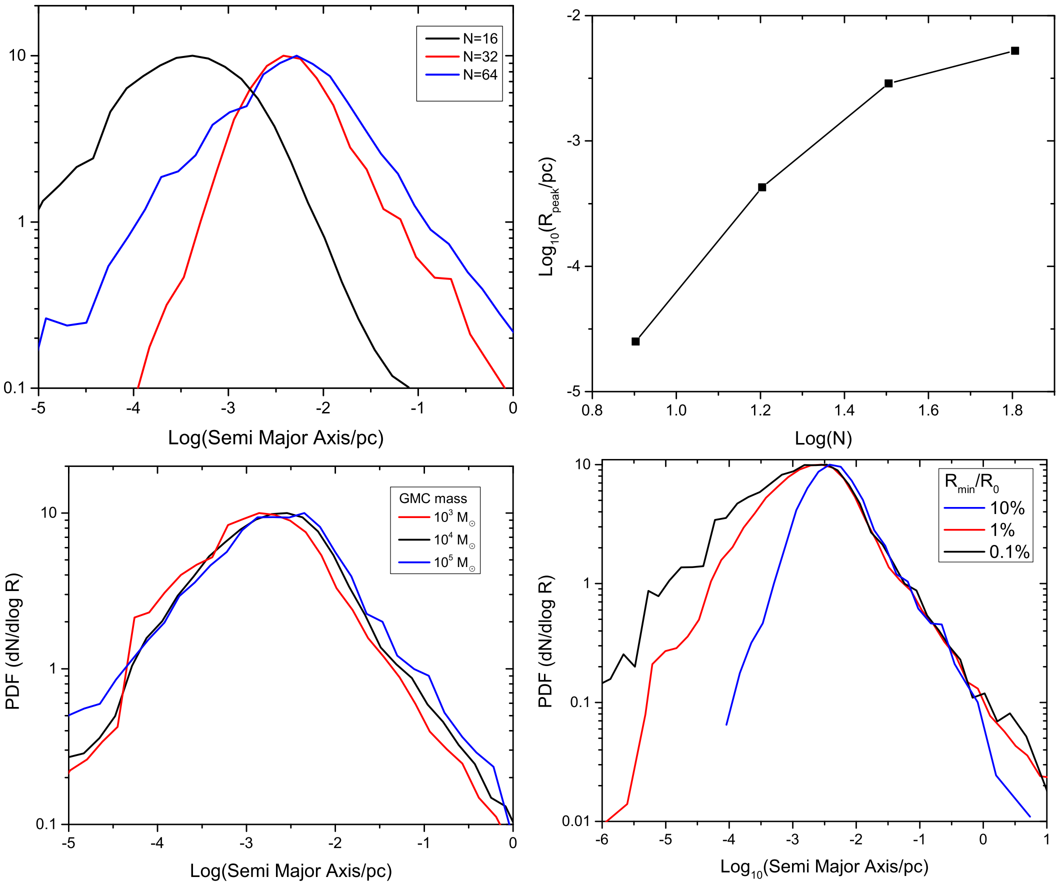

Figure 6.13: Effects of the simulation resolution N (top left and right), parent GMC mass (bottom left) and the relative termination scale $R_{\min}/R_0$ (bottom right) on the stellar correlation function.

This also implies that if some additional physics makes fragmentation harder (increasing the density threshold and thus decreasing ϵ) then the correlation function becomes steeper.

This model has the free parameter ϵ which we can restrict by assuming that the fragmentation criteria is set by the Jeans-instability. It is known that the mass of fragments would be of the Jeans-mass $M_{\mathrm{J}eans} \propto \rho^{-1/2} \propto \epsilon^{3/2}$. The number of fragments is $M/M_{\mathrm{J}eans} = 2$ which leads to $\epsilon = 0.63$. For this value Eq. 6.9 gives $D = 1$, leading to a $\xi \propto r^{-2}$ power law, in perfect agreement with our results from Fig. 6.1.

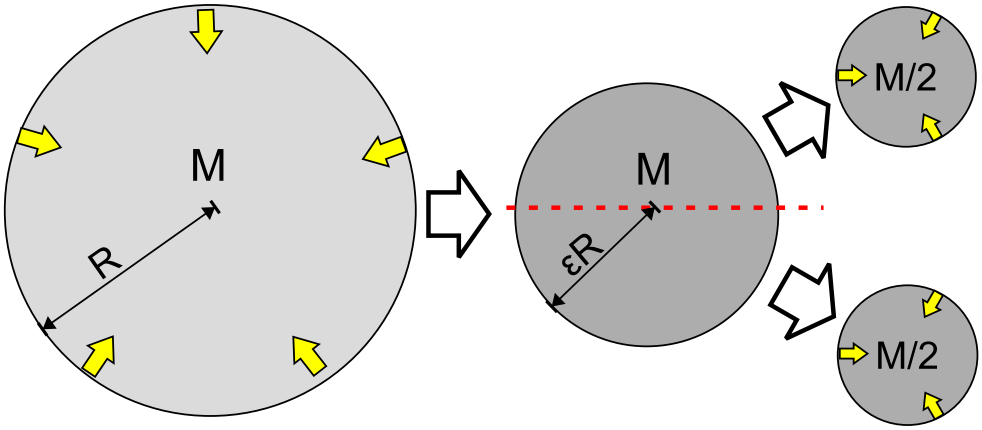

Figure 6.14: The 3D Cantor-set-like toy model of isothermal fragmentation. Every cloud contracts to ϵ relative scale before breaking into two along a randomly chosen plane and the process repeats itself.

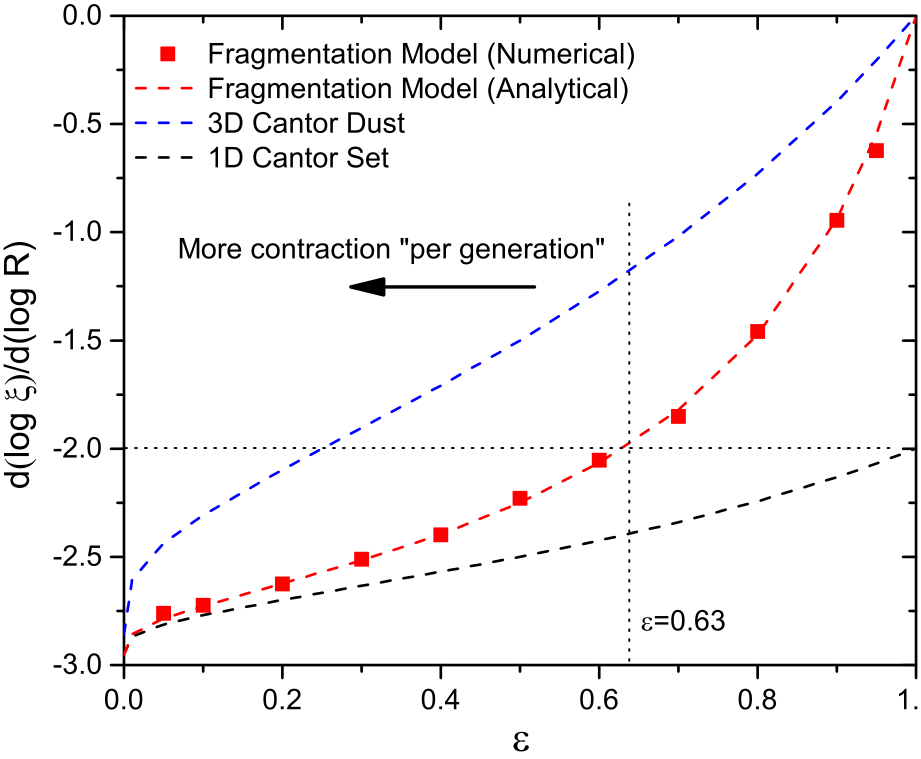

Figure 6.15: Numerically calculated slopes of the 3D Cantor-like model (symbols) along with the analytical approximation (red) and the analytical result for the generalized 1D Cantor set (black) and 3D Cantor dust (blue).

Chapter 7

UNIVERSAL SCALING RELATIONS IN SCALE-FREE STRUCTURE FORMATION

Guszejnov D., Hopkins P. F., Grudic M. Y., 2017, preprint, (http://arxiv.org/abs/1707.05799)

Abstract

A large number of astronomical phenomena exhibit remarkably similar scaling relations. The most well-known of these is the mass distribution $\mathrm{d}N/\mathrm{d}M \propto M^{-2}$ which (to first order) describes stars, protostellar cores, clumps, giant molecular clouds, star clusters and even dark matter halos. In this paper we propose that this ubiquity is not a coincidence and that it is the generic result of scale-free structure formation where the different scales are uncorrelated. We show that all such systems produce a mass function proportional to M^{-2} and a column density distribution with a power law tail of $\mathrm{d}A/\mathrm{d}\ln\Sigma \propto \Sigma^{-1}$. In the case where structure formation is controlled by gravity the two-point correlation becomes $\xi_{2D} \propto R^{-1}$. Furthermore, structures formed by such processes (e.g. young star clusters, DM halos) tend to a $\rho \propto R^{-3}$ density profile. We compare these predictions with observations, analytical fragmentation cascade models, semi-analytical models of gravito-turbulent fragmentation and detailed "full physics" hydrodynamical simulations. We find that these power-laws are good first order descriptions in all cases.

7.1 Introduction

It is well known that the physics of the interstellar medium and star formation are very complex, involving turbulence, gravity, radiation and chemistry. Despite this complexity a number of physical quantities show scale-free, power-law-like behavior over a large dynamic range:

- The initial mass function (IMF) of stars in different regions of the MW and in extragalactic sources is found be close to a power-law for high mass stars with a slope of approximately -2.35 (e.g. Bastian et al., 2010; Offner et al., 2014; Salpeter, 1955).
- Similar to the IMF, the mass function of prestellar cores (CMF) in the MW also resembles a power-law at high masses with slopes close to that of Salpeter (e.g. Sadavoy et al. 2010).

- The mass function of clumps (stellar-mass sized condensations of dust and gas) in molecular clouds exhibits power-law distribution with an inferred slope close to -2 (see Johnstone & Bally, 2006; Kramer et al., 1998).

- The mass function of giant molecular clouds (GMC) in the MW is also found to be close to a power-law at high masses with a slope somewhat shallower than the canonical IMF value (e.g. Rosolowsky, 2005), but there can be significant variation with environment (e.g. see Colombo et al. 2014b where the exponents vary between -1.5 and -2.5).

- The initial mass function of star clusters exhibits a similar power-law behavior with an inferred slope of -2 (e.g. Bik et al., 2003; Fall & Chandar, 2012; Zhang & Fall, 1999).

- The dark matter halo mass distribution is expected to be close to $\mathrm{d}N/\mathrm{d}M \propto M^{-2}$(Press & Schechter, 1974; Warren et al., 2006) over a large dynamic range.

- The column density PDF of star-forming regions can be roughly approximated with a power law $\mathrm{d}A/\mathrm{d}\ln\Sigma \propto \Sigma^{-\gamma}$ (Kainulainen et al., 2009; Lombardi et al., 2014). At low-to-intermediate densities, this appears to be determined by the global mass profile of the cloud with $\gamma \sim 2-3$ (Schneider et al., 2015b), while in the dense star-forming gas the slope appears to approach $\gamma \sim 1$ (Schneider et al., 2015a).

- The stellar two-point correlation function in young star clusters has been measured over a wide dynamic range (about 5 orders of magnitude in radius), with the large-scale behavior of the 2D correlation function similar to a power-law with a slope of -1 (e.g. Hartmann, 2002; Hennekemper et al., 2008; Kraus & Hillenbrand, 2008; Simon, 1997). Note that it has been shown that very different geometries (e.g., fractal vs spherical) can lead to similar correlation function slopes (Gouliermis et al., 2014).

- Similarly the 2D two-point correlation functions of protostellar cores (Stanke et al. 2006) has also been measured and found to be consistent with power law slopes of -1 or slightly shallower.

- Studies have investigated the 2D correlation function of star clusters (see Grasha et al., 2017; Zhang et al., 2001) in nearby galaxies and found it to be close to a power-law of -1 for young clusters within the scale height of the galactic disk. As star formation predominantly happens in GMCs this implies a similar trend for the correlation function of GMCs.

- The 2D correlation function of dark matter halos has also been found consistent with a power-law with -1 slope both observationally (e.g. Baugh, 1996; Sołtan & Chodorowski, 2015) and numerically (e.g. Kauffmann et al., 1999). Numerical studies have shown that on intermediate scales ($\ll$ 10 Mpc <) these results are independent from the initial density power spectrum.

- The mass profile of young star clusters exhibits power-law-like behavior, the observed surface density profile at large scales is well approximated by power-laws consistent with a density profile with slopes between -3 and -5 (see Elson et al., 1987; Mackey & Gilmore, 2003a,b; Portegies Zwart et al., 2010).

- The density profile of dark matter halos is well described by the NFW profile (Navarro et al., 1996) that simplifies to $\rho \propto R^{-3}$ on larger scales.

There have been a number of attempts to formulate theories to explain some of these scaling relations. A popular idea for gas clouds is to assume that the formation of these objects is set by the interplay between turbulence and gravity (e.g. Guszejnov & Hopkins, 2016; Hennebelle & Chabrier, 2008, 2009, 2013a; Hopkins, 2012a,b, 2013c; Padoan & Nordlund, 2002; Padoan et al., 1997). These *gravito-turbulent models* have successfully reproduced the mass functions and even the two-point correlation function above (see Guszejnov et al., 2017b; Hopkins, 2013a). These have a number of attractive properties including the natural appearance of the linewidth-size relation (Kritsuk et al., 2013). Another interesting aspect of this approach is the apparent universality one obtains in the supersonic limit where the process becomes an almost self-similar fragmentation cascade, washing out most of the differences between individual models (Krumholz, 2014).

Another popular approach to explain these relations in star formation is to rely on self-similar growth as small “seeds” grow by accreting from the same mass reservoir (originally proposed by Larson 1982 then worked out by Zinnecker 1982, see review of Bonnell et al. 2007 and references therein for more details). These *competitive accretion models* rely of gravity and hydrodynamics to show that the features of the initial “seed” distribution are washed out by accretion leading to a power-law distribution consistent with the IMF.

Finally, in a somewhat different approach, one cannotice that the apparent similarity in the slopes of the mass functions could be explained by a fractal-like, self-similar ISM out of which structures like stars, cores and GMCs form (e.g. Chappell & Scalo, 2001; Elmegreen, 1997; Elmegreen & Falgarone, 1996; Stutzki et al., 1998). An important property of these models is that they tie structures of different sizes together (stars, cores, clumps) as their mass distribution is the result of the same fractal ISM structure (e.g. Elmegreen, 2002). The density structure predicted by these *fractal ISM models* is in agreement with simulations of supersonic turbulence (e.g. Kritsuk et al., 2006). In general these inherently imply an underlying self-similar process, which serves as the main motivation for this paper.

While the models above tried to explain the ISM-related phenomena, there has been a similarly large effort related to the scaling laws of dark matter. The DM halo mass function was first predicted by the random field approach of Press & Schechter (1974) and Bond et al. (1991), which is actually the same formalism a number of gravito-turbulent theories for star-formation and the ISM are based on (e.g. Hopkins, 2012a). A key feature of these Press-Schechter models is that the phases of the different-scale modes in the density field are uncorrelated; in other words, the different scales are independent (this is the reason one can describe the process as a random walk in Fourier-space).

Note that these classes of models concentrate on quite different physics but still produce similar scaling relations for the mass functions, density PDFs, correlation functions etc. In this paper we aim to demonstrate that these scalings can be explained to first order by *any* scale-free structure building process with a large dynamic range where the different scales are uncorrelated. We argue this point in Sec. 7.2 and then show that all the processes listed at the beginning of this section can be described with the same generic hydrodynamical problem. To demonstrate the properties of this problem we concentrate on one of its subclasses: the scale-free fragmentation cascade. We formulate a general description of a fragmentation cascade in Sec. 7.3 and then use it to derive the mass distribution of stars/objects (Sec. 7.4.1), their correlation function (Sec. 7.4.2), the gas density distribution function (Sec. 7.4.3) and the power law tail of the young star cluster mass profile (7.4.4). Then we compare our predictions from the fragmentation cascade model with observed data, the outputs of MISFIT, our semi-analytical simulation of cloud fragmentation (Guszejnov & Hopkins 2016), and with the results of the detailed multi-physics MHD simulations of Grudić et al. (2016).

7.2 Cause of Universal Behaviour

In Sec. 7.1 we listed a large number of astrophysical objects (stars, molecular clouds, star clusters, DM) that at first glance seem to obey very different physics. Let us first investigate the structures that form out of molecular gas (e.g. stars, cores, GMCs). Since the gas can be described as a fluid it must obey the nonrealtivistic MHD+gravity momentum conservation equation

$$\frac{\partial}{\partial t}(\rho\mathbf{v}) + \nabla\cdot(\rho\mathbf{v}\otimes\mathbf{v}) = \\ -\nabla P + \eta\rho\nabla^2\mathbf{v} + (\zeta+\eta/3)\nabla(\nabla\cdot\mathbf{v}) + \frac{1}{\mu_0}(\nabla\times\mathbf{B})\times\mathbf{B} - \rho\nabla\Phi, \qquad (7.1)$$

where ρ, $\mathbf{v}$ and $\mathbf{B}$ are the usual density, velocity and magnetic fields while P is the thermal pressure, η is the dynamic viscosity, ζ is the bulk viscosity and Φ is the gravitational potential. By dividing with the characteristic scales of the system (size: L_0, velocity: v_0, density: ρ_0, sound speed: $c_{s,0}$, Alfvén velocity: v_A) we can make Eq. 7.1 dimensionless:

$$\frac{\partial}{\partial\tilde{t}}(\tilde{\rho}\tilde{\mathbf{v}}) + \tilde{\nabla}\cdot(\tilde{\rho}\tilde{\mathbf{v}}\otimes\tilde{\mathbf{v}}) = \\ -\mathcal{M}^{-2}\tilde{\nabla}\tilde{P} + \mathrm{Re}^{-1}\tilde{\rho}\nabla^2\tilde{\mathbf{v}} + \tilde{\zeta}\tilde{\nabla}\left(\tilde{\nabla}\cdot\tilde{\mathbf{v}}\right) + \mathcal{M}_A^{-2}\left(\tilde{\nabla}\times\tilde{\mathbf{B}}\right)\times\tilde{\mathbf{B}} - \alpha\tilde{\rho}\tilde{\nabla}\tilde{\Phi}, \qquad (7.2)$$

where $\tilde{t}\equiv tv_0/L_0$, $\tilde{\nabla}\equiv L_0\nabla$, $\tilde{P}\equiv\frac{P}{\rho_0 c_s^2}$, $\tilde{B}\equiv\frac{B}{v_A\sqrt{\rho_0\mu_0}}$ and $\tilde{\Phi}\equiv\frac{\Phi}{G\rho_0 L_0^2}$ where G is the gravitational constant, while $\mathcal{M}=v_0/c_{s,0}$ is the Mach number, $\mathrm{Re}\equiv\frac{\rho_0 v_0 L_0}{\nu}$ is the Reynolds number,$\tilde{\zeta}\equiv\frac{\zeta+\eta/3}{\rho_0 v_0 L_0}$, $\mathcal{M}_A\equiv v_0/v_A$ is the Alfvén Mach number and $\alpha\equiv v_0^2/(G\rho_0 L_0^2)$ is the virial parameter.

Let us now look at the process of star and cloud formation in more detail! In a wide dynamic range of this process the flows are supersonic ($\mathcal{M}\gg 1$) making the pressure term negligible. Magnetic fields are similarly not important on these scales ($\mathcal{M}_A\gg 1$), as shown both in simulations (e.g. Federrath & Klessen, 2012; Grudić et al., 2016) and (to some extent, on large scales) in observations (see review of Crutcher, 2012). Meanwhile, viscous forces only matter close to the dissipation scale (i.e. $\mathrm{Re}\gg 1$ and $\tilde{\zeta}\ll 1$). This leaves us with the following dimensionless equation:

$$\frac{\partial}{\partial\tilde{t}}(\tilde{\rho}\tilde{\mathbf{v}}) + \tilde{\nabla}\cdot(\tilde{\rho}\tilde{\mathbf{v}}\otimes\tilde{\mathbf{v}}) = -\alpha^{-1}\tilde{\nabla}\tilde{\Phi}. \qquad (7.3)$$

Eq. 7.3 describes the motion of a pressureless fluid in a gravitational potential[1]. Note that this equation is completely scale-free (all quantities are normalized) and its only parameter is the dimensionless α, the virial parameter that describes the ratio of kinetic to gravitational energy in the system.

We can do the same exercise for the case of star clusters and dark matter halos. Both can be described by the collisionless Boltzmann equation with self-gravity which we can bring to the dimensionless form

$$\frac{\partial \tilde{f}}{\partial \tilde{t}} + \tilde{\mathbf{v}} \cdot \tilde{\nabla} \tilde{f} - \alpha^{-1} \tilde{\nabla} \tilde{\Phi} \cdot \frac{\partial \tilde{f}}{\partial \tilde{\mathbf{v}}} = 0, \tag{7.4}$$

where f is the 6D phase space density function. Once again we find that the governing equation of structure formation is scale-free and only depends on the virial parameter α . Note that the fluid equation of Eq.7.3 is just the first moment of the dimensionless Boltzmann equation (Eq. 7.4).

Now let us concentrate on what kind of processes we are trying to describe. We are interested in how certain astronomical objects form (e.g. DM halos, GMCs, star clusters). These are gravitationally bound objects, which, by definition, means that they have a specific virial parameter (of order unity). Thus, regardless of their inherent differences, the formation of molecular clouds, star clusters and dark matter halos all follow Eq. 7.4 with a similar virial parameter α. Because of this attractor these different phenomena produce similar scaling relations as shown later in Sec. 7.4.

7.2.1 The Importance of Uncorrelated Scales

It is clear that the equation that describes the evolution of structure formation (Eq. 7.4 or Eq. 7.3) is scale-free; in other words, it does not know about the absolute size of the system. But it is also important to look at whether the process has "memory", i.e. does a structure remember its progenitor?

By looking at Eq. 7.4 we find that it has actually two time scales: the *crossing time* scale $t_{cross}(L) \sim L/v_0 = \frac{L}{L_0} t_0$ and the *gravitational/freefall time* scale $t_{ff} \sim (G\rho_0)^{-1/2} \sim \alpha^{1/2} t_0 \approx t_0$. For marginally self-gravitating structures ($\alpha \sim 1$) the crossing time is shorter than the freefall time on all scales except the largest where they are equal. This means that during the evolution of a self-gravitating object there is more than enough time for mixing on small scales. Since Eq. 7.4

---

[1] Note that supersonic flows are not perfectly pressureless because they create shocks where pressure inevitably becomes important. Nevertheless, the thickness of a shock transition will generally be much smaller than the scales of the flows generating the shocks (represented by the Mach number $\mathcal{M}$) by a factor $\sim \mathcal{M}^{-2}$.

is highly nonlinear (e.g. admits turbulence) this mixing effectively erases the details of the initial conditions ($\tilde{\rho}$, $\tilde{\mathbf{v}}$ etc.) on smaller scales. Thus, as we argue below, the initial conditions for a newly formed self-gravitating substructure (whose evolution is also described by Eq. 7.4) should be independent (at least to leading order) from the initial conditions of its progenitor.

Another way to say this is that, if we consider some sub-volume $\mathbf{\Omega}$ of the parent system which is somehow isolated from its parent (by, say, collapsing under self-gravity), the initial micro-state (exact spatially-dependent values of $\tilde{\rho}(\mathbf{x}, t = t_0)$, $\tilde{\mathbf{v}}(\mathbf{x}, t = t_0)$, etc.) will be "wiped out" by small-scale (e.g. turbulent) motions, on a timescale which is small compared to the global evolution timescale (the dynamical time) of $\mathbf{\Omega}$. The *statistical* distribution of properties can only depend on the one governing parameter of the equations, α – so sub-systems with the same α must be statistically identical (after this initial short time), up to the overall normalization/units of the system (e.g. its size). In other words: if the different scales are uncorrelated, the statistics of objects of different generations are the same[2].

We could, conceivably, imagine a process which "selects" a different value of α for each "level" in scale (say, each time one moves in scale, α doubles). This would imprint a systematic difference in the statistics of small-scale systems as compared to large-scale systems. However, the physics of interest for the properties we study here is gravity, which (by definition) selects the *same* $\alpha \sim 1$ at all scales – if we define "structures" by self-gravitating or collapsing objects, or fragments, or merging agglomerations, then they must be at similar α. Given the assumptions above, this means that each sub-structure must, in turn, have similar statistical properties to its parent.

Consider the specific example of fragmentation where a large structure repeatedly breaks up into smaller objects (or the opposite where small objects join to form larger structures, i.e. hierarchical merging), but leaves some mass "behind" at each scale. Since the process is scale-free the amount of mass "left" at each scale has to be some fraction of the current mass, but because the process has no memory it must be the same fraction at every mass scale. If the process has a wide dynamic range then it follows that it leaves only a small fraction of its mass at every scale so the absolute amount of mass is roughly equal at

---

[2] Note that the cosmological models for dark matter halos (Press & Schechter, 1974) and the excursion set models of turbulent fragmentation (Hopkins, 2012a) all rely on the assumption of uncorrelated scales.

the different scales. This leads to

$$\frac{\mathrm{d}\log M_{total}}{\mathrm{d}\log x} = \epsilon \sim \mathrm{const.} \ll 1, \tag{7.5}$$

where x is some physical quantity in which the process is moving up/down in scale (e.g. size, mass). Due to the scale-free nature of the problem all physical quantities are power-laws of each other thus Eq. 7.5 leads to a large number of scaling laws. Let us further simplify the expression in the limit $\epsilon \longrightarrow 0$, obtaining the following scaling laws:

$$\text{Mass Function}: \frac{\mathrm{d}\log M_{total}}{\mathrm{d}\ln M} = 0 \longrightarrow \frac{\mathrm{d}N}{\mathrm{d}M} \propto M^{-2} \tag{7.6}$$

$$\text{Density PDF}: \frac{\mathrm{d}\log M_{total}}{\mathrm{d}\ln \rho} = 0 \longrightarrow \frac{\mathrm{d}V}{\mathrm{d}\ln \rho} \propto \rho^{-1} \tag{7.7}$$

$$\text{Column Density PDF}: \frac{\mathrm{d}\log M_{total}}{\mathrm{d}\ln \Sigma} = 0 \longrightarrow \frac{\mathrm{d}A}{\mathrm{d}\ln \Sigma} \propto \Sigma^{-1} \tag{7.8}$$

A more rigorous derivation of the above scalings is presented in Sec. 7.4 for the special case of a fragmentation cascade.

Note that the above scaling relations have been derived numerous times for different systems using very different methods (e.g. using random fields for the DM halo mass function Press & Schechter 1974 or competitive accretion for the IMF Bonnell et al. 2007). While these models seem to describe very different physics, they can be all labeled as a realization of scale-free structure formation with uncorrelated scales, and thus they will tend towards the scaling relations of Eqs. 7.5-7.8.

7.3 General Model for Scale-Free Fragmentation

In this section we develop a simple but general model for self-similar fragmentation cascades which describe a significant portion of the physical phenomena we list in Sec. 7.1 (e.g. formation of stars, cores, clumps). Our aim is to clearly demonstrate for this subclass that the scaling relations of Eq. 7.5-7.8 are inherent in these processes. In the model we present here we build on the models presented in Guszejnov et al. 2016 and Guszejnov et al. 2017b henceforth referred to as GKH16 and GH17.

Imagine an initial "cloud" of mass M_0 and size R_0 (e.g. for stars and cores this would be a GMC). This and all subsequently forming clouds are contracting and have a small, but finite chance ϵ of collapsing to infinite density and zero size (forming a star). Alternatively (with probability $1-\epsilon$) it fragments into

Parameters	
ϵ	Probability that a cloud does not fragment as it collapses.
λ	Average contraction scale when fragmentation occurs.
κ	Average mass of fragment relative to parent.
Variables	
M_n	Mass of n^{th} generation clouds.
R_n	Size scale of n^{th} generation clouds.
$M_*(M_n)$	Total mass of n^{th} generation stars.
ρ_n	Initial density of n^{th} generation clouds.
$M_{surv,n}$	Mass of all surviving objects after n fragmentation events.
Initial Conditions	
M_0	Mass of the initial cloud
R_0	Size scale of the initial cloud.

Table 7.1: Parameters and variables in the toy fragmentation model we use to demonstrate the effects of scale-free behavior (see Fig. 7.1).

a number of fragments ($1/\kappa$) with mass=κM_0 after contracting by some factor λ in size (see Fig. 7.1). Afterwards the gas rearranges itself while conserving density. The process is repeated for each newly formed cloud fragment[3]. To make our results normalizable we assume that there is a finite number of fragmentation events, in other words: the cascade is terminated. This is due to the breakdown of the scale-free assumption, in case of molecular clouds this is due to non-isothermal effects at high densities. Table 7.1 shows the parameters and variables of the model[4] . Note that to have an inertial range of significant size it must be true that $\epsilon \ll 1$.

7.3.1 Effects of Gravitational Collapse

Let us assume that fragmentation happens due to the Jeans instability (equivalently we could say all fragments have the same virial parameter). In an isothermal medium $M_{\mathrm{Jeans}} = const. \times \rho^{-1/2}$, so if we have a cloud that is marginally Jeans unstable ($M = M_{\mathrm{Jeans}}(1)$) then after it shrinks to λ times its original size the new Jeans mass becomes

$$M_{\mathrm{Jeans}}(\lambda) = M_{\mathrm{Jeans}}(1)\lambda^{3/2}. \tag{7.9}$$

---

[3] Note that this process is highly hierarchical with multiple object forming out of a single cloud, making it different from the well-known single, spherical cloud evolution models (e.g. Larson, 1969; Penston, 1969).

[4] Note that the three parameters of the model all refer to mean quantities (e.g. κ is the *mean* relative mass of fragments). Our analysis aims to show that regardless of the underlying distributions, all self-similar fragmentation models produce a statistically similar result.

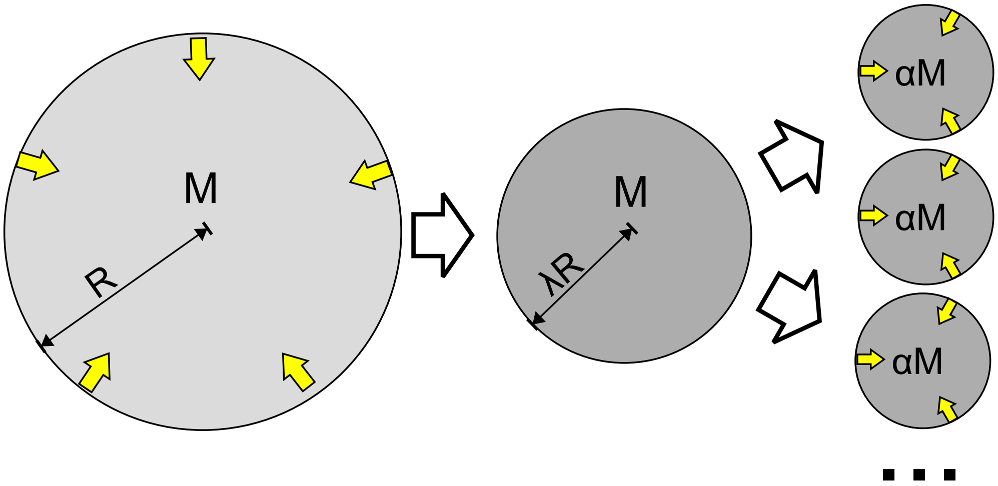

Figure 7.1: Cartoon illustrating the representative toy model for fragmentation, which we use in the text to demonstrate how scale-free fragmentation processes produce universal scalings. In the toy model, every cloud contracts by a factor λ (i.e. from initial radius R to $\lambda\,R$), before breaking into some number of sub-fragments, each with mass fraction κ of the parent clump mass. The fragments have the same density as their parent. A small fraction $\epsilon \ll 1$ of the clouds are “left behind” (or collapse without fragmentation) at each level. In physical systems self-similarity inevitably breaks down after some number of iterations (e.g. non-isothermal physics in molecular clouds at high densities), setting the dynamic range in which the model is applicable.

This cloud then fragments into several pieces, where each is roughly the Jeans mass, and thus the number of fragments is

$$N \equiv \kappa^{-1} = \frac{M}{M_{\mathrm{Jeans}}(\lambda)} = \lambda^{-3/2}. \tag{7.10}$$

In this case there is a clear connection between κ and λ such that

$$\ln\kappa = 3/2\ln\lambda. \tag{7.11}$$

Note that this simplistic analysis neglects other forms of cloud support (e.g. turbulence, rotation). Nevertheless, the simulations of GH17 find that turbu-

Generation (n)	M_n/M_0	R_n/R_0	$M_*(M_n)/M_0$	ρ_n/ρ_0	$M_{surv,n}/M_0$
0	1	1	ϵ	1	1
1	$(1-\epsilon)\kappa$	$\lambda[\kappa(1-\epsilon)]^{1/3}$	$\epsilon(1-\epsilon)$	λ^{-3}	$(1-\epsilon)$
2	$(1-\epsilon)^2\kappa^2$	$\lambda^2[\kappa(1-\epsilon)]^{2/3}$	$\epsilon(1-\epsilon)^2$	λ^{-6}	$(1-\epsilon)^2$
n	$(1-\epsilon)^n\kappa^n$	$\lambda^n[\kappa(1-\epsilon)]^{n/3}$	$\epsilon(1-\epsilon)^n$	λ^{-3n}	$(1-\epsilon)^n$

Table 7.2: Values of different variables (see Table 7.1 for definitions) for objects of different generations in our toy fragmentation model (see Fig. 7.1). Having a large dynamic range implies $\epsilon \ll 1$ (otherwise all the mass would be at the largest scales) which simplifies most of these expressions.

lence based fragmentation models yield results consistent with Eq. 7.11 (see Section 7.4.2). We will return to the importance of Eq. 7.11 below.

7.4 Universal Scaling Laws

For the case of scale-free fragmentation we can use our toy model to calculate the values of the variables from Table 7.1 with relative ease. The results are shown in Table 7.2.

7.4.1 Mass Function

First, if we look at the total mass of final objects (e.g. stars) in a given logarithmic mass bin ($M_*(M_n)$) in Table 7.2, we find it to be proportional to $\epsilon(1-\epsilon)^n$. In realistic cases $\epsilon \ll 1$ (required to have a large dynamic range) so we get

$$\frac{M_*(M_n)}{M_0} = \epsilon \left(\frac{M_n}{M_0}\right)^{\frac{\ln(1-\epsilon)}{\ln(1-\epsilon)+\ln\kappa}} \approx \epsilon \left(\frac{M_n}{M_0}\right)^{\frac{-\epsilon}{\ln\kappa}} \approx \epsilon = \text{const}, \tag{7.12}$$

where we used that $n = \frac{\ln M_n/M_0}{\ln(1-\epsilon)+\ln\kappa}$ in the first equality which we can infer from Table 7.2. The last approximation is only valid while $n \ll \epsilon^{-1}$, after that the expression becomes a very weak power-law (slope of $-\epsilon/\ln\kappa \approx 0$).

There is an equal amount of total mass per object mass in structures per logarithmic interval in mass of the final objects. Since the number of objects is (*Mass per bin*)/(*Mass of an individual object*), this leads to a mass function of $\propto M^{-2}$. This is in rough agreement with the slopes of the IMF, the core, the GMC, the star cluster and the dark matter halo mass functions (Alves et al. 2007; Bik et al. 2003; Offner et al. 2014; Rosolowsky 2005; Warren et al. 2006 respectively, see Fig. 7.2 for examples). Note that this conclusion is *independent* of the model parameters κ, λ and ϵ so long as there is a large dynamic range ($\epsilon \ll 1$) .

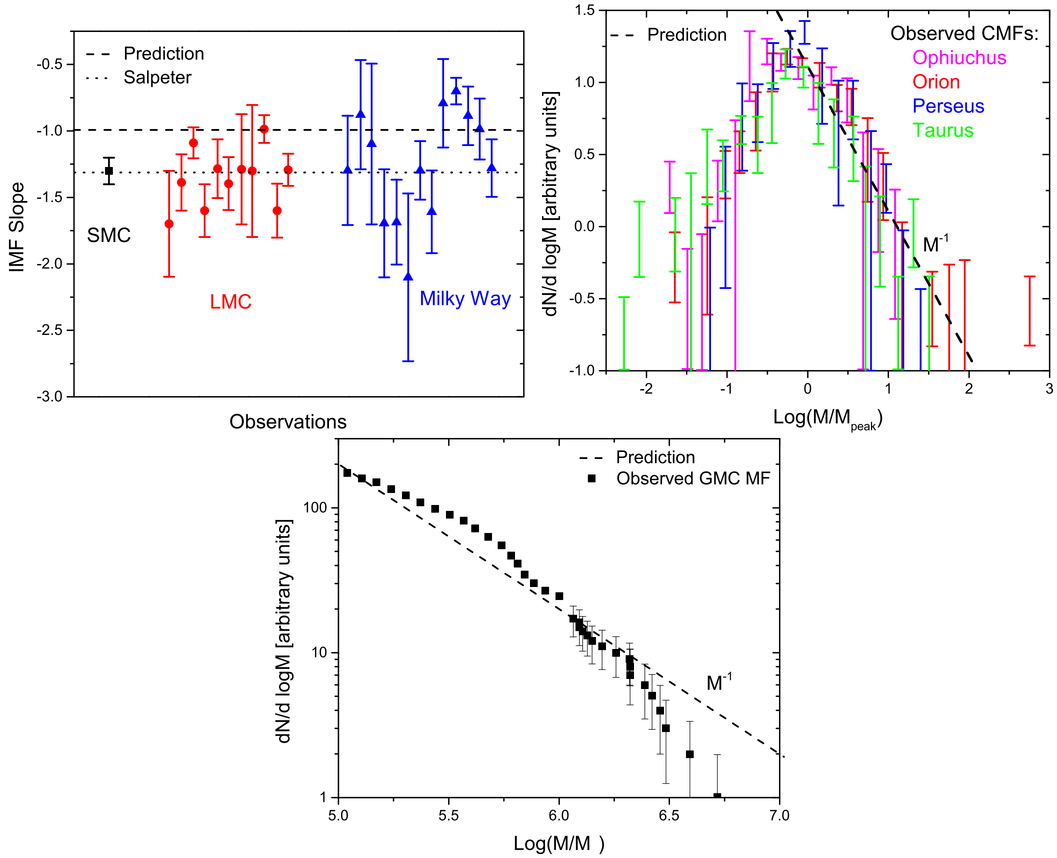

Figure 7.2: **Top Left:** The observed slopes of the high mass end of the IMF (Massey, 2003) along with the canonical Salpeter slope (Salpeter 1955, dotted line) and the prediction from our scale-free model (dashed line). Note that the error bars only account for fitting errors thus one should consider them lower estimates. The scale-free prediction of M^{-1} is slightly shallower than the best fit slope of -1.35 (Salpeter, 1955). **Top Right:** The observed CMF in different regions (Sadavoy et al., 2010) normalized in both axes. The observed high mass slope is roughly consistent with our prediction of M^{-1} (dashed). **Bottom:** The observed GMC mass function (Rosolowsky, 2005) along with our prediction (dashed line). The observations are roughly in line with the scale-free predictions for scales below the high mass cut-off.

7.4.2 Correlation Function

Let us now look at the correlation between objects of the same generation (mass). By only taking objects that formed after exactly n fragmentation events we can calculate the fractal dimension of this ensemble. The number of such objects is $N_n = M_*(M_n)/M_n = \epsilon\kappa^{-n}$. If we focus on one of these objects and draw a sphere of radius R_m around it we have $N_n(R_m) = \epsilon\kappa^{m-n}$ objects in it[5]. Using $R_m = \lambda^m\left[\kappa(1-\epsilon)\right]^{m/3}$ from Table 7.2 we find the fractal dimension to be

$$D \sim \frac{\mathrm{d}\ln N_n(R_m)}{\mathrm{d}\ln R_m} = \frac{\ln\kappa}{\frac{1}{3}\ln\kappa + \frac{1}{3}\ln(1-\epsilon) + \ln\lambda}. \tag{7.13}$$

Combined with Eq. 7.11 this yields $D = 1$. Since our model is isotropic the fractal dimension is related to the the two-point correlation function. For the 3D and the (observable) 2D correlation functions this leads to $\xi_{3D} \propto r^{-2}$ and $\xi_{2D} \propto r^{-1}$ respectively (using Eq. 7.38, see Sec. 7.A for details), which are in agreement with the simulation results from GH17 and Grudić et al. (2016). These predictions also roughly agree with the observed stellar and DM halo correlation functions (see Fig. 7.3) on intermediate scales[6]. This is compared to simulations in Fig. 7.3.

7.4.3 Density PDF

Using Table 7.2 we find the volume occupied by n^{th} generation objects at their formation (V_n) to be:

$$\frac{V_n}{V_0} = \frac{M_{surv,n}/\rho_n}{M_0/\rho_0} = \frac{M_{surv,n}}{M_0}\left(\frac{\rho_n}{\rho_0}\right)^{-1} = (1-\epsilon)^n\left(\frac{\rho_n}{\rho_0}\right)^{-1}. \tag{7.14}$$

Using $n = -\frac{1}{3\ln\lambda}\ln(\rho_n/\rho_0)$ we can replace n, and thus

$$\frac{V_n}{V_0} = \exp\left[-\ln(\rho_n/\rho_0)\ln(1-\epsilon)/(3\ln\lambda)\right]\left(\frac{\rho_n}{\rho_0}\right)^{-1} = \left(\frac{\rho_n}{\rho_0}\right)^{-1-\frac{\ln(1-\epsilon)}{3\ln\lambda}}. \tag{7.15}$$

This fraction of the total volume once had objects of rho_n density inside them (these either fragmented or collapsed), which means that these regions have

---

[5] This can be verified by considering that within R_m radius of such an object are all other object that formed out of a single ancestor of R_m size.

[6] Note that due to the finite age of the Universe the spatial structure of DM on very large scales reflects the primordial density fluctuations and is not related to the subject of this paper.

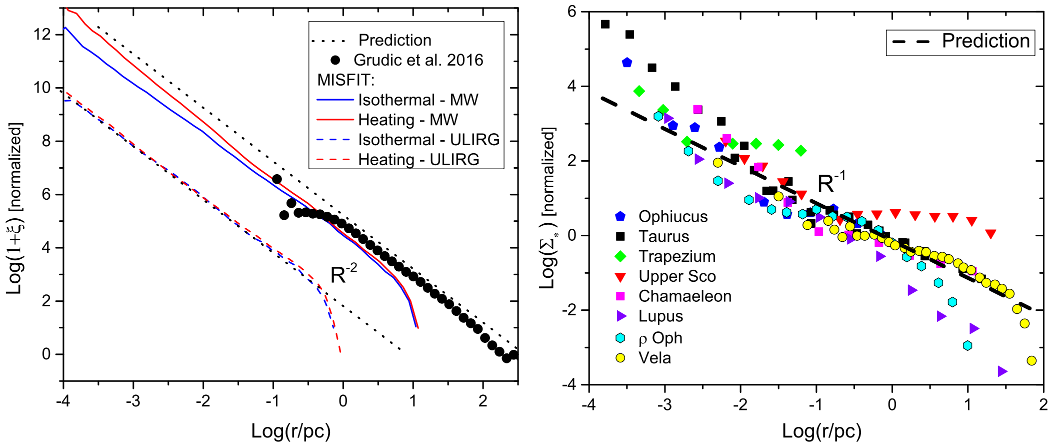

Figure 7.3: **Left:** Stellar correlation function for different detailed semi-analytic star formation models in GH17, specifically an "isothermal" simulation and a model including "protostellar heating", with MW-like and ULIRG-like initial conditions, along with the results of the full-numerical MHD simulations of Grudić et al. (2016). The initial conditions and underlying physics have limited effect on the behavior, which is close to the predicted power law of -2. The different large scale cut-offs are introduced by the different initial cloud sizes, and the different normalization simply results from the different linewidth-size relation between the Milky Way and ULIRG cases. **Right:** Observed surface density of neighboring stars (Σ_*, which is proportional to the projected correlation function ξ_{2D}) observed in different regions (labeled) Chamaeleon, Ophiucus, ρ Oph, Taurus, Trapezium, Upper Sco, Lupus and Vela by Hartmann 2002; Hennekemper et al. 2008; Kraus & Hillenbrand 2008; Nakajima et al. 1998; Simon 1997. Our prediction of a power law with slope of -1 seems to match these on larger scales.

an average density of rho_n. The binning by n is a logarithmic so

$$V_n = \frac{\mathrm{d}V}{\mathrm{d}n} = \frac{\mathrm{d}V}{\mathrm{d}\ln\rho}\frac{\mathrm{d}\ln\rho}{\mathrm{d}n} \propto \frac{\mathrm{d}V}{\mathrm{d}\ln\rho}. \tag{7.16}$$

Thus the volume density PDF $\left(\frac{\mathrm{d}V}{\mathrm{d}\ln\rho}\right)$ should scale as

$$\frac{\mathrm{d}V}{\mathrm{d}\ln\rho} \propto \rho^{-1-\frac{\ln(1-\epsilon)}{3\ln\lambda}} \approx \rho^{-1}, \tag{7.17}$$

where we assumed $\epsilon \ll 1$ in the last step. Note that $\epsilon < 1$ and $\lambda < 1$ so the slope of the PDF is, in general, predicted to be somewhat steeper than -1. However, the approximate slope is, once again, independent of the model details.

Note that this is a prediction for the density PDF of *all material which undergoes complete fragmentation* (e.g. goes on to form stars). It is not the same as the density PDF one would see at a given instant in time. To calculate the latter (the observable PDF), we need to convolve the PDF of clouds as they collapse with some observable "lifetime" (our model, thus far, makes no assumptions about the amount of *time* each step in the process actually takes). Since this requires some outside assumptions (which are unconstrained by the fundamental nature of fragmentation, and could be related to e.g. cooling, or dynamical, or turbulent processes), we do not wish to argue for any particular model for the lifetime in this paper, and so should take the comparison with observations with some caution. A reasonable possibility, however, would be to take the lifetime to be proportional to the freefall time $t_{freefall} \sim \rho^{-1/2}$; this would steepen the proposed slope by $1/2$ (giving an observable slope of $-3/2$). Other assumptions involving "slower" collapse (longer lifetimes) will generally produce slopes between -1 and $-3/2$.

Another important effect comes from the the density profile of the individual clouds. In our model we assumed all clouds to be homogeneous while in reality they develop significant density gradients. The overall density PDF is a convolution of this density profile and the PDF we predicted for homogeneous clouds.

7.4.3.1 Previous Results in the Literature

There have been previous significant theoretical efforts to model the slope of the density PDF. Many of these were based on numerical simulations (e.g. Audit & Hennebelle, 2010; Ballesteros-Paredes et al., 2011c; Federrath & Banerjee, 2015; Federrath et al., 2010c; Klessen & Burkert, 2001; Ostriker et al., 1999; Scalo et al., 1998b; Squire & Hopkins, 2017; Vázquez-Semadeni & García, 2001), which we discuss below. There have also been several analytic models proposed, many of which are similar in spirit to Girichidis et al. (2014), who assumed self-similar collapse, with individual clouds observable (or "surviving") at a given density for a time proportional to their free-fall time, and predict a slope of -1.54 (while our model predicts -1.5, for the same observable-time assumption).[7]

---

[7] Note that there is a small error in Eq. 12 in Girichidis et al. (2014) where the authors inadvertently assumed that volume is conserved in cloud evolution, despite modeling shrinking clouds. This can be easily corrected by replacing their Eq. 12 with the mass-conserving version of the equation (which they present earlier); after accounting for this

7.4.3.2 Column Density PDF

Because the volume density PDF itself is not directly observable, let us calculate the PDF for the line integrated (surface) density Σ. To do that we choose a random line of sight to integrate along that goes through the cloud we are interested in. Let us denote the chance that such a random line goes through one of the dense substructures of the cloud with p ($\epsilon \ll 1$ so we neglect the case when cloud does not have substructure). If the line avoids the substructures the line integrated density is $\Sigma_0 \sim \rho_0 R_0$ whereas if it hits the dense region we get $\Sigma_1 \sim (R_0 - R_1)\rho_0 + R_1\rho_1$. From Table 7.2 it is easy to see that

$$\frac{\Sigma_1}{\Sigma_0} \sim 1 + \frac{R_1}{R_0}\left(\frac{\rho_1}{\rho_0} - 1\right) = 1 + \lambda[\kappa(1-\epsilon)]^{1/3}\left(\lambda^{-3} - 1\right) \approx 1 + \lambda^{-2}\kappa^{1/3}. \tag{7.18}$$

Using the Jeans collapse condition (Eq. 7.11) we find that $\lambda^{-2}\kappa^{1/3} = \lambda^{-3/2}$ which is much greater than 1 for realistic cases. This means that the line integrated density is dominated by the densest substructure along the line of sight. In general we get:

$$\frac{\Sigma_n}{\Sigma_0} = \left(\lambda^{-2}\kappa^{1/3}\right)^n. \tag{7.19}$$

Since p is the probability of hitting the dense substructure of a cloud, the probability of the densest region along our line of sight to be from generation n is $P_n = (1-p)p^n$ as it needs to penetrate exactly n levels of substructure. We can directly calculate p because it is the cross section of the dense subregions relative to their parent (while taking into account that there are κ^{-1} of them), so

$$p = \frac{\kappa^{-1}\pi R_{n+1}^2}{\pi R_n^2} = \kappa^{-1}[\kappa(1-\epsilon)]^{2/3}\lambda^2 \approx \kappa^{-1/3}\lambda^2. \tag{7.20}$$

Now, using Eq. 7.20 and Eq. 7.19 we find the total area with Σ_n surface density is

$$\frac{A_n}{A_0} = (1-p)p^n \propto p^n = \left(\frac{\Sigma_n}{\Sigma_0}\right)^{-\frac{1}{n}n} \propto \Sigma^{-1}. \tag{7.21}$$

Similar to the volume density case the logarithmic binning in n leads to

$$A_n = \frac{\mathrm{d}A}{\mathrm{d}n} = \frac{\mathrm{d}A}{\mathrm{d}\ln\Sigma}\frac{\mathrm{d}\ln\Sigma}{\mathrm{d}n} \propto \frac{\mathrm{d}A}{\mathrm{d}\ln\Sigma} \to \frac{\mathrm{d}A}{\mathrm{d}\ln\Sigma} \propto \Sigma^{-1}, \tag{7.22}$$

where we have used Eq.7.19.

---

correction (which amounts to one power of ρ) the result is that their -1.54 result is directly comparable to our -1.5.

Just like the volume density PDF, the surface density PDF is affected by the finite observable lifetimes of clouds; as noted before this will steepen the slope, most likely producing final slopes roughly between −1 and −2. So any comparison with observations must be considered with caution here.

Fig. 7.4 shows surface density PDFs in two simulations: the MISFIT semi-analytic framework (see Guszejnov & Hopkins, 2016) and the detailed MHD simulations of Grudić et al. (2016). In both simulations star forming regions develop a similar power-law tail once the fragmentation cascade begins, a phenomenon that has been observed in other simulations (e.g. Kritsuk et al. 2011) as well. Here (in the simulations) we have the advantage that we can *specifically* isolate gas which is un-ambiguously known to be star-forming, which also means it is self-gravitating and undergoing fragmentation (thus, is in the regime where our model should apply). In Fig. 7.5 we show that this can have drastic effects. The star forming regions we are observing are embedded in much larger reservoirs of gas which is not undergoing a fragmentation cascade, so our model is not applicable there[8]. Meanwhile the line of sight for our observation integrates the density in these regions too. The net result is that instead of the PDF of the star forming region we see a convolution of that and the background density profile, which leads to a much steeper density PDF than predicted by our model.

Comparing to observations is more difficult because of both the lifetime effects and the difficulty of separating "non-fragmenting" (even if dense) cloud material from that which is truly experiencing runaway fragmentation. But there have been a number of studies of the density structure of molecular clouds (e.g. Kainulainen et al. (2009); Lombardi et al. (2014); Schneider et al. (2013)) which found that the column density PDF in molecular clouds is best described by a lognormal peak at low and a power law tail at high densities. On average these studies have found an average slope of ~ -2.3 (significantly steeper than our analytic prediction). But it has been shown (see Schneider et al., 2015b) that these measurements are actually dominated by the mass profile of the parent clouds[9]. In other words, just like in the simulation, the

---

[8] This does not mean that this larger reservoir is not evolving it roughly follows the isothermal collapse models formulated for spherically symmetric, non-fragmenting clouds, which leads to the development of its own density profile and PDF. The key difference is that in this regime pressure effects are not negligible. For a discussion of the resulting density PDF see Kritsuk et al. (2011).

[9] For a spherically-symmetric cloud with a radial mass profile of $\rho \propto r^{-\beta}$, one obtains a volume-density PDF of $\mathrm{d}V/\mathrm{d}\ln\rho \propto \rho^{-3/\beta}$ and a surface-density PDF of $\mathrm{d}A/\mathrm{d}\ln\Sigma \propto \Sigma^{-2/(\beta-1)}$,

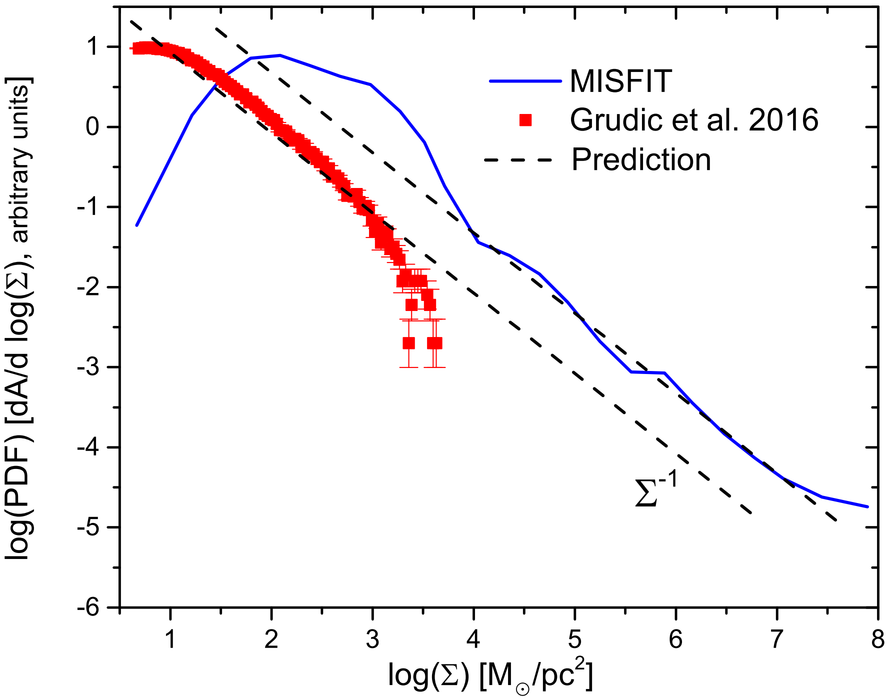

Figure 7.4: Surface density (Σ) PDF of star-forming gas in the detailed MHD simulation of Grudić et al. (2016) and in one of the GMC collapse simulations using the MISFIT semi-analytical framework (see Guszejnov & Hopkins 2016 for details). After the fragmentation cascade begins the system develops a Σ^{-1} power law tail in line with the predictions of the scale-free model. Note that both of PDFs take only the star forming gas into account.

measured surface density PDF is a convolution of the global mass profile, and the PDF driven by fragmentation and turbulence within an annulus of constant density. Our result in Eq. 7.22 is the surface density PDF that would be measured in such a fragmenting, constant background density annulus of a cloud – we intentionally have *not* made any assumption about embedding our (local) fragmentation model inside some (global) mass profile of a parent cloud (if we did, we could easily fit these observations, but it would only reflect the assumed mass profile).

Allowing for a background density profile with locally collapsing regions, one generically expects the following: at the highest densities, the density PDF should be dominated by collapsing, star-forming regions, which should (if our model is correct) follow our prediction with an approximately -1 slope. At lower (intermediate) densities, where not all the material is locally self-

---

so a slope of ~ -2 in $\mathrm{d}A/\mathrm{d}\ln\Sigma$ corresponds to an isothermal-sphere density profile $\rho \propto r^{-2}$.

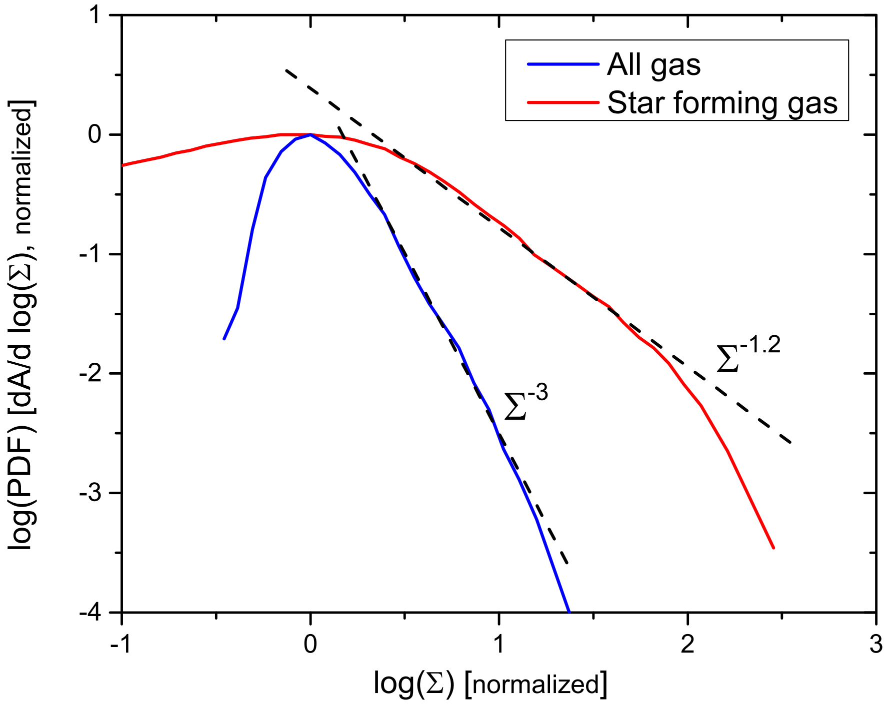

Figure 7.5: Surface density (Σ) PDF of star-forming gas vs all gas associated with the molecular cloud in the detailed MHD simulation of Grudić et al. (2016). We define star forming gas as fluid elements in a converging flow within a self-gravitating structure of molecular gas. Both axes are normalized so that the peak of both PDFs are unity at $\Sigma = 1$. Similar to Lin et al. (2017) we find that star forming gas produces a surface density PDF with a power-law slope of -1.2, close to our prediction of -1, while the distribution for the total gas has a much steeper power-law tail. This is because we integrate along the entire line of sight, and thus our measurement is sensitive to the background density profile of the non-star-forming gas.

gravitating and fragmenting, one becomes dominated by the combination of turbulent density fluctuations and the background density profile of the cloud, and the PDF will have a steeper slope that matches the cloud profile. Interestingly, Schneider et al. (2015a) claim to see almost exactly such a transition, with steeper slopes ~ -2.3 at intermediate densities (matching their fits to the global mass profile) and a shallower slope (or "excess" in their terms) appearing at approximately $\Sigma \gtrsim 100\,\langle\Sigma\rangle$ with a slope $\approx -1 \pm 0.2$. Similarly, Lin et al. (2017) see in the survey of clouds that the PDF becomes systematically shallower, approaching -1, as clouds (or cloud regions) become more actively star-forming. We should also note that similar results have been seen in other numerical simulations (e.g. Burkhart et al., 2015).

7.4.4 Cluster Mass Profile

Let us assume that some fraction of objects formed remain gravitationally bound to each other. We expect that the clustered substructures that formed from fragmentation will eventually merge together into a cluster with a density profile that decreases monotonically. Let us derive the power law index of this profile.

Using our model we can calculate the relation between the densities and the survivor masses before the objects rearrange themselves into clusters. For density, take their at-formation value (ρ_n). We can express the index n as:

$$n = \frac{\ln(M_{surv,n}/M_0)}{\ln(1-\epsilon)}, \tag{7.23}$$

$$n = -\frac{1}{3\ln\lambda}\ln(\rho_n/\rho_0), \tag{7.24}$$

which leads to

$$\frac{\mathrm{d}\ln(M_{surv,n}/M_0)}{\mathrm{d}\ln(\rho_n/\rho_0)} = -\frac{\ln(1-\epsilon)}{3\ln\lambda} = const. \approx 0. \tag{7.25}$$

Let us assume (for now) that after formation the objects rearrange themselves to form clusters, while preserving the local volume density - i.e. the local density (of stars) around a star does not change dramatically before/after the re-arrangement. This is motivated by the fact that during mergers, tidal shredding of an object with density ρ occurs at an orbital radius R, where the mean density enclosed within R is approximately ρ. This means that the amount of mass at different density levels must be the same as before the rearrangement, and thus

$$\frac{\mathrm{d}\ln(M_{cl}/M_{cl,0})}{\mathrm{d}\ln(\rho_{cl}/\rho_{cl,0})} = \frac{\mathrm{d}\ln(M_{surv,n}/M_0)}{\mathrm{d}\ln(\rho_n/\rho_0)}. \tag{7.26}$$

Let us assume the relaxed cluster has a power-law density profile: $\rho_{cl} \propto R^{\beta-3}$. Also, $\epsilon \ll 1$ thus the right hand side of Eq. 7.25 is zero. This leads to

$$\frac{\beta}{\beta-3} = 0, \tag{7.27}$$

thus $\beta = 0$, so the mass profile of a bound cluster that results from the assembly of substructures formed in a scale-free fragmentation cascade is $\rho_{cl} \propto R^{-3}$.

We can repeat the same exercise while assuming that *phase space density* (ρ_p)

is conserved instead of real space density, as per Liouville's theorem. This is only true, however, if ρ_p is resolved on infinitely fine scales, as elements of higher phase space density effectively get stretched out and diluted in phase space so that the final observed coarse-grained phase space density is generally lesser than the initial (Lynden-Bell, 1967). However, we may still suppose that our self-similarity condition means that the evolution operator on the coarse-grained phase space density can only map an initially flat ($\mathrm{d}M/\mathrm{d}\ln\rho_p \sim 0$) phase space distribution into another flat distribution.

We can approximate the phase space density as $\rho_p \approx \frac{\rho}{\sigma^3}$ where σ is the velocity dispersion. Assuming that the collapsing clouds are virialized we can write

$$\sigma_n^2 = \frac{GM_n}{R_n} = \frac{GM_0}{R_0}(1-\epsilon)^n \kappa^n \lambda^{-n} [\kappa(1-\epsilon)]^{-n/3}, \tag{7.28}$$

which leads to

$$\rho_{p,n} = \rho_{p,0} \left(\lambda^{3/2}\kappa(1-\epsilon)\right)^{-n}. \tag{7.29}$$

From here we can formulate the surviving mass per phase density (similar to Eq. 7.25):

$$\frac{\mathrm{d}\ln(M_{surv,n}/M_0)}{\mathrm{d}\ln(\rho_{p,n}/\rho_{p,0})} = -\frac{\ln(1-\epsilon)}{-\frac{3}{2}\ln\lambda - \ln\kappa - \ln(1-\epsilon)} \approx 0, \tag{7.30}$$

where, in the last step, we used the assumption that $\epsilon \ll 1$. Since we are interested in the asymptotic case at large radii. The mass enclosed is approximately converged ($M \approx const.$) thus

$$\sigma_{cl}^2(R) = \frac{GM}{R} \propto R^{-1}, \tag{7.31}$$

so we get

$$\rho_{p,cl}(R) \propto \frac{\frac{M_{cl}(R)}{R^3}}{R^{-3/2}} \propto R^{\beta-3/2}. \tag{7.32}$$

After plugging into Eq. 7.26 and using Eq. 7.30 this yields

$$\frac{\beta}{\beta - 3/2} = 0, \tag{7.33}$$

which, once again, means that $\beta = 0$ leading to $\rho_{cl} \propto R^{-3}$.

Now, let us compare our prediction with observations. The observed brightness profile of young star clusters is often parametrized using the EFF profile (Elson et al. 1987):

$$\mu(r) = \mu_0 \left(1 + \frac{r^2}{a^2}\right)^{-\gamma/2}, \tag{7.34}$$

where μ_0 is a constant, a is the cluster scale radius and γ is the power law index of the outer profile. Because $\mu \propto \Sigma \sim \rho R$ this represents an outer column density profile with $-(\gamma+1)$ slope, so in this parametrization our prediction is $\gamma = 2$. Observations young massive clusters, both within the Local Group (Elson et al., 1987; Mackey & Gilmore, 2003a,b; Portegies Zwart et al., 2010) and in extragalactic environments (Larsen, 2004; Ryon et al., 2015) have found that typically $\gamma \in [2,4]$, with a median around 2.5 (see Fig. 7.6). Meanwhile the density profile of dark matter halos is well fit by the NFW profile Navarro et al. (1996) that simplifies to a $\rho \propto r^{-3}$ on large scales, corresponding to $\gamma = 2$. In Grudić et al. (2017) we explore the physics of hierarchical cluster assembly, and its imprint upon the density profiles of objects thus formed, in greater detail.

7.4.5 Comparison with multi-physics simulations

In Figures 7.3, 7.4 and 7.6 we show that the predictions of our simple scale-free model are in good agreement with the simulations of Grudić et al. (2016) that follow the process of star formation in a molecular cloud. Our toy model of the fragmentation cascade and these simulations represent two extremes of approach to the problem of star formation: one seeks to minimize complexity, whereas the other seeks to maximize realism by including a variety of pieces of physics that could potentially be relevant. Under the forces of MHD and gravity the star-forming clouds collapse into a complicated structure of dense filaments (e.g. Collins et al., 2012) that is difficult to reconcile with an idealized picture of fragmenting gas balls (e.g. Figure 7.1). The realistic ISM equation of state with radiative cooling and stellar feedback (see Hopkins et al. 2017b for details) leads to the formation of a multi-phase ISM, so the isothermality we have assumed does not strictly apply.

Despite all of these complications the simulations and the toy model ultimately arrive at the same scaling relations. The simulation follows hierarchical fragmentation over a significant dynamic range in which the process, despite all the above complications, is roughly scale-free. Although real star-forming systems are more complicated than any simulation, this apparent robustness to such complications suggests that the observed scalings could be (to first order) explained as fundamental consequences of scale-free structure formation.

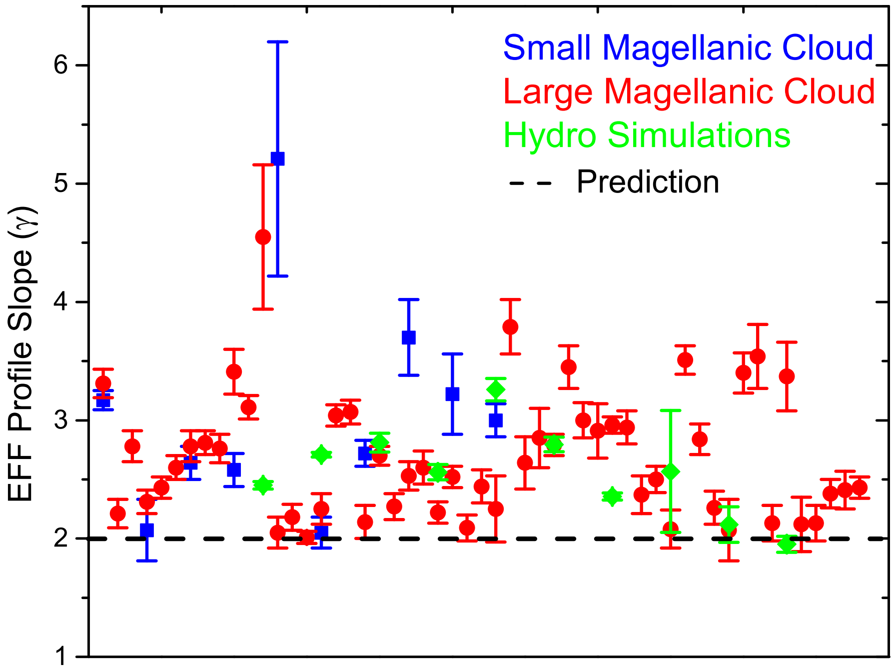

Figure 7.6: The observed surface brightness profile slopes (using the profile of Elson et al. 1987) of several stellar clusters from the LMC (Mackey & Gilmore, 2003a) and the SMC (Mackey & Gilmore, 2003b) along with the scale-free prediction (dashed line). For reference we included the cluster population produced in one of the detailed MHD simulations of Grudić et al. (2016). Both observed and simulated clusters seem to have steeper profiles than predicted by the scale-free model. This is due to the fact that $\gamma \sim 2$ is only the limiting case for an infinitely-extended hierarchical merger history (see Grudić et al. 2017 for more details).

7.5 Conclusions

In this paper we showed that there are universal scaling relations that generally arise in scale-free models of structure formation with a large but finite dynamic range and no correlation between scales. These relations are shared between very different phenomena, including the formation of stars, protostellar cores, clumps, giant molecular clouds, star clusters and even dark matter halos. Despite their differences all these processes can be approximately described by the dimensionless version of the pressure-free Euler equation with self-gravity. The only parameter of this equation is the virial parameter, which is of course how we define gravitationally bound structures. Thus a hierarchical structure building process would follow the same equation for all these systems on a wide range of scales. This means that (to first order) the formation of these (very different) gravitationally bound structures produces the same scaling relations for a wide range of physical quantities.

We demonstrate these universal scaling relations for a subclass of processes that can be described as a fragmentation cascade (e.g. formation of molecular clouds). We present a minimalist model of self-similar fragmentation with which we show that any scale-free model with a large dynamic range where the scales are uncorrelated (the fluctuations on different scales "don't know about each other") is able to reproduce the following scaling relations:

- *Mass functions*: $\frac{\mathrm{d}N}{\mathrm{d}\ln M} \propto M^{-1}$. In the scale-free regime we expect objects of all sizes to follow this scaling relation. For the stellar initial mass function (*IMF*, see Bastian et al. 2010; Offner et al. 2014), the protostellar core mass function (*CMF*, see Sadavoy et al. 2010), the *molecular clump mass function* (see Johnstone & Bally, 2006), the giant molecular cloud mass function (*GMC mass function*, see Rosolowsky 2005), the *star cluster mass function* (see Bik et al., 2003) and the dark matter halo mass function (Press & Schechter, 1974) this regime is observed over a wide dynamic range above/below some minimum/maximum scale where our assumptions are violated. This relation means that there is a comparable amount of mass in objects at all mass scales.

- *Density and column density PDF*: $\left(\frac{\mathrm{d}V}{\mathrm{d}\ln\rho}\right)_{observ} \propto \rho^{-1}$ and $\frac{\mathrm{d}A}{\mathrm{d}\ln\Sigma} \propto \Sigma^{-1}$. The observed *column density PDFs of star forming molecular clouds* exhibit a power-law tail consistent with this prediction (see Schneider et al., 2015a), which is built up by the hierarchical fragmentation of clouds. This is a scale-free process as long as we are in the isothermal phase of the ISM. The scaling can be understood as having an equal amount of mass at all density scales. Note that our model does not account for observational biases (e.g. cloud lifetimes) which can lead to systematic differences with observations.

- *Correlation functions*: $\xi_{3D} \propto r^{-2}$ and $\xi_{2D} \propto r^{-1}$. Note that unlike the predictions above, this depends on the form on the fragmentation criterion so it is not completely generic. But if we assume that the criterion is set by gravity (as it is in all the above cases), this provides a good fit to the observed behavior of the *stellar correlation function* at larger scales (e.g. Hennekemper et al., 2008; Kraus & Hillenbrand, 2008). Similarly the observed *protostellar core correlation function* is roughly consistent with this power-law behavior (see Stanke et al., 2006). For the *correlation function of star clusters*, this prediction agrees well with observations on scales smaller than the galactic scale height, above which the problem changes dimensionality (see Grasha et al., 2017). For the case of DM halos this prediction is consistent with the measured correlation on intermediate scales (Baugh, 1996; Sołtan & Chodorowski, 2015) as the finite age of the Universe causes the very large scale structures to reflect the primordial initial conditions. A possible interpretation of this slope is that it implies a fractal dimension of unity which further implies filamentary structures. Note that this is not generally true, for example our fragmentation model of Sec. 7.3 or even the Cantor-dust produces similar correlation functions, while none of them exhibit filamentary behavior.

- *Cluster mass profile*: $\rho_{cl} \propto R^{-3}$ (or $\gamma = 2$ using the EFF fitting function from Elson et al. 1987), if we further assume that the process responsible for arranging objects into clusters is also scale-free. This is a somewhat shallower slope than what is observed for star clusters (see Mackey & Gilmore, 2003a,b), because $\gamma \sim 2$ is only the limiting case for an infinitely extended hierarchical merger history (see Grudić et al. 2016 for more details). This scaling can be understood as the cluster having equal mass at each distance scale from its centre, as a result of free mixing.

We wish to emphasize that these scaling relation are not unique to the fragmentation cascade paradigm. Any scale-free structure building process that satisfies the requirements of Sec. 7.2 would recover them. The reader should also note that these universal scaling relations cannot explain all observed scaling laws. For example, the linewidth-size and mass-size relations in molecular gas ($\sigma^2 \propto R$ and $M \propto R^2$ respectively, see Bolatto et al. 2008; Larson 1981; Scoville et al. 1987 for details) require additional physics. One possible candidate is supersonic turbulence, which naturally reproduces the linewidth-size relation (Kritsuk et al., 2013) due to its power-spectrum (Murray, 1973). If one further assumes that the clouds are virialized, it naturally follows that $GM/R \sim \sigma^2$ so $M \propto R^2$.

It is easy to see that the arguments in this paper are invariant under time reversal transformation (in other words they don't rely on an "arrow of time"). For the toy model presented in Sec. 7.3, this means that small objects merge to form ever bigger ones. This means that the predicted scalings should be present not only in hierarchical fragmentation but in the time-reversed process of hierarchical merging as well. This is the growth mechanism of galaxies and dark matter halos (Kauffmann et al., 1993; Lacey & Cole, 1993).

Our simple arguments provide a generic, natural reason why so many different models, with seemingly very different physics, have been able to reproduce some or all of these scaling relations: the relations do *not* depend on the detailed physics, so long as it is scale-free. It follows that these scaling relations cannot be used to observationally differentiate theories (i.e. almost any theory can reproduce the IMF slope) because to first order they all give the same answers. One should instead test models against unrelated scaling laws (e.g. linewidth-size relation, see above) or investigate the physical scale where the model predicts the scale-free assumption to break down (e.g. IMF turnover) and compare them to observations in that regime.

7.A Fractal Dimension and the Correlation Function

In this paper we use the fractal D dimension, which we define as

$$D\frac{\mathrm{d}\ln N(r)}{\mathrm{d}\ln r}, \tag{7.35}$$

where $N(r)$ is the average number of objects within r distance of a reference object.

In isotropic systems the fractal dimension is related to the $\xi_d(r)$ d dimensional correlation function, for which we use the standard definition of

$$\begin{aligned} P_d(r,dr) &= \frac{N(r,\mathrm{d}r)}{n,\mathrm{d}V_d(r)} \\ 1+\xi_d(r) &= \lim_{\mathrm{d}r\to 0} P_d(r,dr), \end{aligned} \tag{7.36}$$

where $N(r,\mathrm{d}r)$ is the average number of objects whose d dimensional distance from a reference object is $\in [r, r+\mathrm{d}r]$, n is the density of objects, $V_d(r)$ is the volume of a d-sphere so $\mathrm{d}V_d \propto r^{n-1}\mathrm{d}r$.

Assuming $\xi_d \gg 1$ we get

$$\xi_d(r) \propto \lim_{\mathrm{d}r\to 0}\frac{N(r,\mathrm{d}r)}{r^{d-1}\mathrm{d}r} = r^{1-d}\frac{\mathrm{d}N(r)}{\mathrm{d}r} = \frac{\mathrm{d}N(r)}{\mathrm{d}\ln r}r^{-d}. \tag{7.37}$$

Let us also assume that $N(r)$ is a power-law (this is true in scale-free systems like the ones in this paper), which yields

$$\xi_d(r) \propto r^{D-d}. \tag{7.38}$$

Chapter 8

ISOTHERMAL FRAGMENTATION: IS THERE A LOW MASS CUT-OFF?

Guszejnov, D., Hopkins, P. F., Grudić, M. Y., Krumholz, M. and Federrath, C. 2018. To be submitted to *MNRAS*.

Abstract

The evolution of self-gravitating clouds of isothermal gas forms the basis of many star formation theories. Therefore it is important to know under what conditions such a cloud will undergo homologous collapse into a single, massive object, or will fragment into a spectrum of smaller ones. And if it fragments, do initial conditions (e.g. Jeans mass, sonic mass) influence the mass function of the fragments, as predicted by many theories of star formation? In this paper we show that the relevant parameter separating homologous collapse from fragmentation is not the Mach number of the initial turbulence (as suspected by many), but the infall Mach number $\mathcal{M}_{\mathrm{infall}} \sim \sqrt{GM/(Rc_s^2)}$, equivalent to the number of Jeans masses in the *initial* cloud N_J. We also show that fragmenting clouds produce a power law mass function with slopes close to the expected -2 (i.e. equal mass in all logarithmic mass intervals). However, the low mass cut-off of this mass function is entirely numerical; the initial properties of the cloud have no effect on it. In other words, if $\mathcal{M}_{\mathrm{infall}} \gg 1$, fragmentation proceeds *without limit* to masses much smaller than then initial Jeans mass.

8.1 Introduction

The evolution of a gravitationally bound isothermal fluid is the "base model" for a large number of astrophysical phenomena, including the formation of stars. In the case of star formation the highly efficient cooling of molecular gas produces an approximately isothermal behaviour on a wide range of scales, so many "turbulent fragmentation" theories of star formation are based on the interaction between isothermal turbulence and gravity (e.g. Hennebelle & Chabrier, 2008, 2009, 2013a; Hopkins, 2012a; Padoan & Nordlund, 2002). Of course this neglects a huge range of physics (e.g. radiation, magnetic fields, optically thick cooling), but clearly one would like to understand this nominally simple case before considering additional physics.

Isothermal turbulence with gravity is inherently scale-free (Krumholz, 2014;

McKee & Ostriker, 2007a), so explaining the turnover in the initial mass function of stars (IMF) requires a mass scale from either additional, non-scale-free physics (e.g. protostellar heating, see Krumholz, 2011) or from initial conditions. The specific set of "turbulent fragmentation" models mentioned here all fall into the latter category: they predict that the initial turbulent properties imprint a mass scale ($M_{\rm sonic}$, the sonic mass) where the mass distribution starts deviating from the scale-free result (a power-law). However, other works (including some of the same authors) have argued that in a scale-free fragmentation cascade the initial conditions are quickly "forgotten" by the system (Guszejnov et al., 2016, 2017a) so the turnover in the IMF can *only* come from additional physics (e.g. Bonnell et al., 2006; Jappsen et al., 2005b; Larson, 2005).

There has been significant effort to numerically verify these claims. Most simulations find that "supersonic clouds" (we will define this rigorously below) fragment into a spectrum of smaller objects (e.g. Dobbs et al., 2006; Goodwin et al., 2004; Murray et al., 2015; Walch et al., 2012a) while "subsonic clouds" undergo homologous collapse (e.g. Gong & Ostriker, 2009, 2011) similar to the analytical Larson-Penston solution (Larson, 1969; Penston, 1969). Of the few convergence studies for the fragmenting case, some report non-convergence up to the highest probed numerical resolution (see e.g. Federrath et al., 2017; Kratter et al., 2010; Lee & Hennebelle, 2017; Martel et al., 2006), but a couple have claimed convergence (Gong & Ostriker, 2015; Haugbølle et al., 2017) in the mass function (despite the fact that their absolute resolution is comparable or lower than the studies claiming non-convergence).

It should be noted that there exists an analytic solution for a specific scenario of isothermal collapse, Inutsuka & Miyama (1992) showed that overdense cylinders collapse to infinite line density faster than they can fragment, and that systems that form such filaments (e.g. a slowly rotating Gaussian cloud, as in the widely used code test introduced by Boss 1991) should therefore not fragment to infinitely small scales. Still, it is not at all clear how these results generalize to other initial conditions.

Therefore, in this paper we use extremely high resolution simulations, reaching a maximum density resolution orders of magnitudes higher than the previous studies, to follow the evolution of a self-gravitating isothermal ball of gas, in order to explore the following questions:

- What are the conditions which determine when a cloud will fragment vs collapse homologously?
- Do the initial conditions (e.g. sonic mass, Jeans mass) imprint a mass scale into the mass function of the final fragments?
- Is there a converged low-mass cut-off for an isothermal fragmentation cascade, or does it proceed "indefinitely"?

Our paper is organized as follows. Sections 8.2+8.3 detail the equations solved and the numerical methods. Section 8.4 shows our results. We also detail a number of additional numerical tests in Appendix 8.A.

8.2 Isothermal Collapse

An isothermal, self-gravitating fluid is completely described by the following closed set of equations:

$$\begin{aligned} \frac{\partial}{\partial t}(\rho) + \nabla \cdot (\rho \mathbf{v}) &= 0, \\ \frac{\partial}{\partial t}(\rho \mathbf{v}) + \nabla \cdot (\rho \mathbf{v} \otimes \mathbf{v}) &= -\nabla P - \rho \nabla \Phi, \end{aligned} \tag{8.1}$$

where ρ and $\mathbf{v}$ are the usual fluid density and velocity, while $P = c_s^2 \rho$ is the thermal pressure ($c_s = \mathrm{const.}$ is the isothermal sound speed) and Φ is the gravitational potential ($\nabla^2 \Phi = 4\pi G \rho$, where G is the gravitational constant). By dividing out the characteristic scales of the system (size: L_0, density: ρ_0 and sound speed: c_s) we can make these equations dimensionless:

$$\begin{aligned} \frac{\partial}{\partial \tilde{t}}(\tilde{\rho}) + \tilde{\nabla} \cdot (\tilde{\rho} \tilde{\mathbf{v}}) &= 0, \\ \frac{\partial}{\partial \tilde{t}}(\tilde{\rho} \tilde{\mathbf{v}}) + \tilde{\nabla} \cdot (\tilde{\rho} \tilde{\mathbf{v}} \otimes \tilde{\mathbf{v}}) &= -\tilde{\nabla} \tilde{\rho} - \alpha \tilde{\rho} \tilde{\nabla} \tilde{\Phi}, \end{aligned} \tag{8.2}$$

where $\tilde{t} \equiv t c_s / L_0$, $\tilde{\nabla} \equiv L_0 \nabla$ and $\tilde{\Phi} \equiv \frac{\Phi}{G \rho_0 L_0^2}$, while $\alpha \equiv c_s^2 / (G \rho_0 L_0^2)$ is the (thermal) virial parameter. It is useful to introduce the Mach number $\mathcal{M} \equiv \frac{1}{3} \langle ||\mathbf{v}||^2 / c_s^2 \rangle = \langle ||\tilde{\mathbf{v}}||^2 \rangle$. In other words: by introducing the virial parameter α and the Mach number $\mathcal{M}$ we normalize the density and velocity fields (e.g. Gaussian velocity distribution, dispersion set by $\mathcal{M}$). In other words, the dynamics are *entirely* determined by the two dimensionless parameters α and $\mathcal{M}$, which are fixed by the initial conditions. The only way to imprint scales on the problem is therefore through these ICs.

8.2.1 Usual stability measures

When discussing the stability of an isothermal ball of gas the literature uses a large number of different quantities to characterize these systems. The most common is the *virial parameter*, which is the ratio of energy in random motion over the potential energy. In our case

$$\alpha \equiv \frac{E_{\text{random,kin}}}{E_{\text{pot}}} \sim \frac{M_{\text{cloud}}\left(\frac{3}{2}c_s^2 + \frac{1}{2}\langle||\mathbf{v}||^2\rangle\right)}{\frac{3}{5}\frac{GM_{\text{cloud}}^2}{R_{\text{cloud}}}} = \frac{5R_{\text{cloud}}c_s^2(1+\mathcal{M}^2)}{2GM_{\text{cloud}}}. \tag{8.3}$$

We can similarly define the *thermal virial parameter* that only takes thermal motion into account, which leads to

$$\alpha_{\text{thermal}} \equiv \frac{E_{\text{thermal}}}{E_{\text{pot}}} \sim \frac{5R_{\text{cloud}}c_s^2}{2GM_{\text{cloud}}} = \frac{\alpha}{1+\mathcal{M}^2}. \tag{8.4}$$

Since the behaviour of fluids drastically changes when they become supersonic, another measure is the *infall Mach number*, the characteristic velocity of infalling material relative to the sound speed, which in our case yields

$$\mathcal{M}_{\text{infall}} \equiv \frac{v_{\text{infall}}}{c_s} \sim \frac{\sqrt{\frac{1}{3}\frac{E_{\text{pot}}}{M_{\text{cloud}}}}}{c_s} \sim \sqrt{\frac{GM_{\text{cloud}}}{5R_{\text{cloud}}c_s^2}} = (2\alpha_{\text{thermal}})^{-1/2}. \tag{8.5}$$

Since the collapse of such isothermal clouds is mainly precipitated by the Jeans-instability, another common measure of stability is the *number of Jeans masses in the initial cloud*

$$N_J \equiv \frac{M_{\text{Jeans}}}{M_{\text{cloud}}} \sim \left(\frac{3GM_{\text{cloud}}}{4\pi R_{\text{cloud}}c_s^2}\right)^{3/2} = \left(\frac{15}{4\pi}\right)^{3/2}\mathcal{M}_{\text{infall}}^3. \tag{8.6}$$

In the case of turbulent fragmentation the initial turbulence has a characteristic mass scale, the sonic mass M_{sonic}. To find it let us suppose that the cloud virializes to $\alpha = 1$ as energy is transferred from gravity to turbulent motion. The characteristic size scale of turbulence is the sonic length R_{sonic}. This is where turbulent dispersion becomes supersonic, so

$$R_{\text{sonic}} \equiv R_{\text{cloud}}\frac{c_s^2}{\langle||\mathbf{v}_{\text{turb}}||^2\rangle} = \frac{R_{\text{cloud}}}{\mathcal{M}^2} \sim \frac{R}{\frac{2GM_{\text{cloud}}}{5R_{\text{cloud}}c_s^2} - 1}, \tag{8.7}$$

where we used the supersonic linewidth-size relation ($v_{\rm turb}^2 \propto R$). $M_{\rm sonic}$ is the mass of a self-gravitating ball of gas with $R_{\rm sonic}$ radius (see Hopkins 2013c), so

$$M_{\rm sonic} \equiv \frac{2\pi^2}{3}\frac{c_s^2 R_{\rm sonic}}{G}. \tag{8.8}$$

With Eqs. 8.5, 8.7 and 8.8 we can formulate the *number of sonic masses in the initial cloud*

$$N_S \equiv \frac{M_{\rm cloud}}{M_{\rm sonic}} \sim \frac{15}{2\pi^2}\mathcal{M}_{\rm infall}^2\left(2\mathcal{M}_{\rm infall}^2 - 1\right) \approx \frac{15}{2\pi^2}\mathcal{M}_{\rm infall}^4. \tag{8.9}$$

Note that $\alpha_{\rm thermal}$, N_J and N_S can be all expressed with the infall Mach number (see Eqs. 8.4-8.9) so we use only $\mathcal{M}_{\rm infall}$ as a proxy for all of them for the remainder of this paper.

8.3 Simulations

For our simulation we use the GIZMO code (Hopkins 2015)[1], with the mesh-free Godunov "MFM" method for hydrodynamics (Hopkins, 2015). Note that we get similar results with other numerical schemes (e.g. SPH), see Appendix 8.A.3. Self-gravity is included with fully-adaptive force and hydrodynamic resolution - no minimum force length is enforced. Since we are simulating an isothermal system with only self-gravity, the problem is scale-free and we can work in code units of $L = 2$, $c_s = 1$, $G = 1$, where L is the initial size of the box, c_s is the sound speed of the gas and G is the gravitational constant. We start by performing an isothermal driven turbulent box simulation without self-gravity (e.g. Federrath et al., 2010b; Price & Federrath, 2010; Schmidt et al., 2009) in which the driving force is realized as an Orstein-Uhlenbeck process following Bauer & Springel (2012), and consists of an equal mix of compressive and solenoidal modes. After several crossing times the root-mean-square Mach number saturates to $\mathcal{M} \sim 1$, and $\tilde{\rho}$ and $\tilde{\mathbf{v}}$ are extracted from the simulation to construct the initial conditions of the simulation with self-gravity. These are then rescaled in the following way:

- Velocities are rescaled so that $\langle ||\tilde{\mathbf{v}}||^2\rangle = 3\mathcal{M}^2$.
- The average density $\langle\rho\rangle$ is rescaled to satisfy Eq. 8.3.
- The relative density fluctuations are rescaled to satisfy $\langle|\ln\tilde{\rho}|^2\rangle = \ln\left(1 + b^2\mathcal{M}^2\right)$ (see Federrath et al., 2008), where $b = 1/2$ is the ratio of compressive

---

[1] `http://www.tapir.caltech.edu/~phopkins/Site/GIZMO.html`

and solenoidal driving in our initial condition. Effectively this means $\rho = f\left(1 - \frac{\langle\rho_{\mathrm{old}}\rangle}{\rho_{\mathrm{old}}}\right)\langle\rho\rangle + \langle\rho\rangle$, where $\langle\rho\rangle$ is set in the previous step and f is the appropriate scaling factor.

Note that in these initial conditions the density and velocity fields are not fully self-consistent. In Appendix 8.A.2 we show that using proper turbulent initialization does not affect our results. We also show that our results are insensitive to our choice of decaying or driven turbulence during collapse.

The simulation starts out with $M_{\mathrm{cloud}}/\Delta m$ gas particles, where Δm is our mass resolution (see Table 8.1 for details). These particles evolve (now with fully-adaptive self-gravity) following a discretized version of Eq. 8.2 (see Hopkins, 2015). They are turned into collapsed objects (sink particles) if they satisfy the following criteria, motivated by Federrath et al. 2010d:

1. They are locally self-gravitating at the resolution scale using the criteria from Hopkins et al. 2013a.
2. The mean density of this structure exceeds some ρ_{max}, at this point the thermal Jeans mass becomes unresolved following the Truelove criterion (Truelove et al., 1997).
3. They are part of a converging flow ($\nabla \cdot \mathbf{v} < 0$).
4. They are the densest of all particles within the stencil of interacting hydrodynamic cells, and there is no other sink particle within the kernel radius enclosing these interacting cells.

These sink particles can grow by accreting gas from their surroundings if the gas is gravitationally bound to the sink, within a hydrodynamic stencil, and not tightly bound to any other sink particle. In Appendix 8.A.4 we explore the effects of our choice of sink particle parameters.

Due to finite resolution our simulation cannot resolve the evolution and fragmentation of arbitrarily small structures. This means that we set our mass resolution to the Jeans mass corresponding to ρ_{max} (based on Truelove et al., 1997), so

$$M_{\mathrm{Jeans}}(\rho_{\max}) \sim \Delta m \;\rightarrow\; \rho_{\max} \sim \frac{c_s^6}{G^3 \Delta m^2},$$
$$\rho_{\max} \propto M_{\mathrm{cloud}}(\alpha)^{-2} \left(\frac{\Delta m}{M_{\mathrm{cloud}}}\right)^{-2} \propto \left(\frac{\Delta m}{M_{\mathrm{cloud}}}\right)^{-2} \alpha^2. \tag{8.10}$$

In this paper we examine the effects of varying the two physical parameters (the virial parameter α and the initial turbulent Mach number $\mathcal{M}$) on the evolution of an isothermal cloud. To ensure that our results are physical we carry out a resolution study by varying $\frac{\Delta m}{M_{\mathrm{cloud}}}$. A number of further tests for numerical effects are also carried out. They are detailed in Appendix 8.A. All simulations (with one exception noted) are run until the gas is largely exhausted and the sink particle IMF has remained stable for at least 2 cloud dynamical times.

8.4 Results

We carried out a suite of simulations in the α-$\mathcal{M}$ parameter space (our fiducial resolution is $\Delta m/M_{\mathrm{cloud}} = 4 \times 10^{-6}$) and found two distinct modes of evolution (see Fig. 8.1 for surface density snapshots and Fig. 8.2 for statistics). In the first case the collapse is close to homologous (most of the mass ends up in several massive objects) while in the second case the cloud fragments during collapse, forming a spectrum of low mass objects (most of the mass in low mass objects).

The mass spectrum resulting from fragmentation is the well known $\mathrm{d}N/\mathrm{d}M \propto M^{-2}$ distribution (see Fig. 8.2), which means equal mass at each mass scale (see Guszejnov et al. 2017a and references therein). Note that this mass spectrum is present even in the case of homologous collapse but only a small fraction of the total mass is bound in these low mass objects.

As Fig. 8.3 shows, there is no clear boundary in either the virial parameter α or the Mach number $\mathcal{M}$ between the two regimes. Instead it is the infall Mach number $\mathcal{M}_{\mathrm{infall}}$ that determines the mode of collapse[2]. The transition between homologous collapse and fragmentation occurs around $\mathcal{M}_{\mathrm{infall}} \approx 3$ (see Fig. 8.4). This boundary roughly corresponds to the point where the characteristic velocity of the infalling material becomes highly supersonic. This leads to

---

[2] Note that the number of initial Jeans and sonic masses as well as the thermal virial parameter are equally good predictors, because they are all trivial function of $\mathcal{M}_{\mathrm{infall}}$, see Sec. 8.2.1 for how they relate.

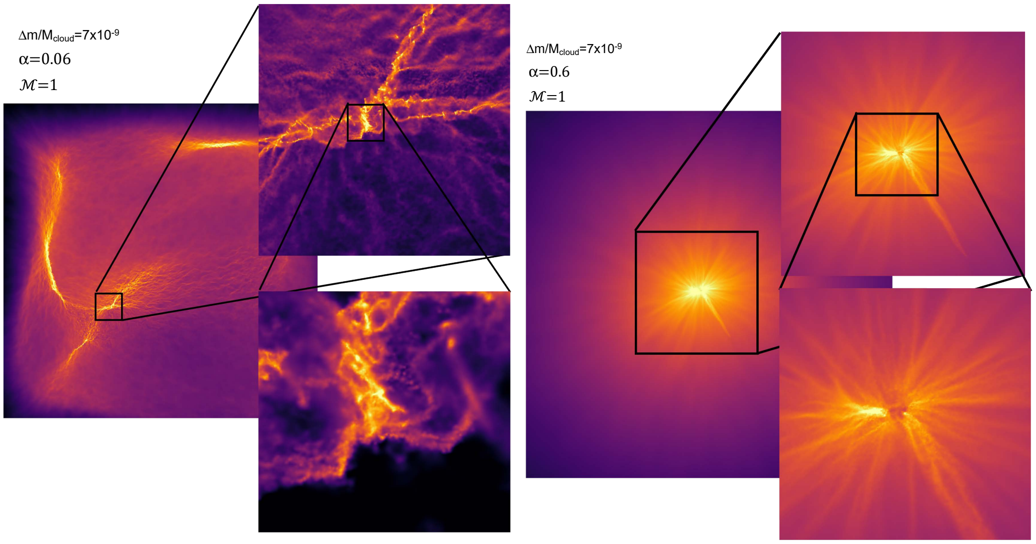

Figure 8.1: Typical density maps for isothermal fragmentation (left) and homologous collapse (right). On each figure the colormap is stretched over a 2 dex interval. In the fragmenting case (left) shocks from supersonic infall create dense, filamentary structures with high density "beads" embedded in them. Many of these structures are self-gravitating and undergo gravitational collapse, either forming sink particles or further fragmenting into even smaller objects. In case of homologous collapse there is only a single high density region at the centre of the cloud, which accretes most of the gas.

shocks which in turn lead to the formation of high density subregions that are self-gravitating and collapse on their own, causing the fragmentation of the cloud.

8.4.1 Effect of Resolution on the Mass Distribution

In the numerical study of isothermal turbulence the dynamic range (resolution) of the simulation plays an important role. If the dynamic range is too small, a multitude of phenomena might not manifest and the results are obscured by artificial edge effects. Since we are primarily interested in the spectrum of self-gravitating objects, let us consider the mass of the smallest resolvable self-gravitating object (Δm) in a generic simulation of isothermal Jeans fragmentation with N particles/grid points. We find that

- for fixed mass element (Lagrangian) codes: $\Delta m/M_{\mathrm{cloud}} \sim N^{-1}$, trivially.
- for fixed volume element (Eulerian) codes: since there is a minimum grid size Δx the smallest resolvable structure has a mass of $\Delta m \sim M_{\mathrm{Jeans}}(\Delta x) \sim$

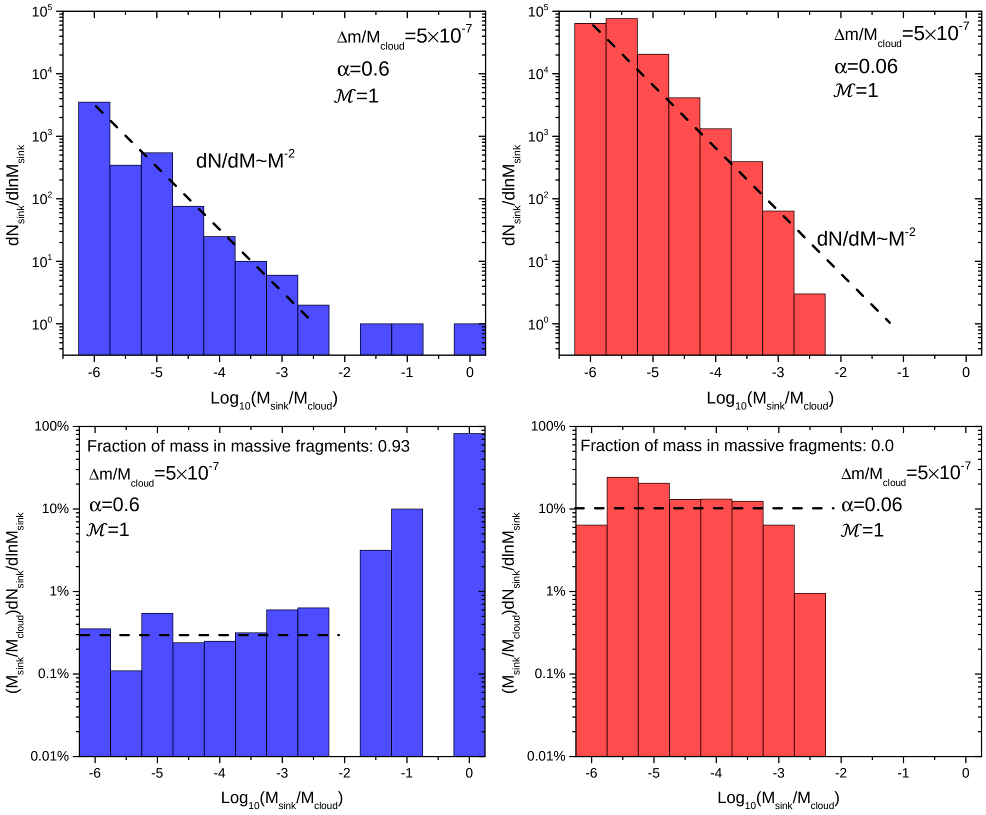

Figure 8.2: The final mass distribution of sink particles in isothermal gravitational collapse for different virial parameters α and fixed initial turbulent Mach number of $\mathcal{M} = 1$, demonstrating the two modes of isothermal collapse. The top row shows the number of particles per mass bin (IMF) while the bottom row shows the total mass of sink particles in each (logarithmic) mass bin. The horizontal axis is normalized by the mass of the initial cloud. In the $\alpha = 0.6$ case (left, blue) most of the mass ends up in a single object comparable in mass to the initial cloud (*homologous collapse*). Meanwhile, in the $\alpha = 0.06$ case (right, red) most of the mass ends up in objects with much lower masses than the initial cloud (*fragmentation*). In both cases the low mass end roughly has equal mass in each logarithmic bin (this means a -2 power-law slope for the IMF), in agreement with theoretical predictions (e.g. Guszejnov et al., 2017a).

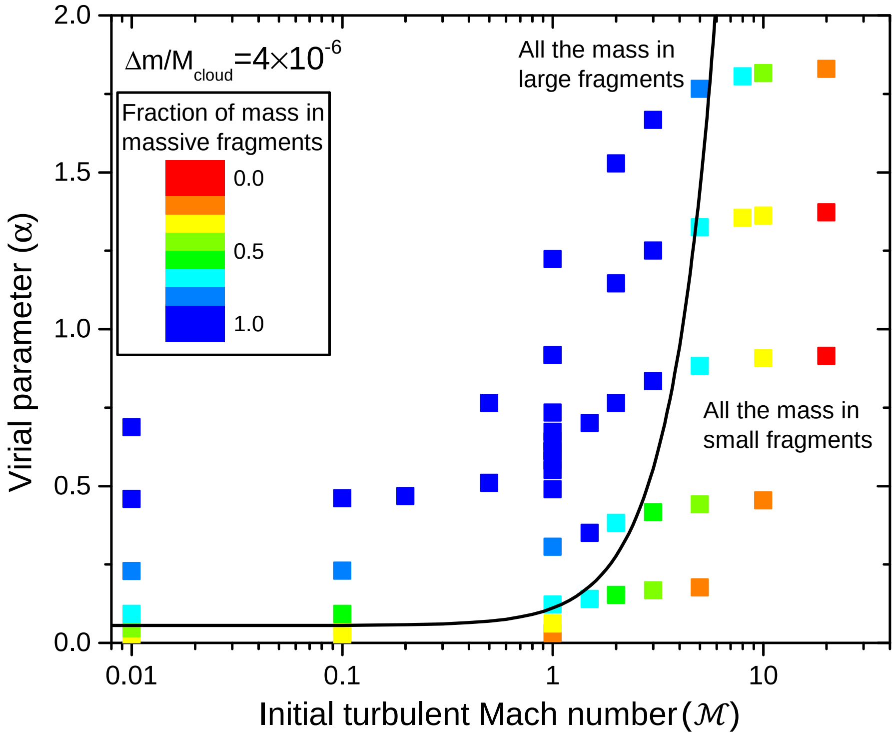

Figure 8.3: Fraction of the total cloud mass that ultimately ends up in massive fragments ($M_{\rm sink} > 0.1 M_{\rm cloud}$) for different initial virial parameters and initial turbulent Mach numbers (blue: most of the mass goes undergoes homologous collapse, red: most of the mass ends up in small fragments). It is clear that there is no specific α or initial turbulent $\mathcal{M}$ value separating the two modes of collapse. However, the boundary is well fitted by $\mathcal{M}_{\rm infall} = 3$ (defined in Eq. 8.5), plotted as a solid black line.

$\frac{c_s^3}{G\rho_{\rm max}}$. Using $\Delta m \sim \rho_{\rm max}\Delta x^3$ we get $\Delta m/M_{\rm cloud} \sim \frac{c_s^2}{G M_{\rm cloud}}\Delta x \propto N^{-1/3}$.

This shows that fixed mass element codes (like the Meshless-Finite-Mass scheme we are using) are (as expected by design) inherently superior at resolving mass distributions in Jeans collapse for a given number of resolution elements because their low mass cut-off scales as N^{-1} compared to the $N^{-1/3}$ for fixed volume codes (see Table 8.1 for specifics), provided they use no minimum softening but allow structures to get as dense as needed to reach the Truelove criterion. It should be noted that although adaptive mesh refinement (AMR) codes follow volume elements (thus are Eulerian by nature), their computa-

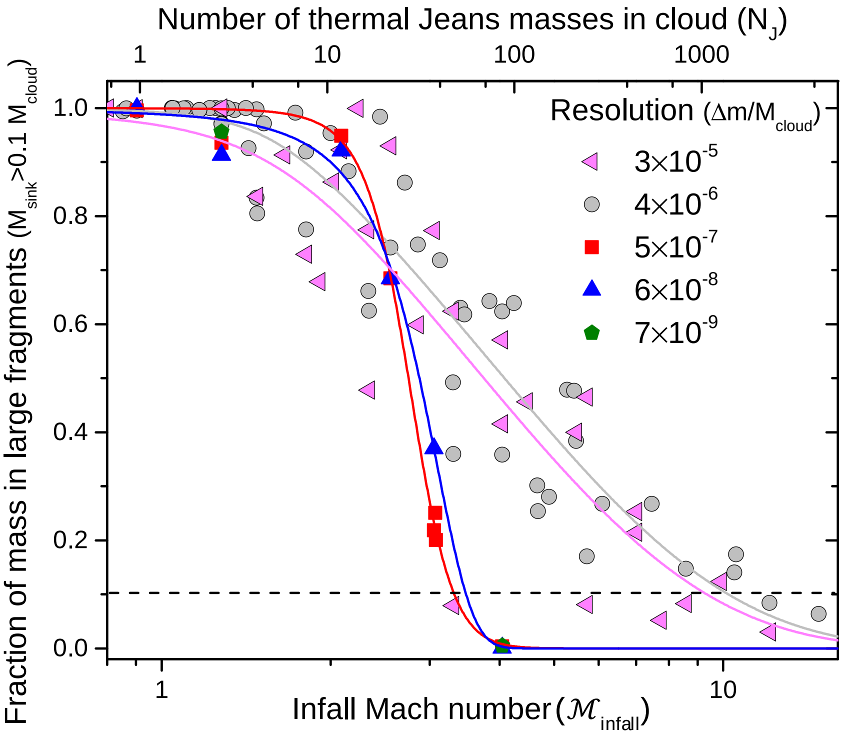

Figure 8.4: Fraction of the total cloud mass that ultimately ends up in massive fragments ($M_{\rm sink} > 0.1 M_{\rm cloud}$) as a function of the infall Mach-number (see Eq. 8.5) or equivalently the number of initial Jeans masses (see Eq. 8.6). We define massive fragments as having at least 10% of initial cloud mass. Below this value (dashed line) we plot the mass of the most massive sink particle relative to the cloud. There is a clear transition around $\mathcal{M}_{\rm infall} \sim 2-4$ between homologous collapse and fragmentation, we fitted generalized logistic functions $\left(f(x) = \left(1 + e^{(x-x_0)/\mathrm{d}x}\right)^{-\nu}\right)$ to the data (solid lines) to make the transition more apparent (no line was fitted at the highest resolution due to the low number of data points, but they lie on the trend line predicted from lower resolution runs). As we go to higher resolutions the transition becomes sharper. Note that the scatter arises from the stochastic nature of the initial conditions (e.g. random velocity field).

$\Delta m/M_{\rm cloud}$	$N_{\rm particle}$	$\Delta x/R_{\rm cloud}\alpha_{\rm thermal}$	$\rho_{\rm max}/(\rho_0^{\rm cloud}\alpha^3_{\rm thermal})$	$\frac{\Delta t_{\rm min}}{t^{\rm cloud}_{\rm dyn,0}}\alpha^{3/2}_{\rm thermal}$	$N^{\rm effective}_{\rm Euler}$
2×10^{-4}	$(16)^3$	9.5×10^{-4}	1.2×10^{6}	1.8×10^{-4}	$(4200)^3$
3×10^{-5}	$(32)^3$	1.2×10^{-4}	7.5×10^{7}	2.3×10^{-5}	$(3.3\times10^{4})^3$
4×10^{-6}	$(64)^3$	1.5×10^{-5}	4.8×10^{9}	2.9×10^{-6}	$(2.7\times10^{5})^3$
5×10^{-7}	$(128)^3$	1.9×10^{-6}	3.1×10^{11}	3.6×10^{-7}	$(2.1\times10^{6})^3$
6×10^{-8}	$(256)^3$	2.3×10^{-7}	2.0×10^{13}	4.5×10^{-8}	$(1.7\times10^{7})^3$
7×10^{-9}	$(512)^3$	2.9×10^{-8}	1.3×10^{15}	5.6×10^{-9}	$(1.4\times10^{8})^3$

Table 8.1: Resolution parameters: 1) Fractional mass resolution $\Delta m/M_{\rm cloud}$, 2) Spatial resolution $\Delta x/R_{\rm cloud}\alpha_{\rm thermal}$ where $\rho=\Delta m/\delta x^3$ becomes high enough that the corresponding Jeans mass becomes unresolved ($<\Delta m$), 3) Highest resolvable density $\rho_{\rm max}/(\rho_0^{\rm cloud}\alpha^3_{\rm thermal})$, the corresponding Jeans mass is Δm, 4) Smallest resolved time scale $\Delta t_{\rm min}/t^{\rm cloud}_{\rm dyn,0}\alpha^{3/2}_{\rm thermal}$ where $\Delta t=\frac{\Delta x}{c_s}$ and 5) the number of grid points $N^{\rm effective}_{\rm Euler}$ required in an Eulerian simulation (satisfying $\Delta x=\varphi\Delta x_{\rm grid}$ from Truelove et al. 1997, where $\varphi\sim1$). Note that the CPU cost of these calculations (at best) scale as $N_{\rm particle}\log N_{\rm particle}\times N_{\rm timesteps}$ which means going up one level in resolution (e.g. from 64^3 to 128^3) increases the computational cost by roughly a factor of 100.

tional cost is similar to our Lagrangian scheme in this specific problem[3].

Fig. 8.5 shows that the mass distribution in the fragmenting case is close to a power-law with a low mass cut-off set by the mass resolution of the simulation[4]. In the homologous collapse case the distribution of low mass fragments exhibit a similar behaviour, although the majority of the mass is still contained in several high mass fragments (see Fig. 8.2 for reference). This appears to contradict some claims in the literature (e.g. Gong & Ostriker, 2015; Haugbølle et al., 2017) that the mass spectrum peak converges around the sonic mass or some other mass scale set by initial conditions. We believe the discrepancy is related to several issues.

First, some authors are using fixed-grid Eulerian simulations (e.g.Gong & Ostriker 2015 for which even the highest resolution calculations cannot resolve the fragmentation of substructures due to the unfavourable $\Delta m\propto N^{-1/3}$ scaling[5].

---

[3] In isothermal collapse the fraction of volume at each AMR refinement level that needs further refinement is roughly constant due to scale-freeness of the problem. This, combined with the increasing number of time steps at higher refinement levels, ultimately lead to a similar computational costs as our Lagrangian scheme.

[4] Note that the highest resolution run ($\Delta m/M_{\rm cloud}=7\times10^{-9}$) was not run until completion due to the CPU cost that arises from modelling tightly bound binaries. At this point the system has turned only about 20% of its mass into sink particles, so we expect the IMF to evolve (e.g. accretion should make it less bottom heavy), but the low mass cut-off is already established.

[5] To reach the resolution of our $\Delta m/M_{\rm cloud}=6\times10^{-8}$ simulation $\approx4\times10^{21}$ grid points

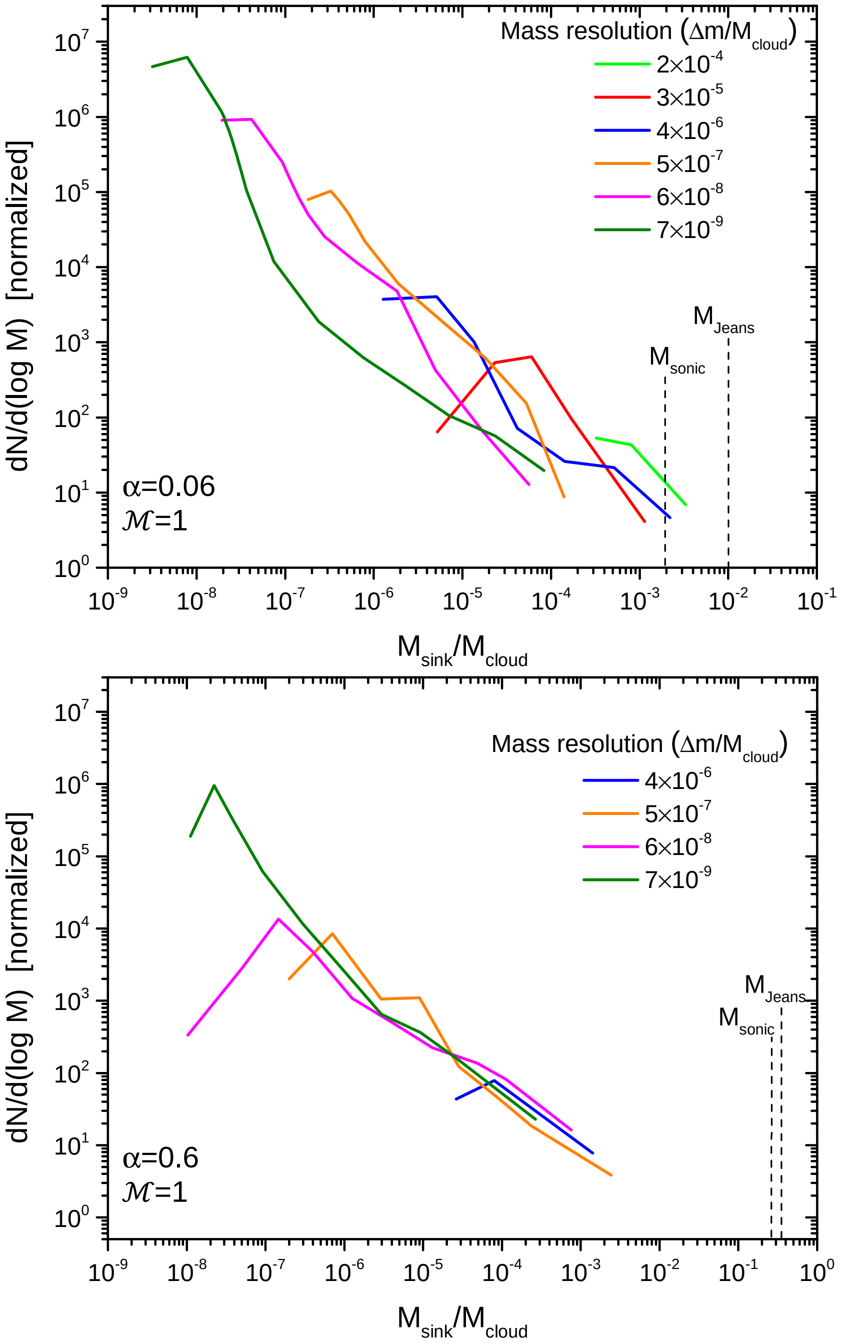

Figure 8.5: The mass distribution of sink particles (IMF) in a fragmenting cloud (Top: $\alpha = 0.06$, $\mathcal{M} = 1$, Bottom: $\alpha = 0.6$, $\mathcal{M} = 1$) for different mass resolutions. The dashed lines mark mass scales from initial conditions (sonic mass M_{sonic} and Jeans mass M_{Jeans}). For clarity the delta-function-like peaks around unit relative mass were removed from the right figure (see Fig. 8.2 for an example). Lower resolution runs are not included in the right figure as they only produced a single sink particle at unit relative mass. It is clear that the peak of the distribution is set by the resolution parameter $\Delta m/M_{\mathrm{cloud}}$, initial conditions imprint no scales into the final result. This means that for the infinitely well-resolved case we would get an infinite fragmentation cascade.

Alternatively, it is possible that these simulations start from initial conditions that are reminiscent of the "homologous collapse" case (e.g. having substructures in the initial density field that undergo homologous collapse), and only small fraction of mass undergoes runaway fragmentation. Although this runaway process is unresolved, the mass function appears converged as most of the mass is bound in objects well above the resolution limit. In some cases authors use AMR codes and claim convergence, but the data is not convincing (e.g. see Figs. 4-6 in Haugbølle et al. 2017, where the IMF peak roughly follows the predicted $N^{-1/3}$ trend at higher resolutions). Finally, there is substantially greater numerical diffusivity in high $\mathcal{M}$ flows, due to lack of Galilean invariance (Springel & Hernquist, 2002), which is well-known to generate spurious heating and suppress small-scale structures in the simulation of "cold" gravitational collapse (see e.g. Hopkins, 2015).

8.5 Conclusions

We investigate the evolution of self-gravitating, isothermal gas with high resolution Lagrangian hydrodynamic simulations. We identify two distinct modes of collapse:

1. Homologous collapse (most of the mass ends up in one or a few massive objects)
2. Runaway fragmentation (most of the mass ends up in a spectrum of low mass fragments, which continues until the resolution limit)

The mode of collapse is set by the infall Mach number $\mathcal{M}_{\mathrm{infall}} \equiv \frac{v_{\mathrm{infall}}}{c_s} \sim \frac{\sqrt{\frac{GM}{R}}}{c_s}$ (equivalent to the initial number of Jeans masses in the cloud), not the initial virial parameter or the Mach number of the initial turbulent dispersion. The difference in behaviour is due to sound waves "smoothing out" density perturbations when the infall is subsonic leading to a scenario similar to the well-known solutions of isothermal collapse (e.g. Larson, 1969; Penston, 1969; Shu, 1977).

In both cases we found that the mass distribution of final objects develops a power-law behaviour at low masses, close to $\mathrm{d}N/\mathrm{d}M \propto M^{-2}$, in agreement with theoretical expectations (e.g. Bonnell et al., 2007; Elmegreen, 1997; Hennebelle & Chabrier, 2008; Padoan et al., 1997). Note that in the case of homologous

---

would be needed, far exceeding the capabilities of even large computer clusters.

collapse most of the mass is actually in several massive fragments that lie outside this power-law regime but the remaining mass which does not end up in the "primary" scale sinks forms a power-law distribution, with no lower limit down to the resolution scale.

We conducted a resolution study to examine whether the low mass cut-off of the power-law in the mass distribution is determined by the initial conditions of the cloud (e.g. its virial parameter or initial turbulent properties) or by mass resolution. We found that there is no convergence in the low-mass spectrum that appears in either mode of collapse. In other words: the fragmentation goes well below the initial Jeans mass, down to the mass resolution. This agrees well with several studies (e.g. Federrath et al., 2017; Kratter et al., 2010; Lee & Hennebelle, 2017; Martel et al., 2006). However, our results and these others do appear to contradict some others in the literature. We believe the discrepancy is explained by different simulation methods and the much wider dynamic range probed in this study.

It is a common argument that subsonic structures don't fragment so the population of such structures (e.g. cores in star formation), whose characteristic mass is set by the large scale turbulent properties (e.g. sonic mass, see Hennebelle & Chabrier 2008; Hopkins 2012b), influences the final mass distribution. This is not the case as these structures form in a larger, supersonic cloud that forms supersonic substructures as well. These substructures have different turbulent properties so they spawn a population of subsonic fragments different from their parent. In the end this cascade washes out any effects the initial conditions might have over the low mass end of the mass spectrum.

Our results show that an isothermal fragmentation cascade has to be terminated by additional physics (e.g. breakdown of scale-free assumption at high densities); the initial conditions (e.g. sonic mass) imprint no mass scale in the final mass distribution. This means that star formation models that tie the IMF peak to initial turbulent properties (e.g. Hennebelle & Chabrier, 2008; Hopkins, 2012a) need to be modified.

More broadly, these results provide insight into the physical character of isothermal gravito-turbulent fragmentation: it is a self-sustaining process, able to continuously generate enough power in the density field on the smallest scales to drive further fragmentation. The requisite energy to drive these small-scale density perturbations must be produced by *local* gravitational collapse, in a manner that is decoupled from energy injection at larger scales.

This is a very different picture from the classical Kolmogorov energy cascade, in which all kinetic energy originates at large scales and cascades to small scales, with none generated at intermediate scales. Hence self-gravity alters isothermal turbulence in a fundamental way. It follows that any model of the ISM based upon the properties of non-self-gravitating isothermal turbulence will fail to describe the internal dynamics of the self-gravitating objects that form.

8.A Additional Numerical Tests

8.A.1 Effects of perturbed initial conditions

Due to the resource intense nature of the simulation, only one initial realization of the initial conditions (e.g. the specific density field) was simulated for a given resolution, virial parameter α and Mach number $\mathcal{M}$ in Fig. 8.3. To test for the magnitude of stochastic effects in different realizations (since the system is chaotic) we consider an experiment where we follow the evolution of 5 different random realizations with the same global Mach number and virial parameter. We also included a set where we added Gaussian noise to the position and velocity of the initial gas particles. Fig. 8.6 shows that the mass distribution of sink particles (IMF) is qualitatively unchanged by these experiments.

8.A.2 Effects of turbulent driving

The simulations mentioned in the main text include no external driving for turbulence as this 1) simplifies the problem and decreases the number of degrees of freedom, and 2) corresponds to a growing body of literature suggesting that turbulence in clouds is driven primarily by their own self-gravity, not an external cascade (Ballesteros-Paredes et al., 2011a; Ibáñez-Mejía et al., 2016; Murray et al., 2015; Robertson & Goldreich, 2012a). However, it is important to check whether this alters our results. To investigate the effects of turbulent driving we carried out several simulations where the initial conditions are generated by driving the turbulence for several dynamical times without self-gravity, then turning on gravity (as in e.g. Schmidt et al. 2009). Note that unlike the simulations in the main text in these cases the density and velocity fields in the initial conditions are self-consistent with the driving and initial Mach number. Fig. 8.7 shows that turbulent driving has no qualitative effects on the resulting IMF.

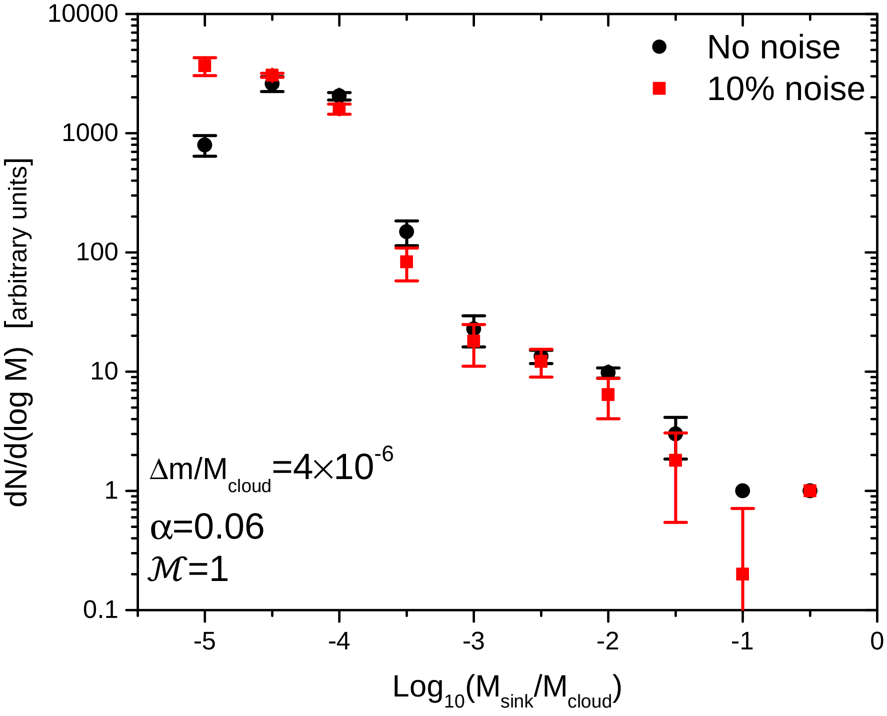

Figure 8.6: The mass distribution of sink particles (IMF) for 5 different simulations of clouds, each with the same initial $\alpha = 0.06$ and turbulent Mach number of $\mathcal{M} = 1$, but the ICs are drawn randomly from different times in a turbulent boy simulation (in other words, these are different "realizations" of the ICs). Points show the median and error bars the 80% inclusion interval of the sink particle IMF for different realizations. In a second set of simulations we added a random Gaussian perturbation to the initial position and velocity of the gas particles. The IMF shape is is qualitatively consistent for different realizations even if we add significant perturbations onto it.

8.A.3 Effects of the hydrodynamic solver

As GIZMO is an inherently multi-method code, we can re-run several simulations with different hydrodynamics schemes, but otherwise identical physics. We compare:

- The Meshless Finite-Mass (MFM) method (Hopkins, 2015), a Lagrangian, finite volume, second order, Godunov method (our default in the text).
- The "Pressure-Energy" formulation of smoothed particle hydrodynamics (SPH) (Hopkins, 2013b), which has various improvements over the original GADGET "Density-Entropy" formulation it is derived from (Springel & Hernquist, 2002).

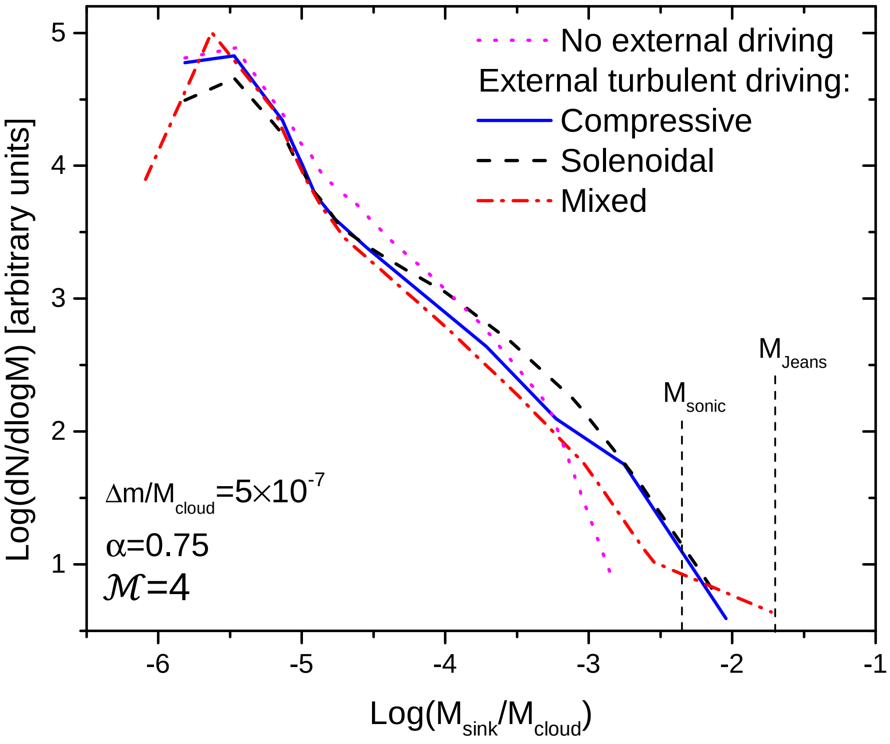

Figure 8.7: The mass distribution of sink particles (IMF) for a cloud with initial $\alpha = 0.5$ and $\mathcal{M} = 4$. We compare our fiducial case of non-driven (but still self-gravitating) turbulence with scenarios with different types of turbulent driving. It is clear that the external driving has little to no effect on the final distribution, regardless of the driving method.

Although both are Lagrangian methods, the two work quite differently. In MFM, inter-cell fluxes are the obtained by solving a Riemann problem across each effective face between neighbouring cells in such a way that mass fluxes cancel and the cells are moved with the local fluid velocity. In SPH, effective forces between interacting neighbour particles are derived from a discrete particle Lagrangian involving the local fluid properties reconstructed from a kernel density estimator. Despite these differences, we found that our choice of hydro solver these has no qualitative effect on our results (see Fig. 8.8).

8.A.4 Effects of the sink particle scheme

In our simulations sink particles are allowed to merge in order to avoid the spawning of spurious sinks, which can significantly affect their mass distribution. Two sink particles are allowed to merge if the following criteria are met (based on Federrath et al. 2010d):

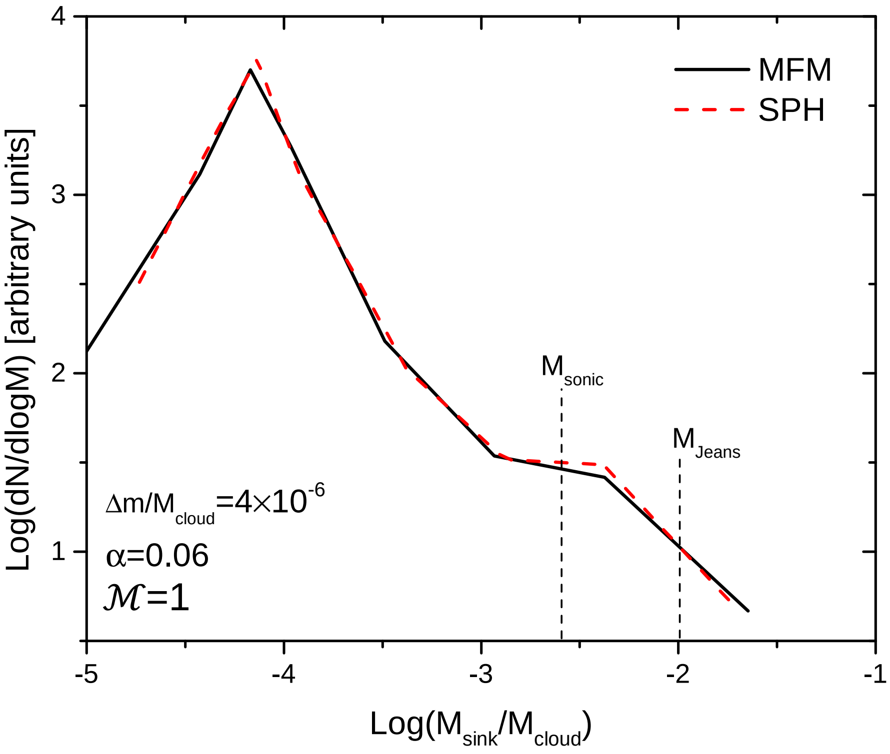

Figure 8.8: The mass distribution of sink particles (IMF) using Meshless Finite-Mass (MFM) and Smoothed-Particle Hydrodynamics (SPH) schemes. The predicted IMF is independent of the details of the hydrodynamics method.

1. Both are in the same interacting hydrodynamic element.
2. They are gravitationally bound.
3. Their epicentric radius is smaller than 3 times the gravitational force softening and $10^{-4} R_{\mathrm{cloud}}$.

To test whether this prescription has any effect on our results we run several simulations where we forbid sink particle mergers. Fig. 8.9 shows that allowing sink particles to merge affects their final mass distribution by decreasing the number of sinks at the resolution limit and thus shifting the peak to a slight higher mass. Overall, it has no qualitative effect on our results as the low mass cut-off is still determined by the mass resolution.

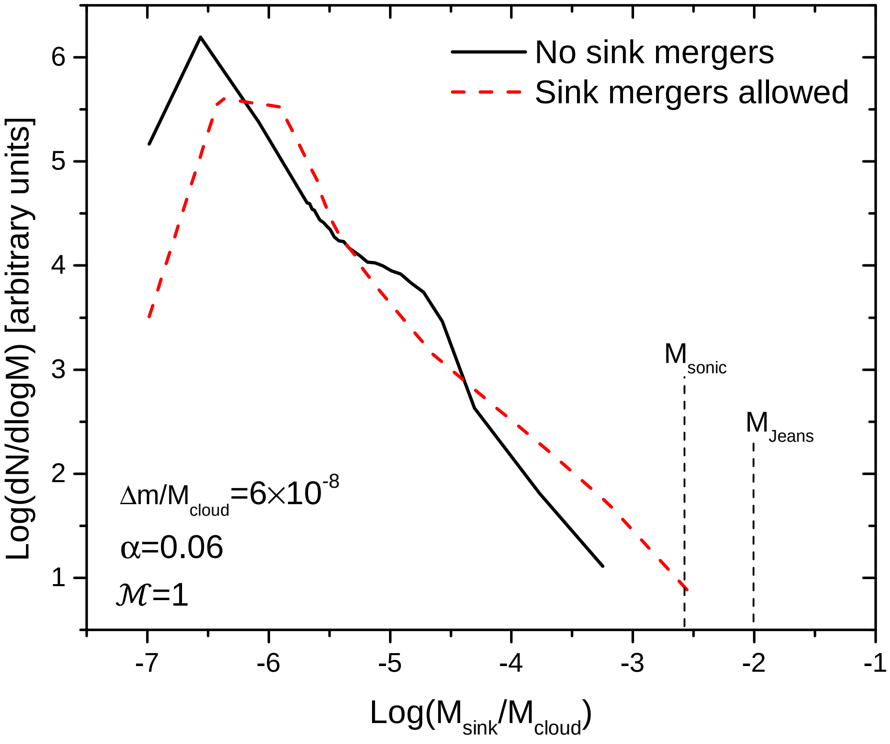

Figure 8.9: The mass distribution of sink particles (IMF), comparing the case where the sink particles are allowed merge (dashed, red) and the case they are not (black, solid). As expected, the overall distribution shifts to larger masses, but the initial conditions (e.g. $M_{\rm Jeans}$ Jeans and $M_{\rm sonic}$ sonic masses) play no role.

BIBLIOGRAPHY

Alves J., Lombardi M., Lada C. J., 2007, A&A, 462, L17

Andrews J. E., et al., 2013, ApJ, 767, 51

Andrews J. E., et al., 2014, ApJ, 793, 4

Arce H. G., Shepherd D., Gueth F., Lee C.-F., Bachiller R., Rosen A., Beuther H., 2007, Protostars and Planets V, pp 245–260

Audit E., Hennebelle P., 2010, A&A, 511, A76+

Ballesteros-Paredes J., Hartmann L. W., Vázquez-Semadeni E., Heitsch F., Zamora-Avilés M. A., 2011a, MNRAS, 411, 65

Ballesteros-Paredes J., Vázquez-Semadeni E., Gazol A., Hartmann L. W., Heitsch F., Colín P., 2011b, MNRAS, 416, 1436

Ballesteros-Paredes J., Vazquez-Semadeni E., Gazol A., Hartmann L. W., Heitsch F., Colin P., 2011c, MNRAS, 416, 1436

Bastian N., Covey K. R., Meyer M. R., 2010, ARA&A, 48, 339

Bate M. R., 2000, MNRAS, 314, 33

Bate M. R., 2009a, MNRAS, 392, 590

Bate M. R., 2009b, MNRAS, 392, 590

Bate M. R., 2009c, MNRAS, 392, 1363

Bate M. R., 2012a, MNRAS, 419, 3115

Bate M. R., 2012b, MNRAS, 419, 3115

Bate M. R., 2014, MNRAS, 442, 285

Bate M. R., Bonnell I. A., 2005, MNRAS, 356, 1201

Bate M. R., Clarke C. J., McCaughrean M. J., 1998, MNRAS, 297, 1163

Bauer A., Springel V., 2012, MNRAS, 423, 2558

Baugh C. M., 1996, MNRAS, 280, 267

Baugh C. M., Lacey C. G., Frenk C. S., Granato G. L., Silva L., Bressan A., Benson A. J., Cole S., 2005, MNRAS, 356, 1191

Bekki K., 2013, ApJ, 779, 9

Bergin E. A., Tafalla M., 2007, ARA&A, 45, 339

Bik A., Lamers H. J. G. L. M., Bastian N., Panagia N., Romaniello M., 2003, A&A, 397, 473

Blancato K., Genel S., Bryan G., 2016, preprint, (arXiv:1612.05658)

Bolatto A. D., Leroy A. K., Rosolowsky E., Walter F., Blitz L., 2008, ApJ, 686, 948

Bond J. R., Cole S., Efstathiou G., Kaiser N., 1991, ApJ, 379, 440

Bonnell I. A., Clarke C. J., Bate M. R., 2006, MNRAS, 368, 1296

Bonnell I. A., Larson R. B., Zinnecker H., 2007, Protostars and Planets V, pp 149–164

Boss A. P., 1991, Nature, 351, 298

Bressert E., et al., 2010, MNRAS, 409, L54

Brown T. M., et al., 2012, ApJ, 753, L21

Brunt C. M., Heyer M. H., Mac Low M.-M., 2009, A&A, 504, 883

Burgasser A. J., Reid I. N., Siegler N., Close L., Allen P., Lowrance P., Gizis J., 2007, Protostars and Planets V, pp 427–441

Burgers J., 1974, The Nonlinear Diffusion Equation. Springer

Burgers J., 1995, in Nieuwstadt F., Steketee J., eds, , Selected Papers of J. M. Burgers. Springer Netherlands, pp 281–334, doi:10.1007/978-94-011-0195-0_10

Burkert A., Bodenheimer P., 2000, ApJ, 543, 822

Burkhart B., Collins D. C., Lazarian A., 2015, ApJ, 808, 48

Canameras R., et al., 2017, preprint, (arXiv:1704.05853)

Cappellari M., et al., 2012, Nature, 484, 485

Cartwright A., Whitworth A. P., 2004, MNRAS, 348, 589

Chabrier G., 2003, PASP, 115, 763

Chabrier G., 2005, in Corbelli E., Palla F., Zinnecker H., eds, Astrophysics and Space Science Library Vol. 327, The Initial Mass Function 50 Years Later. p. 41

Chabrier G., Hennebelle P., Charlot S., 2014, ApJ, 796, 75

Chandrasekhar S., 1951, Royal Society of London Proceedings Series A, 210, 26

Chappell D., Scalo J., 2001, ApJ, 551, 712

Clark P. C., Klessen R. S., Bonnell I. A., 2007, MNRAS, 379, 57

Collins D. C., Kritsuk A. G., Padoan P., Li H., Xu H., Ustyugov S. D., Norman M. L., 2012, ApJ, 750, 13

Colombo D., et al., 2014a, ApJ, 784, 3

Colombo D., et al., 2014b, ApJ, 784, 3

Conroy C., van Dokkum P. G., 2012, ApJ, 760, 71

Crutcher R. M., 2012, ARA&A, 50, 29

Dale J. E., Ercolano B., Bonnell I. A., 2012, MNRAS, 424, 377

Davé R., Finlator K., Oppenheimer B. D., 2012, MNRAS, 421, 98

De Rosa R. J., et al., 2014, MNRAS, 437, 1216

Delgado-Donate E. J., Clarke C. J., Bate M. R., Hodgkin S. T., 2004, MNRAS, 351, 617

Dobbs C. L., Bonnell I. A., Pringle J. E., 2006, MNRAS, 371, 1663

Dobbs C. L., et al., 2014, Protostars and Planets VI, pp 3–26

Duchêne G., 1999, A&A, 341, 547

Duchêne G., Kraus A., 2013, ARA&A, 51, 269

Elmegreen B. G., 1987, ApJ, 312, 626

Elmegreen B. G., 1997, ApJ, 486, 944

Elmegreen B. G., 2002, ApJ, 564, 773

Elmegreen B. G., Falgarone E., 1996, ApJ, 471, 816

Elmegreen B. G., Klessen R. S., Wilson C. D., 2008, ApJ, 681, 365

Elson R. A. W., Fall S. M., Freeman K. C., 1987, ApJ, 323, 54

Enoch M. L., Evans II N. J., Sargent A. I., Glenn J., Rosolowsky E., Myers P., 2008, ApJ, 684, 1240

Fall S. M., Chandar R., 2012, ApJ, 752, 96

Federrath C., 2013, MNRAS, 436, 1245

Federrath C., Banerjee S., 2015, MNRAS, 448, 3297

Federrath C., Klessen R. S., 2012, ApJ, 761, 156

Federrath C., Klessen R. S., 2013, ApJ, 763, 51

Federrath C., Klessen R. S., Schmidt W., 2008, ApJ, 688, L79

Federrath C., Roman-Duval J., Klessen R. S., Schmidt W., Mac Low M.-M., 2010a, A&A, 512, A81

Federrath C., Roman-Duval J., Klessen R. S., Schmidt W., Mac Low M.-M., 2010b, A&A, 512, A81

Federrath C., Roman-Duval J., Klessen R. S., Schmidt W., Mac Low M.-M., 2010c, A&A, 512, A81+

Federrath C., Banerjee R., Clark P. C., Klessen R. S., 2010d, ApJ, 713, 269

Federrath C., Krumholz M., Hopkins P. F., 2017, in Journal of Physics Conference Series. p. 012007, doi:10.1088/1742-6596/837/1/012007

Ferland G. J., et al., 2013, Rev. Mexicana Astron. Astrofis., 49, 137

Ferreras I., Weidner C., Vazdekis A., La Barbera F., 2015, MNRAS, 448, L82

Fukui Y., et al., 2008, ApJS, 178, 56

Fumagalli M., da Silva R. L., Krumholz M. R., 2011, ApJ, 741, L26

Geen S., Rosdahl J., Blaizot J., Devriendt J., Slyz A., 2015, MNRAS, 448, 3248

Geha M., et al., 2013, ApJ, 771, 29

Girichidis P., Konstandin L., Whitworth A. P., Klessen R. S., 2014, ApJ, 781, 91

Glover S. C. O., Mac Low M.-M., 2007, ApJS, 169, 239

Gong H., Ostriker E. C., 2009, ApJ, 699, 230

Gong H., Ostriker E. C., 2011, ApJ, 729, 120

Gong M., Ostriker E. C., 2015, ApJ, 806, 31

González-Alfonso E., et al., 2012, A&A, 541, A4

Goodman A. A., Benson P. J., Fuller G. A., Myers P. C., 1993, ApJ, 406, 528

Goodwin S. P., Whitworth A. P., Ward-Thompson D., 2004, A&A, 414, 633

Goodwin S. P., Kroupa P., Goodman A., Burkert A., 2007, Protostars and Planets V, pp 133–147

Gorski M., Ott J., Rand R., Meier D. S., Momjian E., Schinnerer E., 2017, ApJ, 842, 124

Gouliermis D. A., Hony S., Klessen R. S., 2014, MNRAS, 439, 3775

Gouliermis D. A., et al., 2015, MNRAS, 452, 3508

Grasha K., et al., 2017, preprint, (arXiv:1704.06321)

Grudić M. Y., Hopkins P. F., Faucher-Giguère C.-A., Quataert E., Murray N.,

Kereš D., 2016, preprint, (arXiv:1612.05635)
Grudić M. Y., Guszejnov D., Hopkins P. F., Lamberts A., Boylan-Kolchin M., Murray N., Schmitz D., 2017, preprint, (arXiv:1708.09065)
Guszejnov D., Hopkins P. F., 2015a, preprint, (arXiv:1507.06678)
Guszejnov D., Hopkins P. F., 2015b, MNRAS, 450, 4137
Guszejnov D., Hopkins P. F., 2016, MNRAS, 459, 9
Guszejnov D., Krumholz M. R., Hopkins P. F., 2016, MNRAS, 458, 673
Guszejnov D., Hopkins P. F., Grudić M. Y., 2017a, preprint, (arXiv:1707.05799)
Guszejnov D., Hopkins P. F., Krumholz M. R., 2017b, MNRAS, 468, 4093
Guszejnov D., Hopkins P. F., Ma X., 2017c, MNRAS, 472, 2107
Guszejnov D., Hopkins P. F., Grudic M. Y., Krumholz M. R., Federrath C., 2018, preprint, (arXiv:1804.08574)
Hanawa T., Matsumoto T., 1999, ApJ, 521, 703
Hansen C. E., Klein R. I., McKee C. F., Fisher R. T., 2012a, ApJ, 747, 22
Hansen C. E., Klein R. I., McKee C. F., Fisher R. T., 2012b, ApJ, 747, 22
Hartmann L., 2002, ApJ, 578, 914
Haugbølle T., Padoan P., Nordlund A., 2017, preprint, (arXiv:1709.01078)
Hennebelle P., 2012, A&A, 545, A147
Hennebelle P., Chabrier G., 2008, ApJ, 684, 395
Hennebelle P., Chabrier G., 2009, ApJ, 702, 1428
Hennebelle P., Chabrier G., 2013a, ApJ, 770, 150
Hennebelle P., Chabrier G., 2013b, ApJ, 770, 150
Hennekemper E., Gouliermis D. A., Henning T., Brandner W., Dolphin A. E., 2008, ApJ, 672, 914
Heyer M., Dame T. M., 2015, ARA&A, 53, 583
Heyer M., Krawczyk C., Duval J., Jackson J. M., 2009, ApJ, 699, 1092
Hopkins P. F., 2012a, MNRAS, 423, 2016
Hopkins P. F., 2012b, MNRAS, 423, 2037
Hopkins P. F., 2013a, MNRAS, 428, 1950
Hopkins P. F., 2013b, MNRAS, 428, 2840
Hopkins P. F., 2013c, MNRAS, 430, 1653
Hopkins P. F., 2013d, MNRAS, 430, 1880
Hopkins P. F., 2013e, MNRAS, 433, 170
Hopkins P. F., 2015, MNRAS, 450, 53
Hopkins P. F., Quataert E., Murray N., 2012, MNRAS, 421, 3488
Hopkins P. F., Narayanan D., Murray N., 2013a, MNRAS, 432, 2647
Hopkins P. F., Narayanan D., Murray N., Quataert E., 2013b, MNRAS, 433, 69
Hopkins P. F., Kereš D., Oñorbe J., Faucher-Giguère C.-A., Quataert E., Murray N., Bullock J. S., 2014, MNRAS, 445, 581
Hopkins P. F., et al., 2017a, preprint, (arXiv:1702.06148)

Hopkins P. F., et al., 2017b, preprint, (arXiv:1702.06148)

Hoversten E. A., Glazebrook K., 2008, ApJ, 675, 163

Hubber D. A., Whitworth A. P., 2005, A&A, 437, 113

Ibáñez-Mejía J. C., Mac Low M.-M., Klessen R. S., Baczynski C., 2016, ApJ, 824, 41

Iffrig O., Hennebelle P., 2015, A&A, 576, A95

Inutsuka S.-I., Miyama S. M., 1992, ApJ, 388, 392

Jappsen A.-K., Klessen R. S., Larson R. B., Li Y., Mac Low M.-M., 2005a, A&A, 435, 611

Jappsen A.-K., Klessen R. S., Larson R. B., Li Y., Mac Low M.-M., 2005b, A&A, 435, 611

Johnstone D., Bally J., 2006, ApJ, 653, 383

Kaczmarek T., Olczak C., Pfalzner S., 2011, A&A, 528, A144

Kainulainen J., Beuther H., Henning T., Plume R., 2009, A&A, 508, L35

Kauffmann G., White S. D. M., Guiderdoni B., 1993, MNRAS, 264, 201

Kauffmann G., Colberg J. M., Diaferio A., White S. D. M., 1999, MNRAS, 303, 188

Kauffmann J., Pillai T., Goldsmith P. F., 2013, ApJ, 779, 185

Klessen R. S., Burkert A., 2000, ApJS, 128, 287

Klessen R. S., Burkert A., 2001, ApJ, 549, 386

Klessen R. S., Krumholz M. R., Heitsch F., 2011, Advanced Science Letters, 4, 258

Koda J., Yagi M., Boissier S., Gil de Paz A., Imanishi M., Donovan Meyer J., Madore B. F., Thilker D. A., 2012, ApJ, 749, 20

Korntreff C., Kaczmarek T., Pfalzner S., 2012, A&A, 543, A126

Kouwenhoven M. B. N., Goodwin S. P., Parker R. J., Davies M. B., Malmberg D., Kroupa P., 2010, MNRAS, 404, 1835

Kowal G., Lazarian A., Beresnyak A., 2007, ApJ, 658, 423

Kramer C., Stutzki J., Rohrig R., Corneliussen U., 1998, A&A, 329, 249

Kratter K. M., Matzner C. D., Krumholz M. R., Klein R. I., 2010, ApJ, 708, 1585

Kraus A. L., Hillenbrand L. A., 2008, ApJ, 686, L111

Kraus A. L., Ireland M. J., Martinache F., Lloyd J. P., 2008, ApJ, 679, 762

Kraus A. L., Ireland M. J., Martinache F., Hillenbrand L. A., 2011, ApJ, 731, 8

Kraus A. L., Herczeg G. J., Rizzuto A. C., Mann A. W., Slesnick C. L., Carpenter J. M., Hillenbrand L. A., Mamajek E. E., 2017, preprint, (arXiv:1702.04341)

Kritsuk A. G., Norman M. L., Padoan P., 2006, ApJ, 638, L25

Kritsuk A. G., Norman M. L., Wagner R., 2011, ApJ, 727, L20

Kritsuk A. G., Lee C. T., Norman M. L., 2013, MNRAS, 436, 3247

Kroupa P., 1995, MNRAS, 277

Kroupa P., 2002, Science, 295, 82

Kruijssen J. M. D., 2009, A&A, 507, 1409

Krumholz M. R., 2006, ApJ, 641, L45

Krumholz M. R., 2011, ApJ, 743, 110

Krumholz M. R., 2014, Phys. Rep., 539, 49

Krumholz M. R., McKee C. F., 2008, Nature, 451, 1082

Krumholz M. R., McKee C. F., Klein R. I., 2005, Nature, 438, 332

Krumholz M. R., Klein R. I., McKee C. F., 2007, ApJ, 656, 959

Krumholz M. R., Klein R. I., McKee C. F., 2011, ApJ, 740, 74

Krumholz M. R., Klein R. I., McKee C. F., 2012, ApJ, 754, 71

Krumholz M. R., Myers A. T., Klein R. I., McKee C. F., 2016, MNRAS, 460, 3272

Kuiper G. P., 1935, PASP, 47, 15

Lacey C., Cole S., 1993, MNRAS, 262, 627

Lacey C. G., et al., 2016, MNRAS, 462, 3854

Lada C. J., Lada E. A., 2003, ARA&A, 41, 57

Larsen S. S., 2004, A&A, 416, 537

Larson R. B., 1969, MNRAS, 145, 271

Larson R. B., 1981, MNRAS, 194, 809

Larson R. B., 1982, MNRAS, 200, 159

Larson R. B., 2005, MNRAS, 359, 211

Lee Y.-N., Hennebelle P., 2017, preprint, (arXiv:1711.00319)

Leitherer C., et al., 1999, ApJS, 123, 3

Lin Y., et al., 2017, ApJ, 840, 22

Lomax O., Whitworth A. P., Hubber D. A., Stamatellos D., Walch S., 2014, MNRAS, 439, 3039

Lomax O., Whitworth A. P., Hubber D. A., Stamatellos D., Walch S., 2015, MNRAS, 447, 1550

Lombardi M., Bouy H., Alves J., Lada C. J., 2014, A&A, 566, A45

Low C., Lynden-Bell D., 1976, MNRAS, 176, 367

Luhman K. L., Mamajek E. E., Allen P. R., Cruz K. L., 2009, ApJ, 703, 399

Lynden-Bell D., 1967, MNRAS, 136, 101

Ma X., Hopkins P. F., Wetzel A. R., Kirby E. N., Angles-Alcazar D., Faucher-Giguere C.-A., Keres D., Quataert E., 2016a, preprint, (arXiv:1608.04133)

Ma X., Hopkins P. F., Faucher-Giguère C.-A., Zolman N., Muratov A. L., Kereš D., Quataert E., 2016b, MNRAS, 456, 2140

Ma X., Hopkins P. F., Feldmann R., Torrey P., Faucher-Giguère C.-A., Kereš D., 2017, MNRAS,

Mac Low M.-M., Klessen R. S., 2004, Reviews of Modern Physics, 76, 125

Mackey A. D., Gilmore G. F., 2003a, MNRAS, 338, 85

Mackey A. D., Gilmore G. F., 2003b, MNRAS, 338, 120

Mangum J. G., Darling J., Henkel C., Menten K. M., MacGregor M., Svoboda

B. E., Schinnerer E., 2013, ApJ, 779, 33

Marks M., Kroupa P., Oh S., 2011, MNRAS, 417, 1684

Martel H., Evans II N. J., Shapiro P. R., 2006, ApJS, 163, 122

Martín-Navarro I., La Barbera F., Vazdekis A., Ferré-Mateu A., Trujillo I., Beasley M. A., 2015a, MNRAS, 451, 1081

Martín-Navarro I., et al., 2015b, ApJ, 798, L4

Martín-Navarro I., et al., 2015c, ApJ, 806, L31

Massey P., 2003, ARA&A, 41, 15

Masunaga H., Inutsuka S.-i., 2000, ApJ, 531, 350

Masunaga H., Miyama S. M., Inutsuka S.-i., 1998, ApJ, 495, 346

McKee C. F., Offner S. S. R., 2010, ApJ, 716, 167

McKee C. F., Ostriker E. C., 2007a, ARA&A, 45, 565

McKee C. F., Ostriker E. C., 2007b, ARA&A, 45, 565

McKee C. F., Li P. S., Klein R. I., 2010, ApJ, 720, 1612

Mills E. A. C., Morris M. R., 2013, ApJ, 772, 105

Miyamoto Y., Nakai N., Seta M., Salak D., Hagiwara K., Nagai M., Ishii S., Yamauchi A., 2015, PASJ, 67, 5

Moe M., Di Stefano R., 2016, preprint, (arXiv:1606.05347)

Muraoka K., et al., 2009, PASJ, 61, 163

Muratov A. L., Kereš D., Faucher-Giguère C.-A., Hopkins P. F., Quataert E., Murray N., 2015, MNRAS, 454, 2691

Murray J. D., 1973, Journal of Fluid Mechanics, 59, 263

Murray N., Chang P., 2015, ApJ, 804, 44

Murray D. W., Chang P., Murray N. W., Pittman J., 2015, preprint, (arXiv:1509.05910)

Myers A. T., Krumholz M. R., Klein R. I., McKee C. F., 2011, ApJ, 735, 49

Myers A. T., Klein R. I., Krumholz M. R., McKee C. F., 2014, MNRAS, 439, 3420

Nakajima Y., Tachihara K., Hanawa T., Nakano M., 1998, ApJ, 497, 721

Nakano T., Nakamura T., 1978, PASJ, 30, 671

Narayanan D., Davé R., 2012, MNRAS, 423, 3601

Narayanan D., Hopkins P. F., 2013, MNRAS, 433, 1223

Narayanan D., Krumholz M. R., 2014, MNRAS, 442, 1411

Navarro J. F., Frenk C. S., White S. D. M., 1996, ApJ, 462, 563

Nishimura A., et al., 2015, ApJS, 216, 18

Ntormousi E., Hennebelle P., 2015, A&A, 574, A130

Offner S. S. R., Klein R. I., McKee C. F., Krumholz M. R., 2009a, ApJ, 703, 131

Offner S. S. R., Klein R. I., McKee C. F., Krumholz M. R., 2009b, ApJ, 703, 131

Offner S. S. R., Kratter K. M., Matzner C. D., Krumholz M. R., Klein R. I., 2010, ApJ, 725, 1485

Offner S. S. R., Clark P. C., Hennebelle P., Bastian N., Bate M. R., Hopkins P. F., Moraux E., Whitworth A. P., 2014, Protostars and Planets VI, pp 53–75

Orr M., et al., 2017, preprint, (arXiv:1701.01788)

Ostriker E. C., Gammie C. F., Stone J. M., 1999, ApJ, 513, 259

Ott J., Henkel C., Braatz J. A., Weiß A., 2011, ApJ, 742, 95

Ott J., Weiß A., Staveley-Smith L., Henkel C., Meier D. S., 2014, ApJ, 785, 55

Padoan P., Nordlund Å., 2002, ApJ, 576, 870

Padoan P., Nordlund Å., 2011, ApJ, 741, L22

Padoan P., Nordlund A., Jones B. J. T., 1997, MNRAS, 288, 145

Padoan P., Haugbølle T., Nordlund Å., 2014, ApJ, 797, 32

Pan L., Scannapieco E., 2010, ApJ, 721, 1765

Parikh T., et al., 2018, preprint, (arXiv:1803.08515)

Parker R. J., 2014, MNRAS, 445, 4037

Parker R. J., Meyer M. R., 2014, MNRAS, 442, 3722

Passot T., Vázquez-Semadeni E., 1998, PRE, 58, 4501

Penston M. V., 1969, MNRAS, 144, 425

Pineda J. E., Rosolowsky E. W., Goodman A. A., 2009, ApJ, 699, L134

Portegies Zwart S. F., McMillan S. L. W., Gieles M., 2010, ARA&A, 48, 431

Posacki S., Cappellari M., Treu T., Pellegrini S., Ciotti L., 2015, MNRAS, 446, 493

Press W. H., Schechter P., 1974, ApJ, 187, 425

Price D. J., Federrath C., 2010, MNRAS, 406, 1659

Raghavan D., et al., 2010, ApJS, 190, 1

Rathborne J. M., Lada C. J., Muench A. A., Alves J. F., Kainulainen J., Lombardi M., 2009, ApJ, 699, 742

Recchi S., Kroupa P., 2015, MNRAS, 446, 4168

Rees M. J., 1976, MNRAS, 176, 483

Reggiani M. M., Meyer M. R., 2011, ApJ, 738, 60

Rice T. S., Goodman A. A., Bergin E. A., Beaumont C., Dame T. M., 2016, ApJ, 822, 52

Robertson B., Goldreich P., 2012a, ApJ, 750, L31

Robertson B., Goldreich P., 2012b, ApJ, 750, L31

Roman-Duval J., Jackson J. M., Heyer M., Rathborne J., Simon R., 2010, ApJ, 723, 492

Rosolowsky E., 2005, PASP, 117, 1403

Rosolowsky E., Blitz L., 2005, ApJ, 623, 826

Rosolowsky E. W., Pineda J. E., Kauffmann J., Goodman A. A., 2008, ApJ, 679, 1338

Ryon J. E., et al., 2015, MNRAS, 452, 525

Sadavoy S. I., et al., 2010, ApJ, 710, 1247

Salpeter E. E., 1955, ApJ, 121, 161

Sánchez-Monge Á., et al., 2014, A&A, 569, A11

Scalo J., Vázquez-Semadeni E., Chappell D., Passot T., 1998a, ApJ, 504, 835

Scalo J., Vazquez-Semadeni E., Chappell D., Passot T., 1998b, ApJ, 504, 835

Schmalzl M., et al., 2010, ApJ, 725, 1327

Schmidt W., Federrath C., Hupp M., Kern S., Niemeyer J. C., 2009, A&A, 494, 127

Schneider N., et al., 2013, ApJ, 766, L17

Schneider N., et al., 2015a, MNRAS, 453, L41

Schneider N., et al., 2015b, A&A, 578, A29

Scoville N. Z., Yun M. S., Sanders D. B., Clemens D. P., Waller W. H., 1987, ApJS, 63, 821

Shu F. H., 1977, ApJ, 214, 488

Shu Y., et al., 2015, ApJ, 803, 71

Simon M., 1997, ApJ, 482, L81

Sołtan A. M., Chodorowski M. J., 2015, MNRAS, 453, 1013

Sonnenfeld A., Treu T., Marshall P. J., Suyu S. H., Gavazzi R., Auger M. W., Nipoti C., 2015, ApJ, 800, 94

Spaans M., Silk J., 2000, ApJ, 538, 115

Sparre M., Hayward C. C., Feldmann R., Faucher-Giguère C.-A., Muratov A. L., Kereš D., Hopkins P. F., 2015, preprint, (arXiv:1510.03869)

Spiniello C., Trager S. C., Koopmans L. V. E., Chen Y. P., 2012, ApJ, 753, L32

Springel V., Hernquist L., 2002, MNRAS, 333, 649

Squire J., Hopkins P. F., 2017, MNRAS, in press, arXiv:1702.07731,

Stahler S. W., 2010, MNRAS, 402, 1758

Stamatellos D., Whitworth A. P., Hubber D. A., 2012, MNRAS, 427, 1182

Stanke T., Smith M. D., Gredel R., Khanzadyan T., 2006, A&A, 447, 609

Stutzki J., Bensch F., Heithausen A., Ossenkopf V., Zielinsky M., 1998, A&A, 336, 697

Su K.-Y., Hopkins P. F., Hayward C. C., Faucher-Giguere C.-A., Keres D., Ma X., Robles V. H., 2016, preprint, (arXiv:1607.05274)

Svoboda B. E., et al., 2016, ApJ, 822, 59

Swinbank A. M., et al., 2011, ApJ, 742, 11

Swinbank A. M., et al., 2015, ApJ, 806, L17

Tang X. D., et al., 2017, A&A, 600, A16

Tohline J. E., 2002, ARA&A, 40, 349

Tosaki T., et al., 2017, PASJ, 69, 18

Treu T., Auger M. W., Koopmans L. V. E., Gavazzi R., Marshall P. J., Bolton A. S., 2010, ApJ, 709, 1195

Truelove J. K., Klein R. I., McKee C. F., Holliman II J. H., Howell L. H., Greenough J. A., 1997, ApJ, 489, L179

Urban A., Martel H., Evans N. J., 2010, ApJ, 710, 1343

Vazquez-Semadeni E., 1994, ApJ, 423, 681

Vázquez-Semadeni E., García N., 2001, ApJ, 557, 727

Veltchev T. V., Klessen R. S., Clark P. C., 2011, MNRAS, 411, 301

Walch S., Whitworth A. P., Girichidis P., 2012a, MNRAS, 419, 760

Walch S. K., Whitworth A. P., Bisbas T., Wünsch R., Hubber D., 2012b, MNRAS, 427, 625

Warren M. S., Abazajian K., Holz D. E., Teodoro L., 2006, ApJ, 646, 881

Weidner C., Ferreras I., Vazdekis A., La Barbera F., 2013, MNRAS, 435, 2274

Weisz D. R., Skillman E. D., Cannon J. M., Dolphin A. E., Kennicutt Jr. R. C., Lee J., Walter F., 2009, ApJ, 704, 1538

Weisz D. R., et al., 2015, ApJ, 806, 198

Wetzel A. R., Hopkins P. F., Kim J.-h., Faucher-Giguere C.-A., Keres D., Quataert E., 2016, preprint, (arXiv:1602.05957)

Whitworth A. P., Boffin H. M. J., Francis N., 1998, MNRAS, 299, 554

Wiersma R. P. C., Schaye J., Smith B. D., 2009, MNRAS, 393, 99

Zamora-Avilés M., Vázquez-Semadeni E., Colín P., 2012, ApJ, 751, 77

Zentner A. R., 2007, International Journal of Modern Physics D, 16, 763

Zhang Q., Fall S. M., 1999, ApJ, 527, L81

Zhang Q., Fall S. M., Whitmore B. C., 2001, ApJ, 561, 727

Zinnecker H., 1982, Annals of the New York Academy of Sciences, 395, 226

Zschaechner L. K., Ott J., Walter F., Meier D. S., Momjian E., Scoville N., 2016, ApJ, 833, 41

van Dokkum P. G., 2008, ApJ, 674, 29

van Dokkum P. G., Conroy C., 2010, Nature, 468, 940

van Dokkum P. G., Conroy C., 2011, ApJ, 735, L13

van de Voort F., Quataert E., Hopkins P. F., Kereš D., Faucher-Giguère C.-A., 2015, MNRAS, 447, 140